Caractérisation du fonctionnement des failles actives à l'Est de l'Iran par approches couplées géodésiques (GPS et InSAR) et tectoniques; implications sur l'aléa sismique

Zahra Mousavi

UNIVERSITÉ DE GRENOBLE

THÈSE

Pour obtenir le grade de

DOCTEUR DE L'UNIVERSITÉ DE GRENOBLE

Spécialité : **Sciences de la Terre, l'Univers et l'Environnement**

Arrêté ministérial : 7 août 2006

Présentée par

Zahra MOUSAVI

Thèse dirigée par **A. Walpersdorf, E. Pathier et R.T Walker**

préparée au sein du **Institut des Sciences de la Terre**
et de **l'école doctorale Terre Univers Environnement**

Characterization of active fault behavior in eastern Iran using a combined geodetic (GPS and InSAR) and tectonic approach; implications on seismic hazard

8 November 2013 ,
devant le jury composé de :

M. Talebian
Director of Research Institute for Earth Sciences, GSI, Tehran, Iran, Rapporteur
P. Vernant
Maître de Conférences, University Montpellier 2, , Rapporteur
J. De Sigoyer
Professeur, Université Joseph Fourier, ISTerre, France, Examinateur
B. Fruneau
Maître de Conférences, Universite de Marne-la-Val16e, France, Examinateur
B. Meyer
Professeur, Universite Pierre et Marie Curie, France, Examinateur
A. Walpersdorf
Physicienne, ISTerre, Université Joseph Fourier, Directrice de thèse, Directeur de thèse
E. Pathier
Maître de Conférence, Université Joseph Fourier, Co-Directeur de thèse
R.T Walker
University Research Fellow, University of Oxford, UK, Co-Directeur de thèse

Abstract

Eastern Iran has a crucial role in accommodating the Arabia-Eurasia convergence. We used permanent and campaign Global Positioning System (GPS) networks to estimate the present-day kinematics and the slip rates on most faults in Central-Eastern Iran and Kopeh Dagh. Also we used differential Synthetic Aperture Radar (SAR) interferometry to estimate the interseismic deformation along two major faults in Eastern Iran, the Shahroud and Doruneh faults. In Eastern Iran, 14 mm/yr of right-lateral shear is accommodated on the East-Lut, West-Lut, Kuhbanan, Anar and Dehshir right-lateral faults. These faults slip laterally at 5.6± 0.6, 4.4 ± 0.4, 3.6 ± 1.3, 2.0 ± 0.7 and 1.4 ± 0.9 mm/yr, respectively from east to west and they divide the Central-Eastern Iranian crust in five blocks that are moving northwards at 6-13 mm/yr with respect to Eurasia. The NS faults accommodate additional NS shortening by rotating counterclockwise in the horizontal plane, at current rates of up to 0.8°/Ma. In the North of theses faults is situated the EW orientated left-lateral Doruneh fault. We obtain less than 4 mm/yr of slip rate using SAR ENVISAT data which correspond to the GPS results from average velocity differences to each side of the fault. North of Doruneh, our GPS velocities suggest a rigid-body rotation of the South Caspian Basin (SCB) about an Euler pole that is located further away than previously thought. This NW motion of SCB is accommodated by right-lateral slip on the Ashkabad fault (at a rate of up to 7 mm/yr) and by up to 4-6 mm/yr of summed left-lateral slip across the Shahroud left-lateral strike-slip system. The time series analysis of two ENVISAT SAR images covering the Shahroud faults system helps localizing the left-lateral slip on individual faults. We perform a 2-D elastic half-space modeling of two tracks. The modeling results yield 4.75±0.5 mm/yr of left-lateral slip rate on the Abr (∼ longitude 55°) and Jajarm (∼longitude 56°) strand of the Shahroud fault system with a 10±4 km locking depth, highlighting the important contribution of these faults to seismic hazard in the highly populated NE Iran.

Keywords: Iran, Lut block, GPS, SAR, Shahroud fault, Doruneh fault

Á mes parents.

Acknowledgement

I would like, first of all, to thank my supervisors: Andrea Walpersdorf, Richard Walker and Erwan Pathier. I thank their valuable and constructive suggestions during the planning and development of this research work. I thank their support, their advice, their sympathy, their monitoring and involvement in my work and their availability even during week-ends. I thank them for giving me this opportunity to learn several things from them. I would like to specially thank Cecile Lassere and Marie-Pierre Doin for their constructive suggestions, for their availability, their contribution and their friendship during my thesis.

I would like to thank National Cartographic Center for supporting my thesis and providing me GPS data for my studies. I would like to specially thank Farokh Tavakoli and Hamidreza Nankali for their admirable supporting during my thesis. Also I would like to thank my colleagues of National Cartographic Center who contribued in the GPS networks establishment in Iran: Farokh Tavakoli, Hamidreza Nankali, Yahya Djamoir, Zohreh Rahimi, Fatemeh Khorami, Azadeh Aghamohammadi, Sedigheh Hosseini, Mahnaz Alijanzadeh and Najmeh Eftekharzadeh.

I thank all the members of ISTerre for providing such a comfortable environment to work and their scientific contributions. I would like to thank my colleagues, Guilllemm baque and Romain Jollivet and Fanny Potton. I thank all PhD students of ISTerre for their friendship. I enjoyed the every moment we spent together. Special thanks to Jing, Johanes, Ainhoa, Anne, Hilal, Afifa, Anne, Alex, Stefano, François, Olga and Virginie for their wonderful friendship. I spent great time with them.

Many thanks to my other friends: Alireza, Somi, Shadi, Behrouz, Azadeh, Hiva and Elahe for their wonderful friendship. I thank them for their time and outstanding support from the beginning to the end.

My very special thanks to Amir, Sophie and Sylvain for their great friendship, our scientific discussion and their kindness from the beginning to the end of my thesis.

I thank my family: my parents, my sisters and my brothers for their long distance but limitless support and encouragement that yield a great motivation during all of my long term educations.

Contents

Chapter 1

Introduction

Contents

1.1 Motivation

The Earth's crust is constantly in motion, with every part of the surface moving due to plate tectonics, and constantly deforming. The Earth is subject to a variety of periodic, steady and transient deformations. Nowadays modern space-based geodetic techniques provide the ideal tools for studying the kinematics and dynamics of the earth. Figure 1.1 presents the geodetic velocity field for Alpine Himalayan belt. Using the geodetic studies can help us to answer first order question about deformation pattern and fault slip rates. Also, we can test the kinematic models suggested for tectonic. Altogether it will bring the new information for seismic hazard assessment. But according to the figure 1.1, there is gap in the geodetic velocity field of Iran which is located in the central part of Alpine Himalayan belt.

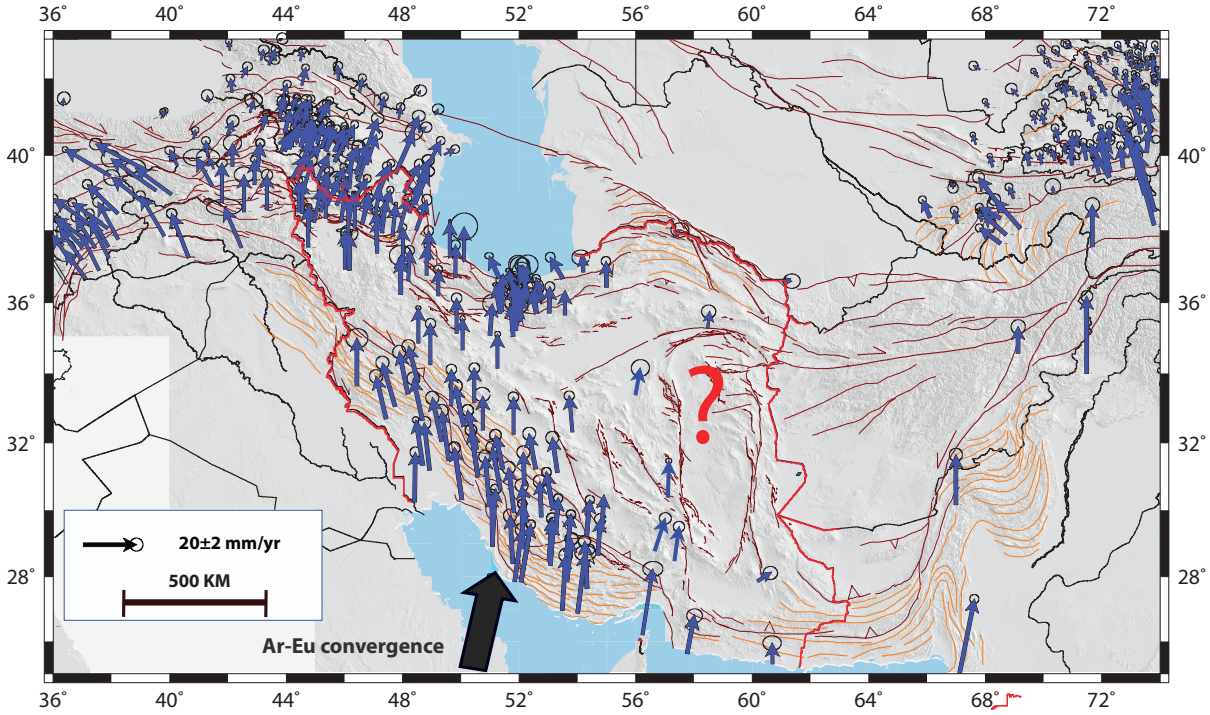

Figure 1.1 – Available GPS velocity field for Anatolian region [Reilinger et al., 2006], Iran global [Nilforoushan et al., 2003, Vernant et al., 2004a, Masson et al., 2005, 2007], Alborz [Vernant et al., 2004a, Djamour et al., 2010], Zagros [Bayer et al., 2006, Walpersdorf et al., 2006, Tavakoli et al., 2008], north west of Iran [Masson et al., 2006, Djamour et al., 2011], Pakistan [Mohadjer et al., 2010], Tibet [Zubovich et al., 2010], Armenia [Karakhanyan et al., 2013]. The red lines shows the political border of Iran. The active faults map is from Isabelle Manighetti.

Iran often experiences large and destructive earthquakes. This active deformation is related to the Arabia-Eurasia plate convergence that takes place inside Iran's political borders, the Persian Gulf coast being situated on the Arabian plate, and NE Iran being part of stable Eurasia. Figure 1.1 presents the different ways of accommodating the shortening in eastern and western part of Iran. In the western part, the deformation is accommodated gradually but in the eastern part the geodetic constraints on the major faults are missing

and this makes a gap in the geodetic velocity field in this active belt. The 16 mm/yr of northward convergence is absorbed on these faults and the velocity vectors die out close to the eastern political border of Iran.

The comparison between seismicity and first geodetic results throughout Iran [Vernant et al., 2004b, Masson et al., 2007] indicates that the high strain is released in different ways in different parts of the country: We observe rather aseismic deformation in southern Iran such as Zagros, but mainly seismic deformation in northern and eastern Iran. Therefore, mainly low-magnitude but frequent earthquakes happen in Zagros, and less frequent but large earthquakes occur in northern and eastern Iran (Fig. 1.2).

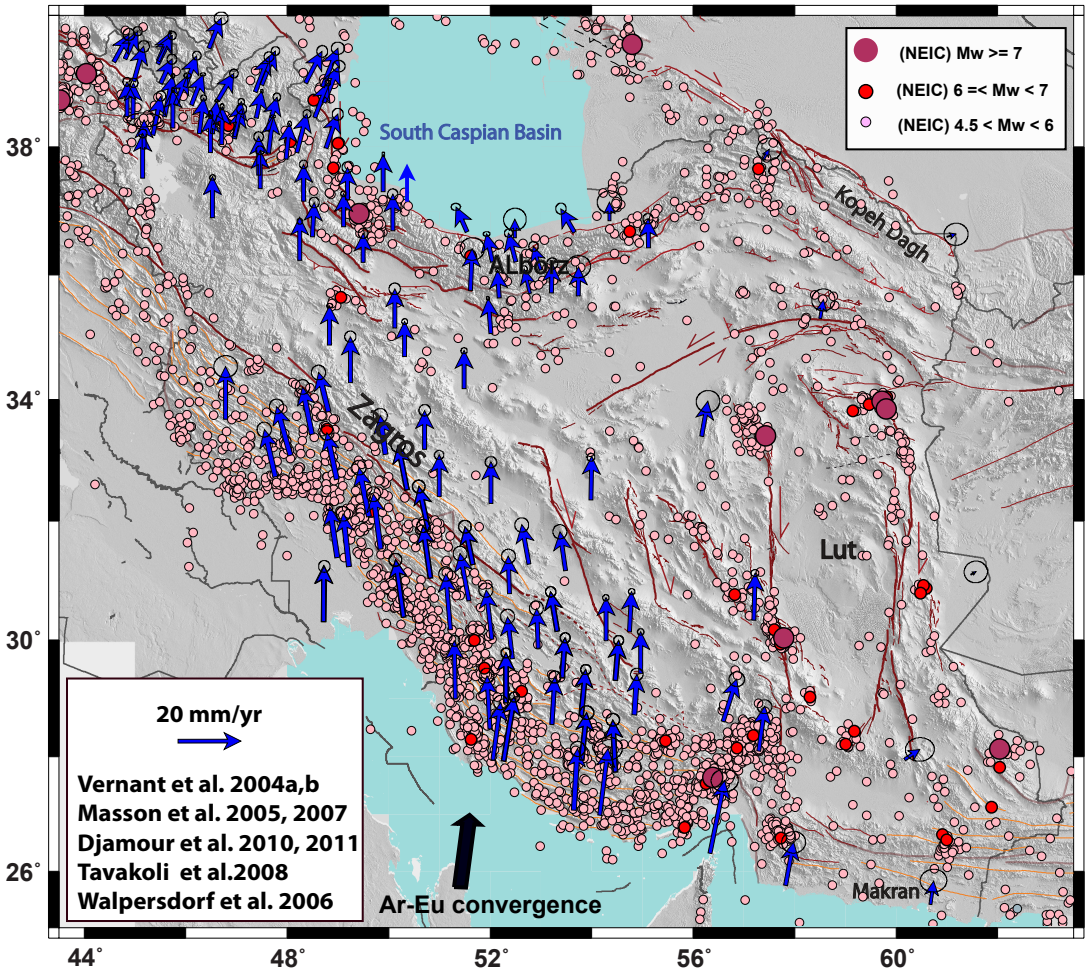

Figure 1.2 – Seismic activity in Iran. The dots present the instrumental earthquakes catalogue (from USGS catalogue NEIC: http://neic.usgs.gov/neis/epic/) and blue vectors are GPS velocity field from [Vernant et al. [2004b], Walpersdorf et al. [2006], Masson et al [2007], Tavakoli et al. [2008] and Djamour et al. [2010], [2012] . The green vector is the direction of Arabia-Eurasia convergence. The black lines are active faults and gray lines are the political border of Iran. The green stars are the Tabriz, Tehran and Mashhad cities from west to the east, respectively. Abbreviations are ALB: Alborz, ZAG: Zagros, D: Doruneh fault, EL: East Lut fault, WL: west Lut fault, DS: Deshir fault, KB: Kuhbanan fault. A: Anar fault.

In order to better evaluate seismic hazard, dense GPS networks have been analyzed in many parts of Iran: (Zagros [Walpersdorf et al., 2006, Meyer et al., 2006, Tavakoli et al.,

2008], Alborz [Vernant et al., 2004a, Djamour et al., 2010], northwestern Iran (Tabriz) [Masson et al., 2006, Djamour et al., 2011]), including regions of large cities like Tehran with a population of around 8.3 million inhabitants and surpassing 14 million in the wider metropolitan area, and Tabriz with 2.5 million inhabitants. However, there is still an observational gap in NE Iran, in particular for evaluating seismic hazard for the ∼3 million inhabitants of the city of Mashhad.

Using GPS networks for measuring present-day deformation studies in NE Iran including the Mashhad region started a few years ago by Tavakoli [2007]. One objective of this thesis was to complete this study and go one step further by combining GPS and satellite radar imagery (SAR). A first look at the active fault map (Fig. 1.2) shows that north-eastern Iran is cut by large faults (East Lut fault, West Lut fault, Doruneh and Shahroud faults) that separate blocks with a relative seismic quiescence (Lut, South Caspian Basin and Central Iran Block) . The present-day kinematics of the area is still not well known, motivating the study of these blocks and faults by establishment of an extensive GPS network. In addition, Using SAR interferometry (InSAR), we focus on the two large left-lateral faults, Doruneh and Shahroud faults, in eastern Iran that have a favorable orientation for InSAR studies in order to investigate their slip rate, hereby completing the GPS network that is particularly sparse around these faults.

In this thesis work, we hope to establish a coherent detailed picture of NE Iran present-day kinematics, including the quantification of precise fault slip rates for helping seismic hazard estimation.

1.2 Arabian-Eurasian convergence

One of the most seismic areas of continental deformation in the world is the Alpine-Himalayan mountain belts which stretch from the Mediterranean to China. It has experienced destructive and disastrous earthquakes totalizing roughly 60% of the global death toll due to earthquakes since 1900.

The deformation in the Alpine-Himalayan belt is the result of the convergence between the Eurasian-African plates (1-2cm/yr), Arabia-Eurasian plates (2-3cm/yr) and Indian-Eurasia plates (3-4cm/yr). Inside this semi-continuous belt, active tectonics in Iran is the result of the roughly northward movement of the Arabian plate with respect to the Eurasian plate.

In the Middle East, the boundary between Arabia and Eurasia is formed by the Zagros suture zone. GPS results indicate that the Arabian plate is moving northward of 18 ± 2 mm/yr relative to Eurasia at a longitude of 48° [McClusky et al., 2000]. The convergence rate increases eastward and reaches 22±2 mm/yr and 26 ± 2 mm/yr at the longitudes of 50.5° and 58.5°E, respectively, as shown in figure 1.3 [Vernant et al., 2004b, Masson et al., 2007]. The Arabia-Eurasia Euler pole is located in the northeast of Africa

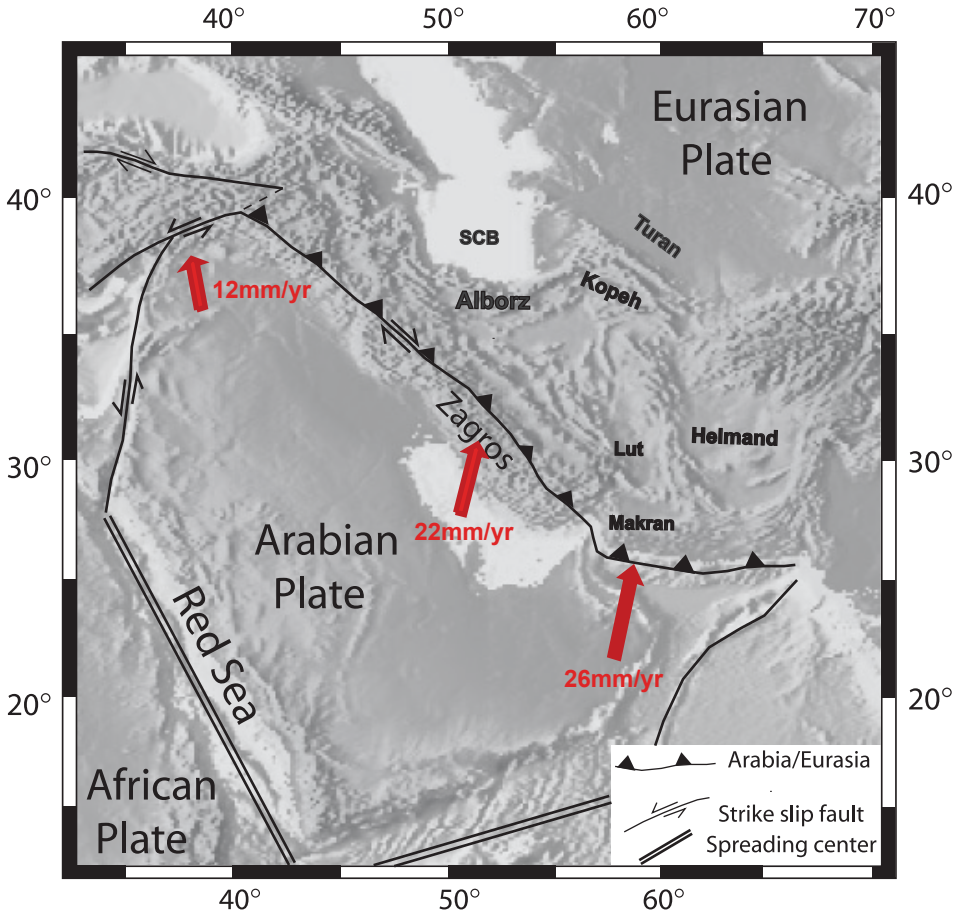

Figure 1.3 – Arabian-Eurasian collision zone: The black lines present the plate boundaries. The vectors show the present-day convergence direction and velocity [Reilinger et al., 2006].

at ∼27.4°N and 18.4°E and the inferred motion of Arabia with respect to Eurasia is a counter-clockwise rotation with a rate of 0.4°/Ma [Vernant et al., 2004b].

The collision of Arabia and Eurasia occurred following the subduction of the Arabian oceanic lithosphere under Eurasia during the closing of the Tethys Ocean (Fig. 1.4). The initiation age of the Arabian-Eurasian collision varies in the range of 3 to 65 Ma according to different authors. Berberian and King [1991] proposed ∼65 Ma of initiation age, later Mcquarrie et al, [2003] suggested less than 10 Ma based on sea floor magnetic anomalies across the Red Sea (Fig. 1.4). Furthermore, Allen et al, [2004] proposed 3-7 Ma for the collision age based on total displacements accommodated across major fault zones since the onset of the collision.

1.3 Seismicity in Iran

Many destructive historical and instrumental earthquakes have been recorded in Iran (Fig. 1.5). Most of the earthquakes inside Iran are related to localized deformation zones such as Zagros, Alborz and Kopeh Dagh. But the rate of seismic deformation is not

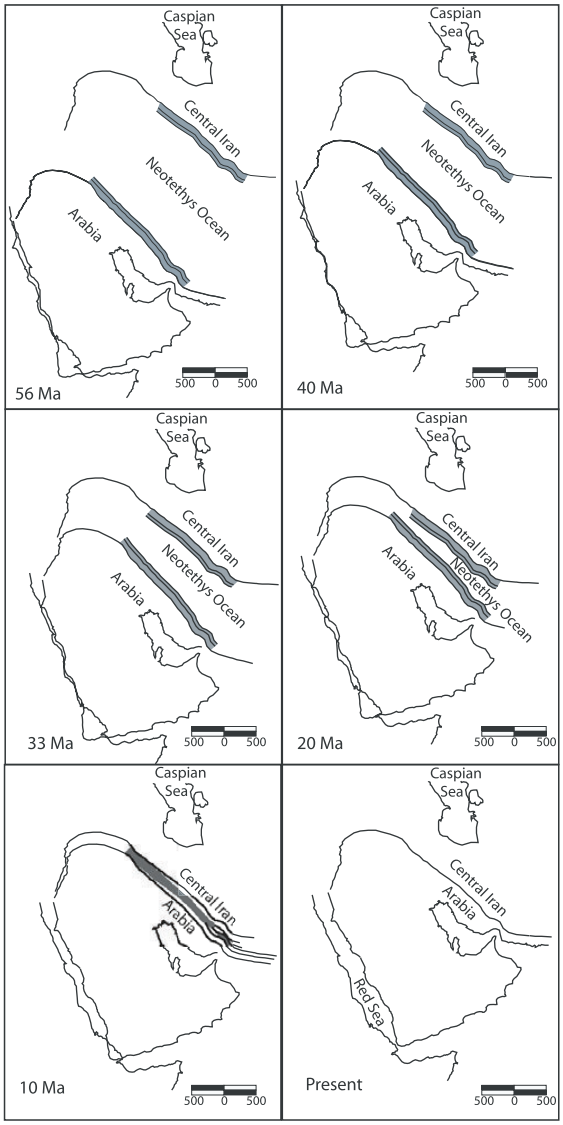

Figure 1.4 – Map reconstruction of the evolution of the Neotethys. The figure presents that oceanic subduction was ongoing in central Iran until 10 Ma, turning since then into continental collision in the Zagros fold belt. [McQuarrie et al., 2003].

uniform [Masson et al., 2005]. The deformation is released mostly aseismically in Zagros (Fig. 1.2), while the Alborz and central Iran suffer from less frequent but destructive large earthquakes. These earthquakes in Iran cause lots of destruction and disaster and make Iran one of the countries with the largest number of victims due to earthquakes worldwide.

Although most earthquake victims are caused by earthquakes occurring inside the continents rather than on the plate boundaries, the locations of intracontinental faults are still unclear as well as their behavior in time, thus it seems a priority to improve seismic hazard knowledge in the continental interiors [England and Jackson, 2011, Walters, 2012].

In Iran, large intracontinental earthquakes, with magnitudes larger than 6, killed 126,000 persons during the last century [Tavakoli, 2007]. Unfortunately, this will continue, as large population centers in Iran are located close to active fault zones, such as Tehran,

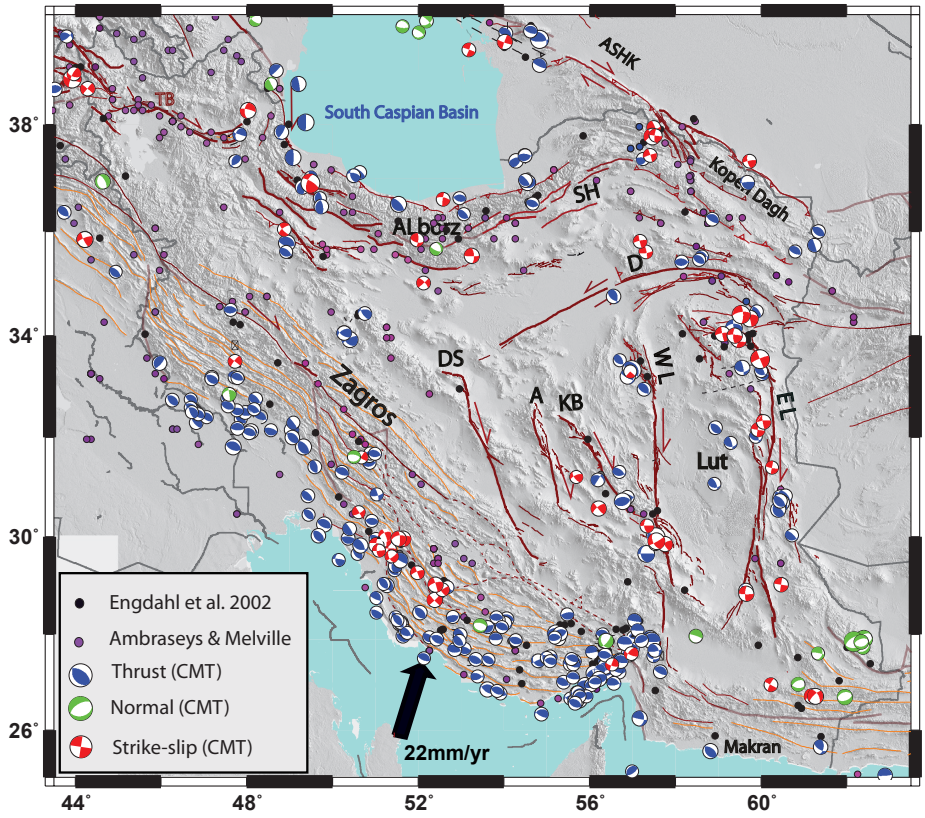

Figure 1.5 – Historical and instrumental seismicity of Iran with magnitude Mw $\geq$ 5 from 1973 to 2012 (from USGS catalogue NEIC: http://neic.usgs.gov/neis/epic/). The blue, green and red focal mechanisms indicate thrust, normal and strike-slip faulting events, respectively.

Tabriz, and Mashhad. This may be partly explained because active faulting is often related to water sources which are important in an arid country like Iran [Jackson, 2006].

1.4 Current deformation in Iran

Iran is located in between relatively rigid, aseismic blocks: Arabia to the southwest, the Turan Shield (belonging to the Eurasian plate) to the northeast and the Hellmand block (Eurasian plate) to the east [Jackson and McKenzie, 1984, Jackson et al., 1995] (Fig. 1.3). Active tectonics of the Iranian plateau is dominated by the continental convergence between the Arabian and Eurasian plates except along the Makran oceanic subduction zone in the southeast of the plateau. This convergence is accommodated by a mixture of thrust and strike-slip faulting in the Zagros, Alborz and Kopeh Dagh mountain ranges (note the earthquake distribution and their mechanisms in figure 1.5). Therefore convergence is absorbed by shortening, thickening of the crust, and strike-slip motions on major faults. These major faults bound more or less rigid blocks that are relatively aseismic such as the Central Iran block, the South Caspian basin and the Lut block [Jackson and McKenzie,

1984, 1988]. The different convergence mechanism in South Iran (continental collision and oceanic subducion) leads to different ways of accommodating the convergence in Eastern and Western Iran.

Since a few years, long-term average slip rates have become available by dating of geomorphological marker offsets for more and more faults in Iran. This work has been done in particular for some major faults in eastern and north eastern Iran, notably on the Doruneh fault[Fattahi et al., 2006b], the Astaneh fault [Rizza et al., 2011], the Abr and Khij fault [Javidfakhr et al., 2011a] and the Baghan Quchan fault zone [Shabanian et al., 2009a]. Tectonic velocities are averaged over several thousands to million years. The individual fault slip rates obtained are between 0.5 and 5 mm/yr. Geodetic slip rates in NW Iran were still rare with only a large scale GPS network in this region before this work. We will be able to compare geodetic and tectonic fault slip rates. In general, the geodetic slip rate for strike slip faults is consistent with geological estimates and shows that GPS fault slip rates can be extrapolated in the past.

Global and local GPS campaign networks have been established in Iran since 1997. These networks provide a global velocity field [Nilforoushan et al., 2003, Vernant et al., 2004b], and more detailed kinematics of the deformation zones in the North and Central Zagros, the Zagros-Makran transition, the Alborz (Central Alborz and Tehran) and the Tabriz region in northwest Iran [Djamour et al., 2010, 2011, Masson et al., 2005, 2007, Tavakoli et al., 2008, Walpersdorf et al., 2006, Vernant et al., 2004a]. According to figure 1.2, the GPS velocities for stations relative to Eurasia decrease to zero at both the northern and eastern borders of Iran. This indicates that the Arabia-Eurasia convergence is accommodated inside the political border of Iran, but it is accommodated differently in the eastern and the western parts of the country.

To the east of 58° E, most of the convergence is accommodated by the Makran subduction zone [Vernant et al., 2004b], with the small remaining shortening taken up by the Kopeh Dagh and other mountain ranges in NE Iran. West of 58°E, the Zagros accommodates oblique compression by a mixture of thrust and right-lateral faulting. The remaining convergence of 16 mm/yr in Central Iran [Vernant et al., 2004b] takes place in the Alborz, Caucasus and Kopeh Dagh mountain ranges. This differential shortening between Makran and the Zagros causes ∼16mm/yr of N-S right-lateral shear between central Iran and Afghanistan, across eastern Iran. This shear is accommodated on N-S right-lateral faults on both sides of the Lut block in Eastern Iran [Vernant et al., 2004b, Walker and Jackson, 2004] and EW left-lateral faults further north, such as the Doruneh fault. Consequently, Eastern Iran has a crucial role in accommodating N-S right-lateral shear between central Iran and Afghanistan. North of the Lut block, the remaining shortening of ∼7 mm/yr is absorbed on deformation zones such as Kopeh Dagh and Eastern Alborz.

The Kopeh Dagh and East Alborz mountains constitute the northern part of the Arabia-Eurasia collision zone in NE of Iran from 52° E to 62° E. These mountain ranges

extend from the south of the Caspian basin to the Afghanistan border and separate the Turan platform, part of Eurasia, from Central Iran. In the northwest, the South Caspian Basin moves independently from both Eurasia and Iran, and it is thought to move to the NW relative to Eurasia at 7–10 mm/yr as it subducts under the Apsheron-Balkhan Sill [Jackson et al., 2002]. This motion is likely to be accommodated on the NE and SE along the Ashkabad and Astaneh-Shahroud fault system.

1.5 Objectives

While the western part of Iran is fairly well instrumented, there is a gap in geodetic studies in eastern Iran (Figure 1.2) as a part of the Alpine-Himalayan belt. Thus the kinematic behavior of the large NS right-lateral faults and EW oriental left-lateral fault in Eastern and NE Iran, as well as active fault behavior in Kopeh Dagh and Eastern Alborz are not well-known. This is the first motivation to go one step further than the global studies and examine in detail the interseismic behavior of the major active faults in north eastern Iran. In particular, we would like to know how present-day deformation

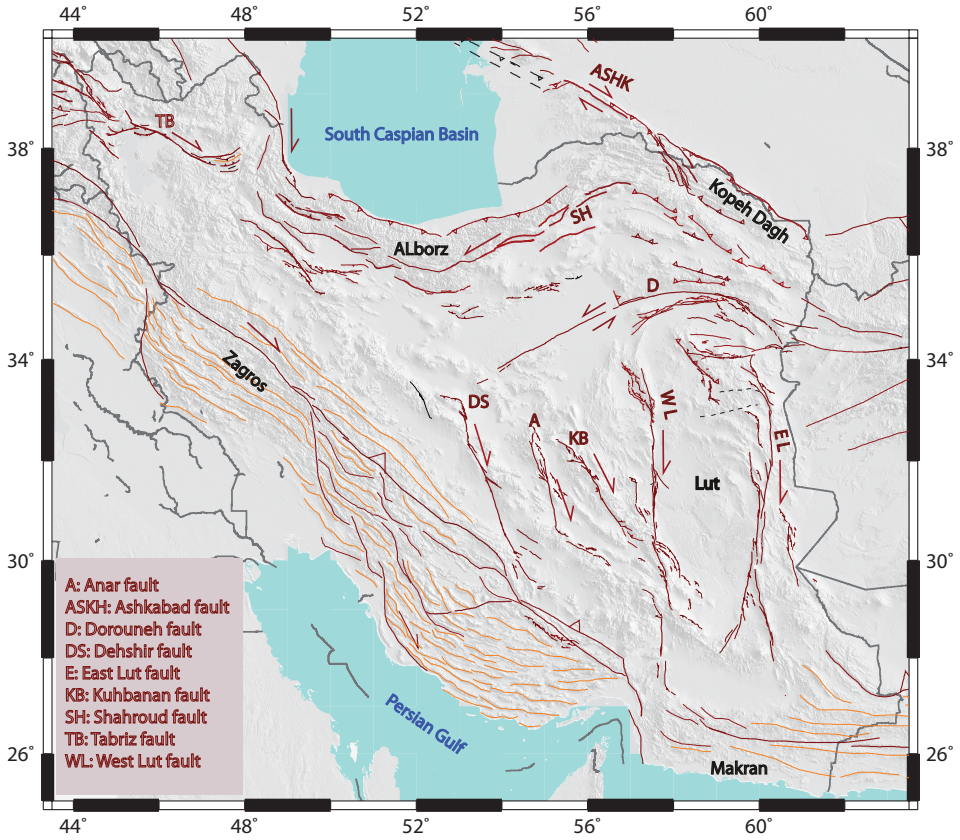

Figure 1.6 – Active tectonic map of Iran. The major active faults (from Manighetti,. I, personal communication and Walker et al., 2009) are imposed on SRTM topography

is accommodated in two key areas:

- First, how is the NS shear between Central Iran and Afghanistan accommodated on NS right-lateral strike-slip faults and EW left-lateral faults bounding the Lut block in eastern Iran.
- Second, how is the remaining shortening north of the Lut block accommodated in Kopeh Dagh and what is the effect of present-day Kopeh Dagh kinematics on the motion of the South Caspian Basin relative to Eurasia. Moreover, what are the consequences on the bounding faults, such as the Shahroud fault and the Ashkabad fault.

Approach for East of Iran (Lut block):

The most popular tectonic model for eastern Iran is the block rotation model [Walker and Jackson, 2004, Allen et al., 2011]. According to this model, south of the Doruneh fault, the NS shear between Central Iran and Afghanistan is mostly taken up on NS oriented right-lateral faults surrounding the aseismic Lut block. On the western boundary is situated the West Lut fault system (Gowk-Nayband), and on the eastern boundary the East Lut fault systems (Sistan suture zone). These active faults in eastern Iran produce large earthquakes (M $\cong$ 7) like Abiz (1997), Tabas (1978) and Bam (2003) and are a large source of seismic hazard. In this study we would like to provide the short-term behavior of the large active faults, and highlight their roles in the recent to current tectonics of Central-Eastern Iran. We would like to investigate whether the block rotation theory can explain the shear accommodation in Eastern Iran.

One of the longest Iranian faults, the EW trending Doruneh fault with 600 km length and clear geomorphologic trace on the surface is located north of 34° N. Fattahi et al., [2006b] estimate 2.4 ± 0.3 mm/year for the Doruneh fault using luminescence dating. The preliminary result of the Iranian permanent GPS network indicates 2.5 ±2 mm/yr of left-lateral slip rate at the longitude of ∼58 °E, 1.5±2 mm/yr at the longitude of ∼ 59 °E and 1±2 mm/yr at the longitude of ∼60.5 °E [Tavakoli, 2007]. Then, the previous SBAS DinSAR analysis technique across the central part of the Doruneh fault indicates a slip rate of 5 ± 1 mm/yr accumulated on the fault below 10 km depth at longitude of 56-57 ° E [Pezzo et al., 2012]. The current slip rate is important for hazard assessment. The difference of 2.5 mm/yr from GPS and 5.0 mm/yr from SAR is significant for it. We want to clarify this discrepancy between two geodetic measurements and examine whether GPS is underestimating the slip rate, or if the DInSAR investigation around Doruneh fault needs to be refined.

Approach for North East of Iran :

We will provide new GPS constraints on the active tectonics of NE Iran and the South Caspian region. This can help to better understand the ongoing tectonics in this part of Iran which is still debated. We would like to see if the deformation of the Kopeh Dagh region can be described as continuous deformation or localized deformation on active faults

bounding rigid blocks [Shabanian et al., 2009a]. West of Kopeh Dagh, the South Caspian Basin kinematics play a key role to infer fault activity on its boundaries. The South Caspian Basin (SCB) motion is accommodated on the Shahroud and Ashkabad faults. It is still under debate whether the SCB is translating or rotating, implying significant different slip rates on the bounding faults. To add some new constraints to this debate, we propose to determine by a combined approach using GPS and InSAR how much left-lateral motion is accommodated on the Shahroud fault system in Eastern Alborz.

1.6 Plan of thesis

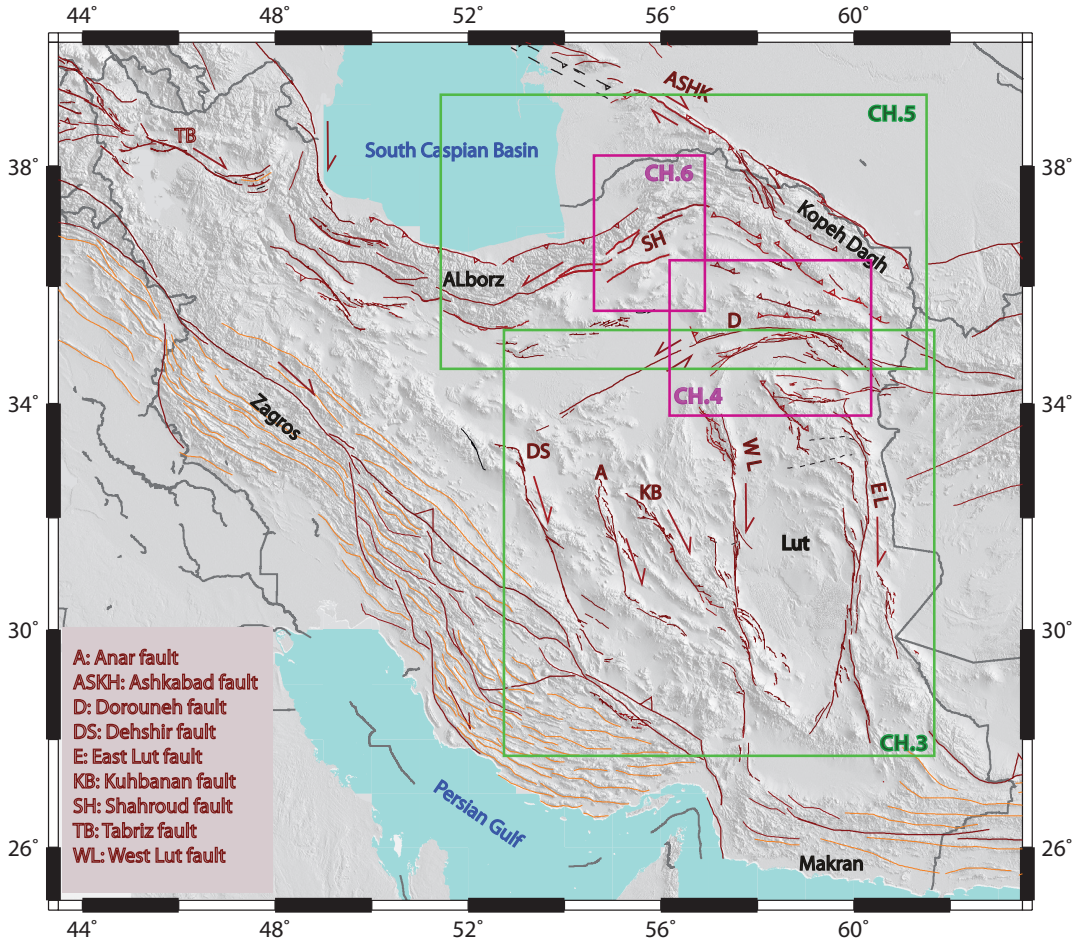

Figure 1.7 – Location of the studied areas: The rectangles show the locations of the study areas for the following chapters. The green rectangles present two chapters which use Global Positioning System to constrain interseismic deformation and the pink ones indicate the area where we used InSAR to estimate interseismic slip rates of faults. The major active faults (from Manighetti,. I (personal communication) and Walker et al., 2009) are super imposed on shaded SRTM topography.

This thesis is organised as follows:

Chapter 2 outlines the geodetic (GPS and InSAR) methodology, shows the present-day understanding of the seismic cycle and explains the principle of the rigid block modeling.
Chapter 3 is adapted from Walpersdorf et al. [2013] (*New insights on the recent and current deformation in Central-Eastern Iran, derived from a combined tectonic and GPS analysis*, in review at Journal of Geophysical Research) and describes the GPS analysis of almost 100 stations in Central-Eastern Iran and the tectonic interpretation of the obtained velocity field.
Chapter 4 describes the results of an interseismic InSAR study of the Doruneh fault.
Chapter 5 is adapted from Mousavi et al. [2013](*Global Positioning System constraints on the active tectonics of NE Iran and the South Caspian region*, Published in Earth and Planetary Science Letters) and describes the implication of new, dense GPS velocity field on active tectonics in NE Iran and the South Caspian region.
Chapter 6 describes the results of InSAR measurements of the interseismic deformation across the Shahroud fault system.
Chapter 7 summarizes the findings of the previous chapters, gives some general conclusions of our study, and describes the further work that can be undertaken in this area.

Chapter 2

Methodology

Contents

2.1 Introduction

Geodesy is the science of measuring size and shape of the Earth and variations of terrestrial gravity. Modern methods like satellite based geodesy solve two aspects of geodesy, physical Geodesy (the study of the physical properties of the gravity field of the Earth) and positional Geodesy (the study of the estimating the position of point), simultaneously. Modern methods started with the development of distance measurement using propagating electromagnetic signals and the launch of Earth-orbiting satellites. With these developments, space-based geodesy allowed global measurements of positions, changes in the rotation of the Earth, and the Earth's gravity field [Herring, 2007]. Here we use two modern techniques of geodesy, Global Positioning System (GPS) and Synthetic Aperture Radar (SAR) interferometry to obtain new observations of the crustal deformation in Eastern and North-Eastern Iran.

The high precision of GPS measurements (1mm level) allows this system to become the geodetic method for studying a wide range of geophysical phenomena which is especially important for monitoring natural hazards. By analyzing repeated measurements on groups of GPS stations, it is possible to study the motion of Earth's tectonic plates, to study deformation around active faults and volcanoes, measure the adjustment of earth's surface due to change in world's ice sheet, and contribute to atmospheric studies [Shrestha, 2003, Outerbridge, 2011]. One specific role of crustal deformation measurements is the study of earthquakes. These measurements play an important role in improving the knowledge of the full earthquake cycle, including interseismic, coseismic and postseismic phases of the cycle. The interseismic period can be monitored by tracking the relative velocities between networks of stations in and around plate boundaries. Earthquake rupture parameters during the coseismic step can be analyzed by using measurements of co-seismic displacements of stations located within a few rupture lengths of the fault. Finally, analyzing the decay signature (exponential, logarithmic, etc.) of station positions in the days to decades following an earthquake helps to study the transient post-seismic processes [Segall and Davis, 1997, Herring, 2007].

Space-borne Synthetic Aperture Radar (SAR) is also an all-weather technique with global coverage. It has the interest to be able to record ground to satellite distance with a high spatial sampling resolution (typically a few tens of meters) [Massonnet and Feigl, 1998, Bürgmann et al., 2000, Zebker, 2000, Rosen et al., 2000, Curlander and McDonough, 1991, Hanssen, 2001]. In the last decades many SAR satellite have been launched and operated such as the European ERS 1 and 2 and their successors ENVISAT, the Canadian RadarSat 1 and 2, the Japanese JERS and ALOS, the Italian Cosmo Sky Med and the German TerraSAR-X and Tandem-X. SAR instruments have been also carried by the US Space Shuttle in 2000, performing one of the major applications of SAR interferometry (InSAR) technique, that is the generation of Digital Elevation Models of the Earth with a

near-global scale and a 30m spatial resolution (but so far only publicly available at 90 m except for the US territory). The Shuttle Radar Topography Mission (SRTM) was using two SAR acquisitions simultaneously with two different viewing angles [Li and Goldstein, 1987, Massonnet and Feigl, 1998, Farr and Kobrick, 2000]. The launch of the ESA satellite ERS-1 in 1991, lead to a large amount of SAR data suitable for a wide range of applications. These data have been used to measure displacements of the Earth's ground due to natural phenomena such as earthquakes. Indeed, InSAR measurements were first applied to large coseismic displacements [Massonnet et al., 1993, Wright et al., 1999] and nowadays, InSAR is also used to measure interseismic deformation around faults [Bürgmann et al., 1998, Wright et al., 2001, Cavalié et al., 2008, Kaneko et al., 2013].

In the first part of this chapter, we present the GPS principles to measure interseismic deformation for active faults and in the second part, we will talk briefly about the basis of SAR and InSAR applied to ground deformation measurements. The limitations by different sources of error will be discussed, in particular tropospheric delay to measure interseismic deformation of low slip rate faults in view of applications in North-Eastern Iran. Finally, in the last section of this chapter we will explain the different approaches used in our works to model interseismic deformation using our geodetic measurements.

2.2 Global Positioning System (GPS)

GPS is the most famous of the satellite-based positioning systems which are known as Global Navigation Satellite Systems (GNSS). The GNSS include nowadays satellite positioning systems such as Global Positioning System (GPS) from USA, Galileo from the European Union, GLONASS from Russia and Compass from China. In our work, only GPS data have been analyzed. The basis of GPS operation is explained in several reference books [Hofmann-Wellenhof et al., 1993, Cobb, 1997, Blewitt, 1998, Xu, 2003, Hofmann-Wellenhof et al., 2008].

The GPS system is an accurate, continuous, worldwide and space-based navigation system designed by the U.S. Department of Defense. This system can be used to obtain three dimensional position, displacement and velocity for a ground station in a common reference system on the Earth. The GPS is established as a ranging system with known position (satellites in space) to unknown positions of stations (on land, sea, in air and space). It is based on the principle of 'trilateration', which is the method of determining positions by measuring distances to points of known positions. This system consists of 32 satellites on orbits at an altitude of 20200km. The satellites are arranged in 6 different orbital planes spaced around the equator with a 60 degree separation. They are all inclined at 55 degrees relative to the equator. With this arrangement of satellites, it is possible to receive signals from at least 4 satellites above a 15 degrees cut-off angle at any station on Earth's surface at any given time of the day [Xu, 2003, Hofmann-Wellenhof et al., 2008].

2.2.1 Principle of positioning with GPS

All satellites use the fundamental frequency $f_0 = 10.23MHz$ and broadcast signals at two frequencies accessible for civil users:

- L1 = 154 , f_0 = 1575.42 MHz, wavelength: 19,0 cm
- L2 = 120 , f_0 = 1227.60 MHz, wavelength: 24,4 cm

The GPS observations are using two codes that are modulated onto the two base carriers (L1 and L2):

- Coarse acquisition code (C/A code): with wavelength 293 m and frequency fo/10 modulated just on carrier L1.
- Precision-code (P-code): with wavelength 29.3 m and frequency f0 modulated on carrier L1 and L2.

The C/A code contains the time according to the satellite clock when the signal was transmitted. For recognition purposes, each of the satellites has a different C/A code. The P-code which designated a Precise Positioning Service (PPS) has 10 times the resolution of the C/A code. In addition to these codes, the navigation messages of the satellites are also modulated onto the carriers. These messages consist of the ephemerides information, predicted GPS satellite orbits, clock corrections, ionospheric model and satellite health status [Hofmann-Wellenhof et al., 2008].

The GPS observables are code and phase pseudoranges which come from measured time and phase difference, respectively, based on a comparison between received signals and receiver generated signals.

a) Code measurement

The code pseudorange measurement is the time the signal takes to propagate from the satellite to the receiver multiplied by the speed of light:

$$R = c.\Delta t \tag{2.1}$$

where c is the speed of light and Δt is the propagation delay of the wave from the satellite to the receiver. The difference between the pseudorange and the actual distance is due to the clock error of receiver and satellite. The travel time of the signal between satellite j and receiver i can be expressed:

$$\Delta t^{ij} = t_R^i - t_S^j \tag{2.2}$$

where t_R^i is the reception time of signal by receiver i and t_S^j is the transmission time of the signal by satellite j. In reality, there is a shift δ_R^i and δ_S^j between the clocks of the

receiver and the satellite with respect to GPS time (t_R^{GPS} and t_S^{GPS}):

$$\begin{aligned} \mathrm{t}_R^i &= t_R^{GPS} \text{ - } \delta t^i \\ \mathrm{t}_S^j &= t_S^{GPS} \text{ - } \delta t^j \end{aligned} \tag{2.3}$$

If we combine equations 2.2 and 2.3, the travel time can be expressed as:

$$\Delta t^{ij} = t_R^{GPS} - \delta t^i - t_S^{GPS} + \delta t^j = (t_R^{GPS} - t_S^{GPS}) + (\delta t^j - \delta t^i) \tag{2.4}$$

The travel time multiplied by the speed of light result in the pseudorange (in meter) between receiver i and satellite j:

$$R^{ij} = c\Delta t^{ij} = c(t_R^{GPS} - t_S^{GPS}) + c(\delta t^j - \delta t^i) \tag{2.5}$$

b) Carrier Phase measurement

The carrier phase measurement is the phase of the received carrier phase with respect to the phase generated by an oscillator in the GPS receiver. The receiver can measure only the fractional part of the carrier phase. The exact number of additional integer wavelength between the satellite and the receiver is not known. The unknown integer number of cycles (N) to be added to the fractional phase measurement is called the initial phase ambiguity. The phase ambiguity will be constant as long as the receiver does not loose lock on the carrier transmitted by the satellite (Fig. 2.1).

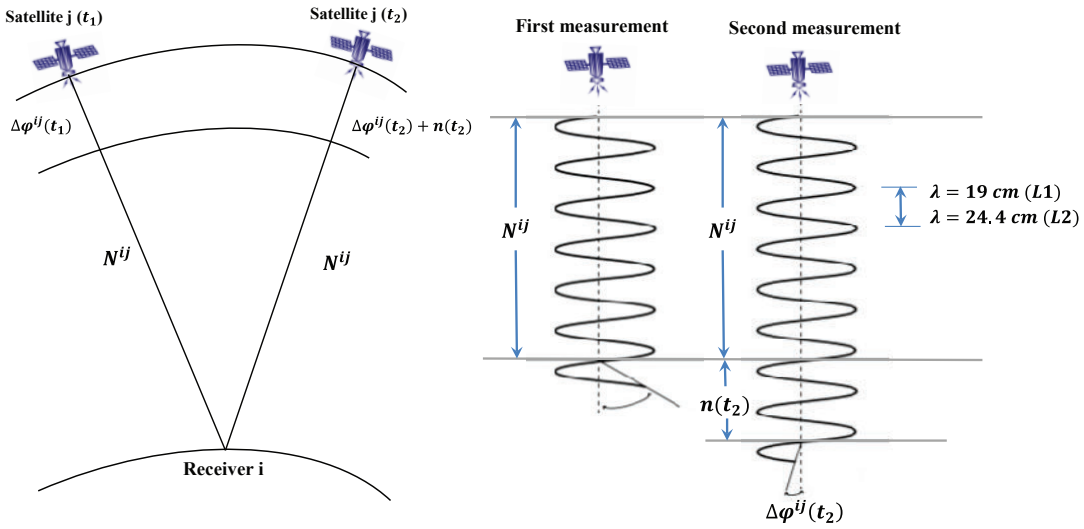

Figure 2.1 – Carrier phase measurement between satellite j and receiver i. [Biessy, 2009]

The phase observable between satellite j and receiver i can be written:

$$\phi^i(t_R^i) - \phi^j(t_S^j) = \Delta\phi^{ij}(t_R^i) + N^{ij}(t_R^i) \tag{2.6}$$

where $N^{ij}(t_R^i)$ is an unknown integer number of cycles that the receiver cannot measure and it consists of two components: first, $N^{ij}(t_1^i)$, the number of cycles measured at time t_R^1 from the initial time t_1 and second $n(t_R^i)$ the integer number of cycles at time t_1 (Fig. 2.1). Thus if there will be no interruption in signal receiving, we can rewrite the equation 2.6 based on the two components:

$$N^{ji}(t_R^i) = N^{ji}(t_1) + n(t_R^i) \tag{2.7}$$

where t_1 is the time of first measurement. Now we can express the phase observable between satellite j and receiver i based on the integer number of cycles (combination of the equation 2.6 and 2.7):

$$\Delta\phi^{ij}(t_R^i) = \phi^i(t_R^i) - \phi^j(t_S^j) - [N^{ij}(t_1) + n(t_R^i)] \tag{2.8}$$

For a satellite j and receiver i, the amount of $N^{ij}(t_1)$ is the same for whole measurement if the signal receiving is not interrupted (Fig.2.1). This value is called phase ambiguity and it will be written N^{ij} for simplification. Now the phase measurement can be explained:

$$\Phi^{ij} = \Delta\phi^{ij}(t_R^i) + n(t_R^i) = \phi^i(t_R^i) - \phi^j(t_S^j) - N^{ij} \tag{2.9}$$

Reminder:
The sinusoidal signal can be expressed by its amplitude and its phase angle:

$$x(t) = Acos(w(t - t_0)) \tag{2.10}$$

where $\omega = 2\pi f$ is the angular frequency in radians per second and ϕ_0 is phase in radians at time t_0. Therefore the phase of this sinusoidal signal in t can be written:

$\phi(t) = 2\pi f(t - t_0) + \phi_0$ (in radians)
$\phi(t) = f(t - t_0) + \frac{\phi_0}{2\pi}$ (in cycles)

Therefore the phase of the emitted signal by satellite i at t_R^i and the generated signal by receiver j at time t_R^j:

$$\phi^i(t_R^i) = f(t_R^i - t_0) + \frac{\phi_0}{2\pi} \tag{2.11}$$

$$\phi^j(t_S^j) = f(t_S^j - t_0) + \frac{\phi_0}{2\pi} \tag{2.12}$$

where f is the frequency and ϕ_0 is the phase in radians for the time t_0. The difference

between these two received and generated signals by the receiver can be expressed:

$$\phi^i(t_R^i) - \phi^j(t_S^j) = f(t_R^i - t_E^j) \tag{2.13}$$

If we combine the equation 2.9 and 2.13, we can write:

$$\Phi^{ij} = f(t_R^i - t_S^j) - N^{ij} \tag{2.14}$$

We can rewrite the equation 2.14 based on GPS time:

$$\Phi^{ij} = f(t_R^{GPS} - t_S^{GPS}) + f(\delta t^j - \delta t^i) - N^{ij} \tag{2.15}$$

According to the relationship between frequency and wavelength ($\lambda = c/f$), the carrier phase difference, $\lambda\Delta\Phi^{ij}$, between receiver i and satellite j at wavelength λ can be expressed [Walpersdorf et al., 2007, Biessy, 2009]:

$$\lambda\Phi^{ij} = c(t_R^{GPS} - t_S^{GPS}) + c(\delta t^j - \delta t^i) - \lambda N^{ij} \tag{2.16}$$

where the complete phase delay $\lambda\Delta\Phi^{ij}$ consists of signal travel time $(t_R^{GPS} - t_S^{GPS})$ between satellite and receiver multiplied by the speed c , the clock errors of the receiver and satellites (δt^i and δt^j, respectively) and the ambiguity (N) multiply by wavelength (λ).

The signal travel time can be related to the geometrical distance (L^{ij}) between satellite and receiver with additional terms due to signal delays created by the ionosphere and troposphere (Δl_{iono} and Δl_{tropo}). Consequently the equations 2.5 and 2.16 can be expressed by the following terms:

$$R^{ij} = L^{ij} + \Delta l_{iono} + \Delta l_{tropo} + c(\delta t^i - \delta t^j) + \epsilon_R \tag{2.17}$$

$$\lambda\Phi^{ij} = L^{ij} + \Delta l_{iono} + \Delta l_{tropo} + c(\delta t^i - \delta t^j) - \lambda N^{ij} + \epsilon_\Phi \tag{2.18}$$

where ϵ is the noise due to receiver and multipath. The code measurement has no phase ambiguity but this observable has only a long wavelength (29.3m for P-code or 293m for C/A code) which in comparison with carrier phase measurements with short wavelength of 19cm (L1) or 24.4cm (L2) is less accurate. Therefore the carrier phase is the observable which is used for precise determination of the GPS station parameters (coordinates and tropospheric delays) but the phase ambiguity should be resolved precisely for carrier phase measurements.

c) Type of positioning with GPS

There are two types of positioning: absolute and relative. In absolute positioning, only observations collected by a single receiver contribute to the determination of its position. Using the precise ephemerides and clock corrections computed by IGS (International GNSS service), the accuracy of absolute positioning can reach a few tens of centimeters. The relative (differential) GPS positioning is an effective strategy to reduce errors. The single difference can be performed between two satellites or two receivers. The difference between the simultaneous measurements from the same satellite at two different stations is the simple difference between stations. The simultaneous observation between two satellites at the same station is called simple difference between satellites. But the most used difference of observable for precise static and kinematic GPS positioning is the double difference between two satellites and two receivers (2.2).

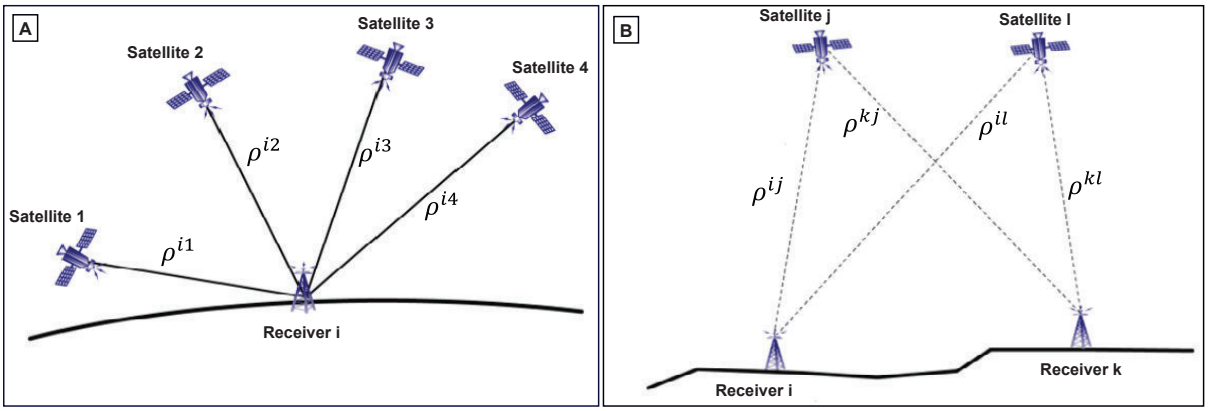

Figure 2.2 – A- Absolute positioning: Several satellites contribute to determine the position of a single receiver. B- Double difference positioning, one type of relative positioning, which can be used for precise positioning. After Biessy [2009]

According to the equation 2.16 and relationship $\lambda = c/f$, the phase measurement between (Sat_j, Rec_K) and (Sat_j, Rec_i) are:

$$\Phi^{kj} = \frac{f}{c} L^{kj} + f(\delta t^k - \delta t^j) - N^{kj} \tag{2.19}$$

$$\Phi^{ij} = \frac{f}{c} L^{ij} + f(\delta t^i - \delta t^j) - N^{ij} \tag{2.20}$$

Then the simple difference between stations (i and k) and satellite j can be expressed by combination of equations 2.19 and 2.20:

$$\Phi^{j-ik} = \Phi^{kj} - \Phi^{ij} = \frac{f}{c}(L^{kj} - L^{ij}) + f(\delta t^i - \delta t^k) - (N^{kj} - N^{ij}) \tag{2.21}$$

In this equation the clock error of satellite j is eliminated. Also the simple difference

between stations (i and k) and satellite l is:

$$\Phi^{l-ik} = \Phi^{lk} - \Phi^{li} = \frac{f}{c}(L^{lk} - L^{li}) + f(\delta t^i - \delta t^k) - (N^{lk} - N^{li}) \tag{2.22}$$

The double-difference observations of carrier phase measurement between two satellites (i,k) and two receivers (j,l) (Fig. 2.2-B) can be expressed:

$$\Phi^{jl-ik} = \Phi^{l-ik} - \Phi^{j-ik} = \frac{f}{c}(L^{lk} - L^{li} - L^{jk} + L^{ji}) - (N^{lk} - N^{li} - N^{jk} + N^{ji}) + \epsilon \tag{2.23}$$

Now the clock errors of satellite and receiver are removed in the double difference equation. In reality they are not completely eliminated from the double difference measurement as the satellite and receiver clock are not perfectly stable because of the variable quality of the oscillators [Vernant, 2003]. For more detail about this error one can refer to [Walpersdorf, 1997, Vernant, 2003]. Thus the ϵ includes the noise due to multipath, remaining clock errors and receiver noise. According to the equation 2.23, the double difference observables are affected by different error sources, some of which can be modeled explicitly, the others being considered as persistent error sources [Walpersdorf et al., 2007]. We will discuss these errors and the approach to reduce them to obtain a better precision in GPS positioning in the next section.

2.2.2 Error sources and progress in their correction in the last decade

To obtain high accuracies in estimating the GPS station positions, it is necessary to distinguish the errors and delays that affect the GPS signal and remove or reduce them as much as possible. According to the equation 2.23, the double difference carrier phase measurements are influenced by two types of error sources. The first group of effects are either corrected a priori or adjusted during the data analysis with the help of specific models. The second group of effects acts mainly as noise, such as multi-path near the GPS receiver antenna [Walpersdorf et al., 2007]. Using the most recent models for correction of the different error sources helps to obtain high precision in GPS positioning. The development of new models mostly started after 2000, when many GPS permanent networks were established to estimate the temporal evolution of the daily stations position. The first consequence of long-term GPS data is improving the precision of position evolution but the second consequence is highlighting new smaller error sources that can influence the precision of GPS data. Therefore, considerable research has been done to improve the processing strategies and the error model of GPS observations in the last decade. The improvements mostly concern the reprocessing of orbits, an update of applied models (troposphere, ocean and hydrology), Antenna phase center calibration and stability of the coordinate reference frame [Steigenberger et al., 2006]. These developments allow us

to process long time series of permanent data for more than 10 years with significantly improved precision. In the following, I explain how these new up-to-date models improve the precision of GPS positioning.

a) Atmospheric delay

One of the main error sources in the GPS precise positioning is atmospheric propagation delay. The signal propagating from the satellite, at about 20,000km altitude to a GPS station on the surface, is slowed and bent due to interaction of the electromagnetic waves with the particles in the ionosphere (50-500 km altitude) and troposphere (0-50 km altitude).

Ionospheric delay:

The magnitude of ionospheric error depends on the signal frequency and the density of free electrons along the signal path. Its first order ionospheric group delay (phase advance) is on the order of 1–50 m depending on the satellite elevation, ionospheric conditions, local time, season, and solar cycle [Kedar et al., 2003]. Using the double difference equation will help to remove this delay for short baselines, but for baselines of more than 10km, it is necessary to remove the ionospheric effect. The first order of ionospheric delay can be virtually eliminated by forming the ionosphere-free linear combination of the L1 and L2 measurements or using the Global ionosphere maps, to a millimeter or less [Steigenberger et al., 2006]. The Global ionosphere maps (GIMs) are estimated from smoothed code observations using the geometry-free linear combination. The major effects of the ionosphere are the carrier phase advance and group delay of pseudorange. The phase advance and group delay are equal in magnitude and opposite in sign. The ionosphere is a dispersive medium for the electromagnetic signals, the intensity of the signals refraction will depend upon frequency.

GPS ionospheric phase advance can be written as a function of frequency of the signal [Walpersdorf, 1997, Vernant, 2003]:

$$\tau_{ion} = 1.35.10^{-7}\frac{N_e}{f^2} = \frac{\Phi_{ion}}{f} \tag{2.24}$$

While τ_{ion} is the time delay due to the ionosphere in the phase measurement, $\Phi_{ion} = 1.35.10^{-7}N_e/f$ is the phase delay due to the ionospheric layer and $N_e = N_e(\rho_e,el)$ is the integrated density of the electrons along the propagation path of the signal. This density depends on the average electron density and the elevation angle of the satellite and the unit is $electrons/m^2(e/m^2)$. ρ_e is the electron density, its value depends on the latitude at which the observation is made, the time of day, season and solar activity.

The total time delay of carrier phase τ includes the real time of signal traveling Φ/f_1 and ionospheric delay time (without considering the ambiguity phase) and it can be

expressed as a function of frequency:

$$\tau = \Phi_1/f_1 + k/f_1^2 \tag{2.25}$$

$$\tau = \Phi_2/f_2 + k/f_2^2 \tag{2.26}$$

where $k = 1.3510^7.N_e$. A linear combination of equations 2.25 and 2.26 can delete the ionospheric delay:

$$\tau = \frac{f_2\Phi_2 - f_1\Phi_1}{f_1^2 - f_2^2} = \frac{1}{f_1}\frac{\Phi_1 - R\Phi_2}{1 - R^2} \tag{2.27}$$

where $R = f_2/f_1 = 1227.60/1575.42 = 0.779$.

This linear combination of observables on L1 and L2 are the ionosphere free linear combination, which is called LC or L3. This leads to a new observable that in a first approximation is independent of the effects of ionospheric refraction:

$$\Phi_C = f_1.\tau = \Phi_1 + \frac{R}{1 - R^2}(R.\Phi_1 - \Phi_2) \tag{2.28}$$

Now it is possible to have a numerical relationship between Φ_1,Φ_2 and Φ_C:

$$\Phi_C = \Phi_1 - 1.984(\Phi_2 - 0.779\Phi_1) \tag{2.29}$$

The LC observable helps to remove the first order ionospheric delay, but it can amplify the non-dispersive part of error sources. Therefore, it is more convenient to use LC in long baseline measurements ($>$ 10km) where ionospheric errors are significant. The higher order ionospheric delay can be of the order of sub-millimeter to several centimeters [Kedar et al., 2003]. In the European GALILEO system which will have more than two frequencies, a triple-frequency method of correcting the 1st and 2nd order ionospheric refraction is suggested.

There is another linear combination (LG) of L1 and L2 which is used to quantify the ionospheric delay:

$$\Phi_G = \Phi_2 - \frac{f_2}{f_1}\Phi_1 \tag{2.30}$$

Tropospheric delay:

This delay in propagating GPS signals is related to the refractivity of the troposphere. It is normally calculated in the zenith direction, and is referred to as a zenith tropospheric delay. It can reach 2.50 m at zenith and 20m for elevation angles of 20°. This delay is not dispersive (independent from the frequency of the signal), so it is not possible to remove it using the linear combination like ionospheric delay. The total tropospheric delay can be divided into two components:

– The dry component is approximately 2m at zenith and it is a relatively stable part

of the troposphere. It is mainly related to ground pressure and can be described by atmospheric models.

– The wet component can reach 0-30 cm at the zenith with possible variations of some centimeters per hour. It is distributed in homogeneously in the atmosphere as the behavior of water in the atmosphere is unpredictable and is a very local phenomenon.

As the changes in the amount of water vapor in the atmosphere are irregular, they are difficult to model and difficult to measure from ground. Therefore they deteriorate the accuracy of GPS positioning. Errors in estimating the wet tropospheric delay lead to an incorrect solution mainly for the vertical component of the station position.

The tropospheric delay can be related to air refractivity by the integration along the signal path through the troposphere:

$$L_{trop} = \int_{path} (n-1)ds \tag{2.31}$$

where n is the refractive index. The equation can be expressed in terms of the refractivity, N:

$$L_{trop} = 10^{-6} \int_{path} N ds \tag{2.32}$$

The atmospheric refractivity can be related to the meteorological quantifies air pressure, air temperature and water vapor pressure [Smith and Weintraub, 1953, Thayer, 1974]:

$$N = k_1 \frac{P_d}{T} Z_d^{-1} + [k_2(\frac{P_w}{T}) + k_3(\frac{P_w}{T^2})]Z_w^{-1} \tag{2.33}$$

where P_d and P_w are the partial pressures of dry air and water vapor respectively, in hPa, T is absolute temperature, k_i are the refractivity constants are determined empirically in a laboratory [Boudouris, 1963, Smith and Weintraub, 1953, Thayer, 1974, Hill et al., 1982, Hill, 1988], Zd and Zw are empirical factors of air compressibility and are usually modeled as a function of pressure and temperature. [Berrada Baby et al., 1988] combine equations 2.32 and 2.33 to integrate the atmospheric refractivity along the zenith. The obtained Zenith Total Delay (ZTD) can be expressed in terms of Zenith Hydrostatic Delay (ZHD) and Zenith Wet Delay (ZWD):

$$ZTD = 10^{-6}[\overbrace{k_1 R_d \int_{z_0}^{\infty} \rho dz}^{ZHD} + \overbrace{\int_{z_0}^{\infty} (k_2 \frac{P_w}{T} + k_3 \frac{P_w}{T^2}) Z_w^{-1} dz}^{ZWD}] \tag{2.34}$$

This equation demonstrates that the tropospheric delay can be divided into two parts: the first part (ZHD) that depends only on surface pressure, and the part (ZWD) that is dependent on the distribution of water vapor on the signal travel path[Saastamoinen, 1972]. The hydrostatic component comprises mostly the effects of dry air, but also includes

a significant component from the non-dipole effects of water vapor. It can be modeled accurately using surface barometric measurements or meteorological models [Tregoning and Herring, 2006]. ZWD depends on the atmospheric water vapor distribution that is highly variable in space and time such that the wet delay cannot inferred from surface measurements very accurately and models do not work well [Bevis et al., 1994].

As GPS measurements are collected from satellites with arbitrary elevation angle, it is necessary to describe tropospheric delay in arbitrary elevation angle which is called Slant Tropospheric Delay (STD):

$$STD(\epsilon) = mf_h(\epsilon).ZHD + mf_w(\epsilon).ZWD \tag{2.35}$$

where mf_h is the hydrostatic mapping function, ZHD is dry zenith delay, mf_w is the wet mapping function and ZWD is wet zenith delay. The GPS observations are the oblique tropospheric delays (from all satellites simultaneously). These observations average to one ZTD for each station. But in reality, it is difficult to project the STD observation to ZTD because each of ZHD and ZWD have a different scale height, so two types of mapping functions are necessary to produce ZTD. This is not possible as the GPS processing algorithm does not distinguish between ZHD and ZWD and only one mapping function can be used to project. This problem can be solved by the following steps (Fig. 2.3):

- Use theoretical models for ZHD and ZWD to estimate an a priori value for ZHD and ZWD at the place of the station.
- Use dry and wet mapping functions to project separately these a priori ZHD and ZWD to each satellite direction.
- Substract theoretical slant delay from observed delay for each satellite to obtain residuals in each satellite direction.
- Use residual slant delays (for all satellites, under different elevations), project them with the wet mapping function to zenith, and average the individual satellite zenith delays to obtain an adjustment to the a priori ZTD.

Consequently, to obtain precise zenith delay, it is required to have updated and precise models and mapping functions to obtain high precision in positioning especially for the vertical component.

There are some hydrostatic delay models which can be used to estimate a priori ZHD. The most common hydrostatic delay model is Saastamoinen model [Saastamoinen, 1972]. If hydrostatic equilibrium is assumed, the hydrostatic delay model may be expressed simply as a function of measured surface pressure[Saastamoinen, 1972].

$$ZHD = \frac{0.00227768P_0}{1 - 0.00266cos(2\phi) - 00000028h_{ref}} \tag{2.36}$$

where P_0 is the surface pressure at the site, ϕ is the site latitude and h_{ref} is the site height (in km) above the sea level.

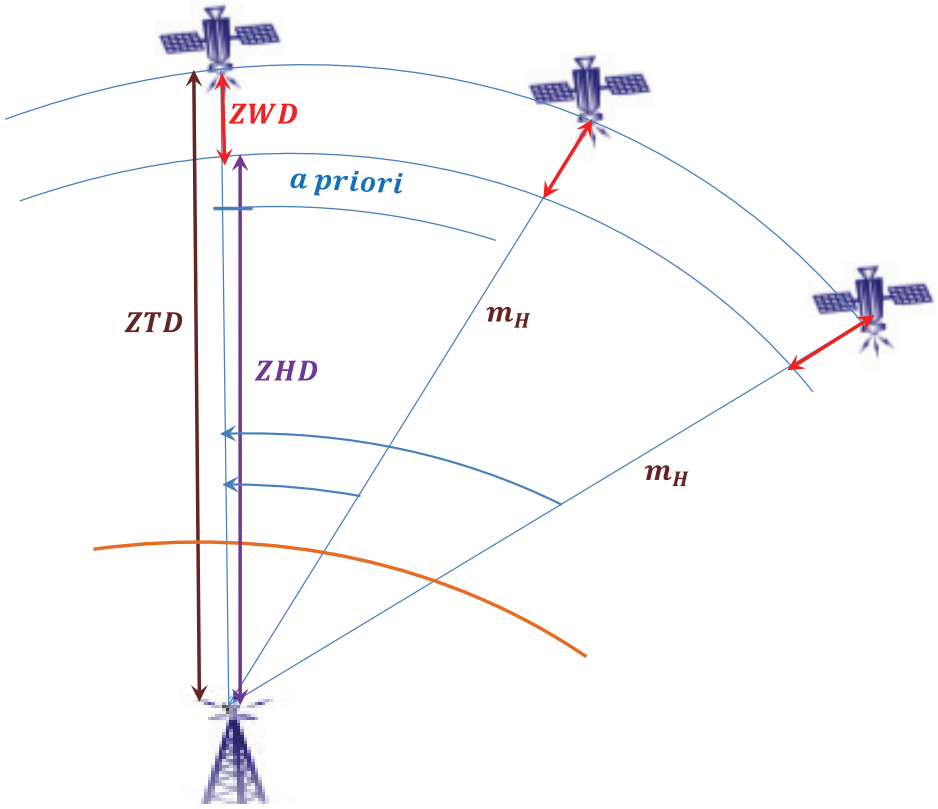

Figure 2.3 – The theoretical models (ZHD and ZWD) and mapping function are used to estimate the Zenith total delay (ZTD).

There are some wet zenith delay models (e.g. Hopfield model [Hopfield, 1969], Saastamoinen model [Saastamoinen, 1972], Berman model [Berman, 1976], Ifadis model[Ifadis, 1986]) which are based either on theoretical assumptions concerning water vapor height profiles or on empirical models. In general, these models are highly dependent on the water vapor pressure at the antenna location. As explained, each of the hydrostatic and wet delay models and mapping function influence in the ZTD estimation. But the most irregular and difficult part of the troposphere for modeling is water vapor due to its local variations. As a result, the variability of the wet part of the troposphere sometimes leads to ZTD variation of one centimeter per hour. Therefore, the tropospheric parameters need to be estimated several times per analysis session. The common strategy is to estimate zenith parameter every two hours.

One condition for precise ZTD estimation is the accuracy of the mapping function. Several high-accuracy wet and hydrostatic mapping functions have been developed in the last few years e.g. NMF [Niell, 1996], IMF [Niell, 2000], VMF1 [Boehm and Schuh, 2004] and GMF [Böhm et al., 2006]. The Niell Mapping Function (NMF) was parameterized based on the ray-tracing of radiosonde profiles spanning the latitudes 43°S to 75°N, by assuming longitudinal homogeneity and symmetry between the southern and the northern hemisphere. This mapping function depends on the station height, station latitude and

day of the year [Niell, 1996]. Thus, only the seasonal dependence of the temporal variation of the atmosphere is taken into account.

After, much effort has been put into the development of mapping functions, e.g. IMF and VMF1, which are based on data from numerical weather fields. The mapping functions Vienna Mapping Function (VMF1) [Boehm and Schuh, 2004] use the output of a numerical weather analysis to provide information specifically for the geographic location of the site with a temporal resolution of six hours. The hydrostatic and wet VMF1 mapping function for an elevation angle e can be expressed [Boehm and Schuh, 2004]:

$$mf(e) = \frac{1 + \frac{a}{1+\frac{b}{1+c}}}{\sin e + \frac{a}{\sin e + \frac{b}{\sin e + c}}} \tag{2.37}$$

Three coefficients a, b and c are sufficient to map zenith delays down to elevations of 3°. In the case of VMF, these coefficients are determined from ray-tracing through the Numerical Weather Prediction model (NWP) [Boehm and Schuh, 2004].

The Global Mapping Function (GMF), based on data from the global ECMWF (European Center for Medium Range Weather Forecast) numerical weather model and its coefficients were obtained from an expansion of the Vienna Mapping Function (VMF1) parameters into spherical harmonics on a global grid. Similar to Niell Mapping Function (NMF), the values of the coefficients require only the station coordinates and the day of year as input parameters [Böhm et al., 2006] .

To achieve the highest accuracy in VLBI and GPS analyses, it is recommended to use troposphere mapping functions that are based on data from numerical weather models. Today, these mapping functions (e.g., VMF1 [Boehm and Schuh, 2004] or IMF [Niell, 2000]) are available as time series of coefficients on a grid $2.5 \times 2.0°$ with a resolution of six hours. However, for particular time periods or stations where NWM-based mapping functions are not available, the GMF can be used without introducing systematic biases in the coordinate time series, although the short-term precision will suffer [Böhm et al., 2006].

Errors in estimating the tropospheric delay, either in the modeling of ZHD and ZWD or using the mapping function, leads to an incorrect solution mainly for the vertical component of the station. In other words, tropospheric delay is correlated with vertical position (Fig. 2.4 and equation 2.38 and 2.39).

$$\Delta V(e) = \Delta V_z . \sin(e) \qquad \begin{cases} max & if \quad \epsilon = 90° \\ min & if \quad \epsilon = 0° \end{cases} \tag{2.38}$$

$$\Delta Trop(e) = \Delta Trop_z . \frac{1}{\sin(e)} \qquad \begin{cases} min & if \quad \epsilon = 90° \\ max & if \quad \epsilon = 0° \end{cases} \tag{2.39}$$

GPS can resolve this problem and decorrelate these two components from each other

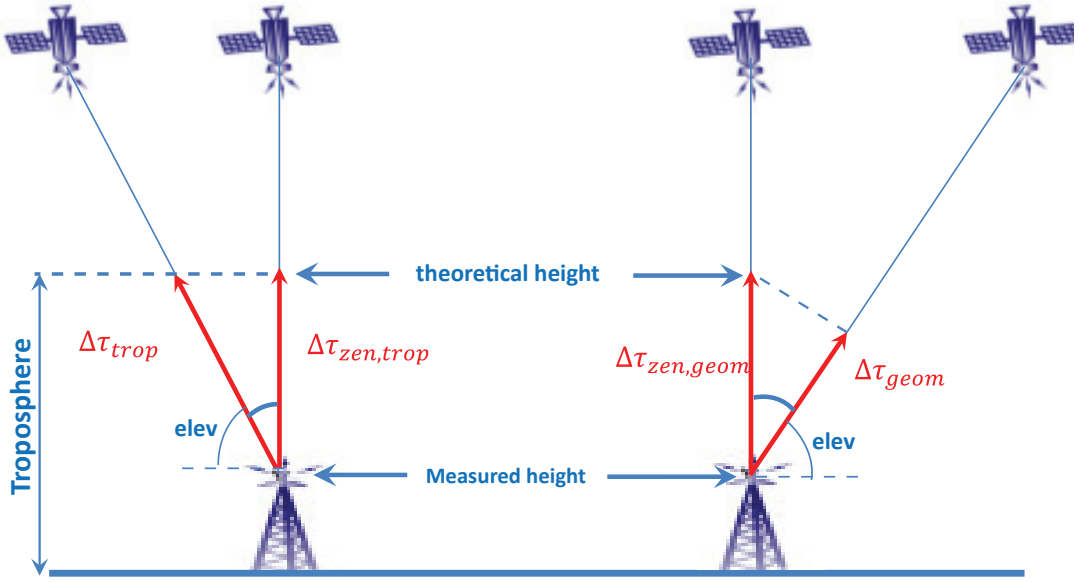

Figure 2.4 – Comparsion of the vertical offsets of a station created by a tropospheric delay (left) and a geometric shift (right).

as several satellites are seen simultaneously under different elevation angles. Every tropospheric signal not attributed to ZTD goes to the vertical position, thus precise estimation of tropospheric delay will help to estimate accurate and precise vertical position.

Since the 90th, it has been shown that GPS evaluates integrated water vapor as precisely as meteorological measurements [Bevis et al., 1992, 1994]. GPS meteorology has developed to estimate the variation of water vapor over time (eg, every fifteen minutes) in the area covered by the network. ZWD can be related to Precipitable Water Vapor (PWV), defined as the height of a column of liquid water that is equivalent to the vertically integrated water vapor through the atmosphere [Askne and Nordius, 1987, Bevis et al., 1994, Businger et al., 1996]:

$$ZWD = \Pi \times PWV \tag{2.40}$$

where

$$\Pi = 10^{-6}(\rho_w R_w[\frac{k_3}{T_m}) + k_2']) \tag{2.41}$$

where ρ_w is the density of liquid water, T_m is a weighted mean temperature of the atmosphere and all other terms have been defined previously. Therefore the feasibility and reliability of the GPS ZTD to estimate precipitable water vapor (PWV) in terms of high-accuracy and low cost helps to have good agreement of ZTD with meteorological observations[Liou and Huang, 2000, Vedel, 2000, Liou et al., 2001, Haase et al., 2001, Shu-Li et al., 2004, Shuli et al., 2006, Walpersdorf et al., 2007].

One of the meteorological applications of GPS can be correcting the tropospheric

delay of Synthetic Aperture Radar (SAR). The delay of the SAR signal passing through the troposphere is one of the major error sources for SAR data. Unlike the GPS, SAR data are acquired using one single satellite and can therefore not distinguish between geometrical and tropospheric delay. However GPS and SAR signal frequencies are very close and result in an identical tropospheric delay. Therefore, simultaneously collected GPS ZTD of stations with well-known positions can be used to correct this delay in SAR images space [Williams et al., 1998, Webley et al., 2002].

b) Phase ambiguity

Since the development of the GPS, integer phase ambiguity resolution has become one of the most challenging fields in the GPS positioning because of its impact on the accuracy. An error of even one cycle on a single phase measurement can result in a position bias of many centimeters or decimeters. Due to the general north–south motion of GPS satellites at all but high latitudes, the east component of the GPS coordinates has the highest correlation with the carrier phase ambiguities [Melbourne, 1985] and it has been shown that the fixing of ambiguities to their correct integer values improves the repeatability of this component more than the others [Blewitt, 1989].

The basic idea for the ambiguity resolution can be considered in three steps. The first step is generating the potential integer ambiguity by search space technique. The second step involves the identification of the correct integer ambiguity combinations that minimizes the sum of squared residuals in the sense of least squares adjustment. These combinations are defined as the best fit of the data. The last step is the validation of the ambiguities [Hofmann-Wellenhof et al., 2008]. Nowadays, there are different methods available to solve the integer ambiguity. These methods apply different techniques such as: using single to dual frequency phase data; combining dual frequency carrier phase data and code data; combinations between triple frequency carrier phase and code data. Here we explain the strategy which is used in GPS data processing in this thesis by the GaMIT/GLOBK software.

Fig 2.1 illustrates the ambiguity $N_{i,j}$ of the transmitted signal from satellite i and received signal by receiver j. This value corresponds to the integer wavelength of the signal from satellite to receiver while the fractional part of the signal can be measured. The initial phase ambiguity for one station remains constant as long as there is no interruption in recording signal. During the GPS data processing with the GAMIT software [King and Bock, 2001], the value of the phase ambiguity is part of the estimated parameters. These parameters are adjusted using a least square method to minimize the difference between the modeled values and the values observed at the GPS receivers. In the first step of the solution which is called "free" solution, the ambiguity can be a real value adjusted to better fit the model. After, a second solution, the "fixed" solution, is calculated. In this step, if the value of the estimated ambiguity is precise enough and close to an integer

value, then the ambiguity parameter is "fixed" to this integer. To fix the ambiguity of phase observation, the value should be close to its true integer value (eg 2.9 or 3.1 for true value 3.). At the same time, the uncertainty of the parameter should be low enough so that within the limits of uncertainty around the estimated real value only a single integer is situated. For example, an estimated value of 2.1 ± 0.2 can be set to 2, but an estimated value 2.6 ± 0.6 could not be assigned an integer value [Walpersdorf, 1997, Vernant, 2003].

To estimate the phase ambiguity, the double difference measurement is used as it has no clock errors. On long baselines (more than a few kilometers), the ionospheric delay is too large to be able to find the correct value of the ambiguity, so it is necessary to eliminate this error. This can be done using the LC combination of both carrier phase [Dong and Bock, 1989] or P-code observations [Blewitt, 1989]. If we add the phase ambiguity in the linear combination LC, we can rewrite the equation 2.29:

$$\Phi_C = \Phi_1 + N_1 + \frac{R}{1-R^2}(\Phi_2 + N_2 - R(\Phi_1 + N_1)) \tag{2.42}$$

$$\Phi_C = \Phi_1 + \frac{R}{1-R^2}(\Phi_2 - R\Phi) - \frac{R}{1-R^2}\overbrace{(N_2 - N_1)}^{WL} + \overbrace{\frac{1}{1+R}N_1}^{NL} \tag{2.43}$$

where N_1 and N_2 are the phase ambiguities of the phase L_1 and L_2. As $R = f_2/f_1$, the term of $N_2 - N_1$ has longer wavelength ($\frac{c}{f_1 - f_2} = 86cm$) relative to L1 (19,0 cm) and L2 (24.4 cm) so it is called Wide Lane (WL). To resolve the ambiguity of WL ($N2 - N1$), a combination of observations phase Φ_1 and Φ_2 and pseudoranges P_1 and P_2 are used. Pseudoranges are obtained by measurements of C / A code on L1 and P2 on L2 and they are unambiguous. According to the equation 2.26, the simplified phase equation for L2 and L2 can be expressed:

$$\Phi_1 = -f_1\tau + N_1 + kf_1 + \Phi_{error} \tag{2.44}$$

$$\Phi_2 = -f_2\tau + N_2 + kf_2 + \Phi_{error} \tag{2.45}$$

Also the simplified version for two codes have the opposite sign in ionospheric delay:

$$P_1 = -f_1\tau - kf_1 + P_{error} \tag{2.46}$$

$$P_2 = -f_2\tau - kf_2 + P_{error} \tag{2.47}$$

By combining of the sum of the equations 2.46 and 2.46 and substracting of equations 2.44 and 2.45, the ionospheric delay terms (k/f_1 and k/f_2) can be removed and the

ambiguity phase of wide lane $N_2 - N_1$ can be estimated:

$$N_2 - N_1 = \Phi_2 - \Phi_1 + \frac{f_1 - f_2}{f_1 + f_2}(P_1 + P_2) + P_{error} - \Phi_{error} \tag{2.48}$$

The most challenging issue in estimating ambiguity phase of wide lane is multipath error. The P-code is sensitive to this error, therefore to obtain a good accuracy for the WL combination, it is important to extend the observations long enough. WL ambiguities can be resolved if the noise is less than 86 cm (the wavelength of the WL). After resolving the WL ambiguity, the second term of ambiguity in equation 2.43 should be resolved. This term is multiplied by $\frac{1}{1+R}$ which is 0.56. In this case the length of L1 (19cm) is reduced to 10.7 cm. This leads to call this term the narrow lane (NL). To be able to resolve this short wavelength ambiguity, the ambiguity value of WL should be fixed in the least square solution. Thus the uncertainties in the remaining free parameters will decrease. With this approach, it is possible to solve the ambiguity for NL [Walpersdorf, 1997].

This method of ambiguity resolution with the LC combination is only effective for long baselines where the influence of the ionosphere is too high to resolve ambiguities N1 and N2 separately. For short baselines, it is easier to solve N1 and N2 directly in the observations on L1 and L2. The length limitation for baselines from which on it is necessary to use the LC combination depends on the latitude of the experiment and the solar activity at that time. Usually, over more than 10-20 kilometers one considers that it is necessary to use the LC combination [Vernant, 2003].

c) Orbital errors

The quality of satellite orbit can be one of the major accuracy-limiting factors in the GPS measurements. Orbital errors occur when the GPS message does not have the correct orbital parameters. Its effect on absolute positioning is a direct error on the position of the station while, for differential positioning, it has indirect effect and influences the baseline between two stations. Figure 2.5 illustrates the effect of the orbit on absolute and differential positioning.

According to the figure 2.5-A, the error in orbit of satellite (δr) induced the same error in the position of the station and position P' is measured instead of position P.

$$P' = P + \delta r \tag{2.49}$$

Therefore the error in the absolute position is: $\delta_{abs} = \delta r$.

Figure 2.5 presents the influence of the orbit error on relative positioning. The error δr results to measure b' instead of b:

$$b' = b - \delta r \tag{2.50}$$

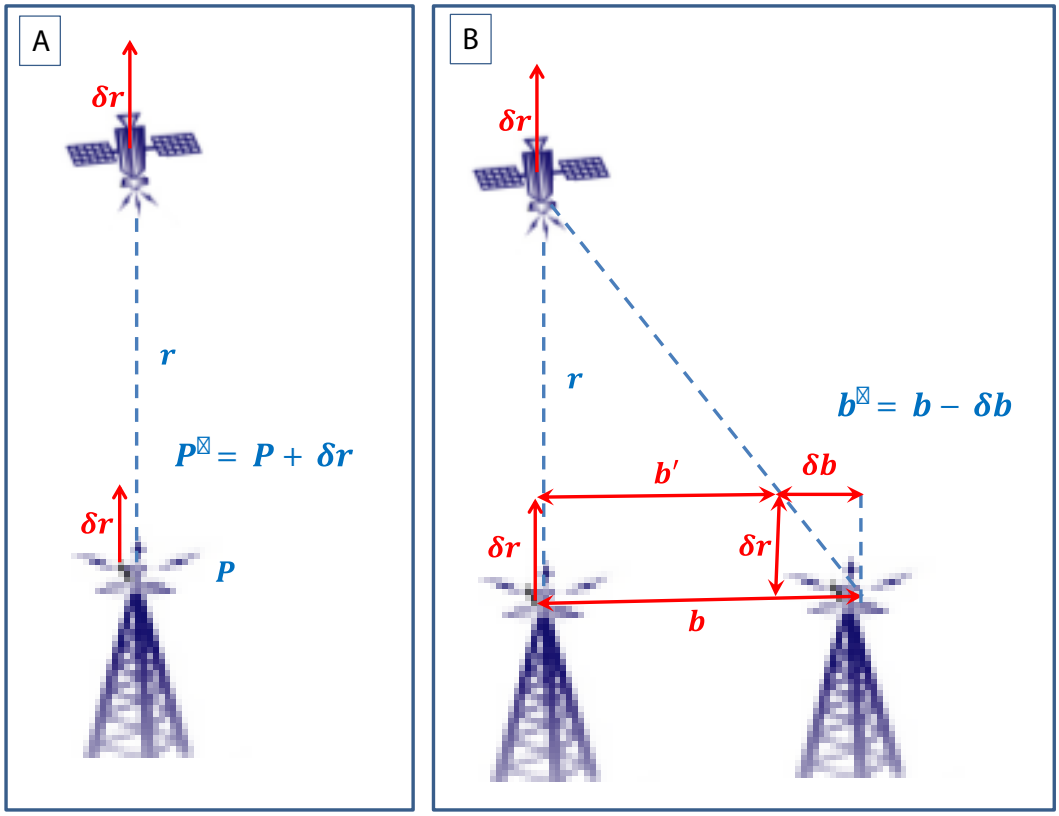

Figure 2.5 – The schematic view of orbiatl error for absolute and relative positioning [Walpersdorf, 1997, Vernant, 2003].

Therefore the error due to an orbital error in relative positioning is: $\delta_{rel} = \delta b$.

Now we can write the following relationship between δr and δb according to the figure 2.5-B:

$$\frac{r}{b} = \frac{\delta r}{\delta b} \Longleftrightarrow \frac{r}{\delta r} = \frac{b}{\delta b} \tag{2.51}$$

Thus the errors in absolute and relative measurement (δ_{abs} and δ_{rel}) can be expressed in terms of the orbit error δr:

$$\begin{aligned} \delta_{abs} &= \delta r \\ \delta_{rel} &= \frac{b}{r}\delta r \end{aligned} \tag{2.52}$$

The relative error δ_{rel} is only a fraction of the absolute error δ_{abs} and it depends of the ratio between the length of the baseline with respect to the altitude of the satellite. Now we can calculate the maximum accuracy of the orbits necessary to obtain 1 cm of precision in baseline estimation if we assume there is just orbit error in the phase measurement (see Table 2.1).

It is possible to obtain 100m of precision without SA (Selective Availability) by using the ephemerides navigation message. Thus it is necessary to have precise information about the orbit of satellite especially for long baseline and precise positioning. The International

Length of the base line	Minimum orbit presicion
1km	200m (precision with SA)
2km	100 m (precision without SA)
10km	20 m
100km	2m
1000km	0.2m (precision IGS)

Table 2.1 – The IGS orbit summary which insist of accuracy, latency, updates and sample interval.

GNSS Service (IGS) produce the precise orbits from the IGS tracking network. The orbit routine products can be broadcast in real time mode with $\sim$ 160 cm accuracy to final precise orbit after 12-18 days after with $\sim$2.5 cm (table 2.2).

Since 1994, the International GNSS Service has provided precise GPS orbit products to the scientific community with increased precision and timeliness [Dow et al., 2009]. During this 19 years, changes in the processing strategies (such as system of reference, the phase center corrections of satellite and receiver antennas, models of the gravity field, the elevation cutoff of GPS observations, taking into account the solid and ocean tides, modeling troposphere, strategies for resolving ambiguities) cause systematic effects on IGS production. Therefore, the orbits are not consistent with each other over time related to their quality or reference frame. Some of these effects can be removed during the processing but it is possible to have residuals of this effect which generates artificial signals in the time series [Steigenberger et al., 2006]. Steigenberger et al. [2006] presented that reprocessing of 11 years of data show 30% improvements in the quality of the orbits. Thus IGS began the full reprocessing of the orbits and global positioning solution after 1994, since February 2008. The benefits of this recalculation are firstly the ability to better determine the phase ambiguities of the old data and to decrease the effects of errors in orbit modeling in long time series [Nocquet, 2011].

orbit type	Accuracy	Latency	Updates	Sample interval
Broadcast	$\sim$160cm	Real time	-	Daily
Ultra-rapid (predicted half)	$\sim$10cm	Real time	Four$\times$ daily	15 min
Ultra-rapid (observed half)	5cm	3h	Four$\times$ daily	15 min
Rapid	5cm	17h	Daily	15 min
Final	5cm	$\sim$ 13days	Weekly	15 min

Table 2.2 – The IGS orbit summary commuting accuracy, latency, updates and sample interval of different IGS products.

d) Antenna phase center

In order to achieve high-precision GPS results it is necessary to know the exact position of the phase center of the transmitting and of the receiving GPS antenna [Rothacher, 2001, Mader GL, 2002, Schmid et al., 2005a], as the phase center variations (PCVs) can

reach an order of magnitude of ± 3-4 mm [Schmid et al., 2005b]. The correction of phase center variations comprises a mean offsets of the electrical antenna phase center compared to the physical antenna reference point. Relative correction values have been derived from GPS data collected over a short baseline with the reference antenna AOAD/M_T (Allen Osborne Associates Dorne Margolin T) at one end of the baseline and the antenna to be calibrated on the other end (Mader, 1999). Corrections from these relative calibrations have been used until 5 November 2006 (Gendt, 2006), despite the arbitrary assumption that the PCVs of the reference antenna were zero and other limitations of the procedure, resulting in systematic errors [Schmid et al., 2005a, 2007]. Comparison of GPS global solutions with those provided by VLBI and SLR showed a significant disagreement on the scale factor, suggesting a systematic bias correlated to the PCV [Nocquet, 2011]. Since November 2006, the relative phase corrections have been replaced by absolute PCV corrections provided by IGS. Apart from systematic changes in the global station coordinates, one can expect the GPS results to be less dependent on the elevation cutoff angle. Absolute PCVs lead also to a significant reduction of tropospheric zenith delay biases between GPS and VLBI. This stands for an important step toward more consistency between different space geodetic techniques and an important step towards improving vertical time series [Schmid et al., 2007, Nocquet, 2011].

Therefore, to obtain high accuracy we should take into account changes in the apparent distance due to variations in the phase centers of both the transmitting and receiving antennas. With ground antennas of the same type in a regional network, these effects nearly cancel, but for longer baselines and/or different antenna types they can amount to several centimeters in estimated heights. Models for the phase center offsets and variations (PCVs) depending on elevation and azimuth for the most commonly used ground antennas have been determined by electro-mechanical measurements [http://gnpcvdb.geopp.de; http://www.ngs.noaa.gov/ANTCAL], and for the satellite antennas by analysis of global tracking data [Schmid et al., 2007, Herring et al., 2010].

e) Atmospheric, hydrological and oceanic loading

Redistribution of atmospheric, hydrological and oceanic mass over Earth's surface produce loading with characteristic patterns of surface deformation [Blewitt et al., 2001]. GPS height estimates reflect ground displacements due to atmospheric pressure, tidal and non-tidal fluctuations in the ocean, and to variations in the distribution of water, snow, and ice on land [Van Dam et al., 2001, Dong et al., 2002, Penna and Stewart, 2003, Penna et al., 2007, Ouellette et al., 2013]. If these phenomena are not modeled correctly, they represent a strong source of error for the estimated parameters, in particular for vertical positioning and zenith tropospheric delay [Walpersdorf et al., 2007].

Ocean loading can reach 6 cm on the vertical position [Scherneck, 1991, Vey et al., 2002], however Vergnolle et al. 2008 showed that the ocean loading effect can exceed

ten centimeters peak-to-peak for the semi-diurnal wave M2 in the French Brittany. The amplitude of the spurious signal strongly depends on the amplitude of the unmodelled displacements and on the site location [Vergnolle et al., 2008]. The first version of global, realistic tidal models (Naval Surface Warfare Center model, [Schwiderski, 1980]) was not accurate enough for satellite altimetry missions (e.g. Topex/Poseidon (T/P) mission) so the international tidal community has undertaken a huge effort to improve or develop new tidal models. The new models are obtained from the combination of a hydrodynamic model and the assimilation of altimetry data, as is the case for the most widely used model today FES2004 [Lyard et al., 2006]. Vergnolle et al. [2008] validate the prediction derived from the new FES2004 at Brittany-Cotentin, France, as a complex region. They conclude that the waves M2, N2, O1 and Q1 are in agreement with the model predictions FES2004 at submillimeter level based on 100 days of measurements of a dense GPS network.

Atmospheric loading by the temporal redistribution of global atmospheric mass is likely to displace the geodetic positions of monuments by tens of millimeters, both vertically and horizontally [Van Dam and Wahr, 1987, Van Dam and Herring, 1994]. The Atmospheric Pressure loading (ATML) effect has been detected in GPS time series [Van Dam and Herring, 1994, Dong et al., 2002] and Very Long Baseline Interferometry analyses [Van Dam and Herring, 1994, MacMillan and Gipson, 1994, Petrov and Boy, 2004]. The direct calculation of this effect is done by a convolution sum between daily, global barometric pressure data and mass loading Green's functions [Farrell, 1972, Van Dam and Wahr, 1987]. Tregoning and van Dam [2005] show ATML effects predicted from global surface pressure data sets. They indicate that sub-daily vertical crustal deformations greater than 10 mm are common at mid- to high-latitude GPS sites, with displacements on the order of 4 mm being common at low-latitude sites. The ATML model applied at the observation level in the GPS analysis was computed in the CM frame (center of mass of the Earth system) [Farrell, 1972, Dong et al., 2003, Blewitt, 2003]. This model has values at intervals of 6-hours interpolated linearly to the time of the observations [Tregoning and Van Dam, 2005]. Atmospheric load can be divided in a "tidal" contribution, derived from the change in air pressure caused by the attraction of the Sun and the Moon and "non-tidal" contribution [Tregoning and Van Dam, 2005]. The present ocean ATML models improve the analysis at sites near the equator but seem to degrade the height estimates elsewhere. The "non-tidal" component is calculated from meteorological models, but these include a partial contribution of atmospheric tides. This can explain why the complete application (tidal + non-tidal) degrades repeatability compared to the absence of a tidal model [Nocquet, 2011]. The majority of the non-tidal deformation can be modeled by using non-tidal ATML model at the observation level or applying a daily averaged correction to daily estimates of coordinates values [Tregoning and Van Dam, 2005].

Hydrological loading comes from the distribution of water mass on continents (soil moisture, aquifers, glaciers and rivers, groundwater, snow and ice) [Blewitt et al., 2001,

Van Dam et al., 2001, Wu et al., 2003]. Van Dam et al. [2001] modeled monthly, global variations of continental water storage and resultant crustal displacements and they suggested that continental water loading can cause vertical displacements of 15 mm or more over large regions of the globe, with displacements of up to 30 mm in some regions, especially in the equatorial basins (Amazon, equatorial Africa), South-East Asia and the west coasts of Canada and Alaska. In contrary to other loading effects which are currently modeled to a fairly high degree of accuracy, no reliable global hydrological model is available yet for current analyses. The availability of gravimetric satellite data from GRACE (Gravity Recovery and Climate Experiment) since March 2002, which shows large seasonal variations in gravity that are assumed to be related to climate-driven fluxes of surface water, provides an opportunity to estimate the height of water equivalent [Davis et al., 2004]. There is good agreement between the annual signal in the vertical component of GPS results and annual regional-scale loading deformations estimated from GRACE satellite products in west Africa [Nahmani et al., 2012] and South America [Davis et al., 2004], but in contrast, Van Dam et al. [2007] demonstrate that the annual height signal from many GPS sites in Europe does not agree with the signal predicted by the continental water storage loading inferred from the GRACE data set. These discriminations can come from: first some small-scale features in the load field which are not captured by the Grace data, or second the existence of some errors in the GPS or GRACE technique. The improvement in both techniques in the future can help to find the reason.

2.2.3 GPS coordinate system

With the development of space-based geodetic systems, it became possible to define purely geometric global coordinate systems. This system is necessary to determine satellite orbits or quantify Earth rotation, tectonic plate motion or mean sea level rise and its variability in space and time. Such a reference coordinate system is realized by the International Terrestrial Reference Frame (ITRF) with origin at the center of the Earth and defined based on space geodetic techniques. More exactly, ITRF is a set of physical points with precisely determined coordinates attached to a Terrestrial Reference System. A Terrestrial Reference System (TRS) is a spatial reference system co-rotating with the Earth in its diurnal motion in space. In such a system, positions of points anchored on the Earth's solid surface have coordinates which undergo only small variations with time [Boucher, 2000]. More detail on versions of ITRF can be found in the references Altamimi et al.,[1993, 2002a, 2002b, 2004, 2007], Altamimi, [2009], Altamimi et al., [2011,2012] . The last 3 realizations of ITRF, ITRF2000, ITRF2005 and ITRF2008, increased significantly the precision of coordinates and velocities. ITRF 2000 used the combination of unconstrained space geodesy solutions for the first time that are free from any tectonic plate motion model. Thus the WRMS of position and velocity estimations reached a level of 2–5

mm and 1–2 mm/yr, respectively [Altamimi et al., 2002]. From ITRF2005 on, the ITRF is based on the time series (weekly from satellite techniques (GPS, SLR and DORIS) and 24-h session-wise from Very Long Baseline Interferometry) of station positions and daily Earth Orientation Parameters (EOPs). Given the fact that the ITRF2005 has 5 years more data since the release of the ITRF2000, the rotation poles of the six major plates appear better determined with the ITRF2005 velocity field than with ITRF2000 [Altamimi et al., 2007]. The clear difference between ITRF2005 and ITRF2000 was the significant drift in the Z-translation amount which had some influence on the North component. Therefore, the ITRF2005 North velocities are always larger than the ITRF2000 by $1.8\cos(\phi)(mm/yr)$, where ϕ is the latitude of the station [Altamimi et al., 2007]. ITRF2008 is a refined version of the ITRF2005 based on reprocessed time series (weekly from satellite techniques and 24-h session-wise from VLBI) of the four space geodetic techniques with longer time span (VLBI, SLR, GPS and DORIS, spanning 29, 26, 12.5 and 16 years of observations, respectively, see Fig. 2.6).

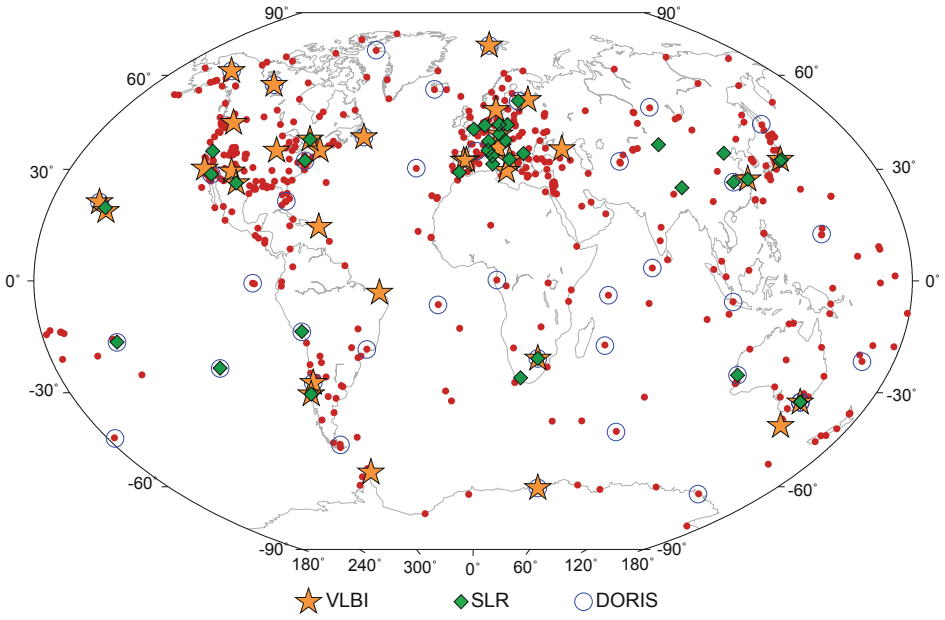

Figure 2.6 – ITRF2008 network highlighting VLBI, SLR and DORIS sites co-located with GPS [Altamimi et al., 2011].

The ITRF2008 follows the series of constantly improved ITRF solutions due to the continuously increasing time span covered by the input data provided by the technique services, and the improved combination strategy. These improvements concern the precision of station positions and velocities and the reference frame defining parameters, specifically the origin and the scale. The level of agreement of the scale and scale rate between VLBI and SLR solutions used in the ITRF2005 combination were 1.4 (±0.11) ppb at epoch 2005.0 and 0.08 (±0.01)ppb/yr, respectively. In comparison, these agreements improved

to 1.05 (±0.13) ppb for scale at epoch 2005.0 and 0.049 (±0.010) ppb/yr for scale rate in ITRF2008. This improvement can come from the reprocessing of VLBI and SLR data for the ITRF2008. The agreement of origin definition at the level of or better than 1 cm of ITRF2008 and ITRF2005 indicate the stabilized strategy in attaining the origin of the reference frame. Unlike the comparison of the translation rate parameter of ITRF2005 and ITRF2000, the translation rate differences between the ITRF2005 and ITRF2008 are zero for Y and Z and 0.3 mm/yr for X-translation. This high level of origin agreement between ITRF2008 and ITRF2005 indicates that the ITRF2000 origin was not precise enough. This improvement may come from the fact that both ITRF2005 and ITRF2008, being based on rigorous time series analysis, are by far more precise than ITRF2000 [Altamimi et al., 2011]. ITRF2008 still achieves improvements on station positions and velocity determinations compared to ITRF2005 (Fig. 2.7.)

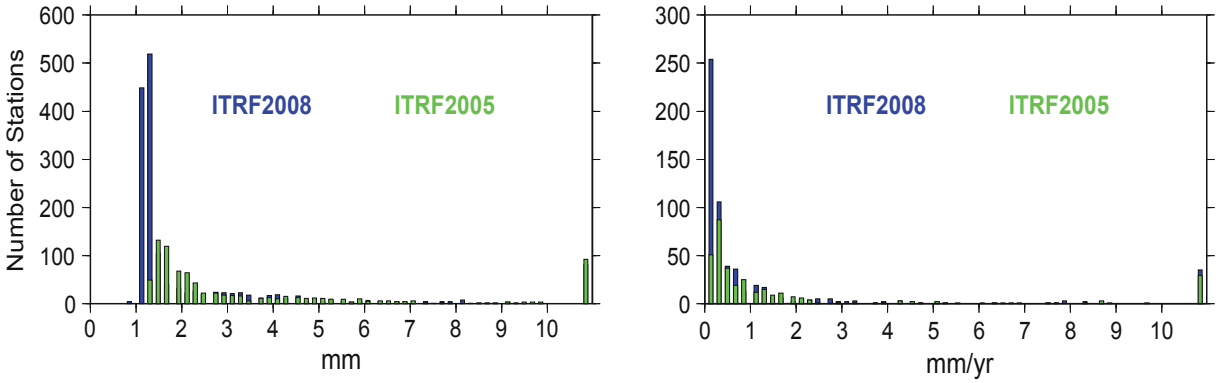

Figure 2.7 – Histogram of the ITRF2008 and ITRF2005 station position and velocity spherical errors. The spherical error measures the dispersion (in the distance sense) of the error vector around the true position of the ith point [Altamimi et al., 2011].

In this study, we used ITRF2008 as the reference frame of the GPS data processing due to the high precision of station position and velocities and the possibility of switching between different reference frames (Eurasia, Arabia,..). To be able to stabilize our network in ITRF2008, we processed the Iranian campaign and permanent GPS data with some core GPS station of ITRF located around Iran. In the following chapter, we will show the availability and distribution of global GPS permanent stations which are operating around the whole world under the umbrella of the International GNSS Service.

2.2.4 Input Data

The GPS data set processed in this study includes 7 years (2004 to 2011) of Iranian Permanent GPS network (IPGN) data in North East and East of Iran, 7 years of campaign networks covering North East and East of Iran and 7 years of continuous GPS sites available at the International GNSS Service (IGS) [Dow et al., 2009].

The Iranian Permanent GPS Network (IPGN) is designed inside the political border of Iran by the National Cartographic Center (NCC) of Iran since early 2005. The network has been established both for crustal deformation monitoring and to build a national DGPS network. This network consists of more than 100 permanent stations. Average distance between stations is 25-100 km. GPS receivers are dual frequency receivers from Ashtech μz12 (CGRS) and scheduled to receive dual band carrier phase data and code data every 30 seconds in daily mode (24h). Master data center for controlling the network and data analysis is settled in Tehran at National Cartographic Center of Iran.

The campaign networks in Iran are established in the framework of the long-lasting Iranian-French collaboration. Each station was measured at least 48 hours with a 30 second interval. In order to optimally correct the antenna phase center variations, all antennas were oriented to the North during setup. In order to eliminate the antenna centering errors during setup, the campaign stations are all installed on bedrock by metal forced centering benchmarks [Tavakoli, 2007]. These networks have been involved in several studies of present-day crustal deformation in Iran: Iran Global [Vernant et al., 2004b, Masson et al., 2005, 2007], Zagros [Walpersdorf et al., 2006, Tavakoli et al., 2008], Tabriz[Masson et al., 2006, Djamour et al., 2011], Alborz networks [Vernant et al., 2004a, Djamour et al., 2010] and Makran [Bayer et al., 2006].

The analysis of the Iranian permanent (IPGN) and campaign stations in this thesis has been combined with 28 permanent stations of the IGS network (triangles in the Fig.2.10) in daily solution analyses in order to produce a stable reference frame. These 28 station are chosen based on some specific criteria; e.g. they should be located around Iran to have short baselines with local stations ($<$1500 km) to be able to record the signal from the same satellite simultaneously (for double difference measurement); the position time series of the stations should have low WRMS with no jump and the stations should be long lasting (not only one or two years). After, the daily solutions are combined with a continuous solution of a network of about 40 IGS stations (circles in the Fig.2.10) distributed globally for a stable reference frame establishment (ITRF).

IGS is an international institution involving more than 100 research teams around the world. The IGS collects and distributes data from 350 global GPS stations covering all continents but still with a heterogeneous distribution (densest station spanning in USA and Europe). As a result of this international cooperation, a culture of data sharing has been developed, with data freely available for research purposes via the Internet from IGS Global Data Centers (http://igscb.jpl.nasa.gov and http://sopac.ucsd.edu). The selected GPS stations are planned and installed for continuous and permanent operation. The installation and performance of these stations are based on the IGS guidelines for stations e.g. stable and long-term operation of the station, and availability of daily (24hr) files at 30 sec sampling in the format RINEX (Receiver Independent Exchange Format) and setting the receiver to track satellites at least down to 5° of elevation angle [Moore et al.,

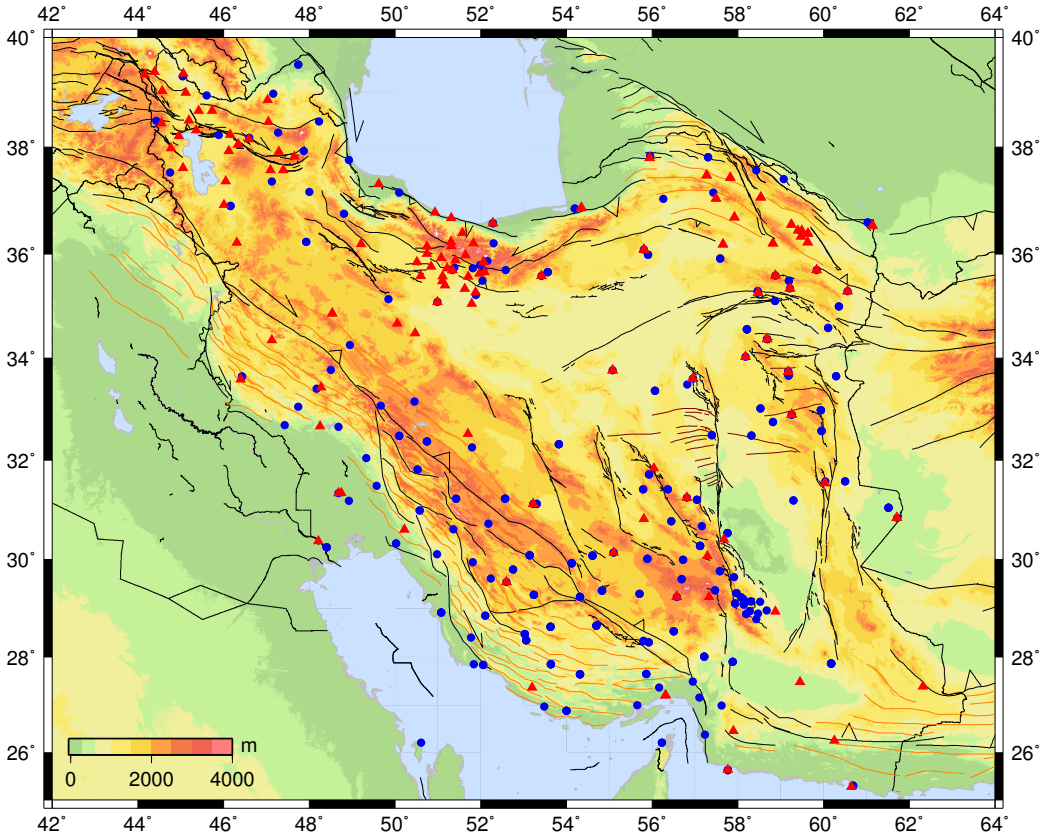

Figure 2.8 – Iranian Permanent (red triangles) and campaign stations (blue circles) (www.ncc.org.ir). NCC has installed more than 120 permanent GPS stations in Iran. The priority for the site selection was to help evaluating seismic hazard for three populate cities (Tehran, Tabriz and Mashhad).

2004]. In Iran, the TEHN station contributes to IGS with daily RINEX data.

2.2.5 GPS Data analysis

For high precision positioning and velocity fields, it is necessary to process the GPS data using scientific software to reduce the various types of errors. Several high precision geodetic software packages are developed such as: BERNESE developed at the University of Bern [Beutler et al., 1996], GAMIT/GLOBK developed at MIT [Bock et al., 1986, Dong and Bock, 1989, Herring et al., 1990, 2008], and GIPSY/OASIS developed at JPL [Lichten and Border, 1987, Blewitt, 1990]. In this study we used the GAMIT/GLOBK software for data analysis of local (e.g.[Vernant et al., 2004a]) and regional (e.g. [Reilinger et al., 2006]) GPS data, over the long term and over long baseline up to thousands of kilometers.

a) Daily GPS positioning

GAMIT uses the double-differenced, ionosphere-free linear combination of the L1 and L2 phase measurements to produce a weighted least square solution for each session (often

Figure 2.9 – A typical Iranian Permanent station. Each station is equipped by Ashtech Z-12 receivers, choke ring antennae and MET3A Meteorological sensor.

1 day). To process the data, the theoretical (modeled) values of the two phases (L1 and L2) are calculated from a model including the orbits of the satellites and a priori values for the coordinates. This model takes into account phenomena such as Earth rotation and the gravitational field of the earth, and the influence of the ionosphere and troposphere on the propagation of signals. The model parameters (Station coordinates, tropospheric delays, ambiguities, and satellite orbits and EOPs) are adjusted to the observations according to the method of least squares to minimize the difference between the observed phases of the GPS signals, and their theoretical values. Thus, the outputs of each daily solution are the 3-dimensional loosely constrained Cartesian coordinates for each station; tropospheric delays every 2h, orbital elements for each satellite, earth orientation parameters and integer phase ambiguities for each daily solution.

For processing the daily GPS data by GAMIT we have followed the processing strategy of Feigl et al., [1993] and Dong et al., [1998]. We use GPS phase observations from the Iranian networks from each day to estimate model parameters. The precise ephemerides incorporated in the processing are the final product of IGS orbits that are readjusted in the least square inversion. To reduce errors in the GPS-derived position, we used up-to-date models of the environmental effects on the GPS measurements. For modeling the troposphere delay, the VMF1 mapping function is used. The absolute IGS antenna phase

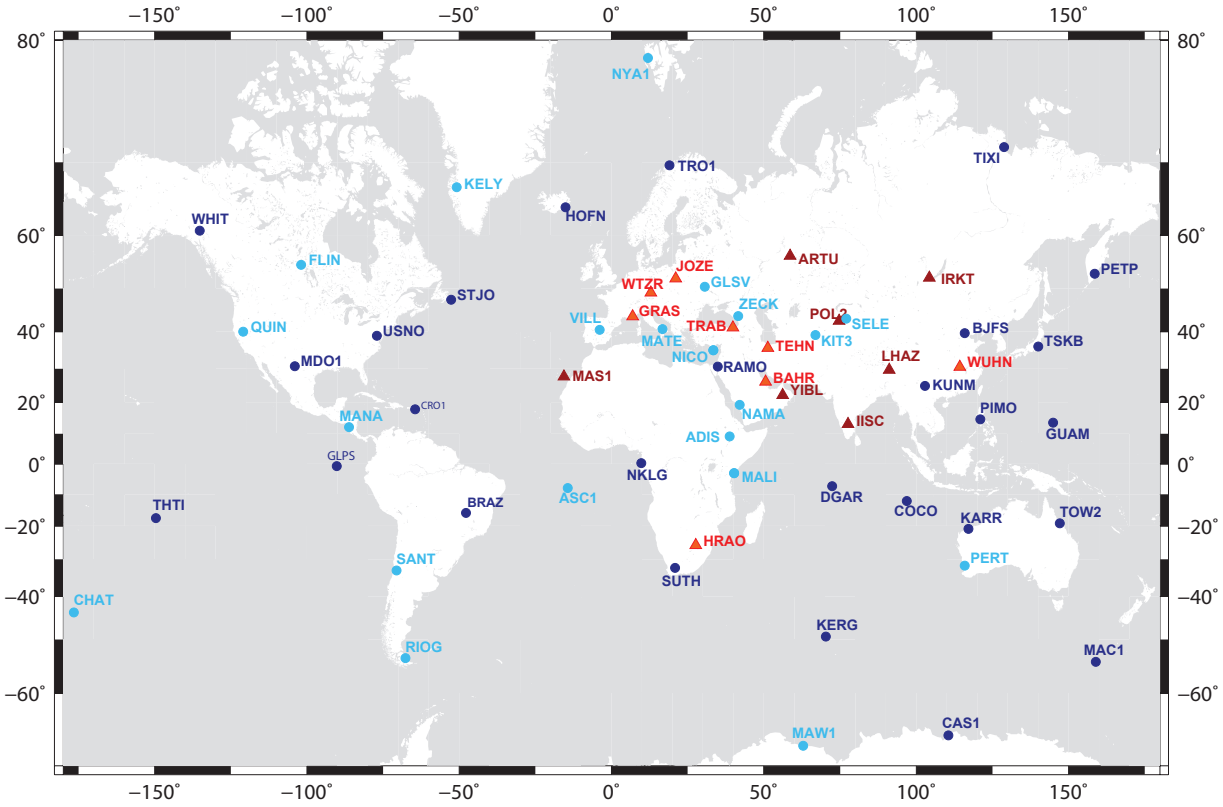

Figure 2.10 – The IGS stations which are used in Iranian daily solutions (triangles) and global daily solutions (circles) in this study. The stations with star are common in regional and global daily solution. The dark color symbols (dark blue circles and brown triangle) are the core stations for estimating the ITRF2008.

center models have been taken into account to remove the phase center error. The solid Earth tides were modeled and the ocean loading effects were taken into account by using the global tide model FES2004 [Lyard et al., 2006, Vergnolle et al., 2008]. Here we can summarize important required input files and tables to gain more accurate results:

- RINEX (Receiver Independent Exchange Format) phase and code observations (one file for each station per day) and navigation files (broadcast ephemerides)
- Station coordinates (a priori)
- Receiver and antenna information for each site (station.info)
- Satellite list and initial conditions for the satellites' orbits
- Antenna phase center correction tables (igs08_1365.atx or antmod.dat)
- Session control table (Sestbl.) contains configuration parameters for the GAMIT run (see Supporting information 8.1.2)
- Site control table (sittbl.) contains constraints on a priori coordinates (see Supporting information 8.1.1)
- Up-to-date tables and modeling files:
  - Ephemerides of Sun and Moon (soltab. and luntab.)

- Nutation tables (IERS/IGS standards) consisting of the position of the Earth's body axis in space (nutabl.)
- Leap second table that is used for conversion from GPS time to UTC (leap.sec)
- Earth rotation parameters (EOP) tables and Polar motion table (ut1. and pole.)
- Global grid file for Ocean Tidal Loading (otl.grd)
- Tropospheric mapping function (VMF1)
- Atmospheric loading grid (atml.grid)
- A priori meteorological model of pressure and temperature such as GPT

In order to tie our local network to the ITRF2008 reference frame, we include 23 IGS stations in our daily solution. These stations are :ARTU,BAHR, DGAR, GRAS, HRAO, IISC, IRKT, JOZE, KIT3, KUNM, LHAZ, MALI, MAS1, NKLG, POL2, RAMO, SELE, TEHN, TIXI, TRAB, YIBL, WTZR, WUHN (see Fig. 2.10 for distribution of stations). At the end of the daily solution, we control several parameters of the solution e.g. the Postfit nrms has a reasonable value which is advised to be less than 0.25 after the least square inversion in GAMIT. Also the adjustments of station coordinates from their a priori position should have small values. Whether phase ambiguities have been solved properly can be seen in the postfit nrms that is unusually high (>0.25) if errors occur.

We used the same strategy to process 7 years (from 2004 to 2011) of continuous data of 50 IGS GPS station around the whole world. These 41 station are COCO, GUAM, TSKB, PIMO, BJFS, PETP, TOW2, KARR, HOFN, TRO1, WHIT, BRAZ, CRO1, THTI, STJO, CAS1, MDO1, GLPS, USNO, SUTH, KERG, MAC1, ADIS, ZECK, NICO, GLSV, MATE, ASC1, CHAT, FLIN, KELY, MANA, MAW1, NAMA, NICO, NYA1, PERT, QUIN, RIOG, SANT, VILL (see Fig. 2.10 for distribution of stations).

b) GPS position time series

The daily solutions of the local Iranian and the global networks are combined using GLOBK, version 5.0. Globk is a Kalman filter whose primary aspect is to combine the loosely constrained solutions. It uses the station coordinates, earth-rotation parameters, orbital parameters generated from the analyses of the primary observations and their associated covariance matrix. These quasi-observations should be processed with loose a priori constraints assigned to the global parameters, so that constraints can be applied uniformly in the combined solution [Herring et al., 2006]. As it is explained before, for stabilizing the ITRF2008 reference frame [Altamimi et al., 2011], we used IGS stations located around Iran (see Fig. 2.10) and in addition a global distribution of IGS stations.

To estimate the precise station positions and linear velocities with respect to the ITRF2008 reference frame we applied the Kalman filter in four steps. In the first step, we combined global and local daily solutions to produce position time series for three components (north, east, up). These daily GPS position time series present velocities due to the tectonic plate motion, such as coseismic and postseismic deformation, magmatic

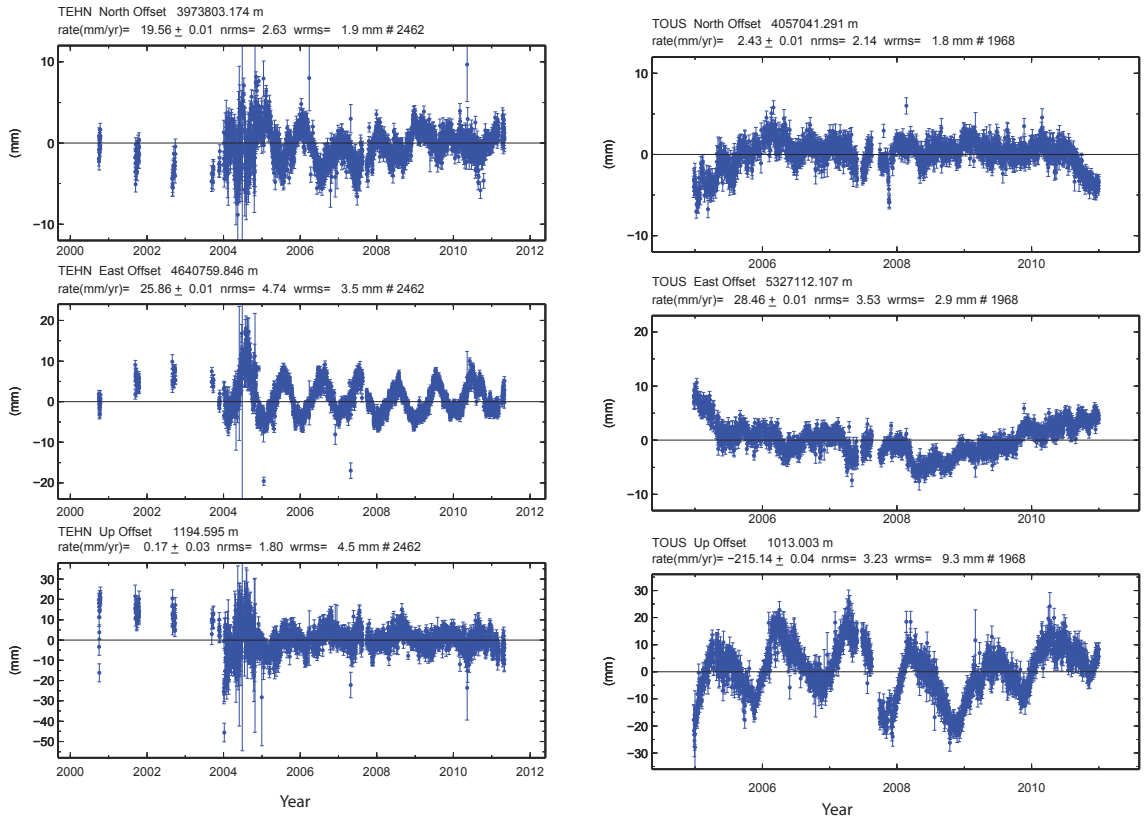

Figure 2.11 – De-trended position time series in NS, EW and UP components. A) 6 years (from 2005 to 2011) time series of TOUS station. B) 11 years (from 2000 to 2011) time series of TEHN station.

uplift, hydrologic deformation, slow slip events [Vergnolle et al., 2010], repeating signals (often seasonal), offsets, outliers and data gaps which we thoroughly examine to identify outliers, offsets, or jumps. Repeating signals often have seasonal periods (i.e., annual and semi-annual). The sources of the seasonal variations may include errors in models of surface mass redistributions, errors in models of antenna phase centers and atmospheric delay [Dong et al., 2002, Ji and Herring, 2011]. It is unlikely that these signals represent perfect sinusoids with temporally constant amplitude [Bennett, 2008]. In the time series of the IPGN network, we can see the seasonal signal after removing the trend of time series. Fig. 2.11 presents time series for two stations TEHN (located in Tehran) and TOUS (located in the North-East of Iran). The time series of TEHN station presents a noisy interval from 2004-2005, the time of changing the antenna and the unstable monument of the station. But for the TOUS station, we can see the highest subsidence rate in Iran with -215 mm/yr that comes from underground water extraction. This high rate of subsidence leads to unstable stations so the horizontal velocity is excluded from tectonic interpretation. After detecting outliers and jumps we improved the position time series by reprocessing the outlier free daily solutions and introducing discontinuities where jumps appear. The precision of the positioning for a station with a linear displacement can be estimated using

the following definition [Larson and Agnew, 1991].

$$WRMS = \sqrt{\frac{N}{N-2} \cdot \frac{\sum_{i=1}^{N} \frac{(x_i-(a+bt_i)^2}{\sigma_i^2}}{\sum_{i=1}^{N} \frac{1}{\sigma_i^2}}} \tag{2.53}$$

where n is the number of measurements, x_i and σ_i are the station position and associated error to x_i, a and b are the intercept and slope of the best fitting linear trend and t_i is the time of the i^{th} observation [Larson and Agnew, 1991]. We found WRMS values of 1.45 mm on average for the NS components (2.5 mm maximum) and 1.7 mm on average for EW components (2.9 mm maximum) and 5.25 mm for the vertical components on average (with 19.1 mm maximum) for the Iranian networks (equation 2.53).

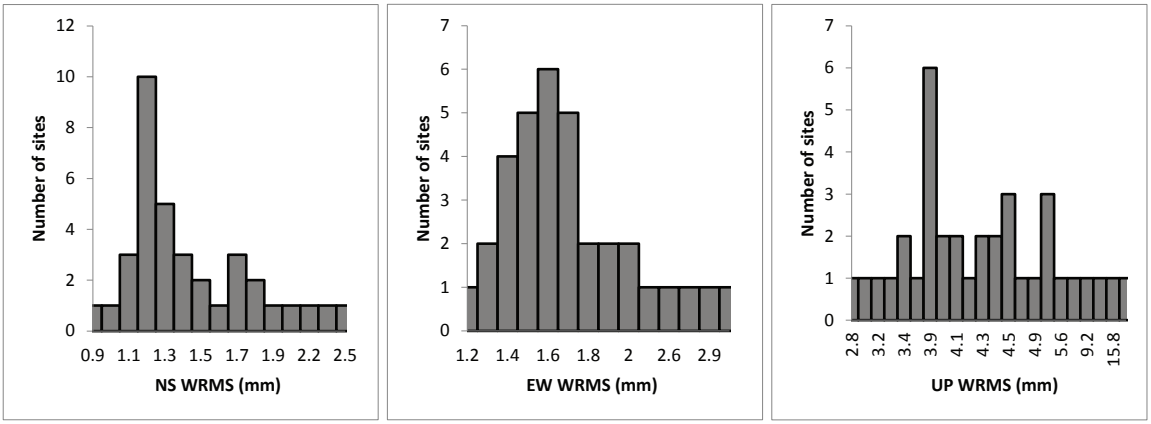

Figure 2.12 – Precision of the GPS solution of Iranian stations presented here as examined from the daily scatter (or long-term repeatability) of individual daily positions.

c) GPS velocity estimation

Noise in GPS position time series is correlated with time [Zhang et al., 1997, Mao et al., 1999, Williams et al., 2004, Langbein, 2008] and space [Wdowinski et al., 1997, Dong et al., 2006] rather than simply independent observations. These space correlated errors can come from the hydrological loading or error in the modeling of orbits, atmosphere or reference frame. If correlated noise is neglected in the least squares estimation of site velocities (i.e., only white noise is assumed), the velocity uncertainties are unrealistically small [Johnson and Agnew, 1995, Williams, 2003, Ji and Herring, 2011]. Thus we used first-order-Gauss-Markov (FOGM) as specific random walk noise to account for correlated noise in velocity estimations [Reilinger et al., 2006, Djamour et al., 2010, Fadil et al., 2011, Saria et al., 2013]. FOGM is implemented in the Kalman Filter of the GLOBK software. We calculate a unique random walk noise model for each station using FOGM by assuming that each time series can be adequately modeled. The algorithm of this stochastic realistic

noise modeling can be described in the following equation [Gelb, 1974]:

$$\phi_{xx}(\tau) = \sigma^2 e^{-\beta|\tau|} \tag{2.54}$$

where $\phi_{xx}(\tau)$ is the FOGM autocorrelation function, σ^2 is the long-term variance, and $1/\beta$ is the correlation time.

The FOGM noise model is estimated from individual station time series by averaging the residuals over increasingly longer intervals. The averaging intervals range from a minimum of 7 days to a maximum of 1/10th of the total time series span increasing sequentially by 7-day increments. This estimated FOGM model is then used to predict the site velocity uncertainty based on the time span of the time series [Reilinger et al., 2006]. Since GLOBK uses a random walk (RW) process noise model (which is a special case of the FOGM model where the correlation time 1/b is infinite) [Herring et al., 2010], we can estimate the RW process noise model that would predict the same velocity uncertainty as the FOGM model over the time span of the time series [Reilinger et al., 2006]. These RW process noise values can be used in the forward run of the GLOBK Kalman filter (using the same data as was used in the time series) to calculate site velocities and their realistic uncertainties. As we need to average over a range of time series, this algorithm can be applied only on continuous time series. For campaign stations we can maximize uncertainties using the maximum value of RW of continuous stations.

d) Establishment of the reference frame

In this step all daily solutions are combined to estimate a linear velocity for each station. To stabilize the result in ITRF2008, a set of 44 IGS stations with a global distribution was used (see Fig 2.10 for distribution of stations). These stations are processed in daily solutions either in the Iranian Network or the global IGS networks (in this thesis with 41 stations) or in both solutions. Then the difference between positions and velocities of sites from our unconstrained solution and a priori values of ITRF2008 positions and velocities are minimized based on estimating a 7-parameter Helmert transformation (translation, rotation, scale) of the network. We chose 45 stations to stabilize our network in ITRF2008. 4 stations with high residuals have been rejected from the process. Thus 41 stations stabilized the network. During this process, the postfit root-mean-square (RMS) of the final reference frame stabilization is 0.12 mm in position and 0.28 mm/yr in velocity in average for the 41 stations. After stabilization of our network in ITRF2008, there are two possibilities to estimate the velocity field with respect to Eurasia. The first typical method is constraining the Eurasian plate by minimizing a selection of GPS velocities from 16 IGS sites distributed across the Eurasian plate. The second method is estimating the velocity field with respect to Eurasia using the a priori coordinate file (itrf08_eura.apr), in which all IGS site velocities are expressed with respect to Eurasia.

Approach	Lat. (deg)	Long (deg)	Mag (deg/My)
itrf08_eura a priori file	55.367 ± 0.178	-96.744 ± 0.167	0.260646 ± 0.000641
Eurasia plate definition	57.077± 0.140	-100.929 ± 0.135	0.273334 ± 0.000495

Table 2.3 – The Comparison between the two approaches of estimating velocity with respect to Eurasia

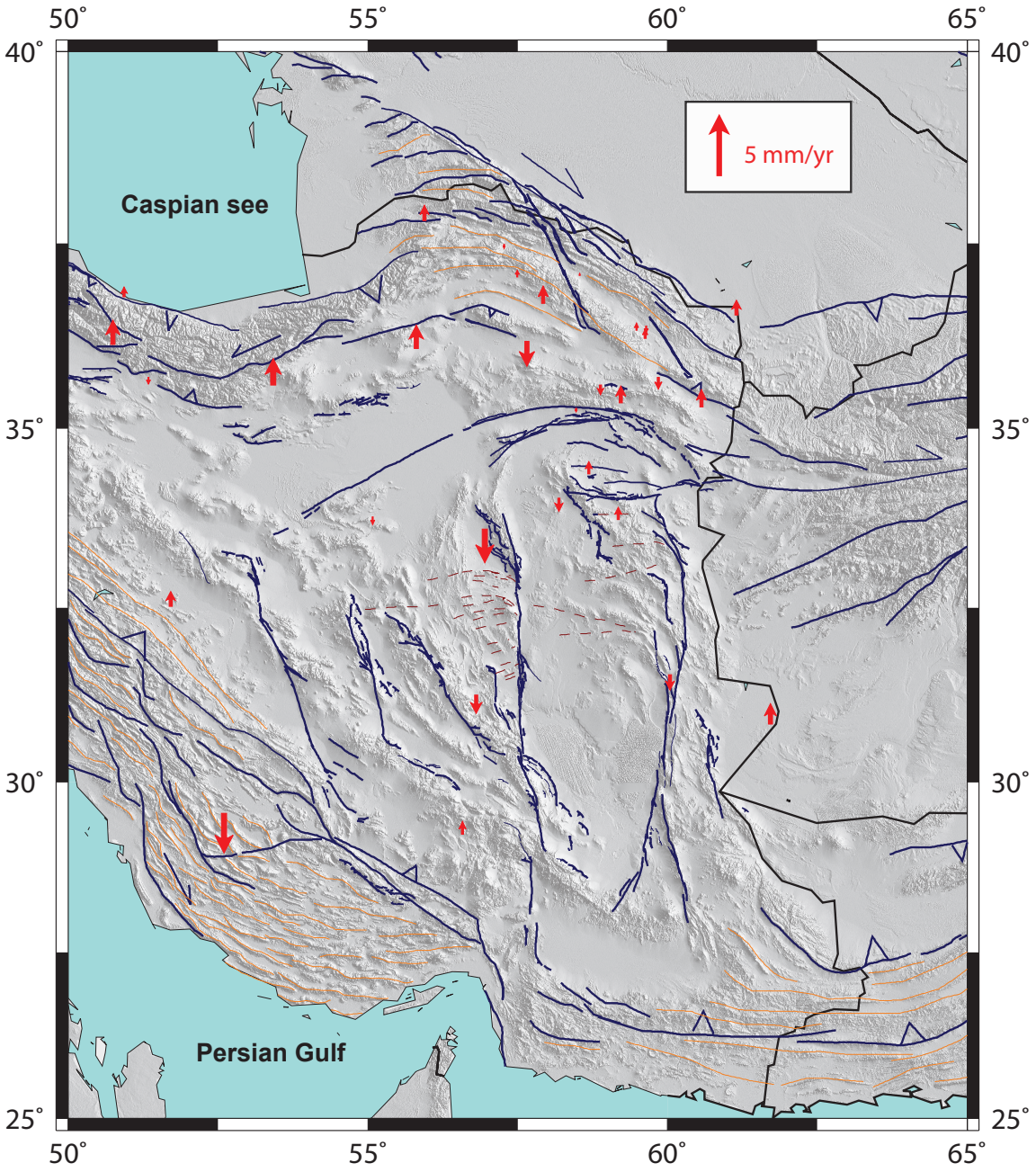

Figure 2.13 – Vertical component of velocity field in Eastern Iran. The northward and southward vectors present the uplift and subsidence motion for GPS stations, respectively

In this thesis, we used both cases to estimate a horizontal velocity field for Eastern and North-East of Iran which I present them in chapter 3 and chapter 5, respectively. Here figure 2.13 present the vertical component of velocity field for Eastern Iran which we

removed some station in Mashhad valley with high rate of subsidence like TOUS, NISH and NFRD.

2.3 Synthetic Aperture Radar Interferometry

Synthetic Aperture Radar Interferometry (InSAR) used in this thesis is based on satellite radar images of the Earth's surface that are obtained by an active remote-sensing method. Images come from side-looking radar that illuminates the ground surface with microwave signal along flight direction (Fig. 2.14). The microwave signals are electromagnetic signals with wavelength that can range from mm to m: X-band (∼3 cm), C-band (∼6 cm), S-band (∼10 cm) or L-band (∼24 cm). The radar antenna receives the backscattered echoes from the Earth's. These echoes are produced since the terrain consists of different scatterers such as, trees, rocks, or buildings on the ground that interacts with the incoming microwave radiation. Radar acquisitions can be made in 'descending' satellite tracks, as the satellite travels roughly from north to south or 'ascending' tracks where the satellite travels S to N (Fig. 2.14).

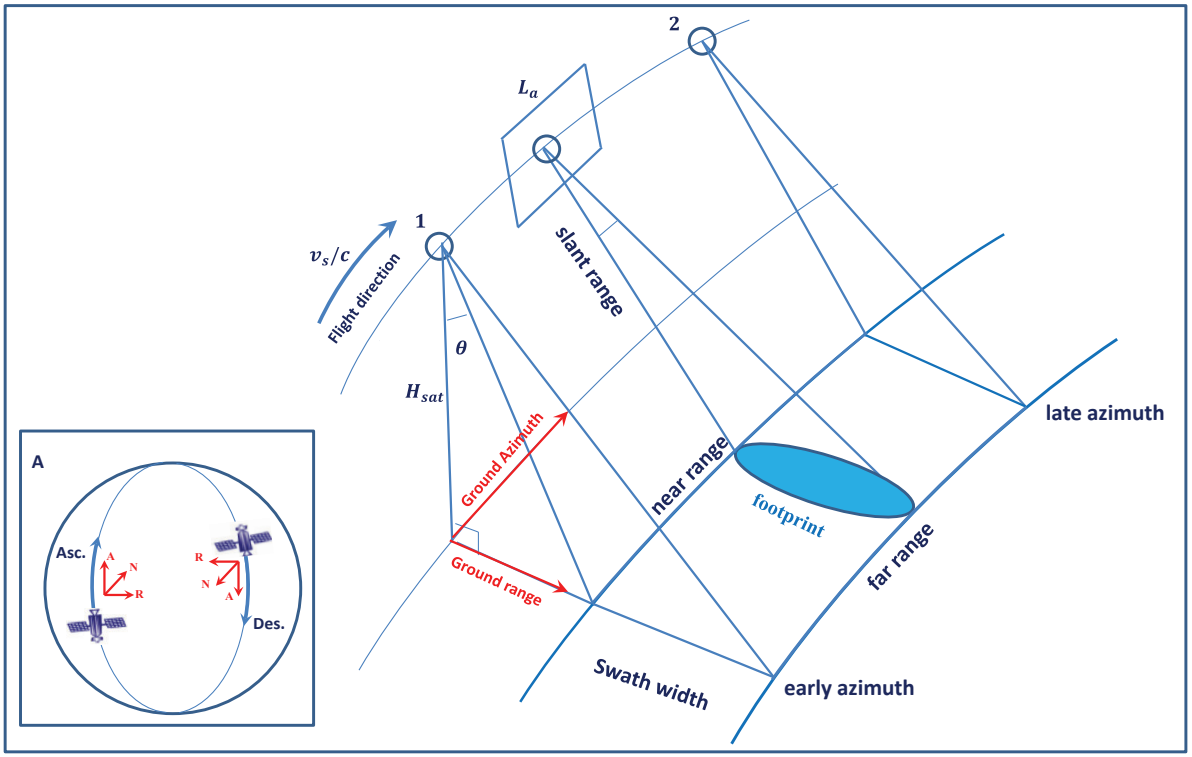

Figure 2.14 – Image geometry of SAR acquisition. Insert map: Dashed lines are the satellite tracks projected onto Earth's surface for ascending (Asc.) and descending (Des.) orbits, in red: A is for azimuth direction that follows the displacement of the satellite, N is for nadir that is the vertical direction from the satellite to the Earth's surface, R is for range that is the range direction corresponding to the looking side direction of the radar (usually on the right). Main figure: The satellite with velocity v_s/c scatter the pulses which illuminate a swath parallel to the satellite direction. The footprint of a single pulse is presented in blue color. The total SAR image starts between "early azimuth and late azimuth time" in azimuth direction, and "near range and far range" in range direction. [Hanssen, 2001]

The radar image geometry is characterized by azimuth and range direction. The azimuth axis is flight direction (along-track), the nadir axis is toward the center of the earth and the range axis is perpendicular to the azimuth (across-track) and nadir axes (Fig. 2.14). These axes define the orbital frame. The slant range is the distance between sensor and objective in range direction. The look angle, θ, is the angle between nadir axis and slant range. The radar instrument images the surface by emitting successive pulses, each of which illuminates a portion of the ground called footprint. The rate at which pulses are transmitted and echoes are received is known as the pulse repetition frequency (PRF). The PRF is high enough so that overlapping footprints are acquired. For the ENVISAT SAR instrument in image mode, the PRF is about 1650Hz, and a target on the ground is seen by several hundred of pulses. For each pulse, the sampling of the backscattered signal (at 19MHz for ENVISAT ASAR) allows to form one line of the raw image (around 5000 samples for ENVISAT, corresponding to 8m sampling resolution in slant range). The samples are sorted by increasing satellite to ground distance: The first sample corresponds to the Near Range (NR) and is the closest to nadir axis, the last sample corresponds to the Far Range (FR). The swath width is the distance between near and far range (Fig. 2.14).

The raw data acquired from the radar are not directly exploitable as images. They required an important signal processing step to form images, resulting in a dramatic improvement of the spatial resolution as explained in the next section. The radar instrument and the associated processing are called Synthetic Aperture Radar (SAR). The SAR interferometry technique uses two or more SAR images to measure ground displacement. At first after SAR image formation, the suitable images need to be accurately coregistered.

Since its birth, InSAR has experienced persistent and rapid methodological improvement to permit to detect the slow slip tectonic signals. This improvement consists of correcting of interferogram of affected error e.g. tropospheric correction [Cavalié et al., 2008, Jolivet et al., 2011, Shirzaei and Bürgmann, 2012], DEM correction [Ducret et al., 2011] or time series analysis [Berardino et al., 2002], Persistent Scatterers [Hooper et al., 2004]. In this study we used the last improvement of SAR data processing strategy to be able to estimate interseismic deformation for some slow slip fault in North Eastern Iran. This was challenging as the tectonic signals is speed of few millimeter per year. After the presentation of the InSAR principles, a section will be dedicated to the different sources of error, and then tropospheric correction method will be presented, followed by the specificity of the time series analysis used in our work. Finally, our InSAR processing strategy is summarized with some details on its practical implementation.

2.3.1 SAR Image Formation and coregistration

The transmitted and received signals are stored as complex numbers, having both amplitude and phase. The received amplitude is characterized by the efficiency of the scatterer, as well as geometrical factors. The recorded phase is determined by the phase of the transmitted signal, the dielectric properties of the medium, and the position of the scatterer. The SAR signal processing needed to improve the spatial resolution, a step called image focalization, should preserve the phase that contains information on the distance from the satellite to the ground. The optimization of the value of certain parameters like the Doppler centroid for the focalization will improve the quality of InSAR measurement. Before the interferometric step, a precise coregistration of the focused SAR images in common image geometry is needed.

SAR Image Resolution :

Spatial resolution is the potential to distinguish two objects close to each other. The resolution of SAR images is different in azimuth and range direction. Range resolution before SAR processing depends on the pulse duration. Range resolution of side-looking image is:

$$R_R = \frac{C\tau}{2sin\phi} \tag{2.55}$$

where τ is pulse duration, ϕ is incident angle and C pulse velocity

Azimuth resolution before SAR processing depends on the ratio between signal wavelength and antenna length. A small ratio provides better resolution, so it will be improved by decreasing wavelength and increasing antenna length. The azimuth resolution of a side-looking image is:

$$R_A = \frac{H\lambda}{lcos\phi} \tag{2.56}$$

where λ is wavelength, H is altitude, ϕ is incident angle, l antenna length. For instance, with the ENVISAT ASAR, in image mode, given λ=5.6 cm, τ=37.1 μs, l=10 m, $H = 700$ km and $\phi = 23°$, then the range and azimuth resolution are respectively: $R_R = 4.8km$ and $R_A = 14km$. The Synthetic Aperture Radar processing allows to dramatically enhancing the resolution in range and azimuth direction [Bamler, 2000] to:

$$R_{Rsar} = \frac{C}{2B} \tag{2.57}$$

$$R_{Asar} = \frac{l}{2} \tag{2.58}$$

where B is the frequency bandwidth of transmitted pulse (16MHZ for ENVISAT ASAR). This gives for ENVISAT ASAR a ground resolution of 20m in range direction

and 4m in azimuth direction. Note that after SAR processing the achieved azimuth resolution is equivalent to the resolution before processing with an antenna of about 10km. Actually, the SAR processing is using the displacement of the satellite to increase artificially the antenna length, and then simulates a large antenna length, 1000 times larger than the real one in the case of ENVISAT. This explains the name "Synthetic Aperture Radar". The focused images are called SLC (for Single look Complex image).

The doppler centroid parameter selection:

A shift in frequency of the radar echo due to the Doppler Effect is registered when recording the radar echoes. This shift depends on the view angle of the radar with respect to the direction of flight. It can be estimated by the Doppler centroid of the SAR data. If the ground has been seen from view angles that are too different between 2 dates of acquisition, it will be more difficult to get information about the ground displacement between these 2 dates. However it is possible during the focalization of SAR images to tune the Doppler centroid, so that the 2 focused images will be as if the radar was looking from the same point of view. But it is at the expense of the spatial resolution, because only the common Doppler frequency band of the 2 acquisitions is kept. One can generalize this approach to a larger number of images, by fixing a minimum percentage of common Doppler frequency bands. If one of the images has Doppler frequency out at this band, the image will not to be used for this dataset.

Super master selection before coregistration:

For InSAR time series analysis it is convenient that all SAR images are exactly in the same geometry. The usual method consists to select one of the images as the super master image. All the other images will be coregistered with respect to this image. To select the super master image, we used the criteria proposed by Hooper et al. [2007], which try to maximize the correlation of all the images. That correlation depends on four terms: time interval (T), perpendicular baseline (B in figure 2.15), difference in Doppler centroid frequency and thermal noise [Zebker and Villasenor, 1992]. The total correlation can be expressed as a function of these terms [Hooper et al., 2007]

$$\rho_{total} = \rho_{temporal} \cdot \rho_{spatial} \cdot \rho_{doppler} \cdot \rho_{thermal} \tag{2.59}$$

While

$$\rho_{total} \approx \underbrace{[1 - f(\frac{T}{T^c})]}_{temporal} . \underbrace{[1 - f\frac{B_{prep}}{B^c_{prep}}]}_{spatial} . \underbrace{[1 - f\frac{F_{DC}}{F^c_{DC}}]}_{doppler} \cdot \rho_{thermal} \tag{2.60}$$

where

$$f(x) = \begin{cases} x & for \quad x \leq 1 \\ 1 & for \quad x1 \end{cases} \tag{2.61}$$

The superscript c is the critical values for parameters and these values depend on the data set. The master image can be selected by maximizing $\sum_{i-1}^{N} \rho_{total}$.

Coregistration of the images :

After focalization and super master image selection, all SLC images have to be coregistered in the geometry of this image. First, for each image, a model of the geometric deformation with respect to the super-master is established. The model we used is defined by a function of the azimuth and range pixel position, defined as:

$$f(x,y) = Ax^2 + Bx + Cy^2 + Dy + Exy + F \tag{2.62}$$

where x and y are range and azimuth, respectively, and A, B, C, D, E and F are parameters to be estimated. The estimation is based on measurement of offsets between each image and the super-master by image correlation technique. Once the parameters are estimated, each image can be resampled on the super-master grid.

2.3.2 Coherency

The phase accuracy in SAR interferometry is mainly affected by phase noise and decorrelation. A quality measure of the interferometric phase quality is the complex correlation coefficient, or complex coherence, defined as [Bamler and Hartl, 1998].

$$\gamma = \frac{E\{P_{sar1} P^*_{sar2}\}}{\sqrt{E\{|P_{sar1}|^2\} E\{|P_{sar2}|^2\}}} \tag{2.63}$$

where $E\{P\}$ is the expectation operator. The expectation operators are often replaced with spatial averaging within a neighborhood of the pixel of interest (usually 3 $\times$ 3 pixels):

$$\hat{\gamma} = \frac{|\sum P_{sar1} P^{sar2}|}{\sqrt{\sum |P_{sar1}|^2\} \sum |P_{sar2}|^2}} \tag{2.64}$$

The values of $\hat{\gamma}$ are between 0 and 1, where a coherence value of 1 or 0 corresponds to perfect or weak phase correlation between the two measurements. In the case of a low coherence value, it is more complicated to measure the displacement. Decrease of the coherence in SAR interferometry can be caused by several effects. Coherence can be related to 3 terms, (1) thermal coherence $\gamma_{thermal}$ related to the thermal noise added by the instrument during data acquisition the data taken and the different steps of the data

processing, (2) temporal coherence $\gamma_{temporal}$ related to the change of the properties of backscatter reflectors of the ground in repeat passes, as for instances vegetation growth, climatic changes and the human presence cause all kinds of modifications in the land cover, (3) geometric coherence $\gamma_{geometry}$ related to the geometrical conditions of the two acquisitions (different incidence or view angle) [Zebker and Villasenor, 1992, Bamler and Hartl, 1998, Hanssen, 2001]. The interferometric coherence can be expressed in a simplified form in function of these effects as:

$$\hat{\gamma} = \gamma_{thermal} \cdot \gamma_{geometry} \cdot \gamma_{temporal} \tag{2.65}$$

Usually, interferograms with large temporal and perpendicular baseline have lower coherences. For large temporal baseline interferogram, the property of the ground will possibly change during time and for large perpendicular baseline, the incidence angle change and consequently the ground is not seen from the same point of view [Massonnet and Feigl, 1998].

2.3.3 SAR Interferometry

An interferogram is obtained by cross-multiplying, pixel by pixel, two SAR SLC image. If we consider the first image as the master image and the second image as the slave image, as a result, the interferogram amplitude is the amplitude of master image multiplied by that of slave image, whereas the interferometric phase is the phase difference between the images. Each pixel is a complex number with a real and imaginary part:

$$\Phi_{1,2} = |A_1|e^{i\phi_1}|A_2|e^{-i\phi_2} = |A_1||A_2|e^{i(\phi_1-\phi_2)} \tag{2.66}$$

From interferometric phase to ground displacement :

If we assume ideal case with no change in atmosphere between the two acquisitions, no orbital and no DEM error, and that the 2 images have been acquired exactly from the same point of view, then one can interpret the phase 2.67 in terms of ground displacement. For instance, if we consider one ENVISAT interferogram (Fig. 2.17 -D), by assuming a reference point, one can count the number of interferometric phase cycles (represented by color fringes in figure 2.17) to recover the displacement with respect to the reference point. Fringes can be seen as line of "iso-displacement" along the Line-Of-Sight (LOS). The interferometric phase is related to the physical distance between the sensor and the target on ground:

$$\Phi_{1,2} = \phi_1 - \phi_2 = \frac{2\pi}{\lambda/2}.(R_1 - R_2) = \frac{4\pi}{\lambda}.\Delta R \tag{2.67}$$

where λ is the wavelength of the radio waves. This LOS displacement cannot be directly interpreted in terms of 3D displacement without some a priori assumptions.

Due to the orbital and viewing geometries of current SAR satellites, InSAR measure-

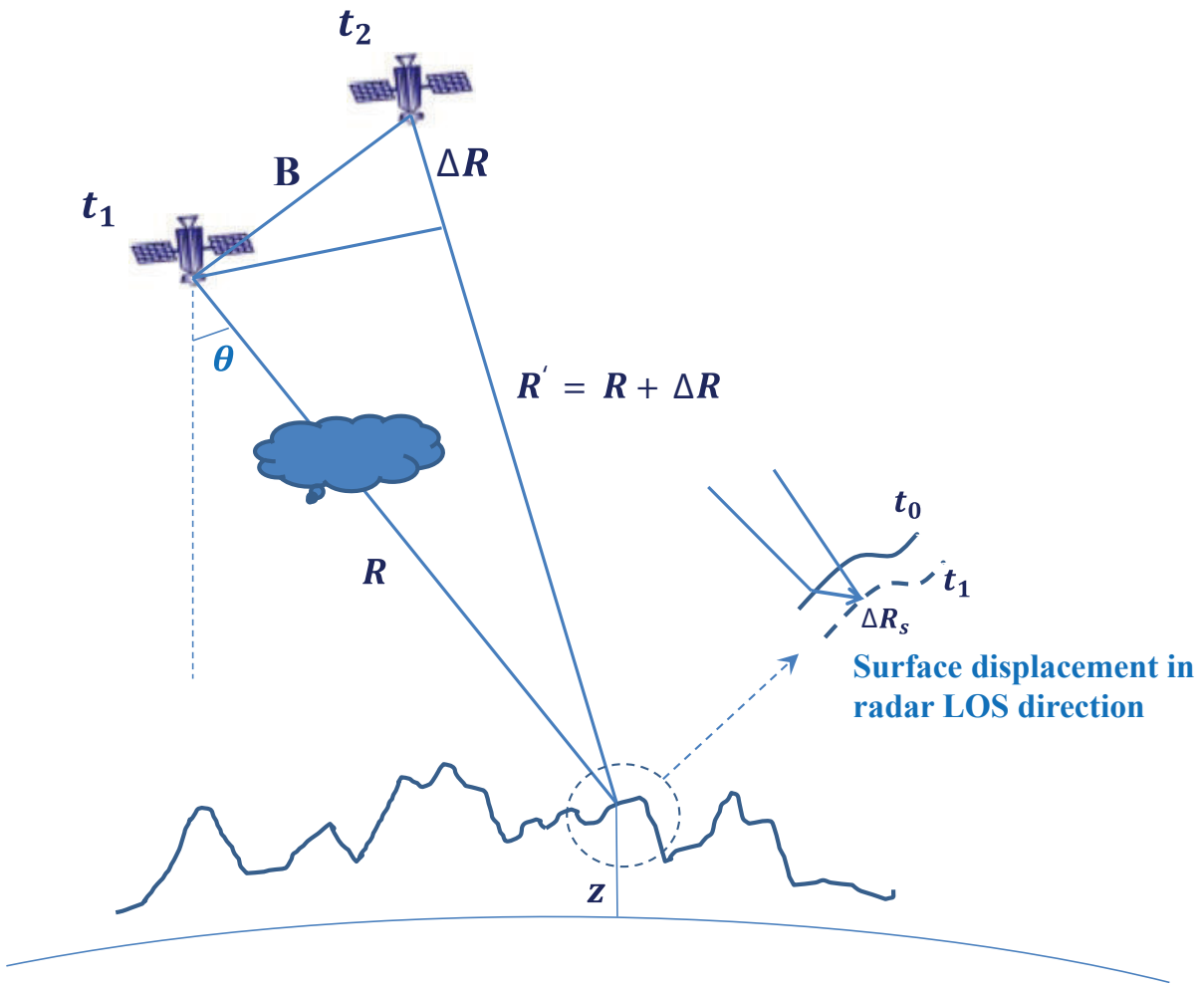

Figure 2.15 – Classical geometric configuration for two-pass space-borne SAR interferometry. The same SAR satellite observed the ground at two different times (t1 and t2) from a slightly different point of view. R and R' are the distances between SAR instrument and the point on the earth surface at elevation z. A possible surface deformation occurring between the acquisition times will lead to an interferometric phase term ΔR_s. B is perpendicular baseline between two orbital path and θ is the angle of incidence of the emitted signal from the first acquisition. The cloud at the t_1 radar acquisition illustrates that atmospheric effects can affect the radar propagation, producing an additional path delay.

ments of ground deformation are particularly sensitive to vertical motions and east-west motions, but are only weakly sensitive to north-south movement. This is a major limitation in the use of InSAR to recover displacements for geophysical applications, where displacements are three-dimensional. This limitation can be partially mitigated by measuring the same area with both ascending and descending datasets [Wright et al., 2004, Walters, 2012], and by combining InSAR observations with GPS measurements or other a-priori knowledge of ground movements [Wang and Wright, 2012].

Perpendicular baseline:

An important parameter is the perpendicular baseline, B. This parameter describes

the geometric orbit difference between two paths of satellite. The orbit difference can be projected on two vectors $B^{\parallel}$ and $B^{\perp}$ (see Fig. 2.16). If there will be large difference in two orbits, this parameter will be large, and then the geometry of the image will be too different from one acquisition to another. This leads to a general lower quality of generated interferograms.

Flattening :

In general, the satellite will not return to the exact same position on successive passes, and there will be a baseline separation B between any pair of acquisitions. This causes phases variations related to the earth-curvature and topography, that are corrected (see previous section, where should add a paragraph on this), using the orbital data and DEM. If we consider two points P and P' located the same altitude, the path $S-P'$ will be longer than the path SP equal to ΔR_{SR} (Fig. 2.16). This difference (ΔR_{SR}) leads to have a residual term due to orbital error in the interferometric phase [Jolivet et al., 2012]:

$$\Phi_{1,2}^{orbit} = \frac{4\pi}{\lambda}\frac{B^{\perp}}{R_1 tan\theta}\Delta R_{SR} \tag{2.68}$$

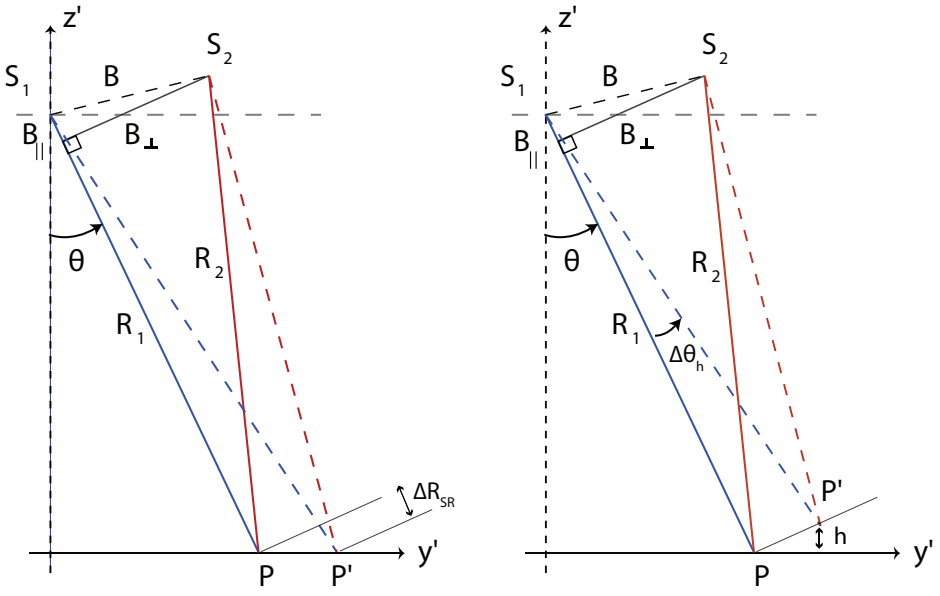

Figure 2.16 – Geometry of SAR acquisition: Schematic view of the two SAR image to calculate the phase related to the orbit error residual (a) and to the topography error residual (b). (Picture from [Guillaso, 2003])

Removing topographic phase :

The topography can introduce different view angle and therefore a phase change between two pixels. If we consider an interferogram of two dates i and j, and a perpendicular baseline of $B^{\perp}$, the topographic term, ϕ_{ij}^{topo}, for a variation in altitude (h) between two

pixel P and P', the topographic phase is (Fig. 2.16):

$$\phi_{ij}^{topo} = \frac{4\pi}{\lambda}\frac{B_{ij}^{\perp}}{Rsin\theta}h \tag{2.69}$$

where λ is the wavelength, θ is the view angle and R is the range. In differential SAR interferometry, a Digital Elevation Model (DEM) is used to remove the topographic component from the interferograms. The amplitude of this effect varies with the perpendicular baseline between the two acquisitions (equation 2.69).

Filtering the interferogram :

Filtering the differential interferogram helps to reduce phase noise to make the phase unwrapping (next section) more efficient and simpler. Several spatial filters can improve the spatial coherence including the adaptive filter developed by Goldstein et al. [1998] .

Due to the low coherency in some interferograms, we need to improve the spatial coherency with averaging interferometric phase in larger windows which is called " multi-looking". This will help to improve the fringe visibility but it will reduce the resolution of images. In our study interferograms are looked by factor of 4 in range and of 20 in azimuth. Figure 2.17 present the effect of filtering and multi-looking in the fringe visibility.

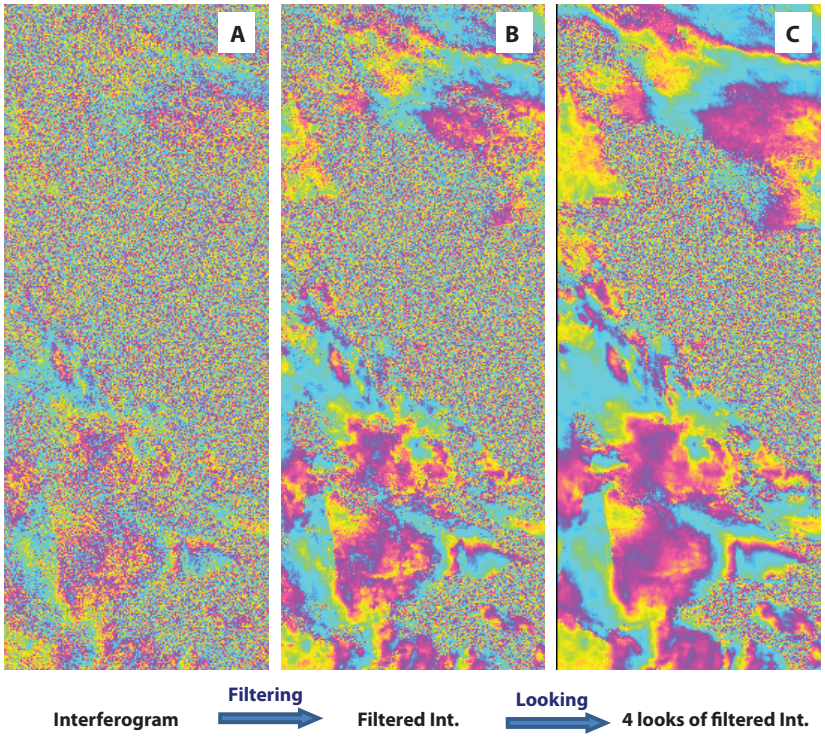

Figure 2.17 – Interferogram between ENVISAT image of dates 20050608 and 20090930. A) Raw interferograms. B) Filtered interferogram using a power spectrum filter. C) Filtered interferogram looked by the factor of 4 in range and 20 in azimuth.

Unwrapping the interferogram : The interferometric phase varies between $-\pi$ and π , therefore the phase is wrapped in this range. In other words, when the signal

phase reaches one of the range value boundaries ($-\pi$ or π), it jumps to the other one (Fig. 2.18). To obtain ground deformation based on InSAR measurement, this 2π wrapped phase should be unwrapped. Then, the unwrapped phase can be defined by equation:

$$\phi_{unwrapped} = \phi_{wrapped} + 2\pi.k \qquad where \quad \phi_{wrapped} \in [-\pi, \pi] \tag{2.70}$$

The recovery of this integer number k or to reconstruct the phase measurement is the phase unwrapping step. The unwrapping step can be done in 2D amongst the different existing algorithms such as the branch-cut [Goldstein et al., 1988] or SNAPHU [Chen and Zebker, 2000]. In our processing it has been done based on a branch-cut algorithm. In some cases, there is disconnection between the phases inside interferogram so we need to make bridge of phase between these two areas.

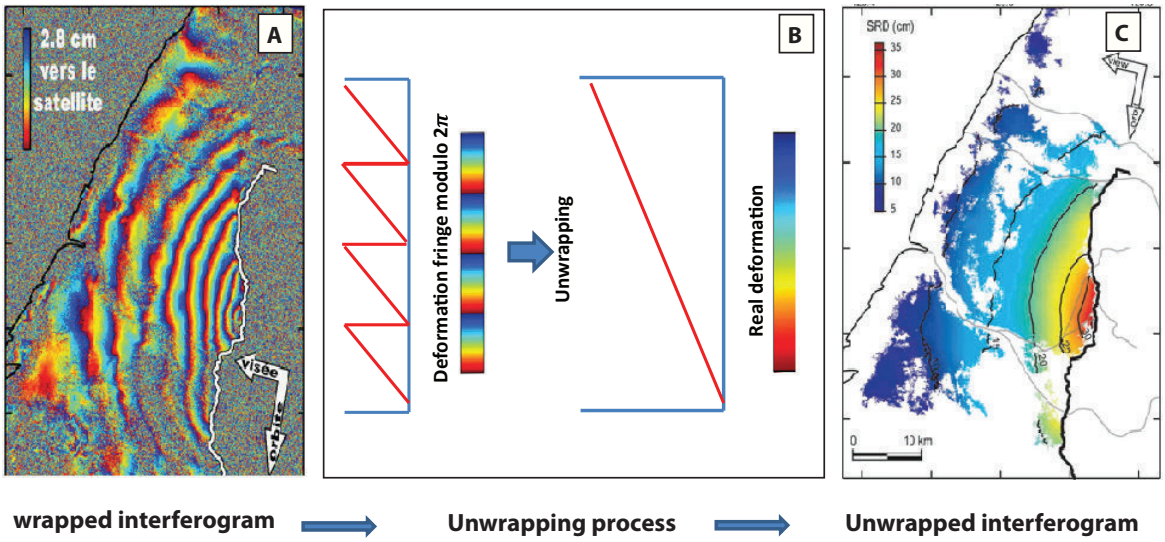

Figure 2.18 – A) The interferometric phase are repeat pattern which wrapped between [$-\pi$,π] and can be present by colored cycles of phase, called fringe. Each fringe indicates one phase difference cycle. Each cycle contain blue, cyan, green, yellow and red with $-\pi$ (blue) to π (red). B) The phase measurement, in terms of multiples of 2π, should be recovered and this is performed by means of the phase unwrapping techniques. C) Unwrapped interferogram [Pathier, 2003]

2.3.4 Sources of errors and interferograms correction

The interferometric phase calculated from two acquisitions 1 and 2, $\Phi_{1,2}$ can be written:

$$\Phi_{1,2} = \Phi_{1,2}^{atmo} + \Phi_{1,2}^{topo\_res} + \Phi_{1,2}^{orbit\_res} + \Phi_{1,2}^{def} + \Phi_{1,2}^{noise} \tag{2.71}$$

where $\Phi_{1,2}^{atmo}$ related to the tropospheric delay, $\Phi_{1,2}^{topo\_res}$ related to the DEM error, $\Phi_{1,2}^{orbit\_res}$ related to the orbital error residual, $\Phi_{1,2}^{noise}$ related to the noise, and the $\Phi_{1,2}^{def}$

related to deformation. For this study, the deformation component of the interferometric is the signal of interest, and the other components are seen as error to be mitigated.

The $\Phi_{1,2}^{noise}$ component typically increases with time span and baseline. The thermal component of noise can reach to the $\frac{1}{30}\frac{\lambda}{2}$, for ENVISAT with $\lambda = 5.6cm$, it correspond to an error of 1mm [Hanssen, 2001]. The change in atmospheric delay and orbital error contributes to an apparent lengthening or shortening of the distance from ground to satellite, that can reach several centimeters for ENVISAT data. To obtain mm level of interseismic deformation, in the following section, we will explain the contribution of each terms and the strategy which we used to reduce them.

The main problem in estimating interseismic deformation from interferograms is that the tectonic signal measured along the radar Line of Sight (LOS) is combined with orbital and topography errors residual and atmospheric phase delays of similar or even larger amplitude (a few millimeters to centimeters, [Zebker et al., 1997, Massonnet and Feigl, 1998]. In some cases, atmospheric effects resulting in strong phase gradients may even be mistaken with the tectonic signal [Puysségur et al., 2007]. Looking at individual interferogram, in our data set, the interseismic deformation can be clearly observed in only a few interferograms. In most of them, atmospheric effects and orbital residual dominate the interferograms and have to be corrected to allow further tectonic signal detection.

a) Orbital error component of the interferometric phase

Phase variations in some interferograms are sometimes dominated by long wavelength phase ramps due to unmodelled orbital errors in the flattening step. Precise DORIS orbital data for ENVISAT satellite provided by ESA are used in SAR image processing (Fig. 2.19). These orbits are accurate to ∼5 cm in the radial direction and ∼ 5-8 cm in the cross-track direction, with radial velocity errors of around 0.5 mm/s [Zandbergen et al., 2003] Therefore a residual of term remains in the interferogram. A classic way of treating with this residual ($\Phi_{1,2}^{orbit-res}$) is fitting a twisted plane in the unwrapped interferogram. Here we follow a different approach that we search for a best fitting ramp in range direction, varying linearly in azimuth, followed by a best fitting ramp in azimuth, using the wrapped interferometric phase. Those parameters are estimated from the weighted mean of local estimations of the phase gradient computed on a sliding window basis.

b) The DEM error component of the interferometric phase

The error in estimating DEM can produce error in removing topography from interferogram. Correction of this error on wrapped interferogram will improve the spatial phase at unwrapping step. Here we will use the approach that Ducret et al. [2013] developed based on a series of wrapped small baseline interferograms with varying perpendicular baselines of up to 500 m. According to the equation 2.69, the residual DEM error is coming from

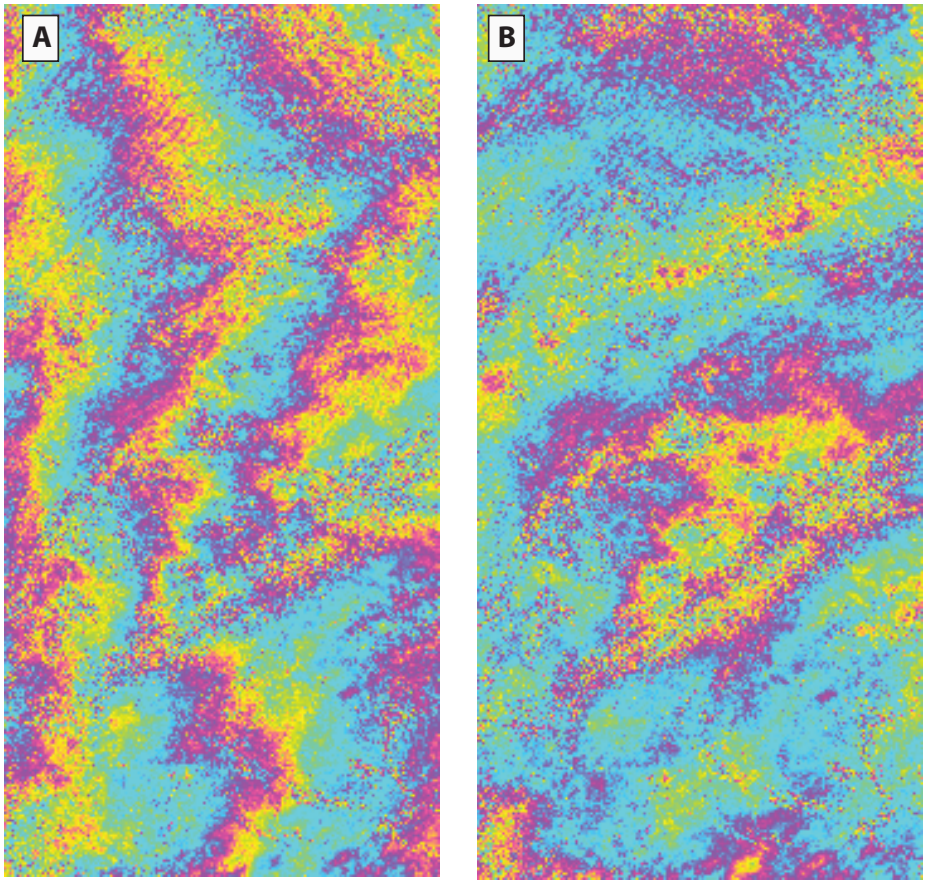

Figure 2.19 – A) It present the interferogram (20100419_20100524) covered the Doruneh fault with orbital error that it parallel to the azimuth (orbit path) for one. B) It presents the interferogram (20100419_20100524) covered the Doruneh after orbit correction with strategy explained in the text.

accuracy in altitude estimation and it can be expressed:

$$\phi_{ij}^{topo\_res} = \frac{4\pi}{\lambda}\frac{B_{ij}^{\perp}}{Rsin\theta}\delta h_{error} \tag{2.72}$$

This residual error is considered as correlated spatially at local scale [Ferretti et al., 2001, Hooper, 2008]. We can write the differential phase, $\delta\phi^{ij}$, with respect to a reference point as a following expression:

$$\delta\phi_{ij} \approx (\delta\alpha B_{ij}^{\perp} + \beta)[2\pi] \tag{2.73}$$

where β is a phase offset and $\delta\alpha$ is the DEM coefficient and can be expressed:

$$\delta\alpha = 4\pi/\lambda Rsin\theta(\delta h_{error} - \delta h_{ref}) \tag{2.74}$$

After dividing each interferogram to overlapping subwindows and select a pixel, with highest spatial coherence averaged on the series of Interferograms, as a reference, the $\delta\alpha$

can be estimated for each pixel [Ducret et al., 2013]. The DEM error coefficients $\delta\alpha$ of each overlapping subwindows should be mosaicked. For the areas with low coherence, we can use the median value of the DEM errors within the subwindow, weighted by the pixel temporal coherency, and subtracts it from all DEM errors of this window. Then the adjustment applied across overlapping area of the sliding windows to have the homogenous DEM correction over the whole SAR image. The outliers of DEM error correction can be removed by using a low-pass filter. The final map is used for DEM correction residual.

This Algorithm is performed on the data sets of this thesis, Doruneh and Shahroud fault system. It is important to have a sufficient number of interferograms and interferograms with smaller temporal baseline will improve the coherency of DEM errors estimation. Figure 2.20 presents how this error correction remove the residual topography effect for interferograms covering the Shahroud fault system, which cross Alborz mountain range. Additionally, this algorithm improves significantly the phase unwrapping step and it decreases the number of unwrapping errors.

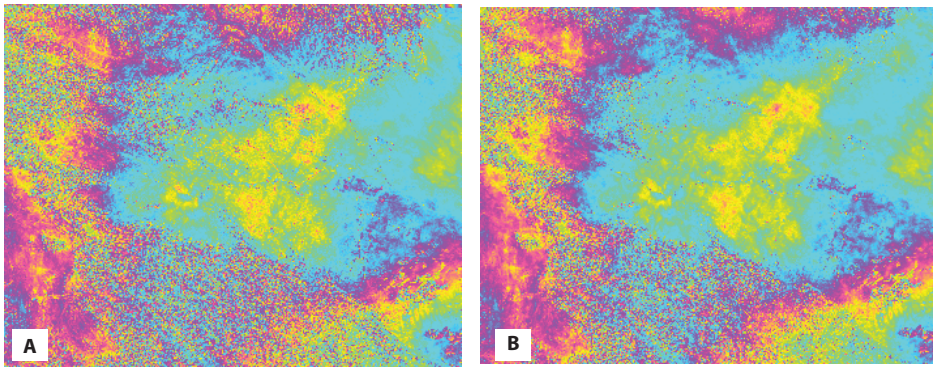

Figure 2.20 – A) The wrapped interferogram before DEM residual correction. B) The wrapped interferogram after DEM residual correction

c) The atmospheric components of the interferometric phase

One of the most important issues in SAR interferometry in interseismic studies with few millimeter of deformation level in a year is the atmospheric component of the interferometric phase. Changes in atmospheric structure between radar acquisitions commonly cause signals equivalent to displacements of the order of several (∼10) cm per interferogram [Zebker et al., 1997]. Therefore the atmospheric signal can be many times of the size of tectonic signal, which is a major limitation to the use of InSAR. For this, removing or reducing this contribution is a key issue in methods of SAR processing in interseismic studies.

As it is explained in section a), spatial and temporal variations in the refractive index of the atmosphere will generate path delay of the electromagnetic wave transmitted by the satellite [Bean and Dutton, 1968, Thayer, 1974, Hanssen, 2001, Puysségur et al.,

2007]. The variation of refractive index comes from the atmospheric humidity, pressure and temperature changes. The radar phase delay for each SAR image depends on the refractivity index N of the atmosphere, N can be expressed by following equation:

$$N = (n-1) \times 10^6 = k_1 \frac{P}{T} + k_2(\frac{P_w}{T}) + k_3(\frac{P_w}{T^2}) + k_4 W_{cloud} + K_5 \frac{n_e}{f^2} \quad (2.75)$$

where n is the refraction index of air at radio frequencies. P is the total pressure (mbar), P_w is water vapor partial pressure (mbar), T is the temperature (K), W_{cloud} is the cloud water content ($km.m^{-3}$), n_e is the electronic density of the ionosphere, and f is the electromagnetic wave frequency, $k_1 = 77.6 \quad K.Pa^{-1}$, $k_2 = -6.0 \quad K.Pa^{-1}$, $k_3 = 3.75 \times 10^5 \quad K^2.Pa^{-1}$, $k_4 \simeq 1.45 m^2.g^{-1}$ and $k_5 \simeq -4.03 \times 10^7 m^3.s^{-2}$. The first term is related to the influence of refraction on the dry air, which is known as hydrostatic delay. The Wet delay is sum of second and third terms which come from the influence of the water vapor contained in the air. The fourth term is related to the non-gaseous components like liquid or solid water, in the form of rain, clouds or snow, and the fifth terms is related to the dispersive effect of the ionosphere on electromagnetic waves.

The term of delay generated by the non-gaseous components in the air is not only significantly smaller than that from the wet and hydrostatic delays but also it ir rarer and much more localize [Solheim et al., 1999]. Variations in electron density in the ionosphere lead to changes in the refractive index, and have been observed to cause distortions or variations in the azimuth direction and kilometer-scale streaks in interferograms [Gray et al., 2000, Walters, 2012]. Gray et al., 2000 described that the ionosphere influence L-band SAR more than an equivalent C-band SAR for two reasons: First, the phase shift arising from a particular integrated electron density will be larger because of the basic dispersive nature of the phenomena, and secondly, the beam width is broader and therefore the possibility of significant spatial change in electron density in the aperture time is larger. However, there is no L-band interferogram processing in this thesis allow us to neglect this effect.

Atmospheric delays affecting a SAR interferogram are measured as a double difference, both in time and space, of propagation delays from satellite to ground then back to satellite [Doin et al., 2009]. This delay can reach to the several centimeters between two pixels located at different altitudes. The LOS single path atmospheric delay $\delta^s_{L0S}(z)$ is the integral of the air refractivity between the surface elevation z and elevation of reference z_{ref} [Berrada Baby et al., 1988, Doin et al., 2009, Jolivet et al., 2011].

$$\Delta L^s_{LOS}(z) = \frac{10^{-6}}{cos(\theta)} \{ \frac{k_1 R_d}{g_m} (P(z) - P(z_r ef)) + \int_z^{ref} ((\mathrm{k_2} - \frac{\mathrm{R_d}}{\mathrm{R_v}} \mathrm{k_1}) \frac{\mathrm{e}}{\mathrm{T}} + \mathrm{k_3} \frac{\mathrm{e}}{\mathrm{T^2}}) \mathrm{d}z \} \quad (2.76)$$

where θ is the local incidence angle, $R_d = 287.05 J/kg/K$ and $R_v = 461.495 J/kg/K$

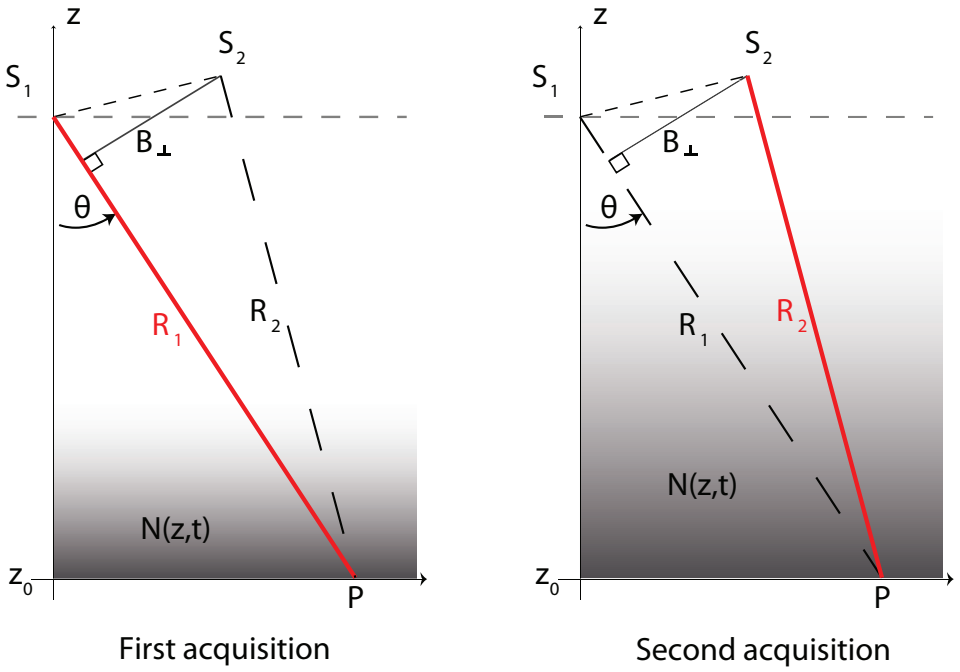

Figure 2.21 – Diagram shows the influence of variations in the refractive index N in the air along the line of sight for first and second acquisitions. (figure from [Jolivet, 2011])

are respectively the dry air and water vapor specific gas constants, g_m is a weighted average of the gravity acceleration between z and z_{ref}, P is the dry air partial pressure in Pa, e is the water vapor partial pressure in Pa, and T is the temperature in K. The constants are $k1 = 0.776 \quad K.Pa^{-1}$, $k2 = 0.716 \quad K.Pa^{-1}$ and $k3 = 3.75 \times 10^3 \quad K^2.Pa^{-1}$. z_{ref} is chosen as the height above which the delay is assumed to be nearly unchanged with time (typically 10000 m). The first term in equation 2.76 is related to the hydrostatic delay path and the second term is related to wet delay path in SAR signal.

Numerous studies have focused on the quantification and mitigation of tropospheric delays using various approaches based on stacking or time series analysis of interferograms, empirical relation of tropospheric delay to the interferometric phase or prediction of tropospheric delay base on independent measurement of interferogram. However still there is no universal method to correct interferogram for atmospheric effects that can work best or can be employed in all condition. In next section I will explain the strategy which I used in this study.

2.3.5 Tropspheric delay correction methods

The detection of low amplitude deformation remains challenging due to atmospheric delay contribution signals that spread over a broad range of spatial wavelengths. The atmospheric delay can be decomposed in two component: stratified and turbulent [Hanssen, 2001]. The major part of atmospheric delay which may reach tens of centimeters comes

from the temporal variation of the stratified troposphere [Hanssen, 2001, Cavalié et al., 2007]. This long-wavelength stratified term of tropospheric delay comes from the difference in the vertical layer of the atmosphere while the short-wavelength signals of turbulent component is taken up from horizontally varying atmospheric layers. As stratified part of atmospheric delay and deformation can be both correlated to the topography, it is difficult to discriminate between the atmospheric and deformation signal. This difficulty is critical for interseismic strain studies in active tectonic region as deformations occur at slow rate and are often masked by atmospheric signals [Elliott et al., 2008, Fournier et al., 2011].

The turbulent part of the delay is random in time and space and can be corrected by stacking approach[Peltzer et al., 2001, Wright et al., 2001, Schmidt et al., 2005] or applying temporal low-pass filtering or smoothing in time series analysis [Zebker et al., 1997, Ferretti et al., 2001, Berardino et al., 2002, Schmidt and Bürgmann, 2003] using numerous acquisitions. However, the stratified component (not random in space, and seasonally dependent) may remain on a result of stacking approach of interferograms if the distribution of interferograms with positive and negative phase-elevation correlation is unbalanced in the data set [Cavalié et al., 2007]. Thus tropospheric delay corrections are necessary before estimation of interseismic strain rate [Doin et al., 2009].

The approaches of direct corrections of tropospheric delays consist of empirical method or using external data. The empirical approach are based on the analysis of the relationship between phase and elevation observed in interferograms away from the main deformation areas [Remy et al., 2003, Taylor and Peltzer, 2006, Cavalié et al., 2007, Elliott et al., 2008]. Details on these methods are given in the next section. The other approach is based on external data. Such data can be collected by ground meteorological stations (pressure, temperature, and humidity [Delacourt et al., 1998]) and extrapolated at higher elevations or some other techniques which are used successfully to map lateral heterogeneities in integrated water vapor content from ground to satellite such as MODIS (MODerate resolution Imaging Spectrometer, [Li et al., 2005] or MERIS (MEdium Resolution Imaging Spectrometer onboard ENVISAT, [Li et al., 2005, 2006c, Walters, 2012] or large network GPS data [Webley et al., 2002, Li et al., 2006a]. Each of these approaches has their advantage and drawback. Although these methods proved successful and accurate to mitigate part of the atmospheric phase delay, they rely on local data assimilation, which is rarely available, For example the GPS data is usually limited due the sparse spatial distribution of the stations, MODIS is limited due to the non-simultaneity of SAR acquisition and MERIS/MODIs are limited due to the calibration and cloud [Doin et al., 2009]. To overcome this limitation, we used the simple method based on the global atmospheric model ERAInterim [Jolivet et al., 2011] provided by the European Center for Medium−Range Weather Forecast (ECMWF) and we validated this approach with few GPS station located within our SAR image coverage.

a) Empirical approaches

One of the most used methods for estimating stratified atmospheric delay is simple empirical relationship between phase and elevation for each interferogram. This delay is not random in space and correlates with the topography [Hanssen, 2001]. This relationship can be defined linear [Cavalié et al., 2007, Doin et al., 2009] or exponential [Taylor and Peltzer, 2006]. Doin et al [2009] demonstrated that delay-elevation ratios predicted by global atmospheric model are in good agreement with the ratios derived from InSAR data away from deforming zones. One of the approaches to apply this method is estimation of tropospheric delay and orbital residual simultaneously by a least square inversion [Remy et al., 2003, Biggs et al., 2007, Cavalié et al., 2008, Lin et al., 2010]. In this case, the inversion process tries to separate three components: the linear relationship between phase and topography, a quadratic function along range and azimuth for removing orbital and the elastic model [Savage and Burford, 1973] to model deformation. These terms can be written:

$$\Phi_{1,2}(x,y) = kz + ax + by + cxy + d + s\phi_{def} \tag{2.77}$$

where z is the height of a pixel of coordinates (x,y) on the interferogram, ϕ_{def} is the phase variton related to deformation model, k, a, b, c, d and s are the coefficient to be estimated by a least square invesrion.

A major difficulty of the empirical method comes when the deformation and the topography signals are correlated. This correlation introduces a trade−off between tropospheric correction and tectonic signal. Another drawback is that in most of the situation the phase/elevation relationship is better established over small area than over the whole image, thus it will difficult to apply the same phase-elevation relationship across all regions of the interferogram.

[Shirzaei and Bürgmann, 2012] use wavelet multiresolution analysis to identify the topography-correlated components of the unwrapped interferogram as an atmospheric delay without using external data in each individual interferogram. In this method, it is possible to attribute tectonic signal into atmospheric signal if both signals are correlated, but the multiscale approach limits the confusion.

b) Direct correction of tropospheric delay

Several approaches have been used to estimate atmospheric phase delay corrections based on external data, including local atmospheric data collection [Delacourt et al., 1998], Global Positioning System (GPS) zenithal delay estimations [Williams et al., 1998, Webley et al., 2002, Li et al., 2006c, Onn and Zebker, 2006], satellite multispectral imagery analysis [Li et al., 2006a] and assimilation of meteorological data in atmospheric models [Wadge et al., 2002, Puysségur et al., 2007].

The first successful experience of using ground measurement of meteorological parameter in tropospheric correction of ERS interferograms was the study of Delacourt et al. [1998] in correcting on Mt. Etna. The authors used empirical relationships from Baby et al. [1988] and Saastamoinen [1972] to extrapolate the surface measurements to higher elevations. This correction result for lower rate ($13 \pm 3mm.mo^{-1}$) of deflation for Etna in comparison to estimation without correction ($20\pm$ mm.mo^{-1}). In our studies, we favor the correction based on high-resolution atmospheric models to generate atmospheric delay maps of [Jolivet et al., 2011]. Jolivet et al. [2011] used outputs from ERA-Interim to correct interferograms over Tibet and the Himalayas for atmospheric effects and demonstrate that this technique reduce the RMS of interferogram by an average of 73% and it improves the unwrapping errors.

ERA-Interim ECMWF Numerical Weather Model

ERA-Interim is the latest global atmospheric reanalysis produced by the European Centre for Medium-Range Weather Forecasts (ECMWF) based on a 4DVar assimilation of global surface and satellite meteorological data [Dee et al., 2011]. This model provides several meteorological parameters such as temperature, relative humidity on a global ∼75 km grid from 1989 to the present day, at 00:00, 06:00, 12:00 and 18:00 UT daily. It has spatial resolution of 0.75° (∼75 km) and stratification layers based on 37 pressure levels between 0–50 km above sea level. The interval between layers varies from 25 hPa for low elevation to 1hPa around 50 km altitude.

Doin et al. [2009] validated the use of global atmospheric models to estimate a priori relationship of linear phase and elevation. Jolivet et al. [2011] developed a simple method for systematic stratified delay mitigation based on ERA-I. This method can provide the delay map for both hydrostatic and wet delays. The first step for applying this method is choosing the closest ERA-I data to the SAR acquisition time. The time of our dataset for both ascending is ∼6pm and ∼6 am, respectively. The second step is the interpolation of the temperature, water vapor and dry air partial pressure provided at each pressure level to predict the delay as a function of elevation $\delta L^s_{LOS}(z)$ on each ERAI grid point LOS in the vicinity of the radar scene. A bilinear interpolation in the horizontal dimensions and a spline interpolation along altitude is then applied to produce a map of the predicted delay. Total delay maps at epoch of acquisitions are then combined by pairs to produce differential delay maps corresponding to each interferogram [Jolivet et al., 2011].

Global Positioning System (GPS)

Direct correction of tropospheric delay can be estimated using a network of continuous GPS network operating [Li et al., 2006a, Onn and Zebker, 2006, Xu et al., 2011]. ZTD

of GPS networks can be converted into ZWD by removing the effect of the neutral/dry atmosphere or zenith hydrostatic delay (ZHD), which is dependent on the surface pressure at the GPS station. The ZWD estimates can then be converted into integrated water vapor (IWV) using a conversion factor (Q), which is dependent on the surface temperature at the GPS station [Askne and Nordius, 1987, Emardson and Derks, 2000]. The ZWD estimates are used to estimate directly the relative delay on the InSAR measurements due to variations in the troposphere [Webley et al., 2002]. The projected delay in the direction of the line-of-sight of the SAR satellite is interpolated to the sampling of the interferogram and is used for corrections. The main drawback for using this method is the number of GPS station for reliable corrections. The few number of poorly distributed stations will not be able to correct the laterally variation of tropospheric delay but it can be used to validate other technique. The use of GPS is limited to areas with dense station coverage, and is not suitable for many of the remote areas where InSAR is particularly useful for monitoring crustal deformation. In the study area of North Eastern Iran, the distribution of permanent GPS stations is not enough to use them for interpolation but GPS station can help to validate ERA-interim correction (Fig. 4.6).

2.3.6 Time series analysis

After residual orbital errors, phase/elevation correlation of interferograms, now it is possible to produce time series of displacement and mean LOS velocity maps. Mean LOS velocity map can be done using staking of interferograms [Peltzer et al., 2001, Wright et al., 2001] or time series analysis, with two main approaches: Small Baselines approach (SBAS) approach [Berardino et al., 2002] or Permanent Scatterers (PS) approach [Ferretti et al., 2000, Hooper et al., 2004]. Time series analysis can be applied for large sets of differential interferogram to reconstruct the evolution of interferometric phase through time [Usai and Klees, 1999, Ferretti et al., 2001, Berardino et al., 2002, Schmidt and Bürgmann, 2003, Hooper et al., 2007, Cavalié et al., 2007]. In this study, we used constrained smoothed time series analysis to estimate the mean velocity map.

a) Constrained smoothed time series analysis

The first step is to select the interferograms for time series analysis. To improve the signal to noise ratio (SNR) of the mean LOS velocity maps, we should choose the unwrapped interferogram with the lowest residual noise. The interferogram selection is based on the evaluation of their SNR. For this we compute the energy function of the residual noise for each interferogram. The energy function, $S(r)$, is the mean absolutes value of the phase difference between two pixels separated by the distance r ([Puysségur

et al., 2007, Cavalié et al., 2008]):

$$S(r) = \frac{\sum_{i,j/d(i,j)=r} |\phi_i - \phi_j|}{N_r} \tag{2.78}$$

where ϕ_i and ϕ_j are the interferometric phases of pixel i and j, respectively, $d(i,j)$ is the distance separating pixel i and pixel j, and N_r is the number of pixel pair which has the distance equal to r.

Now if we consider m SAR images acquired in the order of (t_0,....,t_n), we will have m possible interferogram. It is possible to express following linear equation system for the absolute difference phase $\Delta\phi(i,j)$for the same pixel between two acquisitions i, j:

$$\Delta\Phi_{(i,j)} = \phi_j - \phi_i = \sum_{k=i}^{j-1} \delta\phi_k \tag{2.79}$$

where ϕ_i and ϕ_j are the phase value of the acquisition date i,j among data set [1,N] with $i \neq j$, $\delta\phi_k$ increment of phase between two acquisitions k and k + 1. We can write this linear equation in matric form:

$$\Delta\phi = A.\phi \tag{2.80}$$

where A is a matrix $m \times n$, n is the number of acquisition dates and m is the number of interferograms. each component of matrix A can be -1, 0,1, depends on the interferometric pair. For example if $\delta\phi_1 = \phi_4 - \phi_2$, then A would have the following form (Figure 2.22):

$$A = \begin{pmatrix} 0 & -1 & 0 & +1 & ... \\ ... & ... & ... & ... & ... \\ ... & ... & ... & ... & ... \end{pmatrix} \tag{2.81}$$

By solving this system, we can find the phase evolution of the interferometric phase (ϕ) over time. This can be done by least square inversion:

$$\hat{\phi} = (A^T.A)^{-1}.A^T.\Delta\phi \tag{2.82}$$

The inversion is done pixel per pixel. Depending of the unwrapping results for each interferogram, the phase of certain pixel may not exist at certain dates. Then, for some pixels, the interferogram network may be separated into independent groups of interferograms, with no geometrical and temporal overlap [Jolivet et al., 2012]. Several methods have been developed to solve this inversion problem based on the characteristics of the dataset e.g. the singular value decomposition (SVD) [Berardino et al., 2002, Usai, 2003, López-Quiroz et al., 2009]. Here we will explain the inversion approach of Lopez-Quiroz et al. [2009], improved by Jolivet et al. [2012] to build constraint for making link between independent subsets. Lopez-Quiroz et al. [2009] suggests using a polynomial of order 2, function of

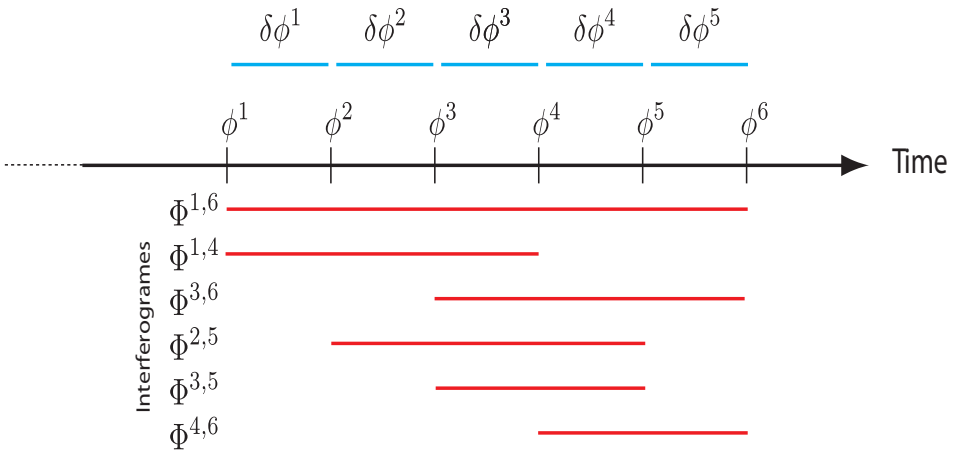

Figure 2.22 – Schematic representation of the inverse problem solution when analyzing time series. Each red line represents the temporal coverage of an interferogram $\phi_(i,j)$ with acquisitions between i and j. The the blue lines shows the phase increments ($\delta\phi_i$ and the time axe i present the evolution of the phase ϕ_i from a reference phase ϕ_1. (After Jolivet [2011]

time to solve the problem of the missing links between independent group of images by imposing a constraint on the inversion (Fig. 2.23).

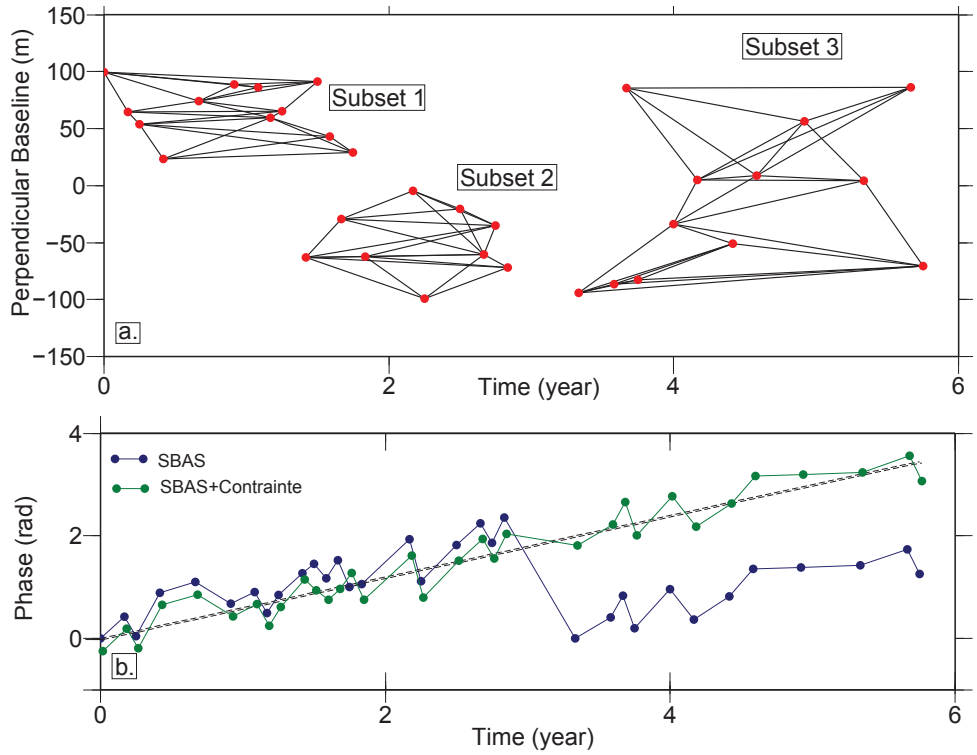

Figure 2.23 – a. Perpendicular baseline of three subsets synthetic interferograms used to compare the inversion methods developed by Berardino et al. (2002) and Lopez-Quiroz et al. (2009). b. Temporal evolution of the pixel derived from the SBAS inversion method proposed by [Berardino et al., 2002] and Lopez2009 (After [Jolivet, 2011])

In this study, we used a linear constraint to connect the subsets. This constraint is

affected by turbulent tropospheric pattern of each image. We put the weight of this component based on amplitude of atmospheric patterns ($1/APS_n$) where APS is Atmospheric Phase Screen of each image. Furthermore we add one more constraint which is a Gaussian temporal smoothing by minimizing the curvature of the inverted phase temporal evolution [Schmidt and Bürgmann, 2003, Cavalié et al., 2007, Doin et al., 2011]. We choose the weighting of this component in the inversion system equal to $\bar{\Delta}t_i^2$. $\bar{\Delta}t_i^2$ is the mean−time interval across the five-point differential operator, to be able to smooth less in the densely spaced acquisitions and to smooth more in scattered space acquisitions [Cavalié et al., 2007, Doin et al., 2011].

$$\begin{cases} \phi = A\phi \\ \sum_{k=1}^{l-1} \delta\phi^k = V\Delta t^l + eB^{\perp l} + c \\ \frac{\partial^2 \phi_n^{smooth}}{\partial^2 t} = 0 \end{cases} \tag{2.83}$$

where V is the mean LOS velocity for the considered pixel, $\Delta t^l = t^l - t^1$ is the time interval between acquisition 1 and l, e is a factor proportional to the DEM error, B^l is the perpendicular baseline of acquisition l with respect to the first acquisition and c is constant [Jolivet et al., 2012]. By solving this system, we can estimate simultaneously the evolution of the phase, DEM error and the average rate of LOS ground velocity.

We can evaluate the system misclosure for each pixel by the RMS for each pixel [Cavalié et al., 2007]:

$$\Phi_{RMS_{Pixel}} = \frac{1}{N}\left[\sum_N \left(\phi_{ij} - \sum_{k=i}^{j=1} m_k\right)^2\right]^{1/2} \tag{2.84}$$

where ϕ_{ij} is the measured interferometric phase between image i and image j, and $\sum_{k=i}^{j=1} m_k$ is the reconstructed phase between the same dates. The RMS sum over all pixels of each interferogram also can be defined:

$$\Phi_{RMS_{Int}} = \frac{1}{P}\left[\sum_P \left(\phi_{ij} - \sum_{k=i}^{j=1} m_k\right)^2\right]^{1/2} \tag{2.85}$$

RMS for each interferogram helps to remove the interferogram with high misclosure. Most of the problem for high RMS is coming from troposphere residual and unwrapping residuals.

2.3.7 Data and summary of the SAR processing strategy

All SAR data used in this thesis were obtained from the European Space Agency's (ESA's) ENVISAT satellite flying at an altitude of 790km with a repeat time of 35 days. The images we used (ASAR image mode, i2) are characterized by a wavelength of 5.6 cm

(C-band), 105 km wide swath, and an incidence angle of 23° at the center of the swath. Ground resolution of ASAR data is $4 \times 20m$ in along-track and cross-track directions respectively. The ENVISAT images cover from 2002 to 2010. The data was obtained through an ESA Cat-1 project (n7023, Principal Investigator: Zahra Mousavi). Figure 2.24 presents the studied area that is covered by several tracks of the SAR ENVISAT data; the Doruneh fault and Shahroud fault system in North Eastern Iran. The Doruneh fault has been covered by 5 descending (D120, D392, D435, D163 and D206) and 1 Ascending track (A156). The Shahroud fault system is covered by 1 descending track (D020) and 1 ascending track (A156).

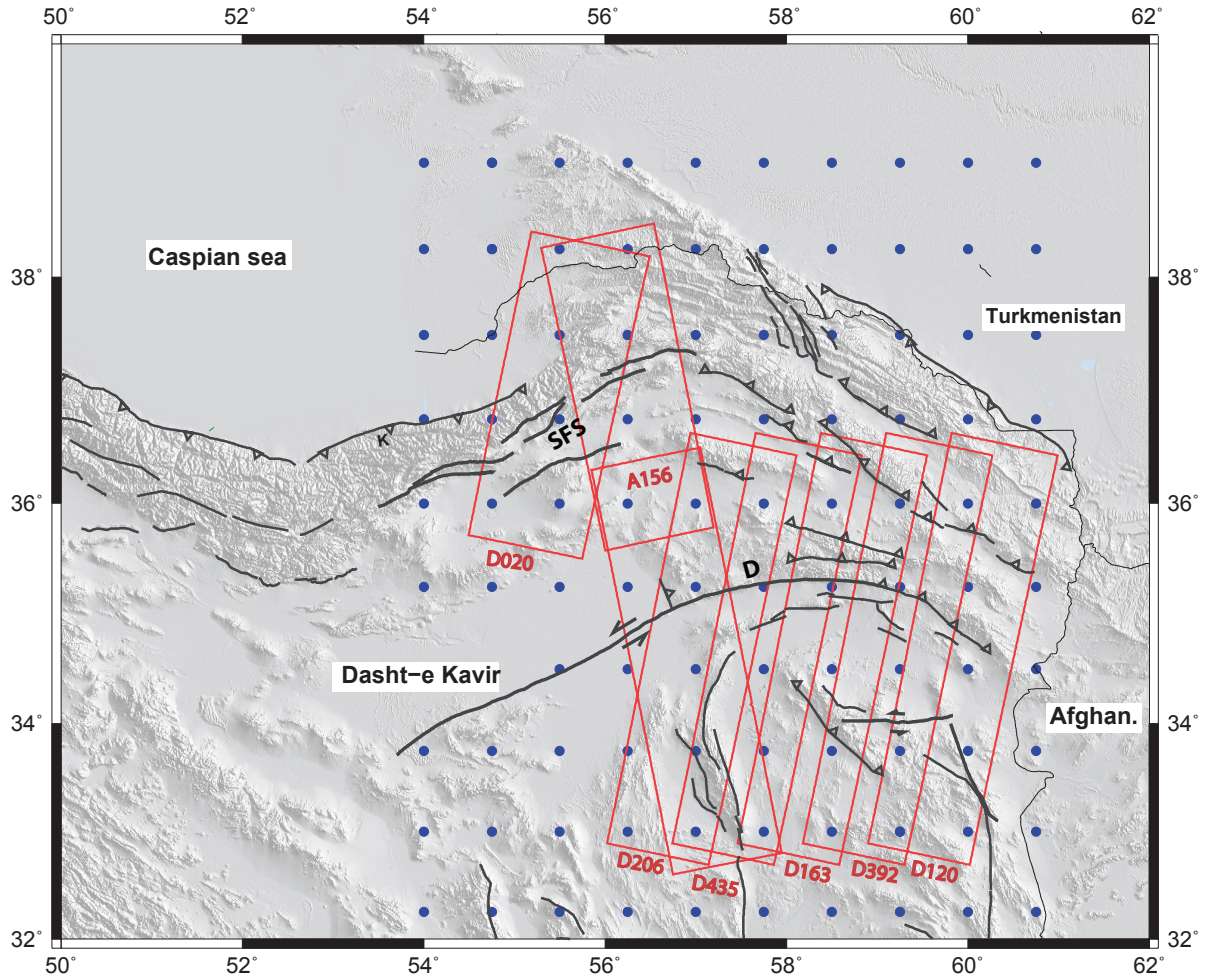

Figure 2.24 – Coverage of ENVISAT images acquired on two different fault systems, Doruneh and Shahroud fault system. Black lines indicate active fault traces and the red vectors are GPS velocity field with respect to Eurasia.

The raw radar images (Processing Level 0) were processed with ROI_PAC (Repeat Orbit Interferometry PACkage) which is JPL/Caltech software [Rosen et al., 2004] and NSBAS package[Doin et al., 2011]. The topographic phase contribution was removed from the SRTM Digital Elevation Model (DEM) at 90m spatial resolution. Precise DORIS orbital data for ENVISAT satellite provided by ESA are used for interferometric processing.

Single Look Complex (SLC) images are estimated using a common Doppler frequency band and then a super master image is chosen based on coherency criteria (see section 2.3.1. After, all images are coregistered in the same geometry using the Digital Elevation Model (DEM). For more detail of the steps from raw image to interferogram in NSBAS package, reader can refer to [Doin et al., 2011]. The SLC images are processed to produce interferogram with perpendicular baseline less than 500 meters and a temporal baseline longer than two months , following a Small BAseline Subset approach (SBAS) [Berardino et al., 2002] (see section 2.22).

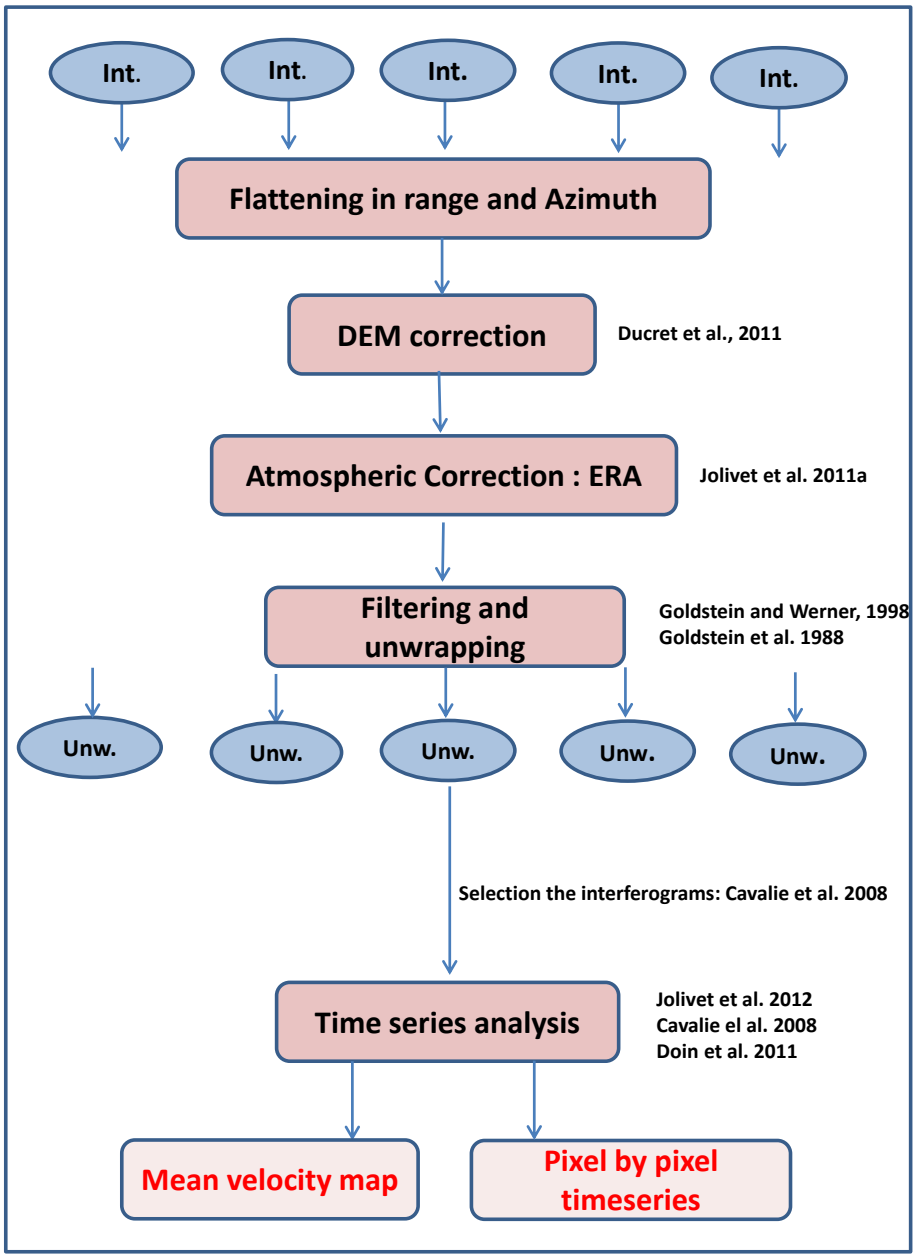

Figure 2.25 – The Schematic veiw of NSBAS chain processing strategy in this study.

The resulting differential interferogram phase is related to phase change due to the

deformation signal, tropospheric delay, orbital and DEM residual and noise. Each of these error and delay are removed according to the strategy explained before (see section 2.3.4). For the time series analysis, we selected the interferograms based on noise energy function (see section 2.22) mean absolute phase difference between two pixels) that is normalized with respect to the temporal baseline of interferograms. For estimating the mean velocity map in LOS direction, we combine the SBAS approach with constraint [López-Quiroz et al., 2009, Jolivet et al., 2012]. We perform this time series analysis pixel by pixel on the unwrapped interferogram. All these steps from differential interferogram to mean velocity map are presented in flowchart 2.25. In Chapter 4 and 6, the result of time series analysis based on ENVISAT data are presented for the Doruneh and Shahroud fault system, respectively.

2.4 The seismic cycle

The elastic rebound theory, proposed first by Reid [1910], is the explanation of how energy spreads during earthquake cycles, where the lithosphere of blocks on opposite sides of faults are subjected to distant forces in between two earthquakes. These blocks are slowly accumulating the energy and deform gradually which can take hundreds or thousands of years. The elastic strain accumulates until the internal strength of rocks on both sides is exceeded. At this step the energy will be released in a few seconds and the crust will rupture along the fault trace. Beside these two steps for one earthquake cycle, there is another period called postseismic that can release some remaining strain for some days or years after the earthquake. Now-a-days, geodetic observations around seismogenic plate boundaries record deformation during the various phases of the seismic cycle, namely the coseismic, postseismic and interseismic period.

2.4.1 Interseismic deformation

Interseismic deformation is the period of slow accumulation of elastic strain. During this period, the velocity of points on a perpendicular line to the fault has a gradient across the fault and strain accumulates near the fault (Fig 2.26). Several geodetic observations have been made across many faults worldwide using both GPS [Reilinger et al., 2006] and InSAR [Wright et al., 2001, Peltzer et al., 2001]

Several analytical models of interseismic deformation along strike-slip faults have been proposed, all based on the premise that the distribution of strain across a strike slip fault is a result of locking of the fault in the upper part of the lithosphere as the plates on either side of the fault move past one another [Johnson and Segall, 2004]. Savage and Burford [1973] introduced an elastic dislocation model for strike-slip faults. They assumed that slip on the fault is zero down to the locking depth d but it is of an amount of v_p

below depth d (in other words the fault is freely slipping below the locking depth), thus the displacement y at the surface at a perpendicular distance x from the fault can be expressed:

$$V = \frac{v_p}{\pi}.arctan(\frac{x}{d}) \tag{2.86}$$

Considering this model, 50% of the motion of the fault are accommodated in a region of width 2d centered on the fault trace and 90% of motion takes place within a region of width 12.6d [Walters, 2012]. The locked fault creates an arctangent shape in deformation centered on the fault (Fig. 2.26). During the coseismic period, the accumulated strain is instantaneously released and the crust moves in the opposite direction to the interseismic phase, but by the same amplitude, canceling the interseismic deformation totally.

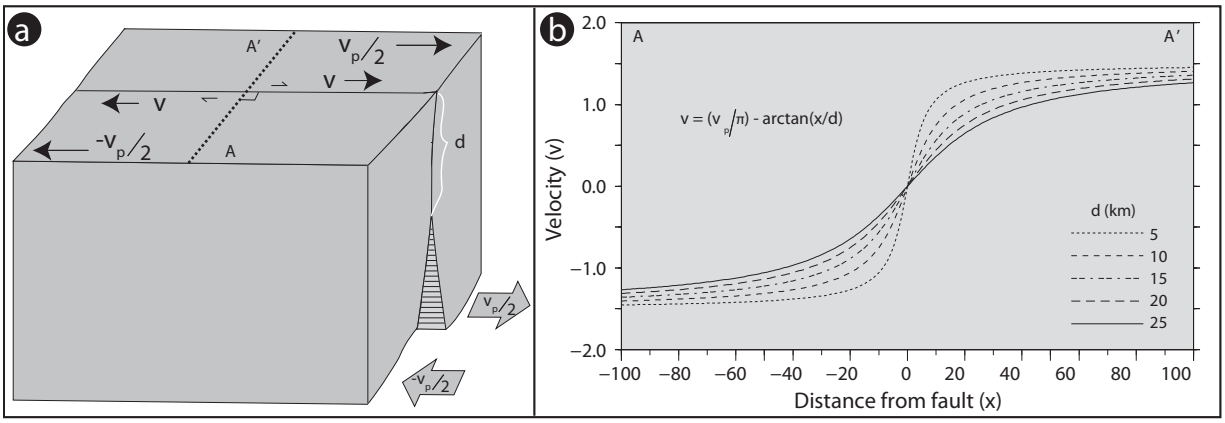

Figure 2.26 – A schematic illustration for elastic interseismic deformation around a plate-bounding, vertical strike-slip fault in a homogenous elastic medium: (a) Block diagram illustrating a right-lateral strike-slip fault locked from the Earth's surface to a depth of d, below which it freely slips at a constant rate equal to the relative plate motion vp (i.e., the far field velocity). (b) Profiles of fault parallel velocity along A–A across the fault for various locking depths. Note the increase in the gradient of the profile around the fault with decreasing locking depth and the difference in the far field velocity on the two sides of the fault [Tatar et al., 2012].

The other method to introduce time-dependent response is to replace the half-space Earth model by a layered model that includes at least one viscoelastic layer to represent the asthenosphere [Nur and Mavko, 1974, Savage and Prescott, 1978]. In layered model, the relaxation of the viscoelastic layer governs the time-dependent response. Figure 2.27 presents an elastic and viscoelastic deformation model of the earthquake cycle.

Figure 2.27-A shows the velocity on a transect across a strike-slip fault. At both ends of the profile, the green velocities show the long term slip rate of the fault. The black line shows the classical, elastic arctangent shape of deformation across a locked fault. In an elastic model, the interseismic velocity is constant in time between earthquakes. The light and dark blue lines show the shape of deformation for a visco-elastic model: right after the earthquake there is an "overshoot" (light blue line), the velocities close to the fault are

faster than predicted by the elastic model, and to compensate to the long term velocity, visco-elastic deformation is slower than elastic deformation (dark blue line) right before the next earthquake.

Figure 2.27-B presents the time series of slip close to the fault: the green straight line is the displacement at the sites at the end of the profile (green vectors on left plot). They do not see the seismic cycle; they are too far away from the fault. The red line shows elastic loading (constant in time between two earthquakes) and coseismic unloading, corresponding to the red vector on the left plot (a site inside the deformation zone of the locked fault). The blue curves show the visco-elastic displacements, faster than elastic right after the earthquake, slower than elastic before the earthquake, and therefore time varying. So if we measure a slower fault slip rate than long term and then elastic interseismic, it seems we are at the end of an earthquake cycle.

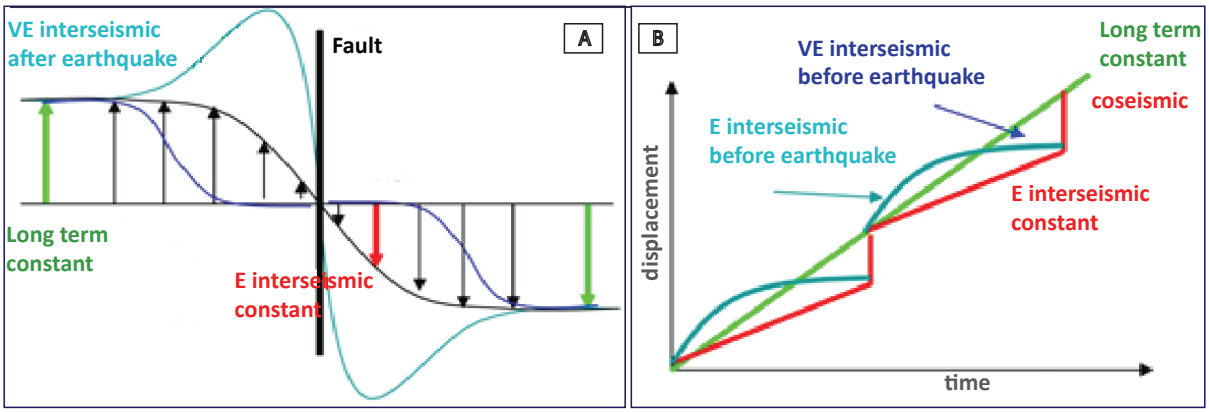

Figure 2.27 – (a)The velocity on a transect across a strike-slip fault. (b) The time series of slip close to the fault in the earthquake cycle.

Figure 2.28 shows the cumulated displacement with distance from the fault at different times in the earthquake cycle. The first line in the bottom is after 0.5 cycles and shows one half of the arctangent. At $T = 1.0^-$, it is just before the earthquake, at 1.0^+ is just after, and the purple displacement is co-seismic. At $T = 2.0$ you are again just before the rupture. The blue displacement is post-seismic with a time constant of $\tau_0 = 5$, plus interseismic. You see that the curve at $T = 1.5$ is not like the one at $T = 0.5$, so something nonlinear is going on = postseismic deformation.

Savage and Prescott [1978] compared a viscoelastic interseismic model to a completely elastic model and found that slip distribution on the surface for both models is very much similar for both models together. Therefore, despite the neglection of the Earth's layered characterization, the elastic half-space model of Savage and Burford [1973] is still commonly used to model geodetically-measured interseismic velocities across strike-slip faults [Wang and Wright, 2012, Metzger et al., 2011, Djamour et al., 2010, Walters, 2012].

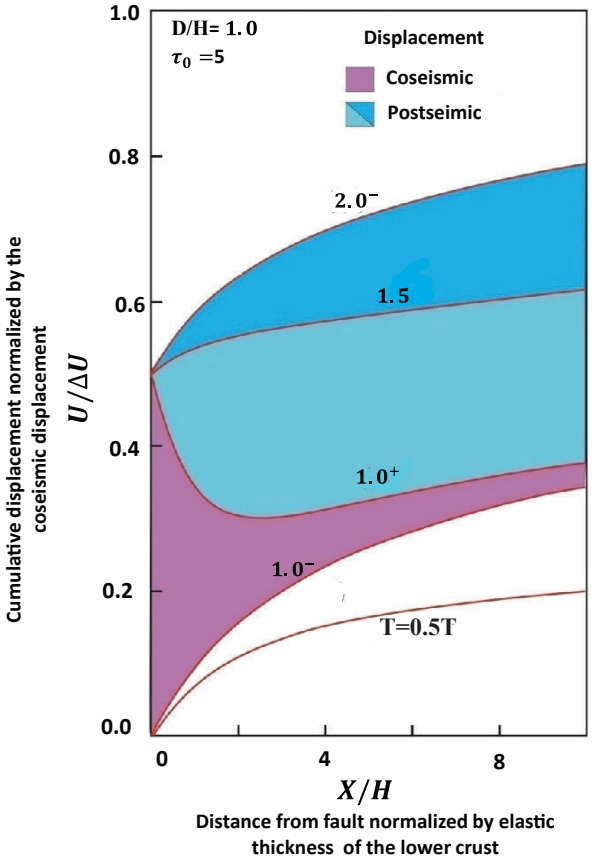

Figure 2.28 – Cumulated displacement with distance from the fault at different times in the earthquake cycle, after Conrtesy M. Vergnolle.

2.4.2 Coseismic deformation

The accumulated strain will be suddenly released in coseismic motion when the stress is no longer supported by friction on the fault. During this step which lasts a few seconds, centimeter to meter displacements of the ground created around the fault rupture and seismic waves are emitted. The displacement can be measured using the geodetic techniques such as GPS and InSAR. InSAR is convenient to the study of coseismic displacements as the deformation (about one to several meters) is often larger than the error sources for InSAR.

In addition to classical earthquakes, slow slip events can be measured using GPS [Vergnolle et al., 2010, Walpersdorf et al., 2011]. These earthquakes generate deformation that occurs over periods of hours to years and they can release energy with the similar magnitude to classical earthquakes. These slow events do not create high-frequency seismic waves so it is impossible to observe them by seismic instruments. Still they represent a significant contribution to the seismic cycle. Therefore it is particularly interesting that the GPS networks [Walters, 2012] and SAR observation [Cavalié et al., 2013] can observe them.

2.4.3 Postseismic deformation

Postseismic deformation is the phase of non-linear step, following an earthquake which can take hours to years. This deformation can be explained by local aseismic afterslip on the fault exactly after the earthquake [Smith and Wyss, 1968, Bürgmann et al., 2002], viscoelastic relaxation of the mantle or lower crust [Nur and Mavko, 1974, Pollitz, 1997] and poroelastic deformation associated with earthquake-driven fluid flow (changes elastic constants) [Peltzer et al., 1998, Jonsson et al., 2003]. However, these mechanisms can be operating individually or in combination. For example different combinations of these models have been proposed for the 1992 Ms=7.4 and the 1999 Mw=7.1 earthquakes in California [Bürgmann and Dresen, 2008, Walters, 2012].

2.5 Modeling the Velocity Field

Regional deformation can be considered as continuous deformation or rigid block motion with active faults at the boundaries. Here we consider that the lithosphere in Iran behaves as rigid blocks, limiting deformation to a narrow zone along the block boundaries, corresponding to active faults. GPS velocities are considered as resulting from the combination of rotation of these blocks and elastic deformation due to fault locking at their boundaries. The relative motion of blocks can be expressed by spherical Earth angular velocity vectors (Euler rotation poles and rates) while the interseismic deformation is modeled on the faults that separate blocks [Okada, 1985, Savage, 1983, Franco et al., 2012]. Therefore the relative motion of the faults can be determined by the Euler vectors describing the motions of the blocks separated by the faults.

Elastic strain in the rocks adjacent to the faults can arise if the blocks are in relative motion and the faults are not slipping freely (creeping) which is called 'locked' or 'coupled'. Faults are modeled in this work as planes with grids therefore fault locking can be parameterized at each node of the fault plane by a coupling factor α. If we consider V as the long-term slip vector on the fault and V_c as the short-term creep vector (the steady displacement rate across the fault surface over a short time, presumably parallel to V), then $\alpha = 1 - V_c/V$. If $\alpha = 0$, creep occurs at the long-term fault slip rate and if $\alpha = 1$, there is no creep on the fault in the interseismic period. The component of the slip vector on a fault that gives rise to the elastic deformation around the fault is therefore αV where V is determined from the angular velocities and permanent strain rates of the blocks that are in contact at the fault [McCaffrey, 2005]. In our work, we assume that the fault is stuck (no creep) from the surface to its locking depth and creeping below that.

2.5.1 Determining an Euler pole from a velocity field

The horizontal components of the GPS velocities are mostly expressed in a spherical coordinate system [Franco, 2008]:

$$\overrightarrow{V}(\lambda,\phi) = (V_e(\lambda,\phi),V_n(\lambda,\phi)) \tag{2.87}$$

where V_e and V_n are the eastern and northern components of the velocity V and are the functions of longitude λ and latitude ϕ of the GPS station. But on a regional scale, the velocity can be expressed in a Cartesian coordinate system:

$$V(x,y) = (V_x(x,y),V_y(x,y)) \tag{2.88}$$

where $V_x = V_e$ and $V_y = V_n$. Indeed, the distortion induced by this assumption on the velocity field can be negligible except for very large spatial studies. In a Cartesian system, the velocity field can be used to construct a velocity gradient tensor L:

$$\overrightarrow{V}(x,y) = L\overrightarrow{X} + \overrightarrow{T} + \overrightarrow{E}(X) \tag{2.89}$$

where X is the position vector, T is a translation vector independent from the position, L is the gradient tensor of velocity and $\overrightarrow{E}(X)$ is the error associated with the velocity field, depending on the position of the point. The gradient tensor can be written as follows:

$$L_{x,y} = \begin{bmatrix} \frac{\partial V_x}{\partial x} & \frac{\partial V_x}{\partial y} \\ \frac{\partial V_y}{\partial x} & \frac{\partial V_y}{\partial y} \end{bmatrix} \tag{2.90}$$

The velocity gradient tensor can be decomposed as the sum of a two other tensors Q and θ such that $L_{xy} = Q_{xy} + \theta_{xy}$ where:

$$Q_{xy} = \frac{1}{2}\left[\frac{\partial V_x}{\partial y} + \frac{\partial V_y}{\partial x}\right] \tag{2.91}$$

$$\theta_{xy} = \frac{1}{2}\left[\frac{\partial V_x}{\partial y} - \frac{\partial V_y}{\partial x}\right] \tag{2.92}$$

where Q is the shear strain tensor and θ is rotation tensor. The velocity gradient tensor L and translation vector $\overrightarrow{T}$ can be determined from the velocity field using the method of least squares. However, in the context of a model of rigid blocks, the movement of the surface of the earth is described as a rigid rotation about an Euler pole.

The velocity field can be written as $\overrightarrow{V} = \overrightarrow{\Omega_R} \times \overrightarrow{X}$, where $\overrightarrow{\Omega_R}$ is the rotation vector. This vector is responsible for the gradient of velocity which depends on the distance of the point to the Euler pole of the rotation. This gradient corresponds to the antidiagonale component of the gradient tensor of velocity ($\frac{\partial V_x}{\partial y}$ and $\frac{\partial V_y}{\partial x}$). The velocity due to the rotation

about an Euler pole at a point is:

$$V = \omega R_T sin(\Delta) \tag{2.93}$$

where ω is the angular velocity, R_T is the radius of the Earth and Δ is the angular distance between the Euler pole and point. Then the gradient of velocity can be written: $wR_T cos(\Delta)$ and it tends to be zero at $\Delta = 90°$.

Thus we can estimate the Euler pole of each rigid block with active faults at the boundaries using the GPS velocity field. This is our approach in chapter 5.

2.5.2 Inversion using DEFNODE

We model the GPS velocity field using the 3D-inversion method DEFNODE which is developed and improved regularly by the team of McCaffrey [McCaffrey, 2002, 2005]. This program is based on finite element method with the exception that the mesh is limited to the block boundaries represented by faults, with no interior deformation. In addition to GPS data, DEFNODE can include earthquake slip vectors, geologic slip rates on faults, surface uplift data, spreading rates, rotation rates, transform azimuths, surface strain rates and surface tilt rates [McCaffrey, 2005]. The estimation of the surface deformation due to slip on the faults is carried out with the Okada [1985] half-space dislocation algorithm. In this program, faults are represented by a series of node points within a spherical Earth that specify their 3-D shapes.

We used DEFNODE to analyze a velocity field as a combination of rotations of rigid blocks and localized deformation on the borders of the blocks. Each block is associated with a center of rotation. These poles describe the kinematics of the blocks and the average slip rate of the faults that limit adjustment blocks. The effect of the fault locking (in the interseismic phase) on the velocity field can be described by the elastic dislocation model of Okada [1985] .

After the definition of blocks and faults, the position of the Euler pole for certain blocks and the magnitude of the rotation can be imposed. Then the inversion of model parameters will be performed. These parameters are the amount of the coupling coefficient for each node if it is not fix, and pole position and the rotation rate of each block. For the inversion, it is necessary to estimate the Green function for each node. The equation for inversion can be expressed [Franco, 2008]:

$$V_i(\overrightarrow{X}) = \sum_{b=1}^{B} H(X \in b)[{}_R\overrightarrow{\Omega}_b \times \overrightarrow{X}]\overrightarrow{i} - \sum_{k=1}^{F}\sum_{n=1}^{N_k}\sum_{j=1}^{2} \phi_{nk} G_{ij}(\overrightarrow{X},\overrightarrow{X}_{nk})[{}_h\overrightarrow{\Omega}_f \times \overrightarrow{X}_n k]\overrightarrow{j} \tag{2.94}$$

where

– $\overrightarrow{X}$ is the position vector of the observation point.

- B is the number of the blocks, $H = 1$ if $\overrightarrow{X}$ belongs to the block b, if not it is zero.
- V_i is the component i of velocity vector ($i = x$,y or z).
- $\overrightarrow{i}$ is the unit vector of the component i.
- ${}_R\overrightarrow{\Omega}_b$ is the rotation vector of block b .
- ${}_h\overrightarrow{\Omega}_f$ is the rotation vector of the footwall block relative to the hanging wall block.
- F number of the fault.
- N_k number of the node which defines the fault k.
- $\overrightarrow{X}_n k$ and ϕ_{nk} present the vector position and coupling of the node n on the fault k.
- $\overrightarrow{j}$ is the unit vector of j^{th} direction on surface of the fault (in depth or sliding direction).
- $G_{ij}(X,X_{nk})$ is the green function of the node nk which is the response of the unit sliding, in direction j along the fault.

The inverse calculation is evaluated by the minimizing the "chi square statistic":

$$\chi^2 = \frac{\sum_{i=1}^{N} \frac{r_i^2}{(f\sigma_i)^2}}{N - P} \tag{2.95}$$

where N is the number of observation, P is the number of free parameter in inversion, r_i is the residual of the observation i and estimated value. σ_i is the uncertainty associated with the observable i. f is the scale factor for uncertainties.

To estimate fault slip rates for the major active faults in Eastern Iran using the GPS velocity field, we use a block model and in particular the DEFNODE code. We consider that there is no significant earthquake that has occurred during the time interval of measurements. Using the DEFNODE code, we minimize the GPS residual motion within the blocks based on the least-square method. As mentioned before, this code uses Okada's formulation [Okada, 1985]. Also we assume that there is no permanent deformation inside the blocks and all faults should be on a block boundary. We define the block boundaries based on active fault map. The major problem in defining block is that some of them have no particular faults in one or two directions, such as the northern and southern boundaries of Anar-Deshir block (ADB) in chapter 3. We used DEFNODE code to estimate the average block velocities, fault slip that can be varying along the faults, Euler poles and velocity residuals between observed and modeled velocity fields in chapter 3 and 5.

2.6 Conclusion

In this chapter, we presented the geodetic measurement techniques (GPS and InSAR) and the data analysis methodologies used in this thesis to establish a precise deformation field in NE Iran. We processed the GPS stations (pink triangles in figure 2.29) following the strategy explained in section 2.2.5 to produce the GPS velocity field in Eastern Iran. This

velocity field is input for two methods establishing fault slip rates: Velocity variations along simple profiles across the fault or rigid block modeling (whose principles are presented in section 2.5) to estimate the interseismic deformation.

Figure 2.29 – The GPS (pink triangles), SAR (green rectangles) and ERA_Interim (blue circles) data that are used in this thesis.

Comparing average velocities between stations on either side of the fault neglects the effect on rigid block rotation on the slip rate estimation of a fault separating two rigid blocks and estimates fault slip of neighboring faults independently (except some recoverage of stations characterizing several block limits on small blocks). A rigid block model estimates all fault slip rates in a correlated way and makes use of all stations on two neighbor blocks to constrain the slip rate of the fault lying in between. However, for a coherent result, the blocks have to be perfectly rigid in their interior and the deformation zone along their boundaries created by fault locking has to be correctly described, requesting information on locking depth and coupling of the faults. For these advantages and inconvenients of each method we have applied both techniques in this thesis to be able to quantify the errors on slip rate estimates due to the different hypotheses and simplifications.

In the InSAR analysis, correcting the errors and delays is important in our study as we are searching for evidence of only a few mm/yr of interseismic deformation on two major faults in eastern Iran. The InSAR data used are ENVISAR tracks covering eastern Iran, highlighted by the green rectangles in figure 2.29. The most challenging error in measuring interseismic deformation is tropospheric delay. We used the ERA-Interim meteorological model (blue dots in figure 2.29) to create tropospheric delay maps that are removed from the interferograms. In future work, GPS tropospheric delays could be used to scale tropospheric refractivity profiles from the meteorological model to still improve the tropospheric corrections, as numerical weather models do not represent all of the rapid and small scale water vapor variations that GPS is perfectly able to monitor.

Chapter 3

Eastern Iran active tectonics

Contents

3.1 Introduction

The active tectonics of Iran are controlled by the northward motion of Arabia relative to Eurasia. The GPS velocities of station respect to Eurasia decrease to zero at both the northern and eastern borders of Iran. This means that major part of the NS continental convergence is absorbed inside the political border of Iran. The differential shortening across the Zagros and the Makran in the South of Iran leads to a significant NS shear between Central Iran and Afghanistan. Part of this NS shear should be accommodated in Eastern Iran. Eastern Iran is characterized by two types of faults N-NW-trending, right-lateral strike-slip faults and EW trending left-lateral strike-slip faults. The N-NW-striking fault set includes 5 major right-lateral faults, from east to west, East Lut fault (EL), West Lut fault (WL), Kuhbanan fault (KB), Anar fault (A) and Dehshir fault (DS). The major E-W trending left-lateral fault is the Doruneh fault north of these 5 major N-NW faults. According to the first GPS global network, 16 mm/yr of shear should be accommodated along these right-lateral fault from west to east [Vernant et al., 2004b]. Some studies used the total geological fault offset and dating to estimate the long-term slip rate of individual faults [Walker et al., 2004, Fattahi et al., 2006b, Allen et al., 2004, 2011]. Also the structural, geomorphologic, and seismic data of the Central-Eastern indicates that these fault may be active at the present day, too [Walker and Jackson, 2004]. But there is no current constraint on individual fault slip rate for all of these major faults in Central-eastern Iran. Thus until now, it is clear that the faulting in Central-Eastern Iran must help accommodate part of the Arabia–Eurasia convergence but precise quantification of individual fault slip rates is necessary to identify a kinematic process that can explain how these faults work together.

3.1.1 Kinematic model

Three possible kinematic models have been proposed for the regional tectonics of this part of Iran based on geomorphic and seismic data [Walker and Jackson, 2004, Meyer et al., 2006, Allen et al., 2011]. These models can work individually or together to absorb the continental shortening in Central-Eastern Iran. The proposed models are vertical axis block rotations [Jackson and McKenzie, 1984, Walker and Jackson, 2004, Allen et al., 2011], indentation [Meyer et al., 2006], and strain partitioning [Allen et al., 2011].

Vertical axis block rotations

The global GPS velocity fields shows that the shortening across the central Iran region is not more than ∼2 mm/yr [Vernant et al., 2004b]. Vernant et al, [2004] therefore define a Central Iran block as a rigid unit. Regions to the east extending between N-NW trending right-lateral strike-slip faults could therefore be rigid as well. Thus one possibility to accommodate the shortening is anticlockwise rotation about vertical axes of blocks between the N-NW-trending right-lateral strike-slip faults [Walker and Jackson, 2004,

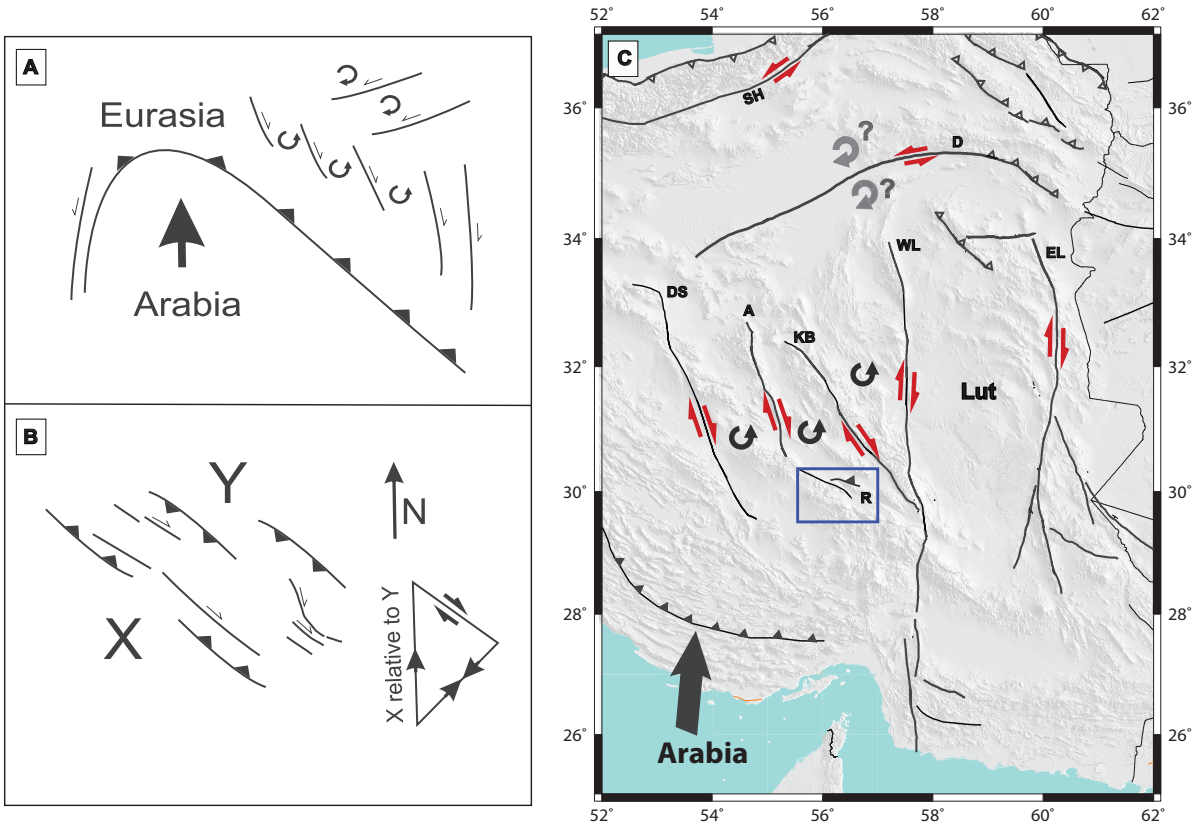

Figure 3.1 – Tectonic models for Central-Eastern Iran. A) The cartoon of the tectonic suggested by Allen et al., 2011 which described two possible models, vertical axis block rotation and indentation. Indentation tectonic results of the Arabian plate northwards motion can be achieved on NNW–SSE right-lateral strike-slip faults. B) Strain partitioning of north–south Arabian-Eurasian convergence via NE–SW shortening on NW–SE thrusts combined with right-lateral strike-slip on NW–SE trending faults. C) It presents the summary of the 3 possible models and simplified active faults. The vertical axis block rotation for right-lateral fault can be constraint by paleomagnetic data and the partitioning behavior may occur in NE-SW right-lateral faults such as Rafsanjan (blue rectangle). Figure A and B are from Allen et al., [2011] and abbreviations are: WL: West Lut fault, EL: East Lut fault, D: Doruneh fault, A: Anar fault, KB: Kuhbanan fault, DS: Dehshir fault, R: Rafsanjan fault and SH: Shahroud fault

Allen et al., 2011] (see fig 3.1-a). Vertical-axis block rotation can explain the lack of crustal thickening in this part of Iran compared with other parts of Iran that accommodated shortening with resulting mountain building such as Zagros and Alborz [Hatzfeld and Molnar, 2010].

This kinematic model is shown in figure 3.1 for the faults Dehshir, Anar and Kuhbanan, from the west to east, respectively. Paleomagnetic results from Oligocene–Miocene sedimentary units in central Iran indicate that there is 20°–35° of counterclockwise rotations in the Tabas and Anarak areas which are surrounded by N-NW-trending right-lateral strike-slip faults [Mattei et al., 2012]. This paleomagnetic data provide the first constraint to the block-rotation model to account for late Cenozoic shortening in central Iran by right-lateral faults. Some of these right-lateral faults have been active during the Qua-

ternary up to present day, suggesting the possibility that block rotation is still occurring in central Iran. Now GPS velocity field may help us to verify it. This block model also describes present-day kinematics area. If the answer is yes, what is the contribution of each fault in this block model?

Indentation

The other possibility in accommodating the right-lateral NS shear is that these right-lateral faults move northward with respect to the crust further east. Also it is possible that the strike-slip faults in eastern Iran together allow the Arabian promontory to impinge northwards in to the Eurasian crust in earlier time but it is hard to say that it is the case fo now [Allen et al., 2011].

Strain partitioning

Another kinematic model which is proposed for the Central-Eastern Iran is strain partitioning. This model was proposed for the current deformation in the Zagros [Talebian and Jackson, 2002, Walpersdorf et al., 2006]. It seems that the Eastern Iranian N-NW-trending strike-slip faults at a high angle to the plate convergence vector of Arabian-Eurasian convergence can have another role in accommodating the overall convergence, where strain is separated in to compressional and strike-slip components [Allen et al., 2011]. Allen et al., [2011] suggests that the partitioning may occur on ∼NE-SW right-lateral faults such as Rafsanjan (continuation of Anar fault, see Fig. 3.1)

The faults in between 48° to 57° are less constraint until now and Vernant et al, [2004b]find just ∼2 mm/yr of shortening in Central Iran region, and seismicity is absent in this region relative to the Zagros or Kopeh Dagh. Allen et al. [2011] suggest that the thrust and strike slip faulting in Central Iran is active in the past as there are offset markers belong to the Eocene volcanic and the deformation rate decreases in Central Iran in the last few million years. They propose this event depend on the time of the collision between Eurasia and India and Eurasia and Arabia. Figure 3.2 present the possible kinematic for 10 Ma (a) and present-day (b) from Allen et al, [2011] . According to this model, 10 Ma years ago, the deformation inside Iran due to the Arabia-Eurasia collusion was distributed on NS right-lateral faults that were able to move eastward to the Afghan block, part of Asia. Because at that time, Afghan block crust could behave as 'free face' due to the oceanic crust further east. But after the Eurasia-India collision, the crust was not able to move southeastward in about $\sim 5-2$ Ma ago. Therefore the author proposed that the other region should achieve the continuing plate convergence such as South Caspian basin and western Anatolia. In this kinematic, deformation is absorb in Zagros and then transferring to the north.

Now we would like to investigate whether this kinematic model occurs inside Iran, and whether Central Iran is no longer active. One of the techniques we can study the present-day deformation is using the geodetic, in particular, GPS networks. Until now, the only GPS constraints of the current deformation pattern in Central-Eastern Iran are

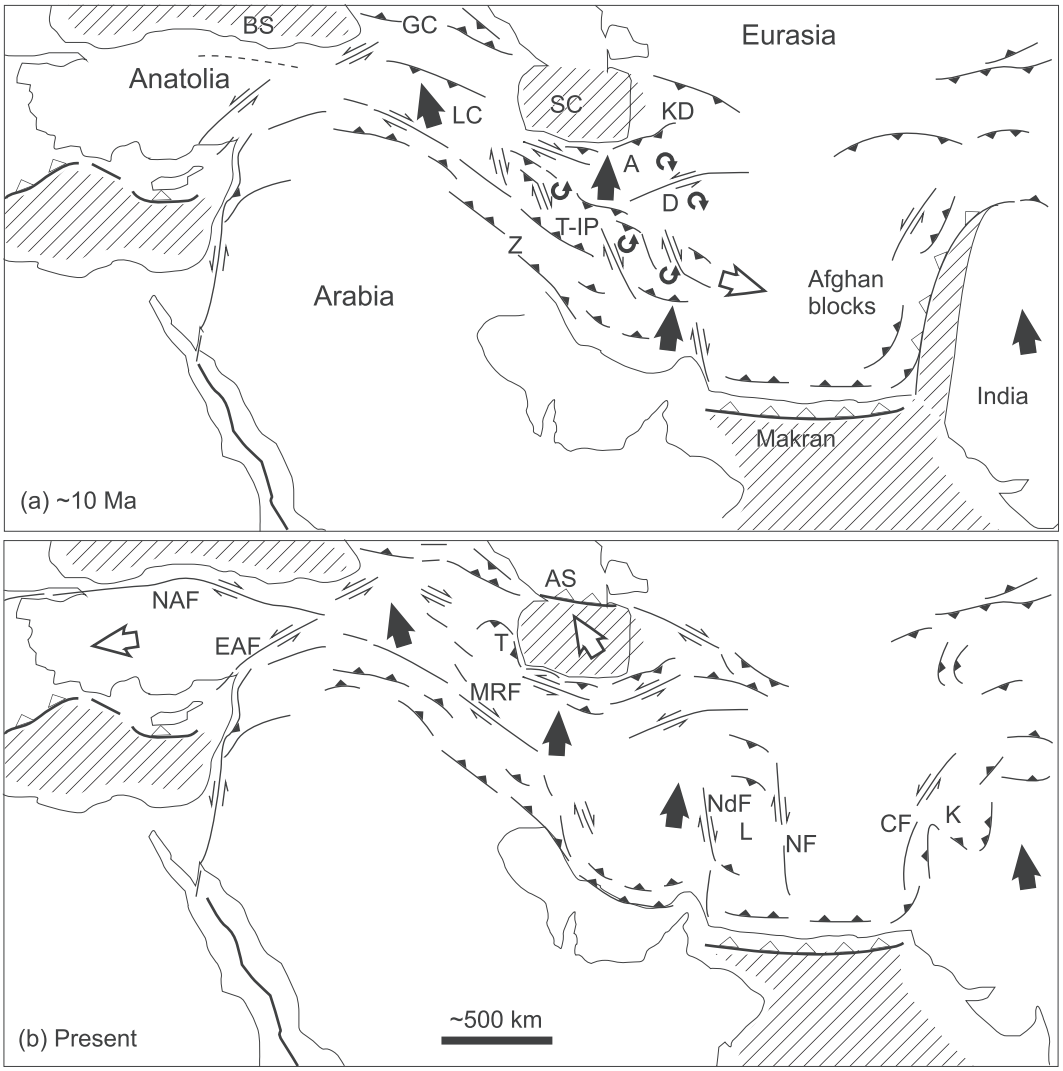

Figure 3.2 – Schematic illustration of the kinematic model for Arabia-Eurasia collision zone proposed by Allen et al, [2011] for 10 Ma (a) and present day (b). The important difference between two cartons is the role of Afghan crust in accommodating the Arabia-Eurasia collision. Afghan crust could move eastward 10 Ma ago (a) but in present-day, due to the India-Eurasia collision, the Afghan crust can be assumed to be semi-rigid blocks. Shaded areas are oceanic crust. Solid arrows present the direction of deformation within the collision zone with respect to stable Eurasia which are adapted for (b) from the GPS-derived velocity field [Vernant et al., 2004b, Reilinger et al., 2006]. Open arrows show elongation of the Turkish–Iranian plateau to the southeast. Abbreviations: A, Alborz; AS, Absheron Sill; BS, Black Sea; CF, Chaman Fault; D, Doruneh Fault; EAF, East Anatolian Fault; GC, Greater Caucasus; K, Katawaz Basin; KD, Kopeh Dagh; L, Lut; LC, Lesser Caucasus; MRF, Main Recent Fault; NF, Neh Fault; NAF, North Anatolian Fault; NdF, Nayband Fault; SC, South Caspian Basin; T, Talesh; T-IP, Turkish–Iranian plateau; Z, Zagros [Allen et al., 2011].

provided by the first global GPS network [Vernant et al., 2004b]. In the following chapter, we provide a dense GPS velocity field covering central-Eastern Iran, then we constrain fault slip rate and finally we try to find how these faults contribute to absorbing the Arabia-Eurasia convergence, in particular whether we can provide geodetic constraints on

the kinematic model for present day deformation in Central-Eastern Iran.

3.2 New insights on the recent and current deformation in Central-Eastern Iran, derived from a combined tectonic and GPS analysis

A. Walpersdorf[1],I. Manighetti[2], Z. Mousavi[1,3], F. Tavakoli[3], M. Vergnolle[2], A. Jadidi[3], D. Hatzfeld[1], A. Aghamohammadi[3], A. Bigot[2], Y. Djamour[3], H. Nankali[3], and M. Sedighi[3].

1. Institut des Sciences de la Terre, CNRS (UMR 5275), Université Joseph Fourier, Maison des Géosciences, 1381 rue de la piscine, 38400 Saint Martin d'Hères, France.
2. Université de Nice Sophia-Antipolis, Centre National de la Recherche Scientifique, Observatoire de la Côte d'Azur, Géoazur, 250 av. Einstein 06560 Valbonne, France.
3. National Cartographic Center, Geodetic Department, Tehran, Iran. ***Submitted for publication in , August 2013***

3.2.1 Summary

We analyze new, 11 years GPS data at 92 stations in Central-Eastern Iran. Combined with a detailed analysis of the seismogenic faults, the GPS data allow estimating, for the first time, the present-day kinematics and the slip rates on most faults in Central-Eastern Iran. The East-Lut, West-Lut, Kuhbanan, Anar, Dehshir and Doruneh faults are confirmed as the major faults and found to currently slip laterally at 5.6 ± 0.6, 4.4 ± 0.4, 3.6 ± 1.3, 2.0 ± 0.7, 1.4 ± 0.9, and 1.3 ± 0.8 mm/yr, respectively. Slip is right-lateral on the ∼ NS striking EL, WL, KB, A, and DS faults, and left-lateral on the ∼ EW Doruneh fault. The ∼ NS faults slice the Central-Eastern Iranian crust in five blocks that are moving northwards at 6-13 mm/yr with respect to the stable Afghan crust at the eastern edge of the collision zone. The collective behavior of the ∼ NS faults might thus allow the Arabian promontory to impinge northwards into the Eurasian crust. The ∼ NS faults achieve additional NS shortening by rotating counterclockwise in the horizontal plane, at current rates up to 0.8°/Ma. Modeling the GPS and available geological data with a block rotation model suggests that the rotations have been going on at a similar rate (1 ± 0.4 °/Ma) over the last 12 Ma. We identify large strains at the tips of the rotating EL, WL and KB faults, which we suspect to be responsible for the important historical and instrumental seismicity in those zones.

Key words: GPS satellite geodesy; Kinematics of crustal deformation; Faults; Continental margins: convergent; Continental tectonics: strike-slip and transform; Iran

3.2.2 Introduction

Iran has been extensively studied over the last decades because its territory offers the rare opportunity to observe and quantify how the convergence between two plates –Arabia and Eurasia– has been accommodated from its onset to its present-day continuation, i.e., continental collision within Iran. Plus, Iran is the site of frequent devastating earthquakes, and it is thus of critical importance to understand how those earthquakes emerge from the overall tectonics that affects the Iranian territory.

As a result of the many prior works that have been conducted in Iran [Berberian, 1976, 1981, Jackson and McKenzie, 1984, Nowroozi and Mohajer-Ashjai, 1985, Jackson et al., 1995, Bellier et al., 1997, Berberian and Yeats, 1999, Nilforoushan et al., 2003, Walker and Jackson, 2004, Walker et al., 2004, 2009, 2010, Allen et al., 2004, 2006, 2011, 2013, Vernant et al., 2004b, Masson et al., 2005, 2007, Reilinger et al., 2006, Meyer et al., 2006, Meyer and Le Dortz, 2007, Le Dortz et al., 2009, 2011, Hollingsworth et al., 2010a, Farbod et al., 2011, Cifelli et al., 2013, Nozaem et al., 2013], the general features of the Cenozoic to present-day tectonics in Iran are fairly recognized. Firstly, the overall kinematics of the Iranian collision zone is broadly understood [Jackson et al., 1995, Talebian and Jackson, 2002, Allen et al., 2011] and references therein]. The convergence is almost N-S and operates at about 2.5 cm/yr at the longitude of Central-Eastern Iran [Sella et al., 2002, McClusky et al., 2003, Vernant et al., 2004b, Reilinger et al., 2006]. To the southwest and southeast, the collision zone is bounded by active subduction in the Aegean and in the Makran regions, respectively. To the west, the North and East Anatolian faults form a strike-slip boundary to the collision zone. To the east, the limit of the zone is less clear and is supposed to be diffuse and to stop at the political boundary between Iran and Afghanistan/Pakistan. Most of the compression occurs at the southern and northern edges of the collision zone, in the Zagros and in the Alborz and Kopeh Dagh mountains, respectively. In between those thrust and fold belts, a number of strike-slip and reverse faults dissect the Iranian territory. Secondly, most seismogenic faults have been identified throughout Iran [Berberian and Yeats, 1999, Walker and Jackson, 2004, Walker et al., 2004, 2009, 2010, Allen et al., 2004, 2006, 2011, 2013], and the relationships between those faults and the largest instrumental and historical earthquakes are fairly well understood. Finally, the overall distribution of present-day deformation in Iran begins to be known thanks to the development of dense GPS networks over the last decades [Nilforoushan et al., 2003, Vernant et al., 2004a,b, Masson et al., 2005, 2007, Walpersdorf et al., 2006, Tavakoli, 2007, Tavakoli et al., 2008].

However, a number of key questions remain posed, especially in Central-Eastern Iran (defined between $\sim$ 52 and 62°E), which is specific in that it forms the eastern boundary –supposed to be diffuse, to the collision zone. Central-Eastern Iran is indeed particular as it is the only part of the territory to show $\sim$ N-S to NNW trending faults, almost parallel to the convergence vector. Those faults are large ($\geq$ several 100 km-long) right-lateral

strike-slip structures that all show a seismogenic activity. They are spatially associated with faults having very different orientations and kinematics. Although many tectonic and paleoseismological studies have been conducted on the Central-Eastern Iranian faults [Allen et al., 2011] and references therein), it is still unclear how those faults have been and are still currently accommodating the convergence and the related shortening. Different scenarii have been proposed [Jackson and McKenzie, 1984, Walker and Jackson, 2004, Walker and Khatib, 2006, Shabanian et al., 2009b, Hollingsworth et al., 2010a, Allen et al., 2006, 2011] but data are still lacking to validate them. In particular, despite of large efforts, little is known on the current slip rates of the Central-Eastern Iranian faults. Another issue in Central-Eastern Iran concerns the understanding of the relationships between 'major' and 'secondary' faults. Indeed, although Central-Eastern Iran is dissected by around ten, well identified, several hundreds of kilometers long faults that are taken to accommodate most of the strain and to slip at fast rates (i.e., the so-called 'major' faults), there also exist a large number of smaller faults more or less associated with the major structures (i.e., the so-called 'secondary' faults). While these secondary faults likely accommodate less strain and slip at lower rates than the major faults, a number of them broke in large devastating earthquakes in the historical times whereas the major faults were basically quiescent (e.g., earthquakes of Mohammadabad 1941 [Ambraseys and Melville, 1982, Berberian and Yeats, 1999, Walker et al., 2004], Dustabad 1947 [Ambraseys and Melville, 1982, Walker et al., 2004], Ferdows 1968 and Tabas 1978 [Ambraseys and Melville, 1982, Walker et al., 2003], South Golbaf [Berberian and Qorashi, 1994, Berberian et al., 2001], Sefidabeh 1994 [Berberian et al., 2000, Parsons et al., 2006], Chahar - Farsakh 1998 [Berberian et al., 2001], Bam 2003 [Talebian et al., 2004], Dahuyieh (Zarand) 2005 [Talebian et al., 2006], Konarak 2010 [Foroutan and Eskandari, 2010, Walker et al., 2013], all are highlighted in Fig. 3.3. The peculiar seismic behavior of the secondary faults in Central-Eastern Iran thus calls for the need to understand why their slip occurs and how those smaller seismogenic faults might be related to the major ones.

Our objective is to contribute addressing the above issues. We approach them through a combined tectonic and geodetic (GPS) analysis. We first examine the overall geometry and organization of the active faults in Central-Eastern Iran with an emphasis on the relationships between major and secondary faults. We then analyze new, dense GPS data (92 stations) to quantify the current strain and the slip rates on all major and most secondary faults in Central-Eastern Iran. The GPS data were acquired over the last 11 years in the framework of the long-going Iranian-French scientific collaboration. Taken together, the tectonic and geodetic data combined with available information such as long-term fault slip rates, provide constrains to better understand the kinematics of the recent (i.e., last few 104-106 yrs) to current deformation in Central-Eastern Iran. This understanding in turn provides a guide to better understand the seismic behavior of the secondary faults in Central-Eastern Iran.

3.2.3 Overall organization of active faults in Central-Eastern Iran

All principal seismogenic faults in Central-Eastern Iran are known and their recent to current activity is not in dispute (see references further below). A number of fault maps have thus been produced. However those maps either show most of the faults together yet with simplified traces [Walker and Jackson, 2002, Walker et al., 2004, Meyer and Le Dortz, 2007, Le Dortz et al., 2009, Allen et al., 2011, Farbod et al., 2011, Nozaem et al., 2013], or provide very detailed mapping yet of isolated faults or local fault sections only [Walker and Jackson, 2002, Walker et al., 2004, Meyer et al., 2006, Walker and Khatib, 2006, Meyer and Le Dortz, 2007, Fattahi and Walker, 2007, Allen et al., 2011, Farbod et al., 2011]. To examine the relationship between major and secondary faults, and to properly analyze the GPS data, we need a geo-referenced, precise tectonic map that would show all active faults together, major and secondary, in great details. Therefore, using satellite imagery (panchromatic and color LANDSAT and ASTER images, resolution 15-30 m), topographic data (SRTM and ASTER DEMs, resolution 30-90 m) and information from the literature, we mapped the Central-Eastern Iranian faults, at a large (Fig. 3.3) and at a small scale (Fig. 3.4). We geo-referenced the fault traces with the Ermapper software. It is now well established that most seismogenic faults can be unambiguously recognized from the specific trace that they imprint in the surface morphology [Tapponnier and Molnar, 1976, McCalpin and Nelson, 1996]. In transpressional settings as that of Central-Eastern Iran, the main indications of recent fault movements are continuous, pronounced, and hence well-preserved traces in the topography and morphology, cutting across or deforming recent morphological 'markers' such as active drainage networks, current ground surface and sediment cover, fresh and hence recent alluvial fans, etc. These characteristic morphological features are observed along most of the Central-Eastern Iranian faults, and this makes quite straightforward to recognize the faults with recent (i.e., late Quaternary) movement, down to structures of $\sim$ 10 km length. Furthermore, even when they are dominantly strike-slip, most faults in Central-Eastern Iran have a minor dip-slip component, which results in the formation of topographic scarps that even more clearly highlight the fault traces. In Figures 3.3 and 3.4, we have mapped with thicker traces the faults that show the clearest morphological evidence of recent movement. In thinner traces are the secondary faults that are, or that we or other authors suspect to be active though the morphological evidence might be less clear. Since most of those faults have been described in prior papers, we only provide a few close-up views of their fresh traces in Supporting Information 8.1.5, which we describe in the figure captions.

Figures 3.3 and 3.4 show that Central-Eastern Iran is dominantly dissected by large, active strike-slip faults, of two types: N-NW-trending, right-lateral strike-slip faults in the central part of the region, and $\sim$ E-W-trending, left-lateral strike-slip faults in its northern part. In both sets, the major faults are few while they extend over several hundred km of

length.

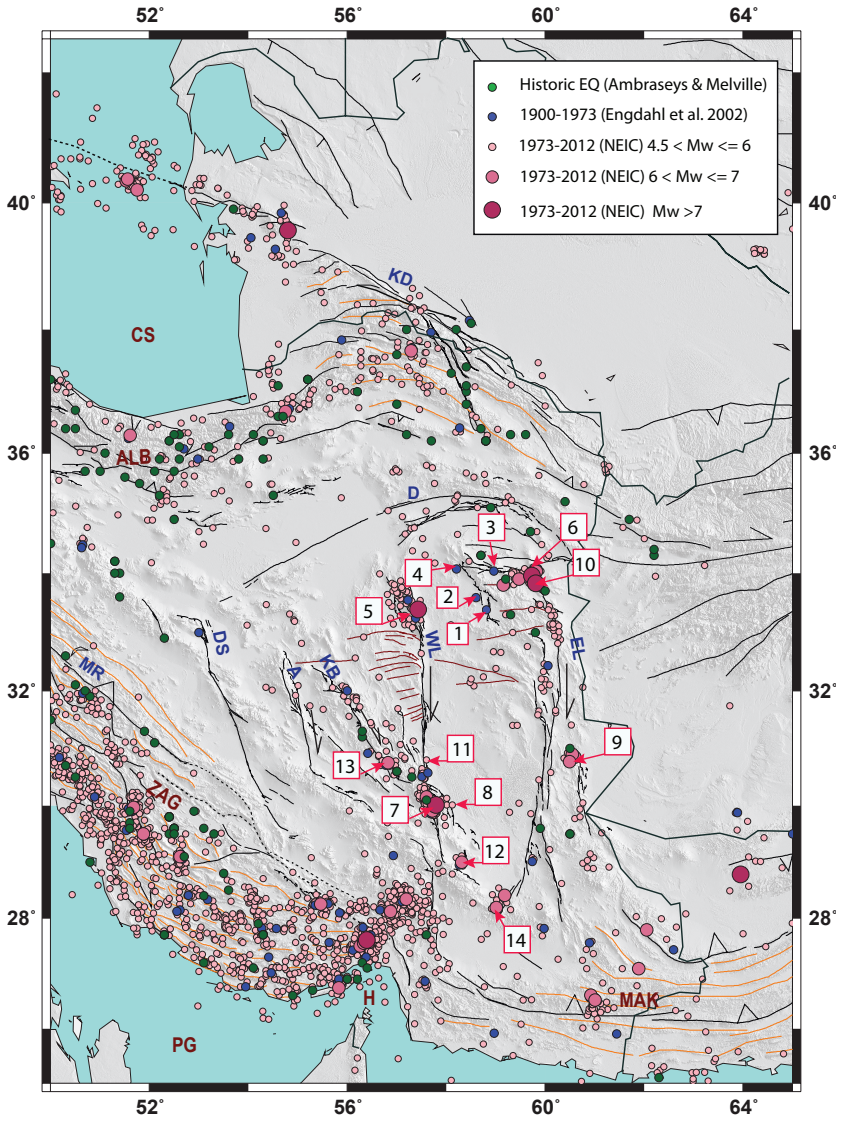

Figure 3.3 – Major active faults and seismicity in Central-Eastern Iran. SRTM topography is shown in background. Faults are in black. Thick and thin lines represent major and secondary faults at this scale. Dotted lines are used for faults for which the morphological evidences of recent activity are subtle or possibly disputable. Arrows indicate sense of lateral slip while triangles indicate reverse components of slip. Orange thin lines indicate major folding. A: Anar fault; D: Doruneh fault; DS: Dehshir fault; EL: East Lut fault; KB: Kuhbanan fault; KD: Kopeh Dagh fault; MR: Main Recent fault; WL: West Lut fault; ALB: Alborz; CS: Caspian Sea; H: Hormuz straight; MAK: Makran; PG: Persian Gulf; ZAG: Zagros. Green dots present historical earthquakes before 1900 (from [Ambraseys and Melville, 1982]), blue dots indicate instrumental seismicity from a centennial earthquake catalog ([Engdahl and Villaseñor, 2002]). Pink dots show instrumental earthquakes from 1973 to 2012 (from USGS catalogue NEIC: http://neic.usgs.gov/neis/epic/). Numbers indicate Central-Eastern Iranian earthquakes that are mentioned in text: 1- Mohammadabad 1941; 2- Dustabad 1947 (Mw 6.9); 3- Dasht-e-Bayaz 1968 (Mw 7.1); 4- Ferdows 1968 (Mw 6.2); 5- Tabas 1978 (Mw 7.4); 6- Dasht-e-Bayaz 1979 (Mw 7.1); 7- Sirch 1981 (Mw 7.3); 8- South Golbaf 1989 (Mw (5.6); 9- Sefidabeh 1994 (Mw 6.1); 10- Zirkuh 1997 (Mw 7.2); 11- Chahar - Farsakh 1998 (Mw 5.4); 12- Bam 2003 (Mw 6.6); 13- Dahuyieh (Zarand) 2005 (Mw 6.4); 14- Konarak 2010 (Mw 6.7).

The N-NW-striking fault set includes 5 major right-lateral faults, from east to west, the two ~ 700 km-long, ~ N-S-striking faults which bound the Lut block (which, for clarity, we name the East and West Lut faults, EL and WL, respectively; Supporting Information 8.1.5-ab) [Walker and Jackson, 2004, Bayer et al., 2006, Walker et al., 2009, 2010], the NW-striking, ~ 300 km-long Kuhbanan fault (KB) (Supporting Information 8.1.5-c) [Berberian et al., 1979, Walker and Khatib, 2006, Allen et al., 2011, Walker and Allen, 2012], the ~ 350 km-long, NNW-striking Anar fault (A) (note that we consider the Anar fault together with the Rafsanjan fault that forms its southern termination) [Le Dortz et al., 2009, Allen et al., 2011, Fattahi et al., 2011] (Supporting Information 8.1.5-d), and the ~ 500 km-long, NNW-striking Dehshir fault (DS) (Supporting Information 8.1.5-e) [Nazari et al., 2009, Fattahi et al., 2010]. The East Lut fault is commonly referred to as the Sistan fault and described as including from south to north the Nostarabad, Asagie, Neh, Zahedan, Avaz-Gazik and Abiz fault segments [Walker and Jackson, 2004]. The West Lut fault is commonly referred to as the Gowk-Nayband fault, the Gowk and Nayband segments forming the southern and northern parts of the system, respectively [Walker and Jackson, 2004]. The five N-NW right-lateral faults listed above are well distant from each other, separated by 150 to 300 km-wide regions that are hardly faulted (more details further below). To the south, the longest of these faults end near the main Zagros thrust in the west, while in the east they seem to connect with the thrusts of the Makran accretionary wedge [e.g., Regard et al., 2005]. To the north, the three westernmost faults (DS, A, KB) terminate with no clear connection with other faults, while, in contrast, the Lut bounding-faults abut and possibly connect with oblique structures including E-W faults.

The E-W-striking fault set includes one very long, left-lateral strike-slip fault –the ~ 800 km long, ~ ENE-trending Doruneh fault ('D', also called Great Kavir; Supporting Information 8.1.5-f) [Sto, Fattahi et al., 2006b, Farbod et al., 2011], and a few shorter ones (100-500 km long), mainly the WNW-trending Torbat-e-Jam (TJ) fault north of Doruneh, and the E-W-striking Dasht-e-Bayaz (DeB) fault south of Doruneh [Walker et al., 2004]. Two other small faults might exist further south (Sedeh (S) and Birjand (B) faults, Fig. 3.4) but those do not show any clear morphological evidence of recent activity. Except these two small faults, all ~ E-W major faults are active, as recognized in prior papers [Walker et al., 2004, Walker and Jackson, 2004, Walker and Khatib, 2006, Hollingsworth et al., 2006, Fattahi and Walker, 2007, Farbod et al., 2011] and confirmed by the close-up views of their typical traces (Supporting Information 8.1.5). As a matter of fact, the Dasht-e-Bayaz fault recently broke in two large earthquakes (Mw ~ 7, 1968 and 1979) [Ambraseys and Tchalenko, 1969, Tchalenko and Berberian, 1975, Ambraseys and Melville, 1982, Berberian et al., 1999, Walker and Jackson, 2004, Walker and Fattahi, 2011]. The faults south of Doruneh are much shorter than those further north (60-150 km versus >300 km, respectively), more closely spaced (30-60 km versus 120-150 km), and confined to a small area enclosed between the northern tip of the East Lut fault and the

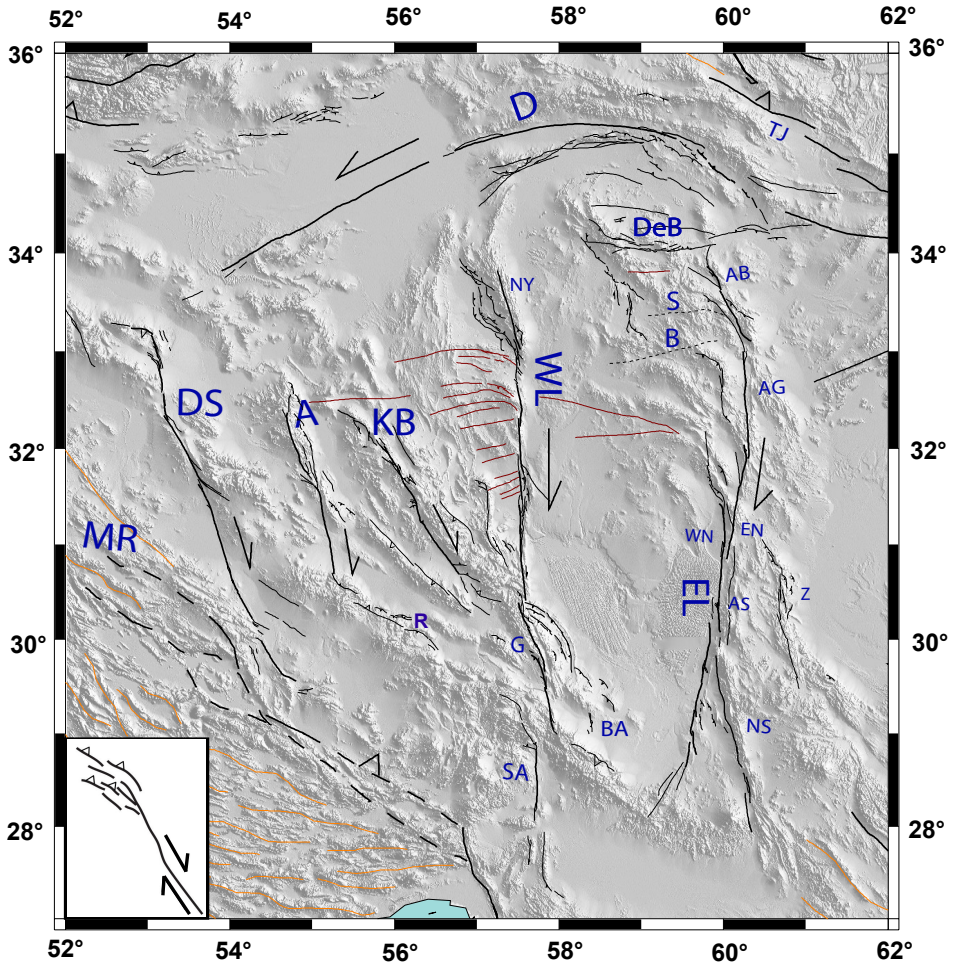

Figure 3.4 – Detailed mapping of major and secondary active faults in Central-Eastern Iran. Symbols as in Fig.3.3. Note that faults south of MR zone, as faults north of Doruneh, have not been mapped in detail. A: Anar fault; AB: Abiz fault; AG: Avaz-Gazik fault; AS: Asagie fault; B: Birjand fault; BA: Bam fault; D: Doruneh fault; DeB: Dasht-e-Bayaz fault; DS: Dehshir fault; EL: East Lut fault; EN: East Neh fault; G: Gowk fault; KB: Kuhbanan fault; MR: Main Recent fault; NS: Nostarabad fault; NY: Nayband fault; R: Rafsanjan fault; S: Sedeh fault; SA: Sabzevaran fault; TJ: Torbat-e-Jam fault; WL: West Lut fault; WN: West Neh fault; Z: Zahedan fault. Inset sketches compressive horsetail faulting.

eastern tip of the Doruneh fault [Farbod et al., 2011]. All together, the ∼ E-W fault set somehow interrupts the NNW right-lateral faults developed further south. Further north, the E-W left-lateral faults give place to the NW-trending, right-lateral and reverse Kopeh Dagh fault zone (Fig. 3.3). The left- and right-lateral motions on the E-W faults and on the Kopeh Dagh fault, respectively, transfer into folding and thrusting east and south of the Caspian Sea [Javidfakhr et al., 2011a, Hollingsworth et al., 2006, 2008, 2010b].

Most of the secondary faults that we identified are connected to the major faults. The large majority of those secondary faults are predominantly reverse, short faults (50-100 km long), associated to folding, that form dense networks at the tips of the master faults (as recognized by Walker and Khatib [2006]). Those secondary networks have strikes that are markedly oblique to the mean direction of the principal faults, which they connect to.

Both the obliquity and slip mode of the secondary faults developed at the master fault tips are in keeping with the sense of lateral motion on those master faults; the secondary networks actually form compressive horsetail terminations to the major faults (inset Fig. 3.4). The clearest cases are the reverse fault and fold networks developed at both tips of the West Lut fault, but similar horsetail secondary networks have developed at both tips of the DS, KB, and EL faults, as at the southern tip of the A fault and at the eastern tip of the Doruneh fault [Farbod et al., 2011]. Some of these secondary oblique faults seem to reactivate preexisting structures [Nozaem et al., 2013, Walker and Khatib, 2006]. One clear case is that of the Anar fault, whose southern section (named the 'Rafsanjan fault' [Berberian, 1976, Walker et al., 2010, Fattahi et al., 2011, Allen et al., 2011]) follows a preexisting fold and thrust system.

Secondary, oblique, short faults are also observed off- the main fault traces which they generally connect to. Again, both the obliquity and slip mode (most are reverse) of those secondary off-fault features are in keeping with the sense of lateral motion on the major faults. The clearest cases are the reverse, $\sim$ NW-trending faults and folds developed along the East Lut fault (Fig. 3.4). Some of these oblique, secondary faults may also reactivate preexisting structural trends. This is particularly clear along the West and East Lut faults, where multiple ancient $\sim$ E-W structural trends exist (in brown in Fig. 3.4) [Walker and Khatib, 2006], some of them are likely reactivated, in particular by the Dasht-e-Bayaz fault. The Sedeh and Birjand faults coincide with some of the ancient features. A few other secondary faults are roughly parallel to the major faults and dissect the regions between the master structures. Such few faults are observed in the southern regions between the A and KB faults ('Jorjafk fault') and between the KB and WL faults (see Allen et al. [2011] for more details), and in the northern region between the WL and the EL faults.

Finally, most major faults have their trace divided into a number of major segments –as it is the case of most faults worldwide [Manighetti et al., 2009, Manighetti I. and Cappa, 2013], and those segments are generally en echelon arranged, with this arrangement indicating the sense of lateral motion on the main fault. The West and East Lut faults show an especially clear, en echelon segmentation (right-stepping, compressive echelons). We may note that, although they form a single fault zone, those major segments have been generally described as separate faults in the literature (East Neh, West Neh and Zahedan faults along the EL fault; Nayband, Gowk and Sabzevaran faults along the WL fault) [Walker et al., 2009]. The en echelon segmentation of the West Lut fault suggests that the fault actually extends further south of its 'Bam termination', via the Sabzevaran fault, up to the so-called Zendan-Minab fault, where it might connect to the thrusts of the Makran accretionary wedge. The total length of the West Lut fault might thus be up to 800 km. As commonly observed on faults worldwide, dense networks of small, secondary faults have developed in many of the zones that separate the major segments within the faults. Those

small secondary faults are oblique to the master fault and are reverse, in keeping with the right-lateral motion on the principal faults. The clearest cases are observed on the A, WL and EL faults.

Therefore, while our fault mapping confirms that the active tectonics of Central-Eastern Iran is dominated by a few large strike-slip faults of different orientation and slip mode –as previously recognized, it also shows that those major faults are connected to a significant number of secondary faults, most accommodate strain off- the principal fault traces, especially at their tips.

Figure 3.3 shows that the historical and instrumental seismicity underlines most of the faults described above, confirming that those faults are currently active. Some faults or fault sections are free of earthquakes however (Dehshir, Anar, central section of West and East Lut faults and of the Doruneh fault). Conversely, some earthquakes cluster at specific sites along the faults, and most of those sites are the fault tips, or zones of fault connection. We come back to these points in the discussion section.

3.2.4 GPS data acquisition and processing

The GPS network that we use includes 92 stations well distributed in Central-Eastern Iran (Fig. 3.5). The data cover an 11 years time span (1997-2008), though some cover shorter times (Table 3.1). They combine campaign and permanent measurements (74 and 18 stations, respectively). The campaign measurements were conducted since 1997 in the framework of the on-going French-Iranian scientific collaboration, with the support of the National Cartographic Center of Tehran. Most campaign sites are identified with screw markers settled in bedrock. During each campaign, the observation time of each site was at least 48 hours. We used Trimble SSE and Ashtech CGRS receivers with choke ring antennas. Note that some of the earliest data have already been used to study the global current kinematics of Iran [Vernant et al., 2004b, Masson et al., 2007] and the Zagros current deformation [Tatar et al., 2002, Walpersdorf et al., 2006, Bayer et al., 2006, Tavakoli et al., 2008]. The temporary measurements are completed with the full time series of permanent GPS data, acquired from both the global permanent IGS network (International GNSS Service, [Dow et al., 2009]) since 1997 (up to 40 stations), and the Iranian national permanent GPS network (18 stations installed in 2005-2006 in Eastern Iran, equipped with Ashtech CGRS receivers and choke ring antennas).

The data analysis is performed with the GAMIT/GLOBK software, version 10.4 [Herring et al., 2006, 2008]. Following Vergnolle et al. [2010], we made a special effort to eliminate the influence of several non-tectonic phenomena from the GPS data (troposphere, ocean and atmospheric loading), in order to enhance the signal to noise ratio and to better measure the tectonic deformation. The daily solutions are combined with the Kalman filter GLOBK to estimate a linear velocity for each site. To obtain realistic velocity uncertainties

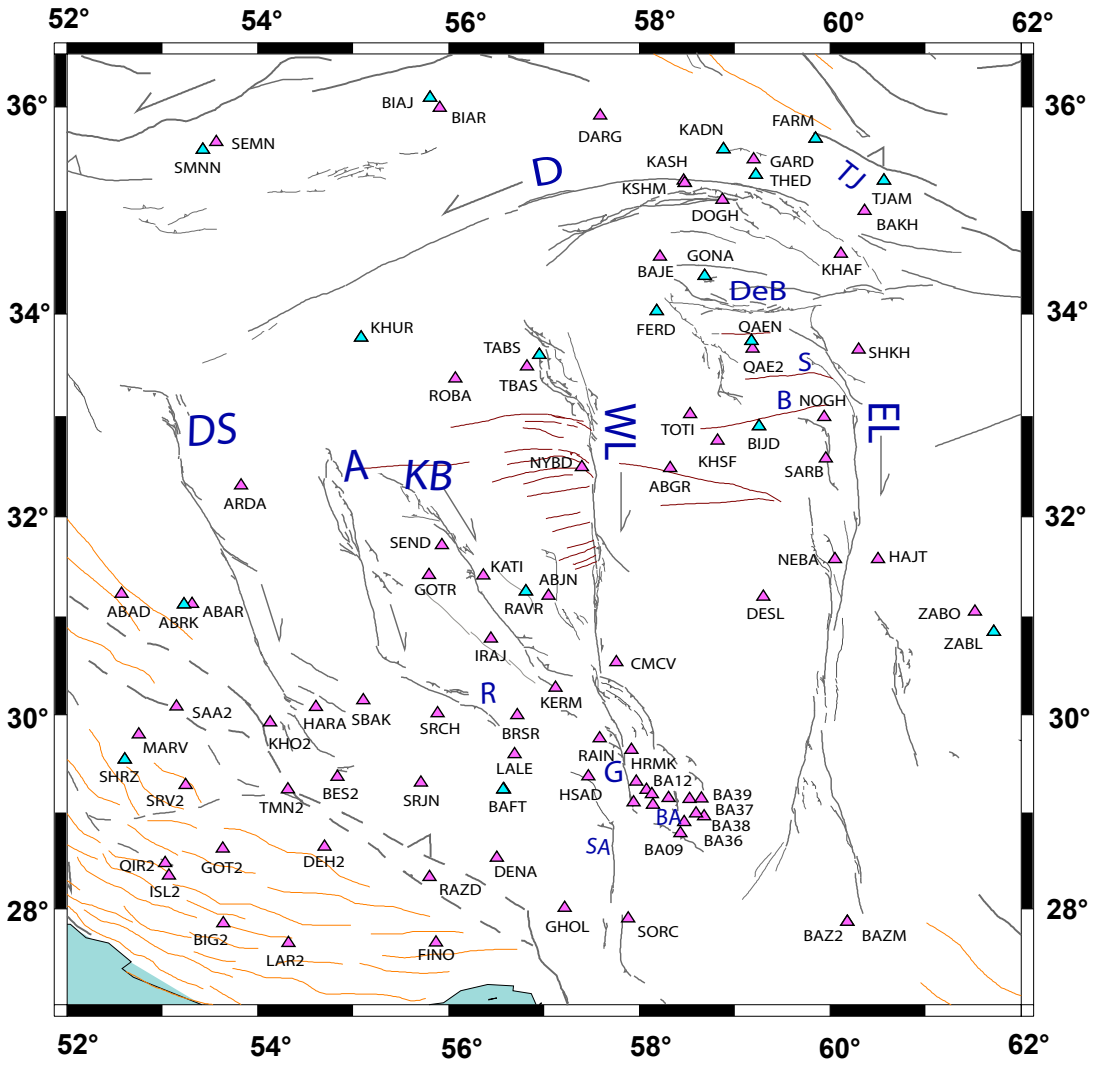

Figure 3.5 – Map of Central-Eastern Iranian GPS stations used in our analysis. Blue and pink triangles represent permanent and campaign stations, respectively. Fault names and symbols as before.

(Table 3.1), stochastic noise is applied to the site positions. The amount of noise is fixed to 4/4/8 mm2/yr on the North/East/Up components for campaign sites [Vernant et al., 2004b], while estimated individually for permanent stations according to the measurement time span and the variability of the coordinate time series. This "real-sigma" procedure of the GAMIT/GLOBK software [Herring et al., 2008] evaluates noise to ~ 0.1 and 1 mm2/yr for the horizontal and the vertical components of permanent stations, respectively.

We conduct our GPS analysis in the Eurasian reference frame that is established by minimizing the velocities of 17 stations on the Eurasian plate (ARTU, GLSV, GRAS, GRAZ, IRKT, JOZE, KIT3, NYA1, POL2, POTS, SELE, TIXI, TRO1, VILL, WTZR, ZECK and ZIMM) using a Helmert transformation. The residual velocities (rms) for these 17 stations are 0.2 and 0.3 mm/yr on the east and the north components, respectively.

Table 3.1 – GPS station velocities sorted by tectonical unit or fault. Eight blocks or units and four faults constrained by GPS station velocities: CIB: Central Iran Block; ADB: Anar-Dehshir Block; KAB: Kuhbanan-Anar Block; NB: Nayband Block; LB: Lut Block; HB: Hellmand Block; NDR: North Doruneh Region; SDR: South Doruneh Region. Sedeh/B.: cumulated Sedeh and Birjand faults; DeB: Dasht-e-Bayaz fault; GF: Gowk fault; BF: Bam fault; Sabz.: Sabzevaran fault. For faults, stations located above/below the horizontal line are located on the western/eastern or northern/southern compartment, respectively. Class 1 stations are highlighted by bold letters; permanent stations are indicated by a star. sol. indicates the number of campaign solutions or weekly solutions for campaign and permanent sites, respectively.

Unit	SITE	Lon	Lat	V_E [mm/yr]	V_N [mm/yr]	sig_{VE} [mm/yr]	sig_{VN} [mm/yr]	span [yr]	# sol.	date mid-point
CIB	**ABAR**	53.308	31.123	-1.93	13.07	0.99	0.98	4.21	5	2006.7265
	ABAD	52.568	31.228	-2.49	13.26	0.99	0.99	4.21	4	2006.6167
	ABRK*	53.226	31.12	-2.12	13.7	1.89	1.89	1.13	16	2006.8417
	KHO2	54.126	29.923	-2.54	14.13	0.91	0.84	5.96	3	2003.737
	SAA2	53.146	30.087	-2.33	13.31	0.73	0.71	8.94	5	2006.7393
ADB	**ARDA**	53.822	32.313	-1.59	13.26	0.82	0.82	6.02	8	2005.6684
	SBAK	55.107	30.146	-0.42	13.17	1.31	1.31	2.39	3	2007.8833
	SRCH	55.885	30.014	0.14	13.28	1.64	1.63	1.73	2	2007.4111
	HARA	54.608	30.079	0.02	13.07	0.82	0.82	6.02	3	2005.6575
KAB	**GOTR**	55.791	31.416	-0.35	10.63	1.61	1.61	1.73	2	2007.5148
	BRSR	56.721	29.997	-0.12	14.6	1.66	1.65	1.73	2	2007.253
	IRAJ	56.445	30.775	-0.87	12.89	1.58	1.58	1.73	2	2007.5479
	SEND	55.929	31.713	-0.52	11.75	1.04	1.04	3.87	5	2007.5585
NB	**RAVR***	56.809	31.252	0.43	10.28	0.73	0.69	2.02	62	2008.8125
	ROBA	56.07	33.369	-0.02	9.23	0.67	0.67	9.09	10	2008.6197
	TABS*	56.951	33.603	-0.76	9.15	0.48	0.34	2.26	107	2008.7908
	TBAS	56.819	33.489	-2.98	7.25	1.58	1.58	1.73	2	2007.6196
	NYBD	57.397	32.492	-0.92	8.81	1.25	1.26	2.63	3	2008.6343
	ABJN	57.046	31.206	2.3	10.9	1.62	1.62	1.73	2	2007.684
	KATI	56.365	31.413	0.55	10.67	1.06	1.06	3.87	5	2007.1043
LB	**DESL**	59.297	31.196	1.33	6.24	1.57	1.56	1.73	2	2007.7681
	BIJD*	59.255	32.9	0.56	6.25	0.4	0.29	2.71	109	2008.8161
	KHSF	58.821	32.755	0.13	5.81	1.15	1.15	3.07	4	2008.6778
	TOTI	58.531	33.019	-0.68	7.4	1.25	1.25	2.63	3	2008.6188
	ABGR	58.319	32.484	0.77	7.09	1.57	1.57	1.73	2	2007.7432
	NEBA	60.047	31.573	0.63	5.27	1.26	1.26	2.63	3	2008.5772
	SARB	59.955	32.578	1.06	4.91	1.16	1.16	3.07	5	2008.6109
	NOGH	59.937	32.988	0.86	4.62	0.98	0.98	4.29	4	2008.6156
	QAE2	59.188	33.663	-0.86	4.23	0.98	0.98	4.29	3	2008.6621
	QAEN*	59.176	33.74	-0.75	4.55	0.35	0.34	2.97	125	2008.8072
	GONA*	58.684	34.373	-0.79	5.38	0.3	0.28	3.15	134	2008.8111
	BAJE	58.215	34.558	-0.53	5.7	0.98	0.98	4.29	3	2008.6643
	FERD*	58.183	34.031	-1.75	7.73	0.38	0.42	2.71	120	2008.8111
	CMCV	57.76	30.537	-0.36	8.2	1.61	1.6	1.73	2	2007.5926

Continued table 3.1

Unit	SITE	Lon	Lat	V_E [mm/yr]	V_N [mm/yr]	sig_{VE} [mm/yr]	sig_{VN} [mm/yr]	span [yr]	# sol.	date mid-point
HB	**ZABL***	61.716	30.841	1.71	1.58	1.05	0.77	1.52	61	2008.8319
	ZABO	61.517	31.049	-0.03	1.42	0.67	0.67	9.09	12	2008.5303
	HAJT	60.502	31.573	1.02	1.64	1.15	1.15	3.07	4	2008.7018
	SHKH	60.296	33.654	-0.38	-1.58	1.16	1.16	3.07	4	2007.4672
	BAZ2	60.177	27.865	4.14	2.37	1.42	1.42	2.16	2	2007.6142
	BAZM	60.18	27.865	2.15	3.09	1.44	1.44	6.02	3	2001.6115
NDR	**DARG**	57.589	35.915	-0.76	5.63	0.98	0.98	4.29	4	2008.6307
	GARD	59.197	35.495	-0.22	2.62	0.98	0.98	4.29	3	2008.6919
	KADN*	58.878	35.592	-0.41	2.18	0.8	0.41	3.43	165	2008.8213
	TJAM*	60.564	35.294	-0.51	3.38	0.64	0.68	2.01	61	2008.8449
	BAKH	60.36	35.002	0.08	-0.01	0.98	0.98	4.29	4	2008.6651
	FARM*	59.843	35.696	0.11	1.12	0.39	0.28	3.47	168	2008.7977
	THED*	59.219	35.347	-0.03	3.51	0.28	0.28	3.51	167	2008.7967
	BIAR	55.906	35.988	0.13	8.43	1.17	1.17	3.07	4	2008.5613
	BIAJ*	55.805	36.086	1.3	8.36	0.52	0.37	2.65	74	2008.8303
	SEMN	53.564	35.662	0.38	8.71	0.82	0.82	6.02	3	2005.5872
	SMNN*	53.421	35.588	0.95	8.82	0.39	0.29	3.23	152	2008.6155
SDR	**BAJE**	58.215	34.558	-0.53	5.7	0.98	0.98	4.29	3	2008.6643
	KHUR*	55.081	33.769	-0.14	10.55	0.65	0.48	2.02	60	2008.8472
	DOGH	58.869	35.108	-0.3	4.99	0.98	0.98	4.29	4	2008.6764
Sedeh/B.	QAE2	59.188	33.663	-0.86	4.23	0.98	0.98	4.29	3	2008.6621
	QAEN*	59.176	33.74	-0.75	4.55	0.35	0.34	2.97	125	2008.8072
	BIJD*	59.255	32.9	0.56	6.25	0.4	0.29	2.71	109	2008.8161
	NOGH	59.937	32.988	0.86	4.62	0.98	0.98	4.29	4	2008.6156
	SARB	59.955	32.578	1.06	4.91	1.16	1.16	3.07	5	2008.6109
DeB	BAJE	58.215	34.558	-0.53	5.7	0.98	0.98	4.29	3	2008.6643
	GONA*	58.684	34.373	-0.79	5.38	0.3	0.28	3.15	134	2008.8111
	QAE2	59.188	33.663	-0.86	4.23	0.98	0.98	4.29	3	2008.6621
	QAEN*	59.176	33.74	-0.75	4.55	0.35	0.34	2.97	125	2008.8072
GF	HSAD	57.465	29.371	1.8	13.78	1.56	1.56	1.73	2	2007.7626
	RAIN	57.584	29.762	0.82	13.55	1.55	1.55	1.73	2	2007.7205
	BA07	58.305	29.149	0.91	11.24	1.41	1.41	2.14	6	2005.9876
	BA13	58.074	29.23	0.87	10.37	1.52	1.52	1.92	5	2005.9697
	BA14	57.94	29.105	4.44	9.4	1.04	1.04	3.87	7	2007.4989
	BA30	57.967	29.316	2.94	9.33	1.05	1.05	3.87	7	2007.4277
	BA31	58.13	29.187	2.1	10.46	1.45	1.44	2.14	7	2005.6475
	BA32	58.141	29.078	2.25	10.88	1.47	1.46	2.14	6	2005.7444
	BA34	58.278	28.944	3.63	9.28	1.55	1.54	1.92	5	2005.6991
	BA35	58.195	28.888	4.48	10.31	1.48	1.47	2.03	6	2005.6818
	HRMK	57.917	29.642	2.02	9.45	1.57	1.56	1.73	2	2007.7086

Continued table 3.1

Unit	SITE	Lon	Lat	V_E [mm/yr]	V_N [mm/yr]	sig_{VE} [mm/yr]	sig_{VN} [mm/yr]	span [yr]	# sol.	date mid-point
BF	BA07	58.305	29.149	0.91	11.24	1.41	1.41	2.14	6	2005.9876
	BA13	58.074	29.23	0.87	10.37	1.52	1.52	1.92	5	2005.9697
	BA14	57.94	29.105	4.44	9.4	1.04	1.04	3.87	7	2007.4989
	BA30	57.967	29.316	2.94	9.33	1.05	1.05	3.87	7	2007.4277
	BA31	58.13	29.187	2.1	10.46	1.45	1.44	2.14	7	2005.6475
	BA32	58.141	29.078	2.25	10.88	1.47	1.46	2.14	6	2005.7444
	BA34	58.278	28.944	3.63	9.28	1.55	1.54	1.92	5	2005.6991
	BA35	58.195	28.888	4.48	10.31	1.48	1.47	2.03	6	2005.6818
	BA12	58.523	29.137	2.6	7.19	1.03	1.03	3.87	8	2007.666
	BA36	58.469	28.898	2.47	8.41	1.41	1.41	2.14	6	2005.9636
	BA38	58.675	28.96	4.86	6.98	1.04	1.04	3.87	6	2007.5495
	CMCV	57.76	30.537	-0.36	8.2	1.61	1.6	1.73	2	2007.5926
Sabz.	GHOL	57.217	28.01	0.16	14.86	1.44	1.44	1.99	4	2001.9282
	SORC	57.884	27.901	0.94	12.57	1.44	1.43	1.99	4	2001.953
not	KHAF	60.11	34.589	-1.38	0.49	0.98	0.98	4.29	4	2008.7051
con-	KSHM*	58.473	35.271	0.54	4.63	0.3	0.24	3.18	153	2008.7988
straining	KASH	58.464	35.293	-0.41	4.67	0.82	0.82	6.02	3	2005.6569
anyunit	BA09	58.428	28.784	5.17	9.46	1.44	1.44	2.14	6	2005.8341
or fault	KERM	57.119	30.277	0.36	14.9	0.71	0.71	8.18	12	2007.3096
	LALE	56.69	29.596	0.86	14.34	1.06	1.06	3.87	5	2007.7217
	BAFT*	56.58	29.239	0.4	13.27	1.44	1.44	1.73	8	2007.8835
	DENA	56.504	28.529	4.05	14.69	1.45	1.44	1.99	2	2001.9122
	HAJI	55.918	28.302	-6.36	14.24	0.91	0.91	5.21	6	2003.6791
	FINO	55.867	27.651	1.41	19.06	1.47	1.46	1.99	2	2001.8072
	RAZD	55.8	28.33	2.52	14.58	0.85	0.84	5.67	5	2005.6256
	SRJN	55.707	29.304	-0.2	14.38	1.59	1.58	1.73	2	2007.6577
	BES2	54.832	29.363	0.9	13.82	0.91	0.84	5.96	3	2003.6079
	DEH2	54.7	28.645	0.91	13.65	0.89	0.84	5.96	4	2003.7662
	LAR2	54.32	27.644	-0.88	17.64	0.94	0.86	5.96	4	2003.5402
	TMN2	54.316	29.239	1.17	13.53	0.7	0.68	8.94	5	2006.5933
	BIG2	53.637	27.852	1.74	16.05	1.01	0.93	5.96	4	2003.7056
	GOT2	53.631	28.624	1.56	15.67	0.73	0.69	8.94	5	2006.6597
	SVR2	53.244	29.281	1.01	13.58	0.71	0.69	8.94	5	2006.4803
	ISL2	53.066	28.347	1.2	16.3	0.7	0.68	8.94	5	2006.5688
	QIR2	53.029	28.477	1.06	16	0.84	0.83	5.96	4	2003.7473
	MARV	52.752	29.798	-0.56	13.44	0.99	0.99	4.21	5	2006.5509
	SHRZ*	52.603	29.544	-1.8	13.76	0.26	0.27	3	65	2008.8276

Table 3.2 – Euler pole estimates, model residuals and local rotation rates of the major tectonic units in Central-Eastern Iran. Notes: N: number of stations on each tectonic unit. Model: lo (locked) or fr (free) faults. Emax, Emin and Az describe the error ellipse for the emplacement of the pole. Res. are the residuals of horizontal velocities between observations and predictions from the block models. Local rotation rate is the rotation rate about a vertical axis in the centre of each block.

Unit	N	Model	Lon [°E]	Lat [°N]	Euler Rot. Rate [°/Ma]	Sig. Euler Rot. Rate [°/Ma]	Emax [°]	Emin [°]	Az [°]	Res. [mm/yr]	Local Rot. Rate [°/Ma]
CIB	5	**lo**	**0.2738**	**11.0664**	**0.1562**	**0.1817**	**80.25**	**2**	**59.95**	**0.44**	**0.094**
		fr	351.583	5.8901	0.1384	0.138	88.65	2.26	58.6	0.39	0.063
ADB	4	**lo**	**31.2772**	**28.067**	**0.3414**	**0.2123**	**18.51**	**1.22**	**75.93**	**0.49**	**0.319**
		fr	26.1311	26.5762	0.2789	0.1937	25.61	1.32	73.34	0.38	0.252
KAB	4	**lo**	**45.6881**	**29.9378**	**0.7629**	**0.5129**	**8.61**	**0.7**	**79.07**	**1.58**	**0.754**
		fr	38.5907	29.3758	0.4197	0.4872	24.86	1.21	78.83	1.2	0.405
NB	7	**lo**	**42.65**	**31.8129**	**0.4057**	**0.1617**	**6.88**	**0.58**	**80.81**	**1.44**	**0.397**
		fr	35.5961	30.4896	0.271	0.1401	13.63	0.82	77.15	1.41	0.257
LB	12	**lo**	**42.2567**	**30.976**	**0.2158**	**0.0944**	**9**	**0.55**	**75.03**	**1.41**	**0.209**
		fr	32.6309	28.5806	0.1335	0.0889	22.36	0.88	70.63	1.39	0.123
HB	6	**lo**	**59.2264**	**32.1358**	**0.3508**	**0.1296**	**1.42**	**0.88**	**310.47**	**1.67**	**0.351**
		fr	58.4797	32.345	0.3111	0.125	1.79	0.97	304.01	1.55	0.311
SDR	3	**lo**	**62.8959**	**34.3467**	**-0.8268**	**0.1249**	**1.15**	**0.41**	**269.32**	**1.17**	**-0.823**
		fr	62.7699	34.368	-0.837	0.13	1.19	0.37	91.39	1.18	-0.834
NDR	11	**lo**	**61.3791**	**35.4116**	**-0.752**	**0.0326**	**0.24**	**0.17**	**99.17**	**1.3**	**-0.751**
		fr	61.6382	35.3008	-0.7274	0.0317	0.24	0.16	97.55	1.33	-0.726

3.2.5 Approach for modelling the GPS data

The GPS data are both dense and broadly distributed and hence might be modelled to estimate the kinematics of present-day deformations in Central-Eastern Iran and the current slip rates on most active faults in the zone. For reasons that we explain below, we had to conduct two types of complementary modelling.

Common to any GPS data modelling is the assumption that, in interseismic time, a fault is a planar, locked feature embedded in an elastic medium and sustaining constant strain loading. Under this assumption, dense GPS networks, especially dense transects of GPS stations perpendicular to a fault, can be used to determine simultaneously the current slip rate on the fault and its locking depth [Savage and Burford, 1973]. Unfortunately, though the number of stations used here is large (92), the GPS network is still too sparse to build these simple elastic strain accumulation models for most of the faults. Therefore, to estimate the fault slip rates as to derive the regional motions, we need to make one additional assumption. That assumption considers that the faults are locked over their entire brittle layer, what is commonly thought as reasonable. The crustal thickness in Central-Eastern Iran is $\sim$ 40 km [Mooney et al., 1998], but the seismogenic thickness is assumed to be lower, $\sim$ 15 km [Maggi et al., 2000, Engdahl et al., 2006]. We thus consider that all faults are locked over 15 km.

To simultaneously derive the regional kinematics and the fault slip rates, a classical

Table 3.3 – Predicted block velocities at the center of each block from block model. The second and third column indicates N and E components, the fourth and fifth column indicates the components in the N13°E AR-EUR convergence direction and in the N103°E perpendicular direction. Components towards N13°E and N103°E are positive.

Block / region	V_N [mm/yr]	V_E [mm/yr]	V_{N13} [mm/yr]	V_{N103} [mm/yr]
HB	1.0 ±0.4	0.8 ± 0.4	1.2 ±0.4	0.6 ± 0.4
LB	5.9 ± 0.2	-0.2 ± 0.3	5.7 ± 0.2	-1.5 ± 0.3
NB	9.2 ± 0.3	0.1 ± 0.4	9.0 ± 0.3	-2.0 ± 0.4
KAB	13.2 ± 0.8	-1.0 ± 0.8	12.6 ± 0.8	-3.9 ± 0.8
ADB	13.4 ± 0.6	-0.5 ± 0.6	12.9 ± 0.6	-3.5 ± 0.6
CIB	13.6 ± 0.4	-2.4 ± 0.5	12.7 ± 0.4	-5.4 ± 0.5
SDR	7.8 ± 0.4	0.0 ± 0.5	7.6 ± 0.4	-1.8 ± 0.5
NDR	5.2 ± 0.1	0.3 ± 0.2	5.1 ± 0.1	0.9 ± 0.2

approach is to use a rigid block model [McCaffrey et al., 2000]. This type of modeling relies on an additional assumption, which is that the major faults accommodate most of the current deformation in the zone under study; in other words, most strain is localized within narrow zones along the major faults, while little deformation is left inside the fault-bounded blocks that may therefore be approximated as rigid and behaving as elastic bodies. The strength of the rigid block model is that it allows quantifying simultaneously all the block motions and the slip rates on the major faults that bound the blocks. Its weakness is that only major faults that bound large tectonic units can be described, while the secondary faults that might cut the interior of the blocks are ignored. We showed in section 2 that many of such secondary faults exist in Central-Eastern Iran and hence should be taken into account in any proper strain modeling. With those limitations in mind, in a first step, we used a rigid block model (Defnode, http://web.pdx.edu/∼mccaf/www/defnode/ [McCaffrey et al., 2000]) to reproduce the GPS data. We imposed fault locking over 15 km with 100 % coupling. This enabled us to include all GPS sites in the modeling; those at a distance greater than twice the fault locking depth from a fault and whose velocities are expected to represent the rigid block motions (Class 1 stations in Table 3.1), and the many additional stations that are closer to the fault traces and whose velocities are affected by the elastic deformation induced by the fault locking (Class 2 stations in Table 3.1).

Modeling the whole area as a single system of faults and blocks is expected to produce realistic slip rate estimates, including the covariance between slip rates on sub-parallel faults. The GPS station velocities were used to calculate an Euler pole for each tectonic unit (Table 3.2), and then to derive the block velocities (Table 3.3). The relative motions of the units inferred from their Euler poles allowed quantifying the slip rates on the major bounding faults. Uncertainties on these rates strongly depend on the uncertainties on the Euler pole locations. These uncertainties might be large, as it is the case in the west of the network where GPS vectors are roughly parallel and hence poorly constrain the Euler

Table 3.4 – Current fault slip rates at the center of the major active faults in Central-Eastern Iran. Fault strike is indicated in column 2. Slip rates are given in fault-parallel and fault-perpendicular directions. Block model calculations with locked and freely slipping faults are discriminated. Last two columns ("average") for fault slip rates determined from differences of average GPS velocities to each side of the fault (and not from block model). RL: right-lateral; LL: left-lateral; EX: extension; SH: shortening.

Fault	azim	comp	Rigid Block Model				Averages		
			Nx/Ny	locked [mm/yr]	free [mm/yr]	Nx/Ny	Class1 [mm/yr]	Nx/Ny	Class1+2 [mm/yr]
Dehshir	N162	para.	5/4	1.4 ± 0.9 RL	1.1 ± 0.8 RL	3/2	0.5 ± 0.2 RL	4/3	0.9 ± 0.3 RL
		perp.		-1.3 ± 0.8 EX	-1.2 ± 0.8 EX		-1.1 ± 0.5 EX		0.9 ± 0.3 RL
Anar	N164	para.	4/4	1.2 ±1.3 RL	1.8 ± 1.2 RL	2/1	2.7 ± 1.3 RL		
		perp.		1.3 ±1.0 SH	0.5 ± 1.0 SH		-0.2 ± 1.7 EX		
KBF	N138	para.	4/7	5.0 ± 1.1 RL	3.1± 0.9 RL	2/1	2.3 ± 1.9 RL	4/3	2.4 ± 0.8 RL
		perp.		0.9 ± 0.8 SH	1.2 ± 0.9 SH		0.6 ± 1.3 SH		0.4 ± 0.7 EX
West Lut	N000	para.	7/12	4.4 ± 0.4 RL	4.2 ± 0.4 RL	3/4	4.7 ± 1.7 RL	15/10	3.7 ± 1.3 RL
		perp.		0.7 ± 0.7 SH	0.5 ± 0.6 SH		-0.3 ± 0.5 EX		-1.0 ± 1.1 EX
East Lut	N012	para.	12/6	5.6 ± 0.6 RL	5.0 ±0.5 RL	5/4	5.7 ± 0.9 RL	8/6	4.3 ± 0.9 RL
		perp.		-1.4 ± 0.6 EX	-1.7 ± 0.6 EX		-1.4 ± 0.6 EX		-1.8 ± 0.8 EX
Doruneh	N077	para.	11/3	-2.1 ± 0.5 LL	-1.9 ± 0.5 LL	1/2	-0.5 ± 1.1 LL	8/4	0.4 ± 0.3 RL
		perp.		2.1 ± 0.4 SH	1.9 ±0.5 SH		2.6 ± 2.7 SH		1.6 ± 2.1 SH
DeB	N090	para.						2/2	0.2 ± 0.1 RL
		perp.							-1.1 ± 0.3EX
Sedeh/B.	N090	para.						2/3	1.7 ± 0.2 LL
		perp.							0.9 ± 0.6 SH
Gowk	N000	para.						2/9	4.2 ± 0.7 RL
		perp.							-1.4 ± 0.8 EX
Bam	N000	para.						8/4	2.1 ± 1.0 RL
		perp.							0.3 ± 1.7 SH
Sabz.	N000	para.						1/1	2.3 ± 2.4 RL
		perp.							-0.7 ± 2.4 EX

Table 3.5 – Local fault slip rate values to each end of the major active faults in Central-Eastern Iran. Slip rates are given in fault-parallel and fault-perpendicular directions. Block model calculations with locked and free faults are discriminated. RL: right-lateral; LL: left-lateral; EX: extension; SH: shortening.

Fault		locked		free	
	azimuth	parallel [mm/yr]	perp. [mm/yr]	parallel [mm/yr]	perp. [mm/yr]
DehshirN	N102	1.0 ± 1.8 RL	1.1 ± 1.3 SH	0.9 ± 1.8 RL	0.8 ± 1.2 SH
Dehshir S	N133	2.1 ± 0.9 RL	-1.2 ± 1.2 EX	1.8 ± 0.8 RL	-1.2 ± 1.2 EX
Anar N	N015	2.2 ± 1.7 RL	1.3 ± 1.5 SH	2.0 ± 1.8 RL	-0.2 ± 1.4 EX
Anar S	N140	0.6 ± 1.3 RL	0.1 ± 1.7 SH	1.5 ± 1.1 RL	0.6 ± 1.6 SH
KBF N	N121	4.6 ± 1.2 RL	1.8 ± 1.3 SH	2.7 ± 1.0 RL	1.9 ± 1.3 SH
KBF S	N151	5.1 ± 1.1 RL	0.7 ± 1.3 SH	3.3 ± 0.8 RL	0.9 ± 1.2 SH
West Lut N	N356	4.4 ± 0.4 RL	1.4 ± 0.9 SH	4.2 ± 0.4 RL	1.1 ± 0.9 SH
West Lut S	N359	4.4 ± 0.4 RL	0.4 ± 0.4 SH	4.2 ± 0.4 RL	0.3 ± 0.4 SH
East Lut N	N014	5.8 ± 0.7 RL	-0.9 ± 0.9 EX	5.2 ± 0.6 RL	-0.9 ± 0.8 EX
East Lut S	N193	5.6 ± 0.6 RL	-2.2 ± 1.1 EX	4.9 ± 0.6 RL	-2.6 ± 1.1 EX
Doruneh W	N061	-2.6 ± 0.5 LL	1.9 ± 0.6 SH	-2.3 ± 0.5 LL	1.9 ± 0.6 SH
Doruneh E	N109	-0.8 ± 0.6 LL	2.7 ± 0.6 SH	-0.7 ± 0.6 LL	2.3 ± 0.6 SH

pole positions. Intrinsically, since they are derived from block rotations, the modeled fault slip rates are slightly variable along strike. We thus chose to characterize them by their value at the center of the faults (Table 3.4, and to depict their variability by the rates at the fault tips (Table 3.5). Finally, we estimated the block 'rigidity' by quantifying the fit between the observed and the predicted velocities (residuals in Table 3.2).

As said above, the existence of many secondary faults in Central-Eastern Iran makes the actual strain and slip accommodation more complex than described with a global block model. Therefore, to examine the role of the secondary faults in the overall strain accommodation, we followed a second, complementary modeling approach of the GPS data. This second approach focuses on the fault slip rate evaluation only. It allows measuring the slip rate on any individual fault by calculating the difference in the average site velocities on either sides of the fault trace. Uncertainties on those slip rates are the sum of the dispersions between the site velocities, with the dispersion being calculated as the root mean square of the differences of individual site velocities with respect to the average velocity. Where only a single GPS station is available and prevents calculating any dispersion, we use its formal velocity uncertainty. Though both modelling procedures provide slip rates on the major faults, only the second approach provides slip rates on (some of) the secondary faults.

3.2.6 Present-day rigid block kinematics in Central-Eastern Iran

The major faults described in section 2 divide Central-Eastern Iran into eight principal units, as shown in Figure 3.6: The Helmand block to the east (HB), bounded by the East Lut fault to the west and the southernmost faults forming the SE end of the Doruneh system in the north; the Lut block (LB) in between the East and West Lut faults; the Nayband block (NB) bounded by the West Lut fault (Nayband section) in the east and the Kuhbanan fault in the west; the Kuhbanan-Anar block (KAB) in between the Kuhbanan and Anar faults; the Anar-Dehshir block (ADB) enclosed between the Anar and Dehshir faults; the 'Central Iranian block' (CIB; name from Vernant et al., [2004b]) enclosed between the Dehshir and the Main Recent faults; the North Doruneh region (NDR) extending between the Doruneh fault in the south, the Kopeh Dagh in the NE and the Caspian fault system in the NW, and the South Doruneh region (SDR) extending between the Doruneh fault and the northern tips of CIB, ADB, KAB, NB and LB. Note that the northern ends of the HB, LB, NB, KAB and ADB units are not exactly defined, as they do not coincide with any clear fault or are the sites of multiple faults. We have thus drawn arbitrary limits made to be in best agreement with the actual faults and to most properly enclose the GPS data (Fig. 3.6).

We characterize the motions of the 8 units defined above, with respect to fixed Eurasia, by both the model velocity (Fig. 3.6) and the horizontal rotation (Fig. 3.7) obtained at the centre of each unit (Tables 3.2 and 3.3). Also we present the residual between the ovserved GPS velocity and modeled velocity in figure 3.8. The block velocities are defined by the Euler pole positions, the corresponding rotation rates, and the uncertainties on those parameters (Table 3.2). Bold numbers in Figure 3.6 show the block velocities calculated with respect to the AR-EUR convergent motion vector at the mean longitude of Eastern Iran (∼N13°E direction at Hormuz, e.g., Masson et al. [2007]) (Table 3.3), that is in both the N13°E (Fig. 3.6a) and in the perpendicular N103°E directions (Fig. 3.6b) (later referred to as NNE and WNW directions, respectively). In Supporting Information 8.1.6 we quantify the block velocities in the classical NS/EW reference frame.

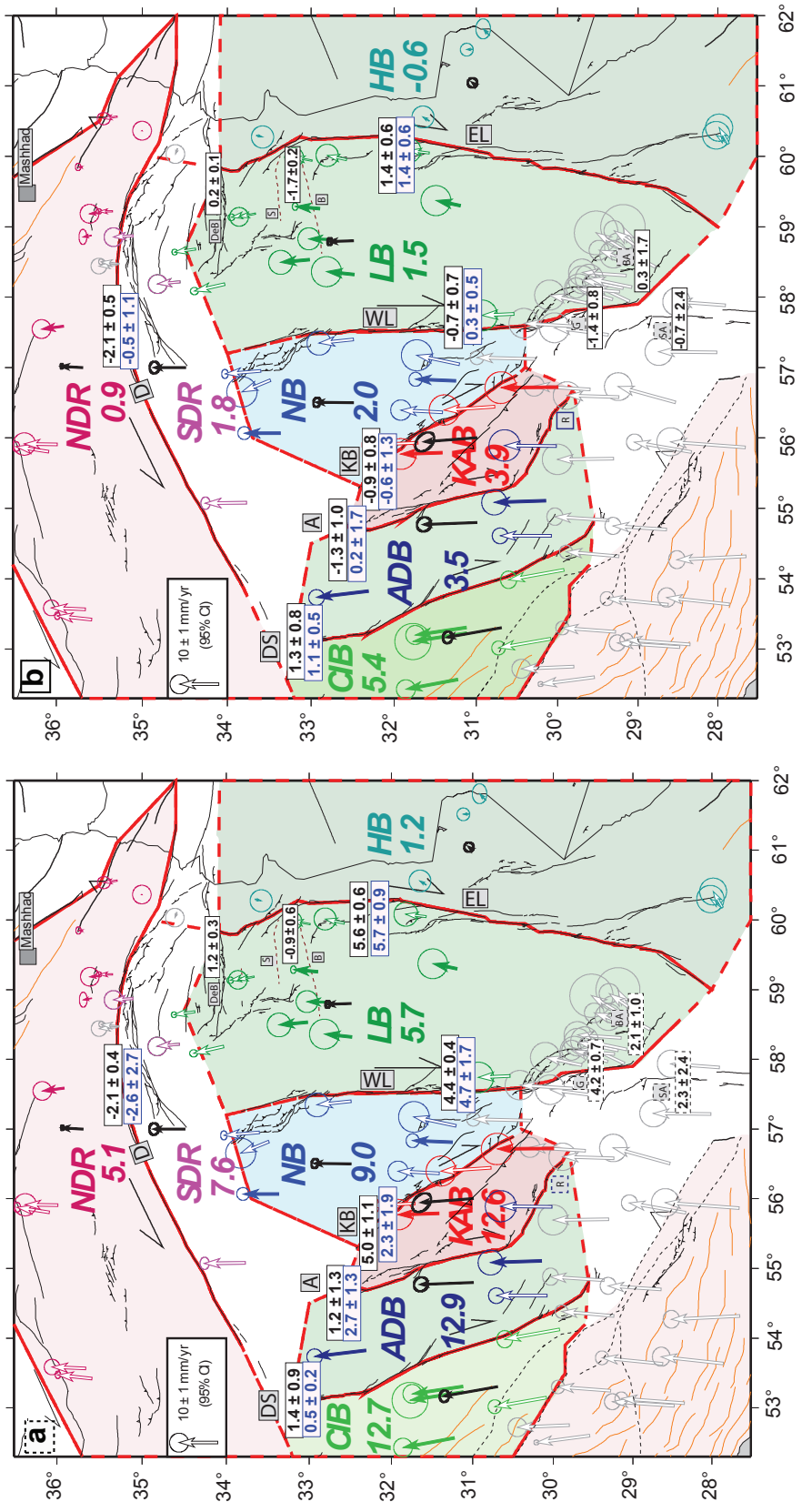

Figure 3.6 – GPS velocity field with respect to Eurasia. The vector error ellipses represent a confidence interval of 95 %. Filled vectors indicate class 1 stations, open vectors class 2 stations (see Table 3.1). Red lines depict the rigid block contours used in the block model with continuous lines where block contours coincide with actual active faults and dashed lines for schematic limits needed to close the block contours. For each block the central velocity obtained from the model is represented by a black vector (Table 3.3). Block model is used with locked faults. Bold colored numbers indicate the block velocity component in N13°E direction (NNE, Fig. 3.3-a) and in N77°W direction (WNW). On right figure (a) with the NNE block velocities, fault parallel slip is indicated for NS faults (positive values are right lateral), and fault perpendicular slip is indicated for EW faults (positive values are extension) (Table 3.4). Black numbers indicate block model predictions; blue numbers are fault slip rates calculated from 'average velocity method'. On left figure (b), with the WNW block velocities, fault perpendicular slip is indicated for NS faults, fault parallel slip for EW faults. Fault velocities from average velocity method are based on class1 stations only, when available (Table 3.4). Fault names as in Fig. 3.4 and 3.5. Major blocks bounded by the faults: CIB: Central Iranian Block; ADB: Anar-Dehshir block; KAB: Kuhbanan-Anar block; NB: Nayband-Kuhbanan block; LB: Lut block; HB: Helmand block; NDR: North Doruneh region; SDR: South Doruneh Region.

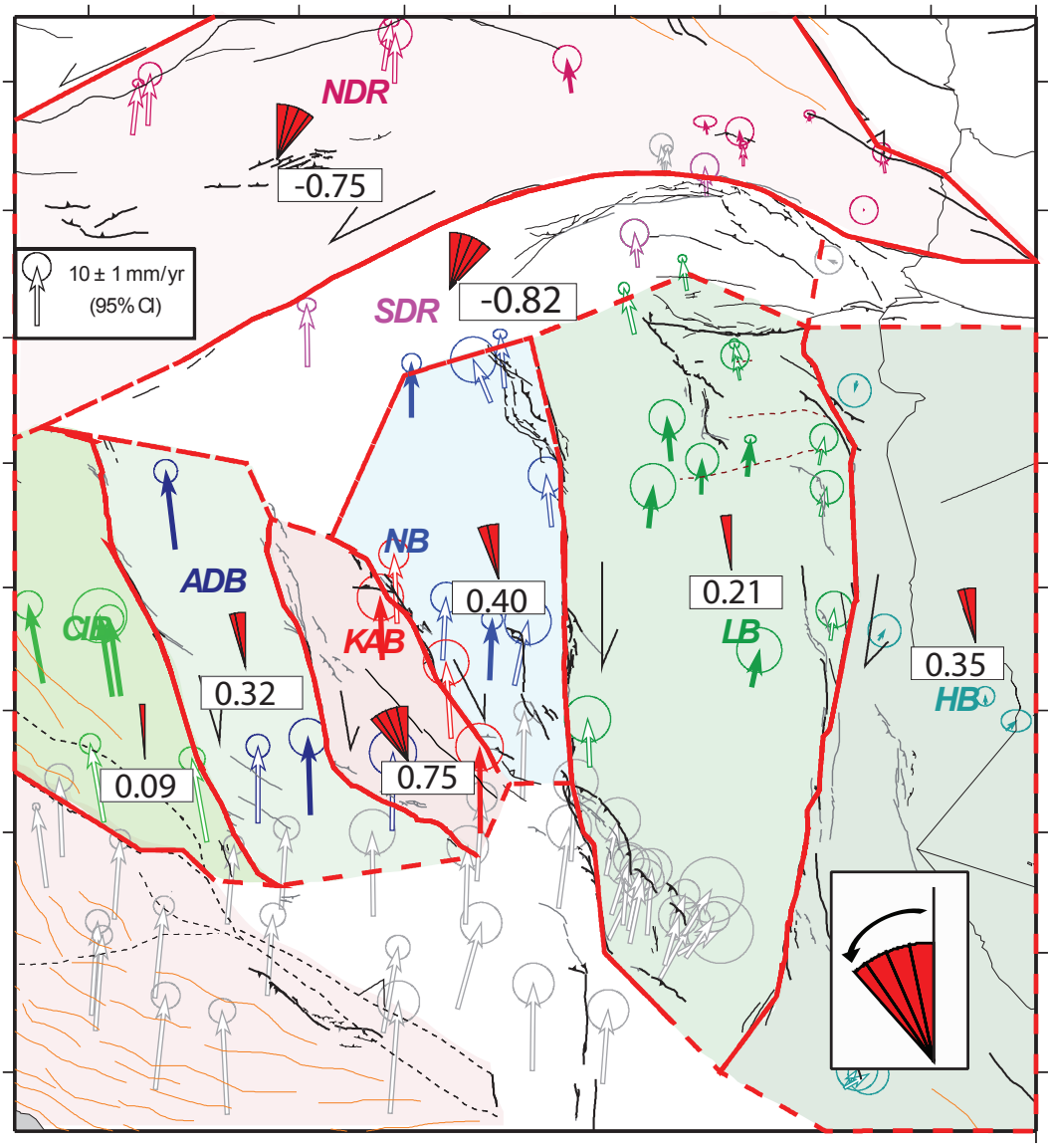

Figure 3.7 – GPS block rotation rates in °/Ma measured in the center of each block (from block model with locked faults) (Table 3.2). Counterclockwise rotation sense is positive. Faults and blocks as before.

The block motion 'residuals' are reported in Table 3.2. Residuals are taken here as the differences between observed and modelled values. Those differences mainly result from the unknown actual locking depth and degree of coupling of the major faults, and from the deviation from the strictly rigid block hypothesis. The two westernmost blocks, CIB and ADB, have small residuals, 0.4 and 0.5 mm/yr respectively, indicating that the rigid hypothesis is rather correct for these blocks. On the contrary, both NDR and SDR units have large residuals, 1.2 and 1.3 mm/yr, respectively, as expected from their dense secondary faulting that makes these regions far from being rigid [Farbod et al., 2011]. Evaluating the degree of rigidity of the other blocks (KAB, NB, LB and HB) is more difficult as the block motions are inferred from many stations close to the faults where

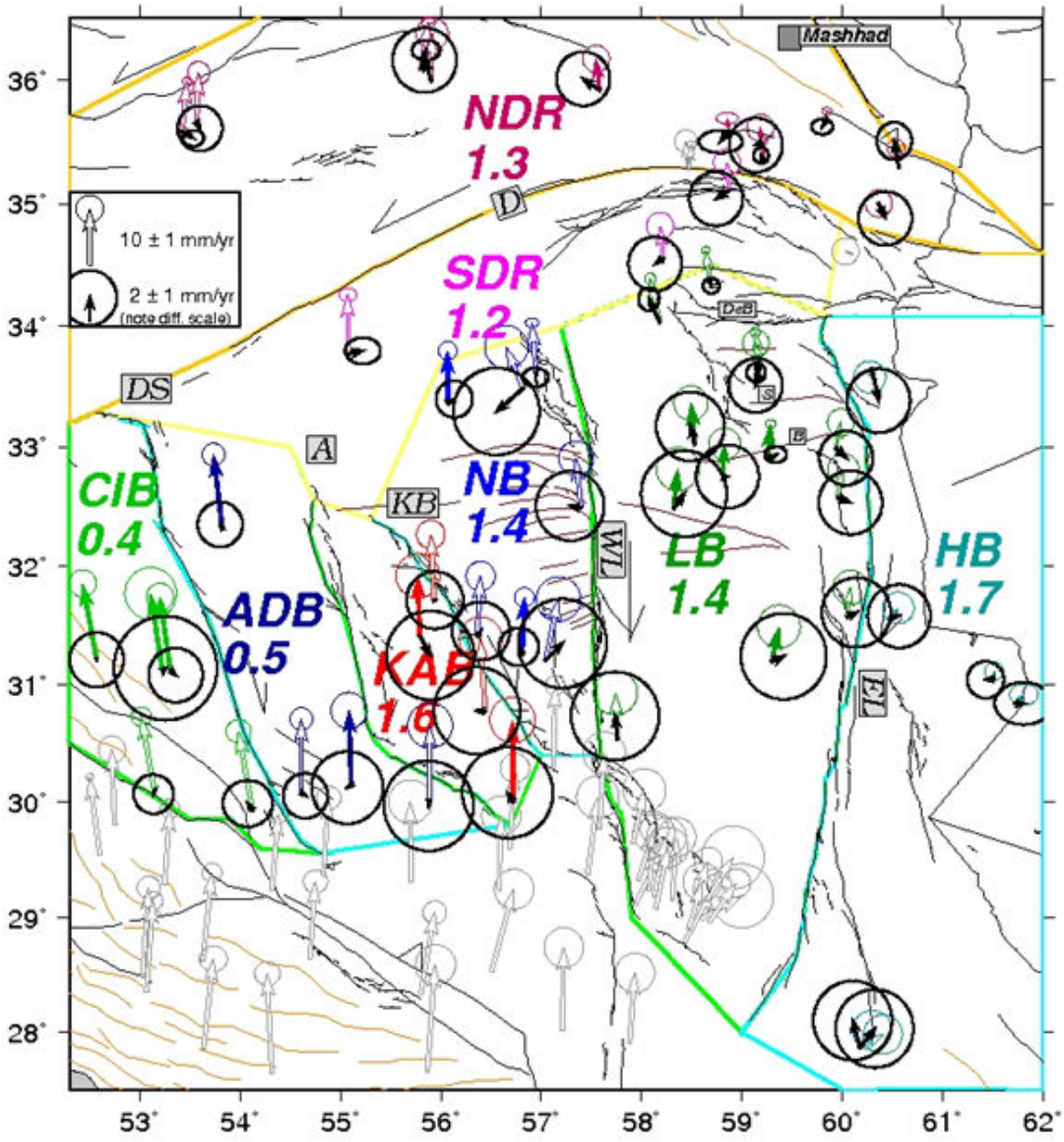

Figure 3.8 – GPS block rotation rates in °/Ma measured in the center of each block (from block model with locked faults) (Table 3.2). Counterclockwise rotation sense is positive. Faults and blocks as before.

uncertainties on depth and degree of locking likely contribute to large residuals. We suggest that KAB, NB, and LB blocks might be less rigid than CIB and ADB, due to the more numerous secondary faults that cut them (Fig. 3.4). Furthermore, 4 over 11 stations that were used to model the Lut Block are located north of the Birjand fault, in an area showing dense secondary faulting. Finally, only 4 stations are used to model the KAB block, two of them are clearly affected by elastic contribution. Altogether these facts may partly account for the quite large residuals for these blocks.

In all cases, the residuals are lower however than the slip rates of the major bounding faults (see next section and Figure 3.6). The GPS data thus confirm that each fault-bounded tectonic unit behaves in a fairly rigid fashion, and hence as a block. All blocks

move both toward the north and toward the west (with the exception of HB). The NNE rates are fast with respect to Eurasia, ranging from ∼ 1 to 13 mm/yr (Fig. 3.6a). The WNW rates are slower, in the range ∼ 1-5 mm/yr (Fig. 3.6b). Taken together, our measurements reveal an overall increase in the NNE velocity from the HB in the east to the CIB in the west, together with a slight increase in the WNW motion. The increase in the NNE velocity occurs in a step fashion across the EL, WL, and KB faults, while the NNE velocity is roughly the same for the KAB, ADB and CIB blocks (12.5-13 mm/yr). The variation in the WNW velocity shows a similar evolution, but step increases rather occur across the EL, KB and DS faults. The rotations of the blocks about a vertical axis are calculated at their centre and reported in Tables 2 and 6 and in Figure 3.7. All N-S blocks are found to rotate counterclockwise at rates ranging from 0.1 to 0.8 °/Ma. The lowest counterclockwise rotation rate is found for CIB, as a result of the sub-parallel GPS velocities on this block. The NDR and SDR regions sustain clockwise rotations at rates of 0.7-0.8 °/Ma. Those rotations are controlled by the progressive increase in GPS velocities from east to west over the large E-W extent of the NDR and SDR regions. As those two regions do not represent rigid tectonic units [Farbod et al., 2011] (Fig.3.4), the clockwise rotation rates calculated from the block model should be interpreted with care. The evaluation of the rotation rates using a block model with freely slipping boundary faults results in similar values (Table 3.2), suggesting that the block rotation rates are fairly robust.

3.2.7 Current slip rates on Central-Eastern Iranian faults

a) Slip rate calculations

For the reasons explained before, we estimate the fault slip rates using two approaches, 1) the block model, in which the slip rates are deduced from the comparison of the rigid motions of the blocks on either sides of the major fault traces; and 2) the calculation of the differences between average GPS velocities on either sides of the fault traces (later referred to as the 'average velocity method'). While the block model permits to establish a coherent fault slip rate distribution over the entire network, it estimates slip rates on the major faults only. Meanwhile, although the average velocity method enables to estimate the slip rates on some of the secondary faults, it neglects the motions caused by the rigid block rotations. The two approaches are therefore complementary and their comparison is an opportunity to quantify the uncertainties on the fault slip rates.

Here we use Defnode to test two extreme hypotheses, one–more realistic, with 100% of fault locking, and one –unlikely, with freely slipping faults. The differences between the two extreme solutions provide a model internal upper bound for uncertainties on the fault slip rates. The rates evaluated at the centre of the faults and their uncertainties are reported in Table 3.4 and shown in Figure 3.6, while the rates estimated more locally along the faults are listed in Table 3.5 and shown in Supporting Information 8.1.7. The largest

differences between the two extreme solutions, and hence the largest uncertainties, are found for the slip rates of the KB (1.9 mm/yr on the right-lateral component, exceeding the formal error limit) and the Anar faults (0.8 mm/yr of across strike shortening, but within the formal error limits) that both bound the KAB block. Those large uncertainties on both fault slip rates likely result from the imperfect description of the KAB motion by the rigid block model (2 out of the 4 stations are within a deformation zone close to the fault and the block is cut by a secondary fault, the Jorjafk fault). The formal uncertainties on the other fault slip rates, generally of 0.5 mm/yr, are larger than the differences between the two extreme solutions and therefore likely realistic. The solution with locked faults (more realistic fault description) is the one we retain as providing the more robust fault slip rates and uncertainties (we consider the formal uncertainties, except for KB where a large 1.9 mm/yr uncertainty is retained), in the rigid block model.

The second approach to quantify fault slip rates is based on the elastic deformation model of Savage and Burford [1973], where the deformation field across a locked fault recovers the total fault slip rate at distances about twice the locking depth. With this assumption, the GPS sites located at a distance greater than twice the fault locking depth from a main fault trace –30 km here–and not obviously affected by other adjacent faults, can be used to derive a slip rate on that fault. These most appropriate sites (referred to as Class 1) are highlighted in bold in Table 3.1. Many additional stations exist, which are either closer to a main fault trace, or in between secondary adjacent faults, and hence are possibly slightly perturbed by these faults (referred to as class 2). Together these make us perform two calculations (Table 3.4). In a first step, wherever possible, we derive a slip rate on each fault from using only the Class 1 GPS data. This slip rate is thus derived from fewer but rigorously selected sites. In a second step, we combine both the Class 1 and Class 2 data to derive a slip rate on each fault that is constrained by a larger number of stations, yet some of them might show some perturbations. Comparison of fault slip rates based on Class 1 stations only and on Class 1 and 2 stations together shows that, in most cases, the slip rates estimated by including the Class 2 stations are lower than the slip rates based on the Class 1 stations only. This is in keeping with the Class 2 stations being generally close to the fault trace, and hence being in the zone expected to sustain elastic strain. This result confirms that our classification of the sites is appropriate, and that the slip rates estimated from the Class 1 stations are the best constrained, and hence those to be retained when they exist.

For the six major faults (Dehshir, Anar, KB, WL, EL and Doruneh) we can compare the slip rates obtained with the two approaches (Table 3.4). Generally, the actual sense of fault slip is appropriately recovered with the two techniques. The slip rates are similar for the WL, EL and Dehshir faults (within $\pm$ 1.0 mm/yr for both fault parallel and fault perpendicular components). We showed before that the KAB unit is poorly represented with a rigid block. This likely explains why the two methods provide significantly different

slip rates on its two bounding, Anar and KB faults; while the block model attributes a high right lateral slip rate on KB (5.0 ± 1.9 mm/yr) and a weak slip rate on Anar (1.2 ±1.3 mm/yr), the other method yields more balanced values with 2.3 ± 1.9 mm/yr and 2.7 ± 1.3 mm/yr of right-lateral slip on KB and Anar, respectively. Furthermore, while the block model predicts shortening across the Anar fault (at 1.3 ± 1.0 mm/yr), the second approach does not suggest any significant across-fault deformation (-0.2 ± 1.7 mm/yr). More GPS data in the central part of the KAB unit are clearly necessary to determine which slip rates are more realistic on the KB and Anar faults. The Doruneh fault also shows fairly different slip rates depending on the approach. While both approaches conclude to a similar across strike shortening of 2.1-2.6 mm/yr, the block model predicts a higher left-lateral slip rate (-2.1 mm/yr) than the velocity averaging method (-0.5 mm/yr). None of the two approaches seems to be satisfying; the NDR and SDR regions are clearly densely offset by secondary faults and hence cannot be appropriately described as rigid units; due to the great length of the fault, the velocity averaging approach neglects a significant component of rotation in the estimation of the fault parallel slip rate. Our data thus only reveal that the Doruneh fault is sustaining about 2 mm/yr of across strike shortening. Its left-lateral strike slip rate is weakly constrained in the range 0.5-2.1 mm/yr.

Both approaches lead to similar results but on the few exceptions that we discussed above. For those fault exceptions, we retain that their slip rate is in the range of the values provided by both methods. For all the other faults, we retain the slip rates estimated from the block model (i.e., for major faults), to which we add the secondary fault slip rates estimated from the velocity averaging method.

b) Current fault slip rates

East Lut fault system

This is the first time that the East Lut fault slip rate can be estimated in isolation with that on the West Lut fault. The differential motion of the HB and LB blocks results in a right-lateral slip operating at 5.6 ± 0.6 mm/yr along the East Lut ∼ N12°E mean strike. An additional, fault-perpendicular component of extension is revealed, operating at a rate of 1.4 ± 0.6 mm/yr. The right-lateral slip rate is roughly constant along the fault, ranging from 5.6 ± 0.6 mm/yr in its southern part to 5.8 ± 0.7 mm/yr in the north.

West Lut fault system

The LB and NB differential motion induces a roughly constant 4.4 ± 0.4 mm/yr right-lateral slip on the West Lut fault. An across-strike shortening component also exists that averages 0.7 ± 0.7 mm/yr and increases from 0.4 ± 0.4 mm/yr in the north to 1.4 ± 0.9 mm/yr in the south.

Kuhbanan fault

The differential motion of the NB and KAB yields a right-lateral strike-slip rate of 5.0 ± 1.9 mm/yr on the N140°E mean strike of the KB fault, and an across-strike shortening of

0.9 ± 0.8 mm/yr. Yet, as seen before, the lateral slip rate might rather be in the range 2.3-5.0 mm/yr and hence be on the order of 3.6 ± 1.3 mm/yr. The lateral slip rate seems to vary along-strike, increasing from NW to SE.

Anar fault

The Anar fault slip rate is evaluated from the KAB and the ADB motions. We estimate 1.2 ± 1.3 mm/yr of right-lateral slip on the fault and 1.3 ± 1.0 mm/yr of shortening across its strike. Yet, as seen before, the lateral slip rate might rather be in the range 1.2-2.7 mm/yr (hence 2.0 ± 0.7 mm/yr), while the across-strike motion might not be well constrained. In the block model solution, both lateral and across-strike slip rates increase from south to north.

Dehshir fault

The ADB and CIB relative motion constrain 1.4 ± 0.9 mm/yr of right-lateral slip on the Dehshir fault and 1.3 ± 0.8 mm/yr of fault perpendicular extension. Though these low velocities are at the limit of resolution of the available GPS measurements, they are the first current slip rates determined on the Dehshir fault. Both the right-lateral and extensional slip rates seem to increase from NW to SE.

Doruneh fault

The GPS stations in the SDR and the NDR regions are both sparse (only 3 stations on SDR) and unevenly distributed, with most of them located in the east. Furthermore, the Doruneh fault strike markedly varies along its length, bending from ∼ E-W in its eastern part to ∼ N60°E in its western half. Together these make that, as said before, the lateral slip rate on the Doruneh fault is not well constrained. We find it to be in the range 0.5-2.1 mm/yr on the average N077°E strike of the fault (Fig. 3.6b). It might additionally vary along the fault from 2.6 ± 0.5 mm/yr in the west to 0.8 ± 0.6 mm/yr in the east. The relative NDR and SDR motion more robustly constrains a fault perpendicular shortening of 2.1 ± 0.4 mm/yr (Fig. 3.6a). The across-strike compressive component slightly increases towards the east.

Dasht-e-Bayaz fault

Four stations are used to evaluate the Dasht-e-Bayaz fault slip rate to a NS extension of 1.2 ± 0.3 mm/yr combined with an EW lateral slip of 0.2 ± 0.1 mm/yr, yet being dextral while the fault is unambiguously left-lateral (two Mw ∼ 7 events in 1968 and 1979 on the fault)

Sedeh and Birjand faults

It is noteworthy that the GPS data constrain some current slip in a region where there exists only two small EW-trending faults due south of Dasht-e-Bayaz, the Sedeh and Birjand faults, whose morphological signature does not reveal any clear recent activity (Fig. 3.4). According to the GPS data, those faults are candidates to accommodate together a significant left-lateral motion, at a rate of 1.7 ± 0.2 mm/yr, associated with a northward compression operating at 0.9 ± 0.6 mm/yr. Further work is deserved to validate their

seismogenic activity, and to determine whether the current motions that we observe along those secondary faults characterize their interseismic behavior or reflect large wavelength and long lasting postseismic deformations induced by nearby historical earthquakes as those that occurred in the Dasht-e-Bayaz area.

Gowk, Bam and Sabzevaran

The available GPS stations allow isolating the right lateral slip rate on the Gowk fault, 4.2 ± 0.7 mm/yr, from that on the Bam fault, 2.1 ± 1.0 mm/yr. Note that these rates are estimated from the GPS stations that were not affected by the 2003 Bam earthquake, and hence are likely robust, though we cannot preclude that post-seismic deformation might affect them. Further south, the West Lut fault system continues into the Sabzevaran fault, whose right-lateral slip rate is estimated at 2.3 ± 2.4 mm/yr.

3.2.8 Interpretation and Discussion

a) Accommodation of current strain in Central-Eastern Iran

For the first time, the GPS data demonstrate that the 6 major faults that dissect Central-Eastern Iran, East Lut, West Lut, Kuhbanan, Anar, Dehshir and Doruneh, are all currently active, as attested by their morphological traces . We provide the first estimates of the present-day slip rates on these faults (Fig. 3.6). The three easternmost faults, EL, WL and likely KB, have the fastest along-strike slip rates in the range 4-6 mm/yr, whereas all the other faults have lower slip rates in the range 1-3 mm/yr (Table 3.4). Our slip measurements furthermore confirm that the 5 major northerly-striking faults that dissect Central-Eastern Iran are dominantly right-lateral, while the Doruneh fault is left-lateral, slipping at 0.5-2.5 mm/yr.

Though the Central-Eastern Iranian faults are dominantly strike-slip, they also show an additional component of across-strike motion. This motion is extensional on the two outermost faults, DS and EL, and compressional on all the other faults, including Doruneh. In all cases, the across-strike motion operates at a rate of $\sim$ 0.5-2 mm/yr (Table 3.2).

The tectonic units bounded by the major $\sim$ NS faults behave as more or less rigid blocks, that are all found to rotate counterclockwise about a vertical axis, at rates ranging from 0.1 to 0.8°/Ma and averaging 0.4 ± 0.25°/Ma (Table 3.5). By contrast, the SDR and NDR regions sustain clockwise rotations at a rate of $\sim$ 0.8°/Ma (Fig. 3.7). This clockwise rotation is not strongly constrained however since neither the NDR nor SDR region is a rigid block over its overall, large E-W extent.

All tectonic units and blocks move toward the N13°E direction at fast rates with respect to Eurasia, ranging between $\sim$ 1 and 13 mm/yr (Fig. 3.6a). Although the overall NNE motion decreases northwards across the major faults –as those accommodate part of it– it remains elevated north of the northerly-striking fault set, on the order of 8 mm/yr due south of Doruneh, and 5 mm/yr north of it. The total NNE shear between Central

Iran (represented by the westernmost CIB block) and Eurasia (represented by the HB block) is 11-12 mm/yr. Though large, this value is smaller than previous suggestions (16 mm/yr) [Vernant et al., 2004a]. The NNE shear is absorbed successively by the major N-S faults, each of the East Lut, West Lut and Kuhbanan faults accommodating about 25-40 % of that shear. In addition to their overall NNE motion, all northerly-trending blocks move towards the WNW with respect to Eurasia, at significant rates varying from $\sim$ 1 to 5.5 mm/yr from east to west (Fig. 3.6b).

b) Short-term versus long-term fault slip rates in Central-Eastern Iran

We synthesize the information available in the literature on the long-term history of the major active faults in Central-Eastern Iran, including their initiation age, maximum cumulative slip, and Holocene slips rates. Those parameters are compiled in Table 3.5 where the long-term slip rates can be compared to our current slip rate estimates.

The Dehshir fault is taken to have slipped laterally by up to 80 km over the last 20 Ma [Walker and Jackson, 2004, Meyer et al., 2006, Nazari et al., 2009] and more likely 12 Ma [Şengör and Kidd, 1979, Şengör, 1990, Allen et al., 2004]. A minimum Late Quaternary slip rate of 0.8-2.5 mm/yr is estimated at one central site of the fault from the measurement and dating of offset stream channels [Nazari et al., 2009]. If the incision has occurred in the Holocene optimum (8 $\pm$ 2 kyrs) as suggested elsewhere in Central-Eastern Iran [Le Dortz et al., 2009], the Holocene slip rate on the Dehshir fault would rather range between 2.5 and 4.2 mm/yr. Recent slip and age measurements at two nearby sites of the fault rather suggest a Late Quaternary slip rate of 1.2 $\pm$ 0.3 mm/yr [Le Dortz et al., 2011]. Therefore, according to available data, the Dehshir fault might have slipped at 0.8-4.2 mm/yr, and hence at 2.5 $\pm$ 1.7 mm/yr over the Late Quaternary. The current right-lateral slip rate that we estimate averages 1.4 $\pm$ 0.9 mm/yr, and hence is in the range of the geological estimates.

The Anar fault would have slipped laterally by a minimum of 30 km over the last 20 and more likely 12 Ma [Walker and Jackson, 2004, Meyer and Le Dortz, 2007]. From the measurement and dating of offset stream risers, a minimum Holocene slip rate of 0.8 mm/yr is inferred at one central site of the fault [Le Dortz et al., 2009]. The long-term and Holocene slip rates on the Anar fault might thus range between 0.8 and 1.5 mm/yr [Fattahi et al., 2011]. The current right-lateral slip rate is evaluated to 1.2-2.7 mm/yr, thus in a similar range.

The Kuhbanan fault is taken to have slipped laterally by a minimum of 20 km over a period of time that is unknown but likely similar to the other faults [Allen et al., 2011] (the offset has been measured on the Dehu fault which is part of the Anar fault zone). From a few cumulative slip measurements with supposed ages, a poorly constrained Holocene slip rate is suggested around 1.5 mm/yr [Berberian et al., 1979, Talebian et al., 2006, Allen et al., 2011]. The GPS measurements suggest that the fault has a significant current

right-lateral slip rate in the range 2.3-5.0 mm/yr, and is therefore presently active and possibly slipping faster than over the Holocene and geological times.

The West Lut fault is taken to have slipped laterally by a minimum of 15 km (measured on its southern Gowk segment) [Walker and Jackson, 2002]. Its initiation age is unclear. From the measurement of morphological offsets whose ages were assumed to be 5-8 Ma, a long-term slip rate of 1.5-2.5 mm/yr was estimated [Walker and Jackson, 2002]. More recently, Walker et al. [2010] estimated a minimum Holocene slip rate of 3.8 ± 0.7 mm/yr on the Gowk segment of the WL fault, and a 2.2 Ma slip rate of 1.4 ± 0.5 mm/yr on its Nayband segment. Regard et al. [2005] estimated a Late Quaternary slip rate of 5.7 ± 1.7 mm/yr on the southern Sabzevaran-Jiroft fault. The current slip rate that we find on the WL fault is 4.4 ± 0.4 mm/yr, with local estimates of 4.2 ± 0.7 mm/yr on the Gowk fault segment, 2.1 ± 1.0 mm/yr on the Bam fault segment, and 2.3 ± 2.4 mm/yr on the Sabzevaran fault segment. The current and long-term slip rates of the West Lut fault are thus fairly similar.

The East Lut fault would have accumulated up to 95 km of lateral slip (when considering the overall fault system including the eastern Zahedan fault, Fig. 3.4) since its onset of activity [Walker and Jackson, 2004, Meyer and Le Dortz, 2007], at a time not well established, but likely similar to the age of the other faults, at most 12-20 Ma. Lateral offsets of 40-60 m have been measured in river channels of assumed Holocene age [Meyer and Le Dortz, 2007]. If the channel incision occurred in the Holocene optimum [Le Dortz et al., 2009], the Holocene slip rate on the East Lut fault is 8 ± 4 mm/yr. The current slip rate that we find is 5.6 ± 0.6 mm/yr, and hence is on the same order within uncertainties than the assumed Holocene rate. It is also similar to the current slip rate on the companion West Lut fault.

A minimum Holocene left-lateral slip rate of 2.5 mm/yr is estimated on the western section of the Dasht-e-Bayaz fault from the lateral offset of ancient man-made features [Berberian and Yeats, 1999]. The cumulative lateral offset on the fault is taken to be at most a few km [Walker et al., 2004], while its initiation age is unknown. Our GPS measurements do not resolve any significant current slip rate on the fault (0.2 ± 0.1 mm/yr), which suggests that the current slip rate of the fault might be low. By contrast, the GPS data allowed us to measure a total left-lateral slip rate of 1.7 ± 0.2 mm/yr on two nearby EW faults (Sedeh and Birjand faults, Fig. 3.4 and 3.6), and this cumulated slip rate is on the same order than the Holocene rate estimated on the Dasht-e-Bayaz fault.

The cumulative slip on the Doruneh fault is unknown, as is its initiation age [Farbod et al., 2011]. On the basis of a simple model, Walker et al. [2004] suggest that the Doruneh fault might have slipped by 2.5-10 mm/yr over the long-term. From the measurement and the dating of one offset alluvial terrace at one fault site, a local Holocene slip rate of 2.4 ± 0.3 mm/yr is estimated [Fattahi and Walker, 2007], reaching ∼3.0 mm/yr at a nearby site [R. Walker, pers. comm., 2012]. Our GPS data suggest that the fault has a current

left-lateral slip rate in the range 0.5-2.1 mm/yr on its mean ~ ENE direction, associated to a 2.1 ± 0.4 mm/yr NNW compression. The left-lateral slip rate might be up to 2.6 ± 0.5 mm/yr on the western half of the fault. The current and Holocene Doruneh slip rates are thus in the same range. Our comparative analysis thus shows that the Central-Eastern Iranian faults are currently slipping at fast rates that are fairly similar to those they had in the Holocene and possibly longer time spans.

c) Accommodation of the North-South convergence in Central-Eastern Iran

The GPS data as a test of the possible scenarios

Our data sheds light on the way faults in Central-Eastern Iran accommodate the overall north-south convergence between Arabia and Eurasia. The question is especially posed as most major faults in Central-Eastern Iran strike approximately parallel to the convergence vector, and hence cannot accommodate the convergence in a simple, classical way (i.e., convergence-perpendicular thrusting and folding). This situation motivated many authors to suggest different scenarios of fault and deformation kinematics across Central-Eastern Iran [Jackson and McKenzie, 1984, Walker et al., 2004, Walker and Jackson, 2004, Allen et al., 2006, 2011, Walker and Khatib, 2006, Hollingsworth et al., 2010a]. However, until now, those scenarios were lacking data, especially current motion data, to validate them. As synthesized by Allen et al. [2011] , three principal kinematic roles have been suggested for the Central-Eastern Iranian faults.

Table 3.6 – Bookshelf-faulting model test using the fault characteristics and slip rates determined in sections 2, 4 and 5. Column 1: Block names as in Figure 3.4. Column 2: Names of corresponding bounding faults. Eastern fault in bold, for which all calculations are done. Column 3: Age of initiation of the faults, in Ma, as inferred from literature (see text). Column 4: Length L of the faults, in km. Column 5: Width Wb of the rotating blocks, in km. Column 6: Cumulative lateral slip on eastern bounding fault, in km, as reported in literature. Column 7: Holocene right-lateral slip rate SH on eastern bounding fault, in mm/yr, as reported in literature (average and deviation, as for columns 8, 10 -12, 14 - 16). Column 8: Current GPS right-lateral slip rate Sc on eastern bounding fault, in mm/yr, estimated in the present study. Column 9: Total rotation in ° inferred over the long-term from the bookshelf-faulting model. Column 10: Inferred long-term rotation rates, in °/Ma. Column 11: Holocene rotation rates, in °/Ma, inferred from the bookshelf-faulting model. Column 12: Current rotation rates, in °/Ma, inferred from the bookshelf-faulting model. Column 13: Current rotation rates, in °/Ma, inferred from the rigid block model with locked faults. For uncertainty, see Table 3.2 and text. Column 14: Long-term shear rate Vsh, in mm/yr, inferred from the bookshelf-faulting model. Column 15: Holocene shear rate Vsh, in mm/yr, inferred from the bookshelf-faulting model. Column 16: Current shear rate Vsh, in mm/yr, inferred from the bookshelf-faulting model. Average values are provided for columns 14, 15 and 16, at the bottom of the columns. See text for more details.

Fault Name	Age of eastern fault [Ma]	L [km]	Wb [km]	Cumulative long-term slip S_L [km]	Holocene slip rate S_H/yr [mm/yr]	Current GPS fault slip rate SC/yr [mm/yr]	Total Rotation inferred from long-term SL [°]	Long-term rotation rate inferred from long-term SL [°/Ma]	Holocene rotation rate inferred from Holocene slip rates SH [°/Ma]	Current rotation rate inferred from GPS slip rate SC [°/Ma]	Current rotation rate inferred from rigid block model [°/Ma]	Inferred long-term shear VshL [mm/yr]	Inferred Holocene shear VshH [mm/yr]	Inferred current shear VshC [mm/yr]
MR & **Dehshir**	< 12-20	470	200	80	1.7 ± 0.9	1.4 ± 0.9	22	1.5 ± 0.4	0.7 ± 0.5	0.4 ± 0.3	0.1	6.3 ± 1.6	2.9 ± 2.0	1.6 ± 1.1
Dehshir & **Anar**	< 12-20	380	150	> 30	1.2 ± 0.4	1.3 ± 1.3	> 11.3	> 0.8 ± 0.2	0.5 ± 0.2	0.3 ± 0.3	0.3	> 2.6 ± 0.7	1.5 ± 0.5	1.6 ± 1.6
Anar & **Kuhbanan**		300	150			5.0 ± 1.1				1.9 ± 0.4	0.8			5.0 ± 1.1
Kuhbanan & **West Lut**	< 12-20	700	200	*>> 15*	3.8 ± 0.7	4.4 ± 0.4	*>> 4*	*>> 0.3 ± 0.1*	1.1 ± 0.2	1.3 ± 0.2	0.4	>> 1.8 ± 0.5	6.7 ± 1.3	7.7 ± 0.7
West Lut & **East Lut**	< 12-20	700	300	95	8 ± 4	5.6 ± 0.6	17.6	> 1.2 ± 0.3	1.5 ± 0.8	1.1 ± 0.1	0.2	7.4 ± 1.9	9.4 ± 4.6	6.5 ± 0.8
												Average = 4.5 ± 1.2	Average = 5.1 ± 2.1	Average = 4.5 ± 1.0

The first possible role of the Central-Eastern Iranian faults is to permit the Iranian crust to move northwards with respect to the presumed stable Afghan crust at the eastern boundary of the collision zone [Meyer et al., 2006, Masson et al., 2007]. We show here that such a northwards motion does occur and results from slip on the major $\sim$ NS striking Central-Eastern Iranian faults. The faults cut the Iranian crust into five major crustal slivers, and those crustal blocks are currently moving northwards at 6 to 13 mm/yr while the Afghan crust is stable. Their northward progression is driven by significant synthetic lateral slip on the major faults, especially on the three easternmost faults EL, WL and KB. It is noteworthy that the northward velocity that we measure for the westernmost CIB, ADB and KAB units ($\sim$ 13 mm/yr) is similar to the northward velocity estimated by Regard et al. [2005] for the Hormuz promontory due south of those units. This may suggest, as proposed by Allen et al. [2011] , that the collective behavior of the $\sim$ NS faults contributes to allow the Arabian promontory to impinge northwards into the Eurasian crust.

Another possible role suggested [Allen et al., 2011] for the Central-Eastern Iranian faults, at least for those having an obliquity with the convergence vector, is to accommodate the lateral component of slip, so that the rest of the slip, purely compressional, might be absorbed in NW-trending thrust and fold systems (i.e., slip partitioning). Our data do not allow examining this hypothesis. However we note that our fault mapping, as most available fault maps in Central-Eastern Iran, do not show much parallel NW-trending strike-slip and reverse faults as those that would be expected from this scenario. Rather, most of the NW trending thrust faults and folds that are observed in Central-Eastern Iran have developed at the tips of the major NS faults, in mechanical response to their right-lateral slip.

Finally, a third possible role that has long been suggested for the NS Central-Eastern Iranian faults is to achieve NS shortening by rotating counterclockwise in the horizontal plane [Jackson and McKenzie, 1984, Walker et al., 2004, Walker and Jackson, 2004, Walker and Khatib, 2006, Allen et al., 2011]. The rotation would provide a plane-strain way of taking up across zone shortening by NS reduction of the crustal width and along-strike elongation of the rotating zone. This mechanism requires however that the faults strike with some obliquity to the convergence vector. Our GPS data show for the first time that the crustal slivers which the NS faults bound in Central-Eastern Iran are indeed currently rotating counterclockwise, at significant rates in the range 0.1-0.8°/Ma. We thus may use the GPS data to quantitatively test the rotation scenario. More, by combining the GPS data with the information available on Holocene and longer-term fault movements we may test the scenario over different time scales. We perform those tests below.

Vertical axis block rotations in Central-Eastern Iran

First, it is important to note that the $\sim$ NS faults have strikes that rotate counterclockwise from $\sim$ N10°E in the east (EL) to $\sim$ N160°E in the west (DS fault), so that the faults

resemble a fan anchored due north of the Hormuz promontory. The Lut faults, in best continuity with this promontory, strike almost parallel to the plate convergence vector at that longitude ($\sim$ N13°E, Masson et al., 2007). This suggests that the $\sim$ NS faults of Central-Eastern Iran might have formed originally in a N-NNE direction, then rotated counterclockwise by amounts increasing westward from $\sim$10° in the east to $\sim$ 30° in the west. Recent paleomagnetic data provide support to this suggestion [Mattei et al., 2012]. The development of the faults in the prolongation of the Hormuz promontory might have been induced by the northward impingement of the Hormuz promontory into the Iranian crust –as observed in similar contexts in the world [Tapponnier and Molnar, 1976], and favored by the existence of inherited NS faults and sutures in this area [Walker and Khatib, 2006, Cifelli et al., 2013, Nozaem et al., 2013].

Vertical axis block rotations have been documented in many places in the world, and shown to be an efficient mechanism to accommodate and to transfer strain (Fig. 3.9 modified from Manighetti et al. [2001]) [Freund, 1970, 1974, Macdonald et al., 1984, Ron et al., 1984, 1986, McKenzie and Jackson, 1986, Nur et al., 1986, Mandl, 1987, Kleinrock and Hey, 1989, Tapponnier et al., 1990, Acton et al., 1991, Morgan and Kleinrock, 1991, Wetzel et al., 1993, Martínez et al., 1997, Manighetti et al., 2001]. The mechanism operates in a similar way regardless of the scale [Manighetti et al., 2001]. It implies the rotation about a vertical axis of a limited number of rigid blocks bounded by sub-parallel synthetic strike-slip faults. Generally, the block rotation is driven by oblique stress acting on the edges or on the tips of the rotating blocks [Freund, 1970, 1974, Ron et al., 1984, 1986, McKenzie and Jackson, 1986, Nur et al., 1986].

Below we use the available data to examine whether they agree with the vertical axis block rotation scenario. All these data are gathered in Table 3.6. They include the geometrical characteristics of the Central-Eastern Iranian blocks and faults that we estimated from our tectonic maps (fault lengths, block widths; Fig. 3.3 and 3.4), the times of fault initiation inferred from literature, the cumulative maximum slips known on the faults, the Late Quaternary –generally Holocene, slip rates available in the literature, and the current fault slip rates and block rotation rates that we estimated from the GPS data. If the blocks and faults have rotated counterclockwise by an angle γ, the right-lateral slip (S) resulting on each bounding fault depends on the width of the rotating block (Wb), such as $S = Wb \times tan(\gamma)$. We can thus use S to infer γ. Using the available data to perform the above calculations, we estimate that the CIB, ADB, KAB and LB blocks have rotated counterclockwise by about 22, $>$ 11, $>$ 8 and 18° since 12-20 Ma (Table 3.6). NB is indicated in Table 3.5 for completeness but lacking constraints. These rotation amounts are in fair agreement with those previously inferred from the fault strikes, as from paleomagnetic data [Mattei et al., 2012]. The rotations occurred at moderate rates, on the order of 0.6 - 1.5 °/Ma and averaging 1.0 $\pm$ 0.4 °/Ma (Table 3.5). The Holocene and current fault slip rates can also be used to estimate the Holocene and current rotation rates. Those

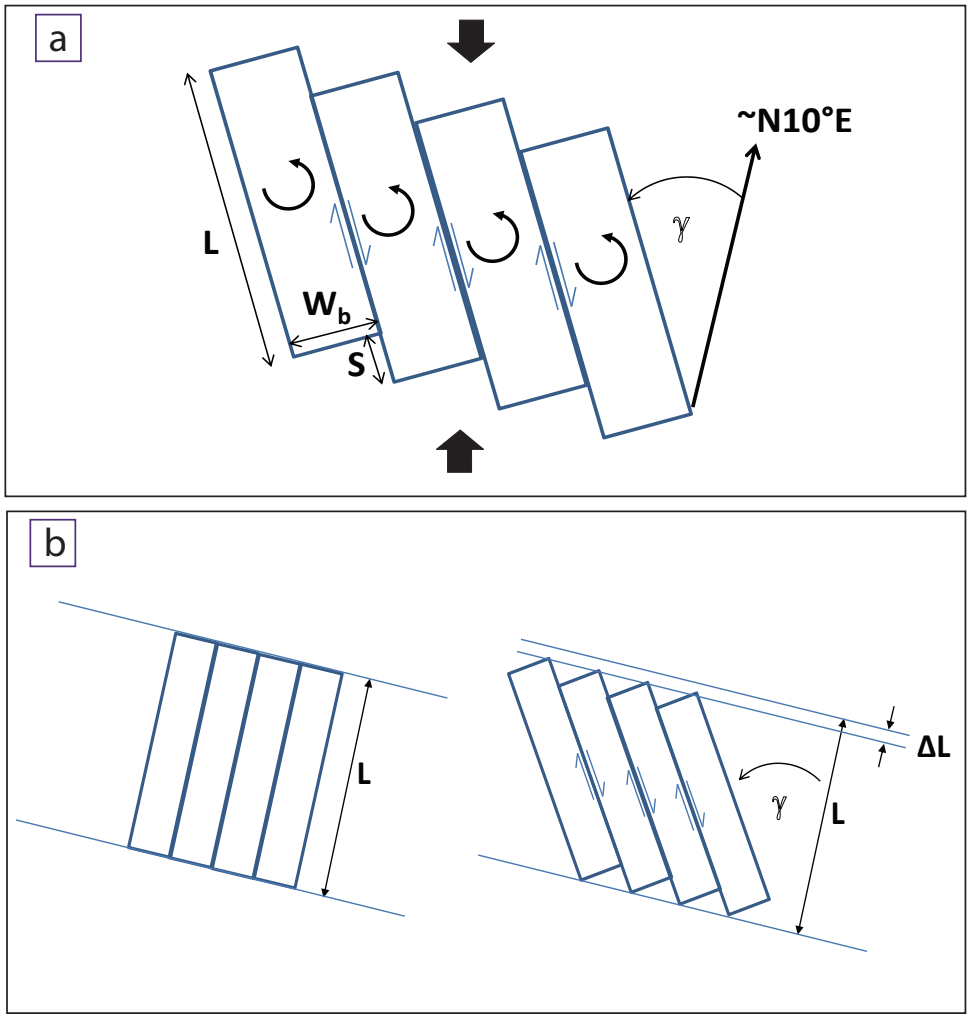

Figure 3.9 – (a) Schematic representation of the vertical axis block rotation model under NS compression. The blocks have a length L and a width Wb. The rotation implies right-lateral slip (by a total amount S) on the faults bounding the blocks. (b) As blocks and faults are rotated, a width decrease (ΔL) in the total width of the rotating zone is induced (modified from [Manighetti et al., 2001]). This decrease may contribute to the progressive southward displacement of the fault traces north of the rotating zone, especially the Doruneh fault trace.

are found to be of the same order as the long-term rotation rates, with similar values of 0.3 – 1.5°/Ma (Holocene) and 0.4 – 1.4 °/Ma (current) over the five blocks (Table 3.5). The average rotation rates are actually the same over the three periods of time, 1.0 ± 0.4 °/Ma, Table 3.5). The rotation rates inferred from the block rotation model, including the current rates, are similar within uncertainties to those that we measured in the GPS data (0.4 ± 0.25 °/Ma). This suggests that the vertical axis block rotation scenario satisfactorily describes the kinematics of the ∼ NS Central-Eastern Iranian faults.

The next question is to understand why the ∼ NS faults and blocks have been led to rotate in the horizontal plane. Over 'recent times' (i.e., likely few last Ma up to present), the obliquity of most of the (already rotated) ∼ NS faults with respect to the convergence vector easily accounts for the origin of the lateral shear that drives the rotations (Fig. 3.9).

In contrast, if the faults formed initially with a strike primarily parallel to the convergence vector, they were not sustaining any lateral stress and hence had no reason originally to start rotating. The block rotation model allows calculating the block-perpendicular, lateral shear (V_{sh}) that might be needed to make the blocks to rotate ($\gamma = arctan(2V_{sh} \times T/L)$, with γ the total rotation, L the length of the rotating blocks, and T the duration of the rotation) [Tapponnier et al., 1990, Manighetti et al., 2001]. The shear V_sh can thus be expressed as $V_{sh} = (S \times L)/2(T \times Wb)$. The long-term, Holocene and current fault slips and slip rates (Table 3.5) can be used to estimate V_sh (considered here on each side of the rotating zone). We find that V_sh is in a similar range in the three periods of time, 3-7 mm/yr. At the time the $\sim$ NS faults were formed, the two parallel, overlapping, NW-trending Kopeh Dagh and Main Recent faults were slipping right-laterally at 7-16 mm/yr [Lyberis and Manby, 1999, Allen et al., 2004, Shabanian et al., 2009b] and 10-15 mm/yr (at least west of $\sim$ 52°E) [Talebian and Jackson, 2002, Bachmanov et al., 2004], respectively. We hypothesize that the coeval right-lateral motions on those two overlapping faults might have induced $\sim$ E-W lateral shear at the tips of the $\sim$ NS faults and blocks enclosed between their traces, which forced them to start rotating counterclockwise, away from their original NNE strike.

The block rotation scenario is necessarily a simplification of the actual processes. In particular, the blocks have slightly different sizes and thus rotation rates, and those differences might induce extensional or compressional deformation across the faults, as the rotating blocks indent or separate from each other. This observation is in keeping with the small across-strike fault motions found in the GPS data.

The vertical axis block rotation model also allows calculating the westward and eastward velocities of the northern and southern tips, respectively, of the rotating faults (calculations in Supporting Information 8.1.8, and Table 3.5). These velocities may be taken as indicators of the strain that is cumulating at the tips of the rotating faults and blocks. From GPS fault slip rates and block dimensions we find that the fault tips are moving (perpendicular to the tips) currently at significant velocities, averaging 1-2 mm/yr for the Dehshir and Anar fault tips, 3 mm/yr for the Kuhbanan fault tips, and 7-8 mm/yr for the WL and EL fault tips. Since those velocities are inferred from simple calculations, they should be considered with caution. However they suggest that important deformations likely occur at the tips of the rotating faults, as suggested in prior works [Freund, 1970, 1974, Ron et al., 1984, 1986, Nur et al., 1986, Manighetti et al., 2001, Walker and Jackson, 2004]. Dense, distributed, secondary faulting is expected to develop at the rotating tips, and be mainly compressional in the NW and SE tip-quadrants of the faults, while mainly extensional in their NE and SW tip-quadrants. These expectations are consistent with the observed development of dense secondary thrust fault networks at the NW and SE tips of all northerly-striking Central-Eastern Iranian faults, especially the West and East Lut faults. The tip velocities that we inferred from the rotating block model suggest that

secondary faulting might be most developed and most active at the tips of the EL and WL faults, significant at the tips of the KB fault, and more moderate at the tips of the Anar and Deshir faults. Figure 3.3 shows that the fault tips that we infer as being most active are those showing the densest and largest seismic activity. In contrast, the fault tips that we infer as sustaining lower strain are those free of earthquakes. Together these suggest that a significant part of the earthquake activity in Central-Eastern Iran might result from the secondary faults at the tips of the rotating faults breaking to release the large strain and stress that they sustain due to the rotation of the master faults.

The specific role of the Doruneh fault

Prior studies have suggested that the Doruneh fault and possibly also nearby $\sim$ EW faults might sustain vertical axis clockwise rotations in the horizontal plane [Jackson and McKenzie, 1984, Walker et al., 2004, Walker and Jackson, 2004, Allen et al., 2006, Walker and Khatib, 2006, Hollingsworth et al., 2010a]. No data were available however to test this hypothesis. The rotations were proposed to result from the eastward increase in the right-lateral slip rates of the Central-Eastern $\sim$ NS Iranian faults. Yet, as pointed out by Farbod et al. [2011], the mechanical reasons for those supposed clockwise rotations along the entire length of the Doruneh fault are not clear, whereas the present strike and geometry of the Doruneh fault are difficult to conciliate with the supposed clockwise rotations. Furthermore, recent paleomagnetic data show no significant clockwise rotation over the Neogene along the Doruneh fault [Mattei et al., 2012]. The GPS data suggest a 0.7-0.8°/Ma clockwise rotation in the Doruneh area. The rotation is constrained, however, by GPS stations spread over large distances that certainly exceed the limits of a rigid unit. Therefore, the available data cannot be used to test the scenarios that have been proposed so far. Additional data and possibly further thoughts are needed to understand how the Doruneh and nearby $\sim$ EW faults collectively accommodate part of the NS convergence.

The GPS data do not allow discussing the kinematic and mechanical reasons for the formation of the Doruneh fault, almost perpendicular to most major faults in Central-Eastern Iran. However we speculate that the curved shape of the Doruneh fault trace might result from the block rotations further south. The fault might be forced to 'follow' the overall southwestward displacement of the rotating $\sim$ NS blocks ('space opening' or reduction of the region width, because of the rotations; Fig. 3.9b) [Manighetti et al., 2001]. This 'southwestward attraction' might have contributed to curve the overall fault trace. The curving might have occurred through the southward jump of the principal fault segments, identified by Farbod et al. [2011]. The southwestward 'pulling' of the fault trace might force the fault to propagate southwestward. If the Doruneh fault does propagate towards the SW, we may anticipate that it might eventually connect with the Main Recent fault. Would such connection occur, the vertical axis block rotations in Central-Eastern Iran would likely stop.

3.2.9 Conclusions

We have analyzed new, dense, 11 years-long GPS data (92 stations) that we acquired in Central-Eastern Iran in the framework of the long-lasting Iranian-French collaboration. The density and quality of the GPS data, combined with our detailed analysis of the seismogenic faults that accommodate the current strain, allowed us to estimate, for the first time, the present-day kinematics and the slip rates on most faults in Central-Eastern Iran. The current kinematics is fairly well described by a rigid block model although a number of secondary faults exist which complexify this scenario. We confirm that the East Lut, West Lut, Kuhbanan, Anar, Dehshir and Doruneh faults are the major and fastest-slipping faults in Central-Eastern Iran, and we show that those faults are currently slipping laterally at 5.6 ± 0.6, 4.4 ± 0.4, 3.6 ± 1.3, 2.0 ± 0.7, 1.4 ± 0.9, and 1.3 ± 0.8 mm/yr, respectively. The slip is right-lateral on all five N-NNW striking faults (EL, WL, KB, A, DS), while it is left-lateral on the Doruneh fault. The N-NNW faults bound fairly rigid blocks that move in the N13°E ARA-EUR convergence direction at fast rates with respect to Eurasia, ranging between ∼ 1 and 13 mm/yr from east to west. The blocks also move towards the WNW at rates between 1 and 5 mm/yr from east to west (with respect to Eurasia), and each rotates counterclockwise in the horizontal plane at rates ranging from 0.1 to 0.8°/Ma. The current fault slip rates are roughly similar to the long-term and Holocene slip rates provided in the literature. A vertical axis block rotation model well describes the current kinematics in Central-Eastern Iran. Available data on longer-term fault motions are also well reproduced with the model, which suggests that the counterclockwise rotations might have been operating at a similar rate since at least 12 Ma.

Therefore, the GPS data suggest that the northward convergence is accommodated in Central-Eastern Iran in two ways. Firstly, the Central-Eastern Iranian crust is sliced in five large ∼ NS trending slivers, and those crustal slivers are moving northwards at fast rates (6-13 mm/yr) with respect to the stable Afghan crust at the eastern edge of the collision zone. It is likely that the collective behavior of the ∼ NS faults contributes to allow the Arabian promontory to impinge northwards into the Eurasian crust. Secondly, the ∼ NS Central-Eastern Iranian faults achieve NS shortening by rotating counterclockwise in the horizontal plane. The rotation has been occurring over the last 12-20 Ma up to present, at a similar rate averaging 1 ± 0.4 °/Ma. The vertical axis block rotation mechanism provides a plane-strain way of taking up across zone shortening by NS reduction of the crustal width and along-strike elongation of the rotating zone.

Our work might have implications on the understanding of part of the earthquake activity in Central-Eastern Iran. We expect that, over the several million years of block rotations, long-term diffuse and complex secondary faulting was created at the rotating fault tips. Such secondary faulting is actually observed. We used the GPS data to estimate

the westward and eastward velocities of the rotating fault tips. We found those velocities especially elevated at the tips of the EL, WL and KB rotating faults, exactly where historical and instrumental earthquake activity is remarkably localized and important. We thus suggest that a particular attention be put on the major fault tips, as those zones are the locus of elevated stresses and strain induced by the counterclockwise rotations. GPS data would also be needed in those zones to accurately measure the strain which accumulates there, in preparation to forthcoming earthquakes. We suggest that the Dasht-e-Bayaz, Sedeh and Birjand faults might have formed recently to contribute to the westward displacement of the East Lut rotating fault trace, whereas the Doruneh fault might have its trace forced to migrate southwestward as the $\sim$ NS blocks rotate counterclockwise. It has been shown that young, immature faults produce higher stress drop earthquakes than long-lived faults [Manighetti et al., 2007]. The presumed immaturity of the Dasht-e-Bayaz fault might explain why, despite the fault has a low slip rate, it broke in two large, high stress drop earthquakes within a very short time interval (1968 and 1979). We suggest that a similar behavior might be expected on the Sedeh and Birjand faults due south of Dasht-e-Bayaz, and possibly on the western half of the Doruneh fault. A special attention might thus be put on those faults, as they might be locus of forthcoming large earthquakes.

Chapter 4

Characterization of Doruneh fault behavior using a combined geodetic (GPS and INSAR) and tectonic approach

Contents

4.1 Introduction

The 700 km long Doruneh fault is one of the most prominent faults in Iran which extends from the eastern border of Iran to the central Dasht-e-Kavir [Wellman, 1966, Tchalenko and Berberian, 1975, Jackson and McKenzie, 1984, Walker and Jackson, 2004, Fattahi et al., 2006b, Farbod et al., 2011, Pezzo et al., 2012]. The Doruneh fault is thought to be rotating clockwise around a vertical axis to accommodate the N-S right-lateral shear [Jackson and McKenzie, 1984, Jackson et al., 1995, Walker and Jackson, 2004] between central Iran and Afghanistan [Vernant et al., 2004b] (see figure 4.2). Fattahi et al., [2007] determined 2.4 ± 0.3 mm/yr of slip rate of left-lateral displacement on this fault in the Shesh-Taraz region at longitude ∼58 ° based on the Infrared Stimulated Luminescence (IRSL) dating technique.

The first results from the Iranian GPS network indicate a decrease of the left-lateral slip rate of the Doruneh fault from west to east: 2.5 ±2 mm/yr at the longitude of 58°E to 1±2 mm/yr at the longitude of ∼60.5°E [Tavakoli, 2007]. According to more recent data from the permanent and campaign GPS networks the slip rate is estimated to 2mm/yr from a rigid block modeling approach and to less than 1mm/yr from the difference of average GPS velocities of stations located on opposite sides of the fault (see section 3, Walpersdorf et al. in review.

If the fault is accommodating less than 1mm/yr of slip in present-day, the geodetic measurements may not be representative of the long-term slip rate of this fault. This discrepancy of 1mm/yr by GPS and 2.4± 0.3 mm/yr by IRSL dating can come from variation of slip rate through time. Slip variations in time have been observed Garlock fault in eastern California [Peltzer et al., 2001]. Doruneh's slip rate variation is based on a single date geomorphological offset and on a GPS network that is extremely sparse except on the eastern part of fault.

For improving our knowledge of Doruneh fault and its role in accommodating the NS convergence, we propose to provide additional constraints on the geodetic fault slip rate. We can increase the spatial coverage of our geodetic observations that are too punctual. The InSAR technique has the potential to fulfill this objective.

An InSAR analysis done by Pezzo et al. [2012] using the SBAS approach (see Berardino et al. [2002] and section 2.22) suggests that 5±1mm/yr of displacement accumulates on the fault below 10 km depth in the central part of the Doruneh fault (see figure 4.1). The modeled slip is not purely strike-slip (left-lateral) but has also a significant thrust component. This result raises again the question of the uncertainty and significance of the GPS measurements. However, it should be noted that this InSAR study covers only a 100km-long strip of data across the fault which can be too short to well discriminate between the long-wavelength orbital error signal and the elastic interseismic deformation around the fault. That is why we decided to investigate the interseismic deformation on

a larger scale using about 600 km-long strips on 6 different tracks covering 600km of the Doruneh fault (see Fig. 4.4).

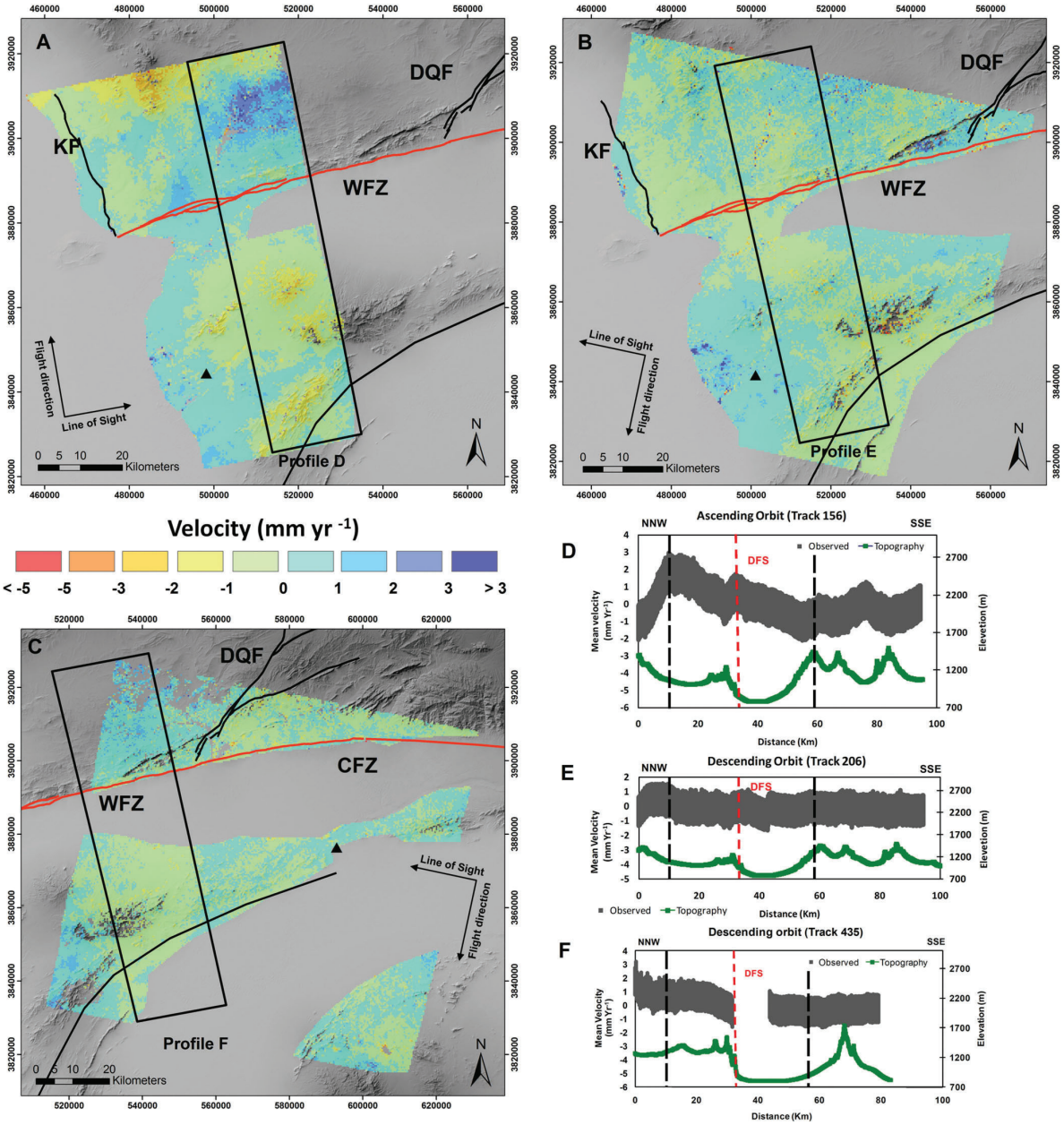

Figure 4.1 – Mean LOS velocity maps from (A) ascending track 156, (B) descending track 206 and (C) descending track 435. Positive velocity values (blue colours) indicate ground movement toward the satellite along the LOS direction (inclined 23° from the vertical), negative ones (red colours) indicate the opposite. Red line is Doruneh fault and black lines present the other faults in the region. Black triangles indicate the reference point; black boxes mark the 20 km buffered velocity profiles reported with the profile (D), (E) and (F), where the topography is also reported in green; dashed red lines mark the intersection with the DFS trace, whereas dashed black lines mark the truncation of profile, around the DFS trace, used in the inversion processing [Pezzo et al., 2012].

4.2 Tectonic setting

The 700 km long Doruneh fault in eastern Iran extends from the eastern border of Iran to the central Dasht-e-kavir and has already given place to many studies [Wellman, 1966, Walker and Jackson, 2004, Fattahi et al., 2006b, Farbod et al., 2011, Pezzo et al., 2012]. It is a left-lateral strike slip fault trending east-west with bend at ∼58°E. The eastern part of the Doruneh fault is bending to the south. The western part trends WSW and crosses the Dasht e-Kavir.

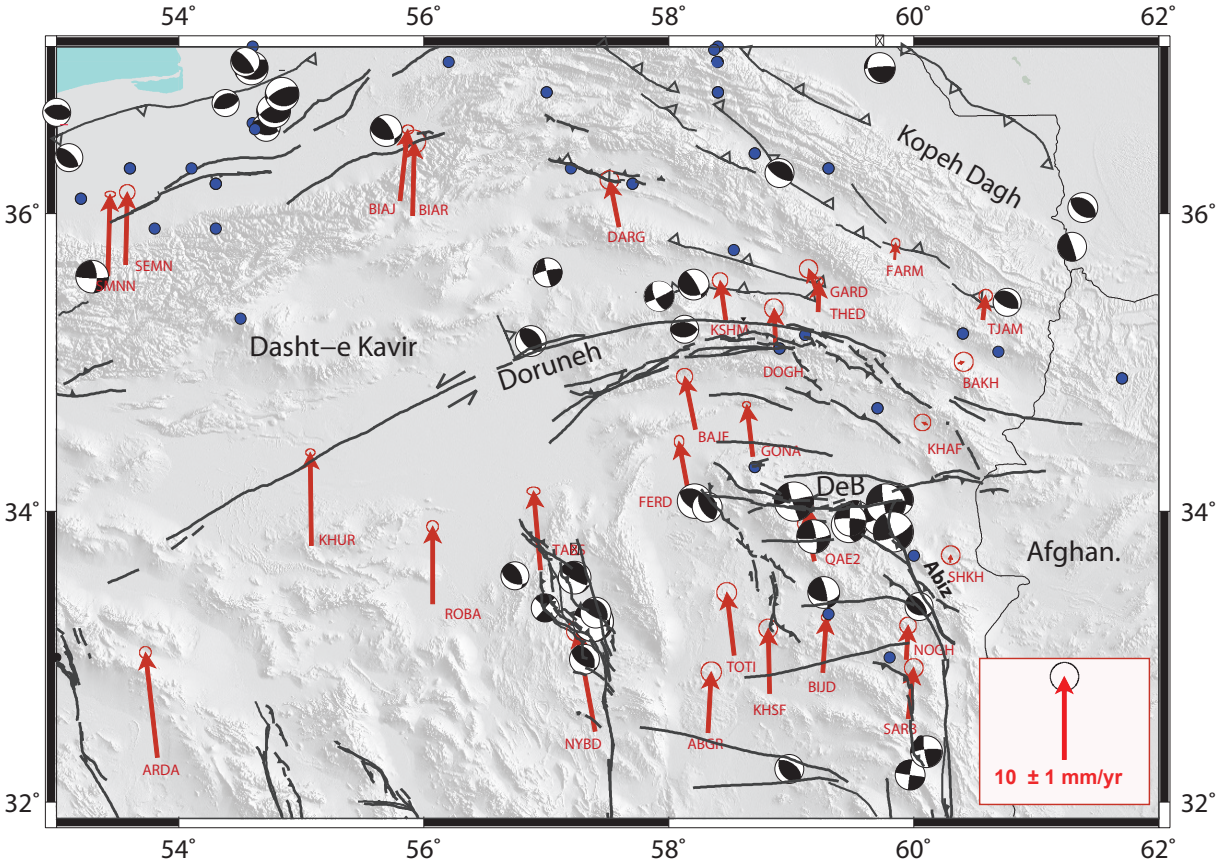

Figure 4.2 – Tectonic setting of Doruneh fault. The red vectors are the GPS velocity field from section 3, the focal mechanisms are first-motion and waveform-modeled solutions from [McKenzie, 1972, Baker et al., 1993, Berberian and Yeats, 1999, Jackson et al., 2002, Walker and Jackson, 2004, Engdahl et al., 2006] and Harvard catalogue http://www.globalcmt.org/CMTsearch.html) during the period 1976-2012. Historical earthquakes (blue dots) come from [Ambraseys and Melville, 1982]. Characteristics of earthquakes that are numbered (EQ1 to EQ5) are presented in table 4.1. The green triangle presents the location of geologic slip estimation [Fattahi et al., 2006b].

This fault is one of the longest faults in Iran which can play a significant role in regional tectonics. Until now, no large earthquake has been recorded on this fault [Ambraseys and Melville, 1982, Jackson and McKenzie, 1984] (see figure 4.2). However, if we consider a scaling relationship [Scholz, 1982, Wells and Coppersmith, 1994] between the length of a fault and the recurrence time of its ruptures, one may make a rough estimate of a recurrence time close to thousands of years (∼ 2000 years) for large earthquakes (∼

7 Mw) [Fattahi et al., 2006b]. As the Doruneh fault is far from urban area due to the dry climate of the region, the historic earthquake catalogue could be not complete. In brief, the historical and instrumental catalogue for Doruneh fault argues that this area is experiencing less destructive earthquakes than adjacent faults like Dasht-e-Bayaz ; 1968(Mw 7.10), 1979 (Mw7.10) [Walker et al., 2004, 2011], Tabas; 1978 (Mw 7.4) [Walker et al., 2003], Kopeh Dagh; 1948 (Mw 7.2), 1997 (Mw 6.4) [Tchalenko and Berberian, 1975, Berberian and Yeats, 1999, 2001, Hollingsworth et al., 2006, Shabanian et al., 2009a]. In table 4.1, a summary of the recent earthquakes occurring close to the Doruneh fault trace is presented.

Event	Date	Time (GMT)	Lat.	Long.	Depth	Mw	Strike	Dip	Rake
1	1971.05.26	02:41:35	35.56	58.23	13	5.6	89	26	32
2	1972.12.01	11:39:35	35.45	57.92	8	5.3	65	87	25
3	1979.12.09	09:12:35	35.15	56.87	9	5.5	325	36	99
4	1996.02.25	17:42:04	35.65	57.07	33	5.4	82	77	10
5	2000.02.02	22:58:01	35.29	58.22	26	5.3	83	43	79

Table 4.1 – Epicentre and source parameters of earthquakes in the Doruneh region [Fattahi et al., 2006b].

The kinematic behavior of the Doruneh Fault inside the NE Iran deformation pattern is not well-known. Indeed, the way NS shear is accommodated in eastern Iran with NS right-lateral and EW left-lateral faults is still an unresolved question in the active tectonic of Iran. The complexity of the geometric interaction of these two types of perpendicular faults increases the difficulty in assessing their role in accommodating the deformation driven by the Iranian-Arabian plate convergence [Jackson and McKenzie, 1984, Walker and Jackson, 2004, Allen et al., 2006, Farbod et al., 2011].

Jackson and McKenzie (1984) suggest that the N-S right-lateral shear can be taken up by clockwise rotation around a vertical axis of the Doruneh fault. This vertical axis can be located at the border with Afghanistan in order to accommodate the N-S shear.

Later, Walker and Jackson (2004) proposed a tectonic model for the Lut region based on rigid block rotations. NS shear is increasing eastward across the NS oriented right-lateral strike-slip faults in eastern Iran (Deshir and Anar faults: small displacement; Nayband fault 15 km, Sistan fault system ∼70 km). This is supposed to lead to eastward increasing clockwise block rotations north of the NS faults (north of 34° N), centered on the Doruneh fault trace. This block model can explain the left-lateral slip mechanism of the Doruneh fault as well as the curvature, with most of the clockwise rotation affecting the eastern part of the fault to rotate it out of the initial EW orientation. This initial orientation is still visible on the young Dasht-e-Bayaz fault just south of Doruneh (Fig. 4.3-B).

Recently, Farbod et al. [2011] suggested a segmentation model for the Doruneh fault which can provide evidence of geomorphic, structural and seismogenic fault behavior variation along strike. According to detailed geomorphic and structural analyses of satellite

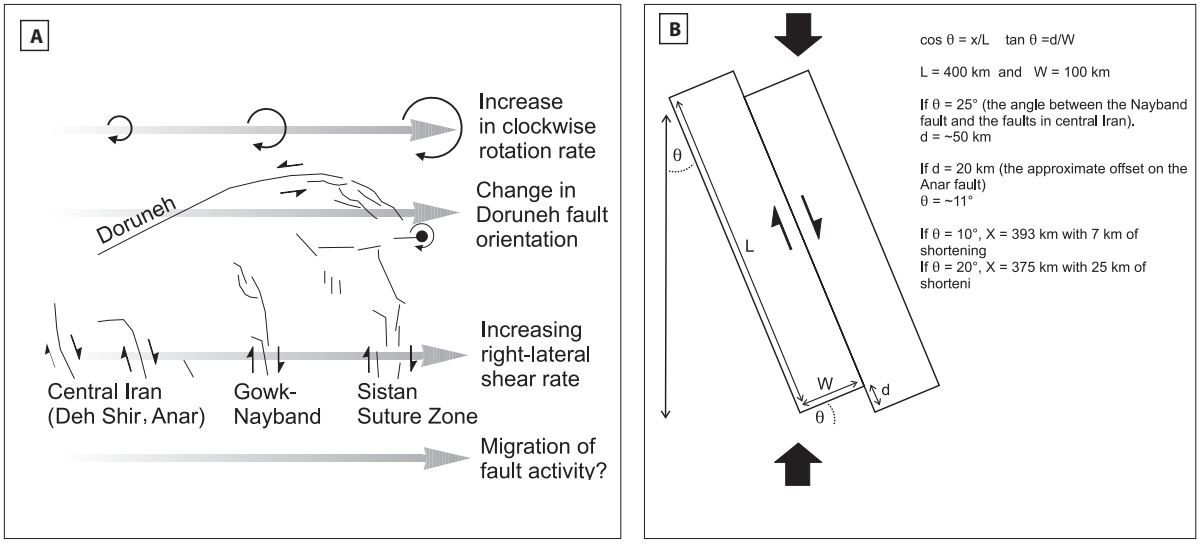

Figure 4.3 – Kinematic model proposed by Walker and Jackson [2004] . A) Schematic illustration of accommodating the NS shear in central Iran. B)Cartoon showing how NNW–SSE right-lateral strike-slip faults in central Iran can accommodate N–S shortening by anticlockwise rotation about vertical axes [Walker and Jackson, 2004].

images and digital topographic data at different scales, along with field surveys, the authors establish a fault segmentation model in which three discrete fault zones are distinguished: (1) the western fault zone characterized by reverse left-lateral mechanism with left-handed step-over geometry, (2) the central fault zone which is pure left-lateral strike-slip and comprises nearly parallel faults, and (3) the eastern fault zone that is a trailing imbricate fan fault-termination characterized by reverse faulting and fault-related folding.

The six satellite tracks that are analyzed in this study cover a large part of the fault trace and could therefore possibly highlight this variable fault character along strike.

4.3 Multi temporal INSAR data analysis

Synthetic Aperture Radar (SAR) images from the ASAR instrument (wavelength of 5.6 cm) on board the ENVISAT satellite have been used to investigate the interseismic deformation across the Doruneh fault. In the "image mode" of the ASAR instrument (swath of 100km), the studied area is covered by several tracks of the satellite (Fig 4.4). The use of 400km long interferograms was chosen to be able to integrate regions far from the fault trace, in contrast to the study of Pezzo et al. [2012] that consider than only area close to the fault trace and do not correct for DEM error or atmospheric effects.

The raw radar images from 2003 to 2010 (Processing Level 0) were processed with ROI_PAC software [Rosen et al., 2004] and NSBAS package [Doin et al., 2011]. The topographic phase contribution was estimated from the SRTM Digital Elevation Model (DEM) at 90 m spatial resolution [Farr et al., 2007]. Precise DORIS orbital data for the

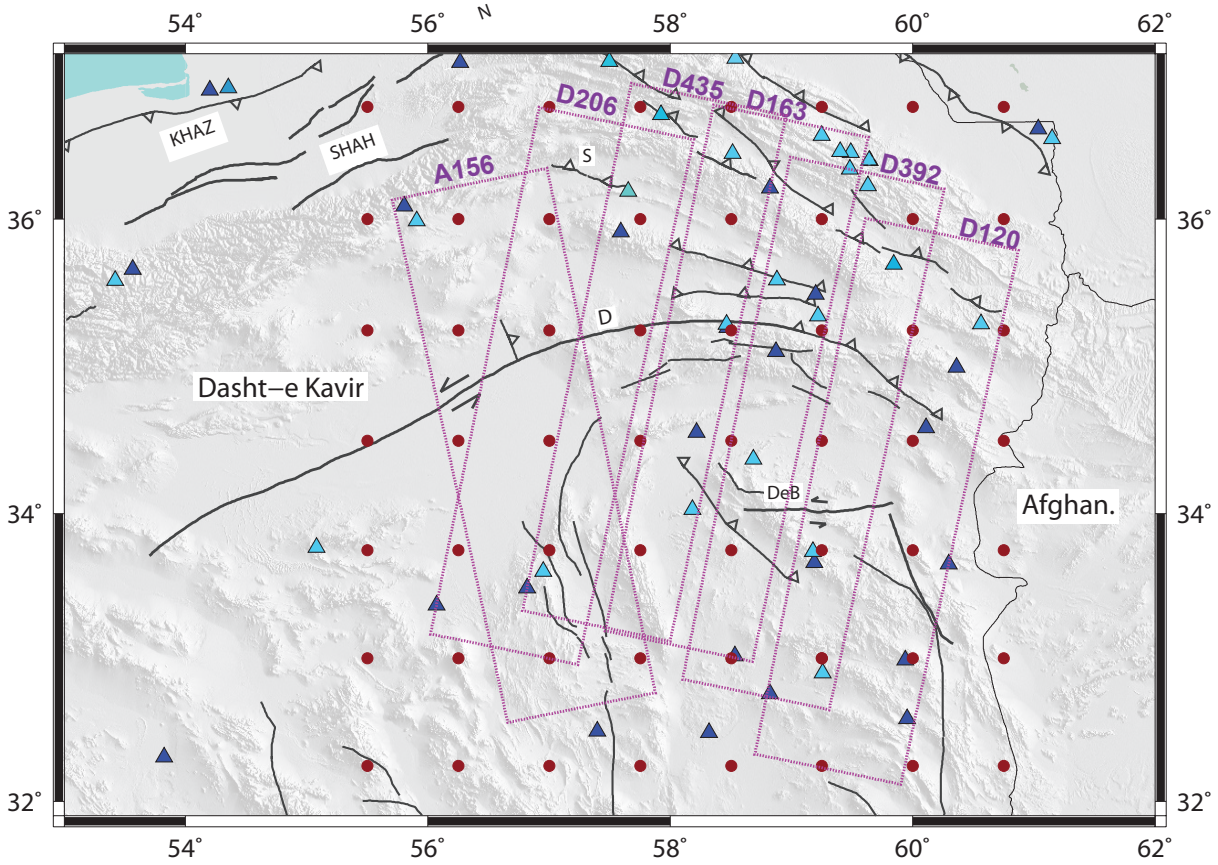

Figure 4.4 – The spatial coverage of the ENVISAT SAR tracks across the Doruneh fault is presented as pink rectangles. We used the ERA_Interim model, (the red dots) to correct the tropospheric delay and we used the permanent GPS stations (light blue triangles) and campaign GPS stations (dark blue triangles) to validate the tropospheric delay map.

ENVISAT satellite provided by ESA are used for interferometric processing.

We produce Single Look Complex (SLC) images with a common Doppler frequency band. A single master image is chosen following Zebker and Villasenor [1992] and Hooper et al. [2007] and all other SLC are coregistered in the master image geometry using the DEM (see section 2.3.3). We processed amongst all possible interferograms having baseline differences less than 500m to minimize the signal decorrelation. The perpendicular baseline difference between two images is an important parameter for the interferogram coherency. The perpendicular baseline distributions of the available images through time for tracks D392 are given in Figure 4.5. A small baseline means that the two images were taken from a close point of view, which optimizes the quality of the InSAR signal.

In the case of North-Eastern Iran, an important factor that affects the coherency of interferograms is the fact that part of the studied area is covered by sand dunes. As these sandy areas are changing rapidly through time, the spatial coherence of the interferometric phase is very low in interferograms spanning several years. It is then impossible to unwrap the phase for the whole interferogram.

Apart the problem from sand dunes that affects only part of the images, the main

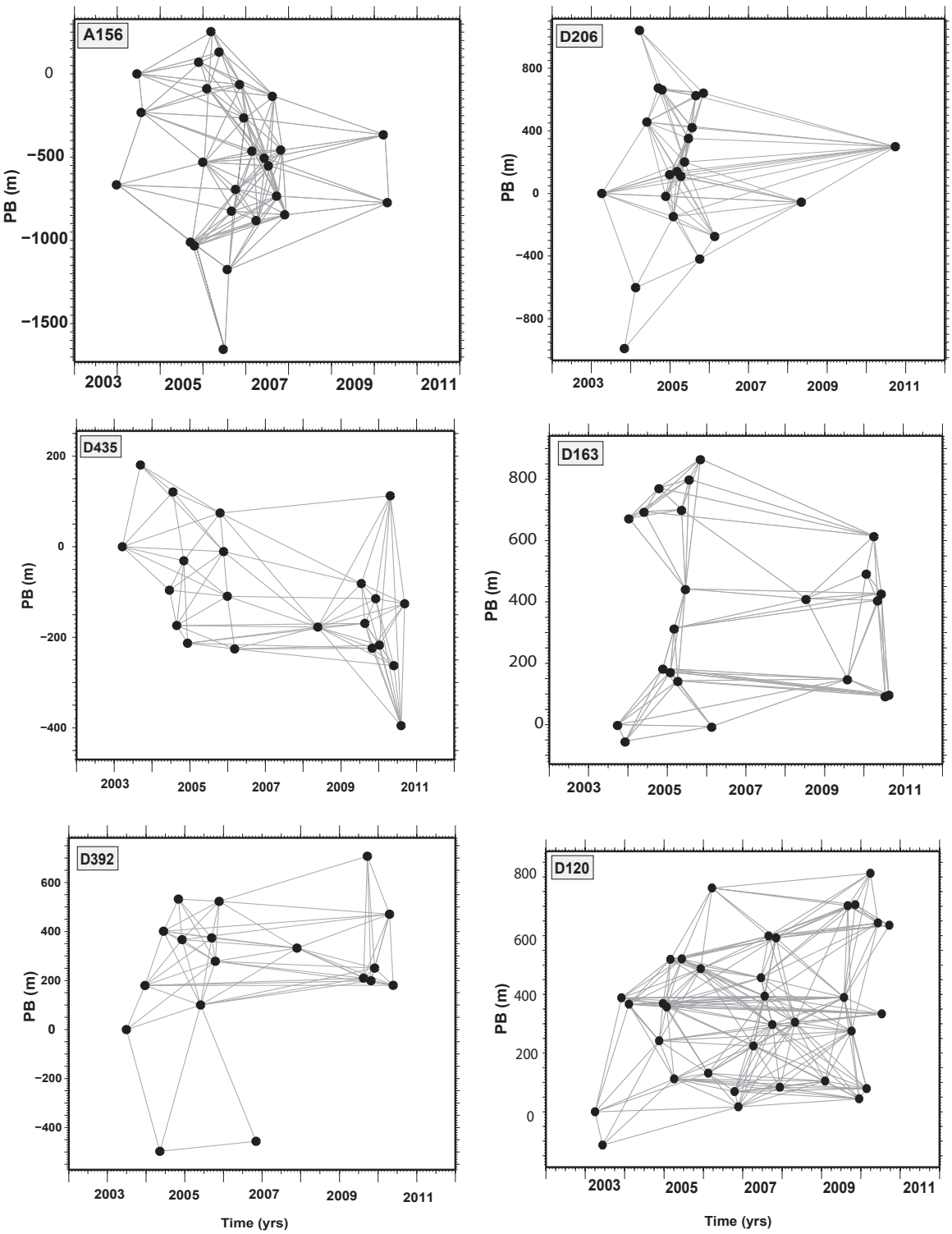

Figure 4.5 – Diagram showing the network of processed interferograms (gray lines) for each of the six tracks used in this study (5 descendings and 1 ascendings). Each plot shows the relative perpendicular baselines as a function of acquisition dates. Each date of ENVISAT images acquisition represented by a black dot.

limitation of detecting interseismic deformation from the interferometric phase ϕ^{ij} between two dates i and j is due to atmospheric artifacts, DEM errors, orbital residual and poor

coherence, which can be expressed by the following equation:

$$\phi^{ij} = \phi^{ij}_{DEM\_res} + \phi^{ij}_{orb\_res} + \phi^{ij}_{atmo} + \phi^{ij}_{disp} + \phi^{ij}_{noise} \tag{4.1}$$

where $\phi^{ij}_{orb\_res}$ is the phase component related to the orbit error, ϕ^{ij}_{atmo} is the change in atmospheric delay (Atmospheric Phase Screen, APS), $\phi^{ij}_{DEM\_res}$ is related to topography errors, ϕ^{ij}_{disp} is ground displacement and ϕ^{ij}_{noise} is the residual noise from co-registration, and unwrapping.

Although atmospheric and orbital errors are perturbing the tectonics phase signal, if a shallow creep on a fault were present, it could be detected in such interferograms as it will result in a sharp phase variation located exactly along the fault trace. We performed a close visual examination of the interferograms with respect to the active faults map looking for such a signal. Local deformations related to subsidence phenomena were found in some valleys but there is no evidence over the 2003 to 2010 period for any sharp creep deformation signal located along the fault.

The trade-offs of the tectonic signal with orbital errors and atmospheric phase delays make it necessary to correct orbital, DEM residual errors and stratified tropospheric delay [Zebker et al., 1997, Massonnet and Feigl, 1998]. The DEM residual errors can be reduced using the method presented in section 2.3.4 of selected interferograms with perpendicular baselines lower than 500m and temporal baselines lower than 4 years [Ducret et al., 2013]. The unmodelled orbital errors in the flattening step can be removed using best fitting ramp in range, followed by a best fitting ramp in azimuth. More complex models could have been used, but we rather used the ramp model to avoid removing the expected interseismic signal located around the fault. After the orbital and DEM residual corrections, the most important source of errors in this area of Iran is the change in atmospheric conditions between acquisition dates that may be deteriorated by the climatic contrasts between different zones covered by the interferograms. For example, track D163 covers a desert area in the south, mountain area in the middle of the image and moderate topography dominate in the north of the track. The tropospheric delay can be split in two components, stratified and turbulent. The turbulent component can be assumed to be distributed randomly both in space and time, and can be reduced by stacking or by smoothing during time series analysis. However, the stratified component can causes systematic errors and should be removed before the time series analysis. In this study we used the ERA-Interim global analysis to correct for the atmospheric effect in InSAR (see section 2.3.4 for more details).

The global atmospheric model provides meteorological parameters (temperature, water vapor and dry air partial pressure) on a 75km grid (see Fig 4.4), 4 times per day. The first step is selecting the meteorological parameters at the time step that is closest to the SAR acquisition time, which is at 6AM for descending tracks and 18 PM for ascending tracks in our case. The delay map is obtained in two steps: The first step consists in an in-

terpolation of pressure, water vapor partial pressure, and temperature onto height profiles for each ERA-I grid node using a spline interpolation. This interpolated parameters are used to predict the LOS tropospheric delay as a function of elevation on each ERA-I grid node. After, these LOS delay profiles (function of height) are horizontally interpolated to the resolution of a SRTM DEM with a bilinear interpolation. For each point (with xyz position) from the DEM, the LOS delay value at that location is then selected. These values are used to produce a predicted delay map. These delay maps at acquisition date can be combined to obtain a differential delay map for each interferogram. Figure 4.6 presents an example delay maps for two dates and their corresponding differential delay map.

Furthermore, GPS data can independently valid our ERA-Interim delay correction of interferograms. GPS phase measurements are processed, using GAMIT/GLOCBK to derive tropospheric delay parameters (Zenith Total Delay, ZTD) for the individual stations of the network for each ENVISAT acquisition date. This can be performed in two steps:

- First, the tropospheric delay can be determined together with the site position.
- Second, the site position was fixed to the average position for that day, and only the ZTD were estimated.

This is done in two steps because ZTD is correlated with height and real variations of ZTD can lead to misestimating of height. Thus if we estimate height and ZTD simultaneously it will be less reliable. Figure 4.6 presents the ZTD value for each permanent station (triangles) located on the area cover by track D392.

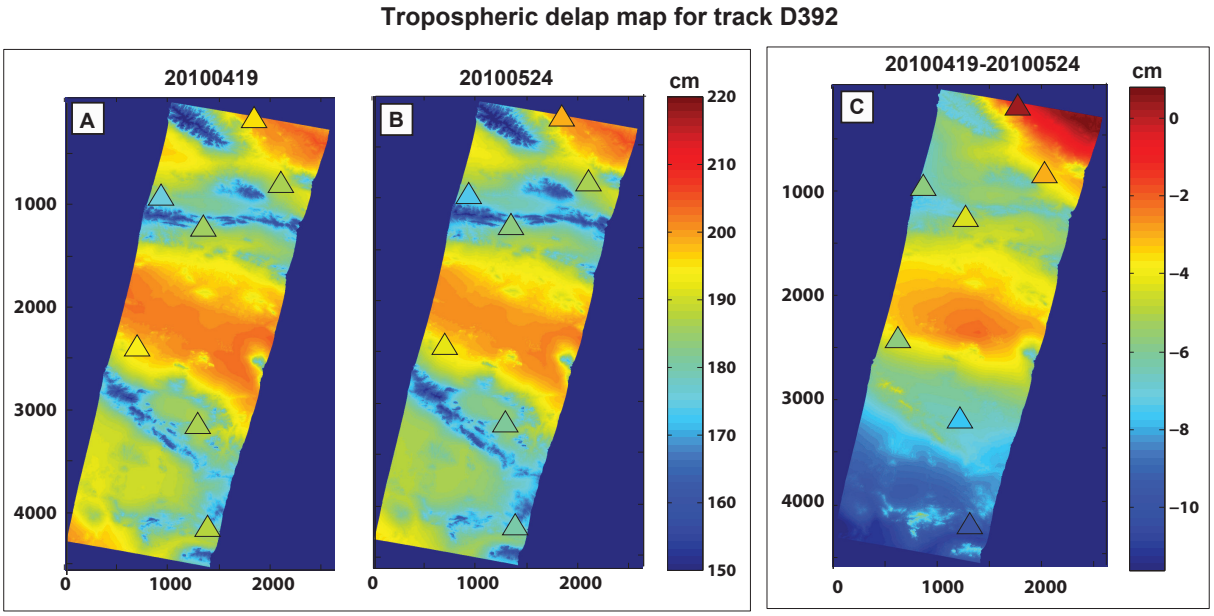

Figure 4.6 – The tropospheric delay map estimated by ERA-I (for track D392). A) and B) The delay map for dates 20100419 and 20100524, respectively. The triangles show the GPS station and the color of triangles presents the value of GPS tropospheric delay according to color bar, taken at the SAR image date. C) The delay map for one month interferogram (20100419-20100524).

Then these interferograms are averaged by a factor of 4 in range and of 20 in azimuth

(see section 2.3.3), filtered using a power spectrum filter [Goldstein and Werner, 1998], and unwrapped using a branchcut algorithm [Goldstein et al., 1988].

4.4 Time series analysis

In order to estimate interseismic deformation from interferograms, multi temporal InSAR technique can be used. Using networks of interferograms, this technique, such as Permanent Scatterers (PS) and small baseline InSAR (SBAS) [Berardino et al., 2002], will generate time series of ground deformation. Corrected interferograms are inverted to solve for the phase of successive images using a least squares inversion method [Cavalié et al., 2007] :

$$\Delta\Phi = A.\phi \qquad where \qquad \phi_1 = 0 \tag{4.2}$$

where $\Delta\Phi$ includes N interferogram observations, ϕ corresponds to M phase at M time steps, and G is a $M \times N$ matrix where M is the number of acquisition dates and N is the number of successive interferograms (see section 2.22). We did a smoothed constraint time analysis which is explained in section 2.22.

We add two constraints on the SBAS time series analysis [Schmidt and Bürgmann, 2003, Cavalié et al., 2007]. The first is the temporal smoothing constraint which is introduced to the SBAS time series system as it is difficult to make any other a priori assumption on the deformation behavior with time for the Doruneh fault. The second constraint is related to the residual DEM error. Note that although these errors might be negligible for baselines of less than 300 m, they may cumulate in the inversion as the cumulative baseline reaches $\sim$ 2000 m. Then the inversion system becomes (the matrix version of equation of 2.83):

$$\begin{pmatrix} W.\Delta\Phi \\ 0 \end{pmatrix} = \begin{pmatrix} W.A & W.b \\ \gamma^2 w_i \frac{\partial^2}{\partial t^2} & 0 \end{pmatrix} . \begin{pmatrix} W.\phi \\ e_{DEM} \end{pmatrix} \tag{4.3}$$

where b is the perpendicular baseline vector, W is a weight, e_{DEM} is the proportionality coefficient between phase and baseline due to the DEM error, γ is the smoothing coefficient introduced to ponderate the minimum curvature constraints $d\phi^2/dt^2$ (where t is time) and w_i is the weighting factor that can be 1, $\bar{\Delta}t_i$ or $\bar{\Delta}t_i^2$ and can be selected based on the smoothing strategy.

The aim of the time series can be temporal evaluation of ground deformation or second the APS removal. The option one can be homogeneous across the time series by assuming $w_i = 1$ and option two can be homogeneous across the time series by considering $w_i = \bar{\Delta}t_i^2$ (where Δt_i is the mean time interval across the five-point differential operator). Cavalie et al. [2007] find that if the weighting factor is the intermediate solution ($w_i = \bar{\Delta}t_i^2$)

then the APS removal is not negligible for widely spaced acquisitions and the ground motion will not vary too much between densely spaced acquisitions. We can evaluate the system misclosure for each pixel by the RMS for each pixel using the equation 2.84.

Now this inversion can be applied to a very large number of pixels using the least square inversion [Cavalié et al., 2007] to estimate the long wavelength of the tectonic signal due to the interseismic deformation of the Doruneh fault. Figure 4.7, 4.8 and 4.9 presents the mean velocity map for 6 tracks which cover the Doruneh fault from west to east and their corresponding RMS misclosure map.

4.5 Results

Figures 4.7,4.8 and 4.9 present the mean velocity map of the 6 processed tracks (see figure 4.4 for location of tracks) and their corresponding RMS misclosure map. The RMS misclosure map is not directly a measure of uncertainty of the LOS mean velocity map, but rather gives the relative accuracy of the different parts of the interferogram, it is a measure, for each pixel of the misclosure of the unwrapped interferometric phase (expressed here in mm) through the network of interferograms. For that it is very useful to help detecting unwrapping errors that is significant in some of the tracks.

Track A156: A long wavelength signal can be seen in this track which is consistent with the left-lateral movement (the satellite is looking from the west in ascending orbit and the northern part of the fault is going toward the satellite with respect to the southern part) but it is not centered on Doruneh fault. Also it should be mentioned that this track have not enough images to be able to detect with reliability a tectonic signal as the time series analysis for both tracks depend strongly on the two last images in 2010, where APS will not be easily attenuated by the temporal regression (see figure 4.5).

Track D206: This track also has the same problem as A156 due to the irregular sampling in time through the network (Fig. 4.5). Therefore the mean velocity map is strongly dependent on two images (2008 and 2010). However, at first order, the regional phase gradients is coherent with the A156 and roughly present the left-lateral fault (in this descending track, the satellite is looking from the East, and the area north of the fault is rather going away from the satellite with the respect to the southern part). However, the long wavelength signal is somehow oblique with respect to the fault trace and in addition there is strong local deviation like the red patches south of the fault that can be seen on figure 4.7. According to the RMs misclosure map, the unwrapping problems can be responsible of this red patch, and also may affect the northern part of the interferogram.

Track D435: The phase gradient across track D435 is located exactly on Doruneh fault, it seems there is unwrapping problem in this track as shown by the RMS misclosure map. Indeed, in most of the interferograms of this track, it was necessary to bridge manually between patches of unwrapped phase in order to make the link between the

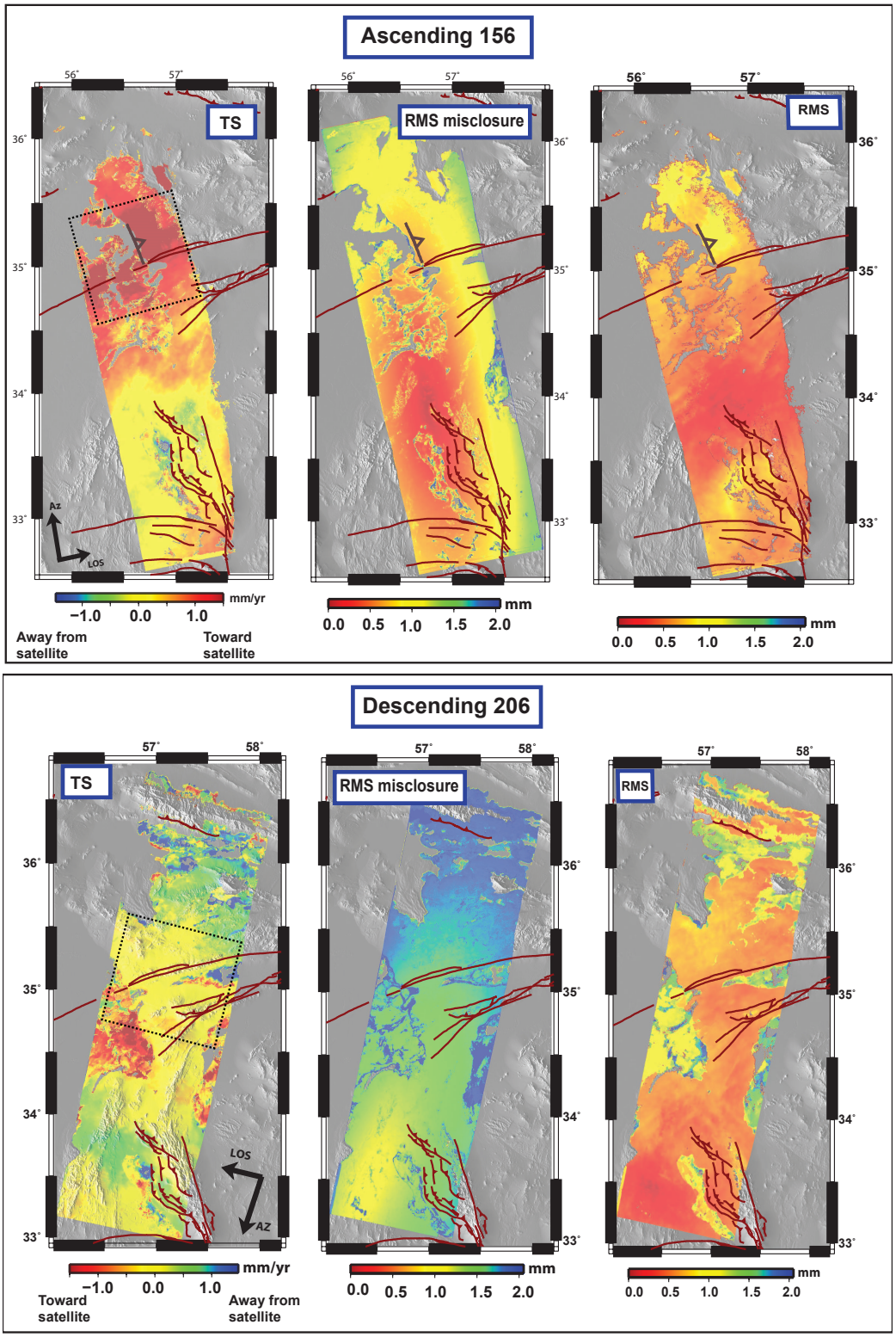

Figure 4.7 – Mean velocity map along line of sight (LOS) for the available ENVISAT images of one ascending (A146) and descending tracks D206 from west to east. The map with label TS is the mean velocity map and the map with RMS is the Root Mean Square map for the correspond track. The dashed rectangle are the location of SAR images used by [Pezzo et al., 2012].

northern and southern part of the interferogram, which is source of errors. The high value of RMS misclosure incites us to be careful about this phase variation across the fault.

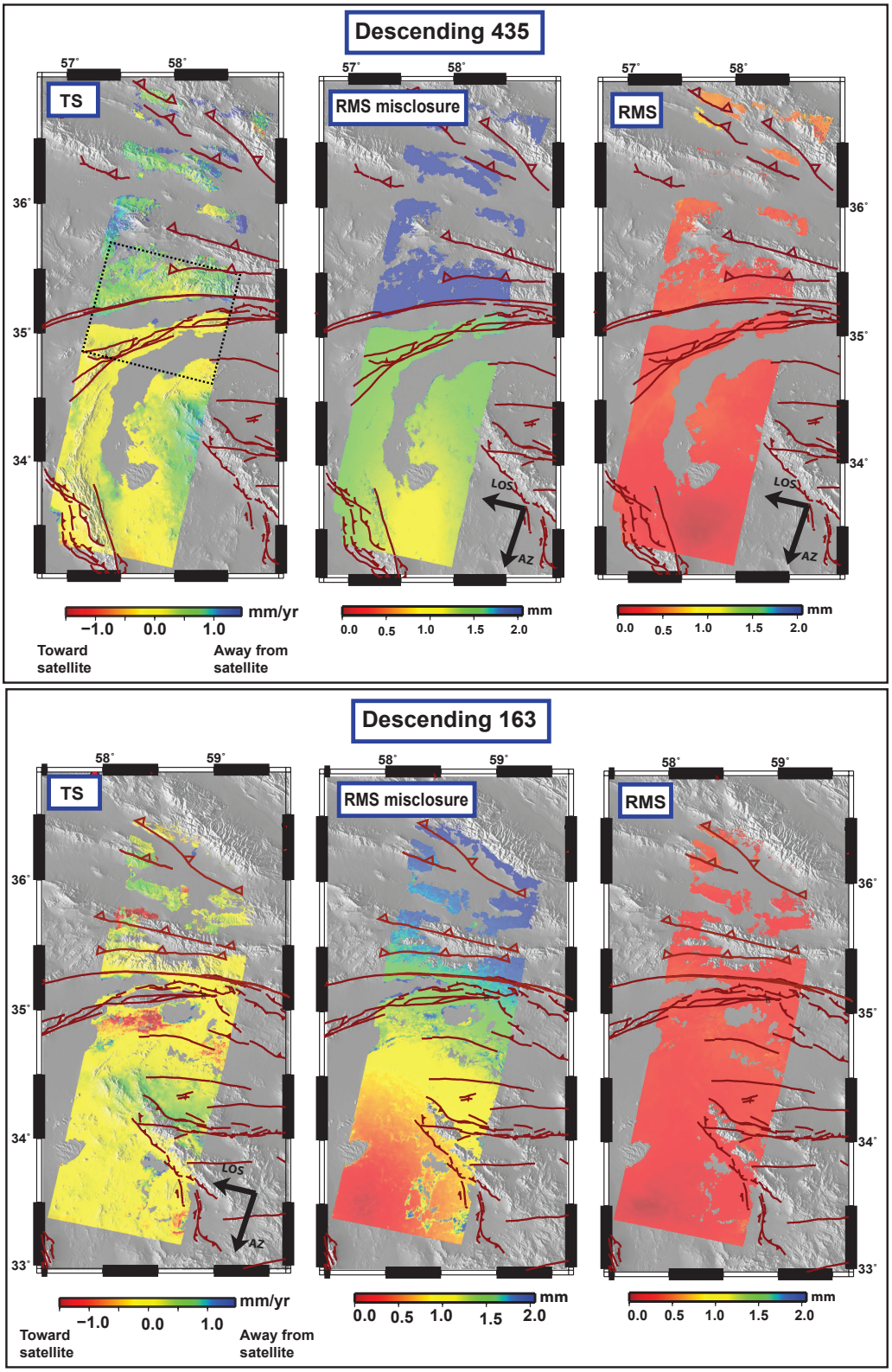

Figure 4.8 – Mean velocity map along line of sight (LOS) for the available ENVISAT images of two descending tracks D435 and D163 from west to east. The map with label TS is the mean velocity map and the map with RMS is the Root Mean Square map for the correspond track. The dashed rectangle are the location of SAR images used by [Pezzo et al., 2012].

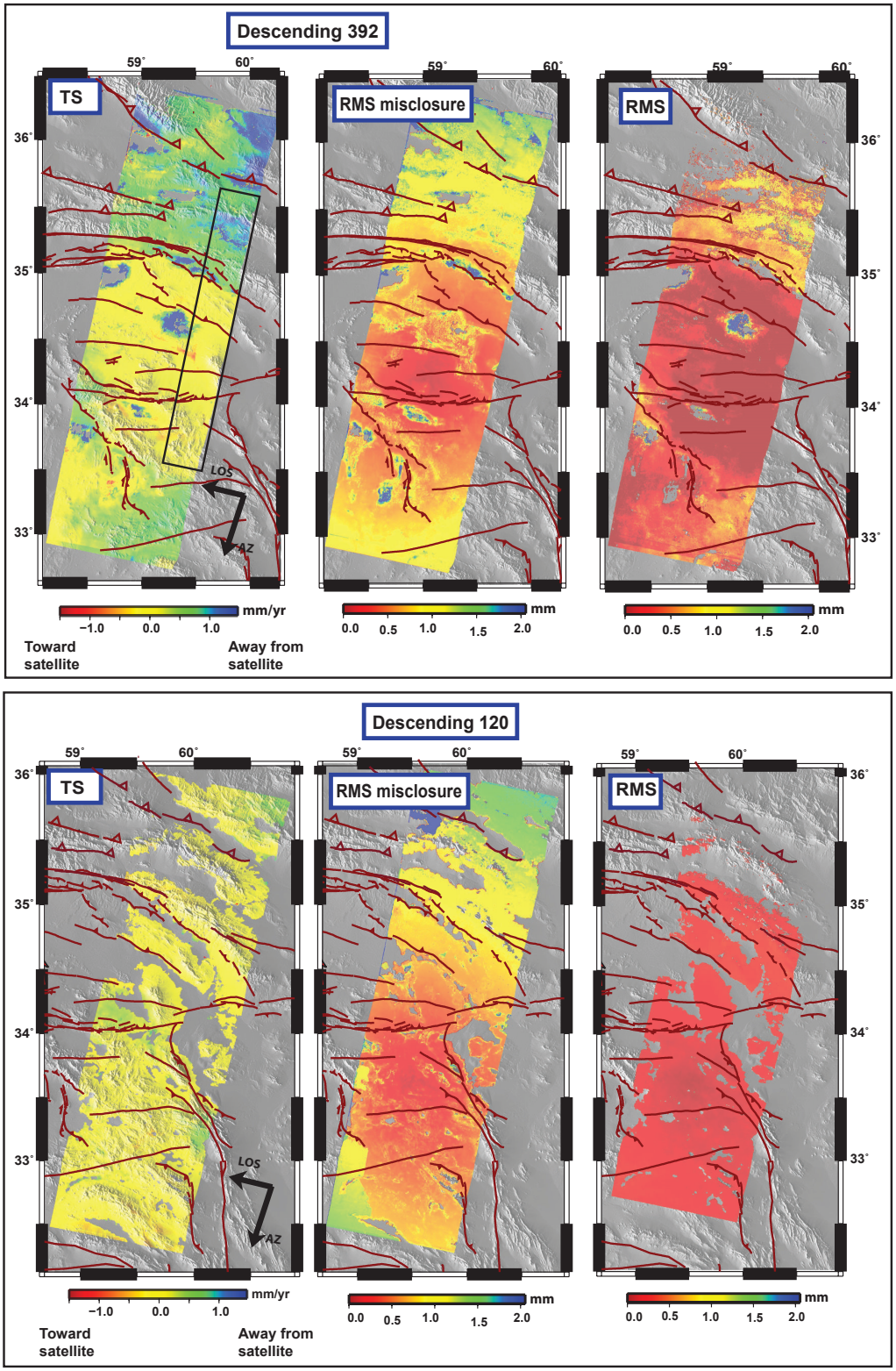

Figure 4.9 – Mean velocity map along line of sight (LOS) for the available ENVISAT images of two descending tracks D392 and D120 from west to east. The map with label TS is the mean velocity map and the map with RMS is the Root Mean Square map for the correspond track. The rectangle in track D392 presents the location of profile of figure 4.10.

Apart from these limitations, this track is also compatible with a left-lateral displacement of the Doruneh Fault.

Track D163: This track has a similar unwrapping problem as in track D435, with higher RMS misclosure in northern part of the track and lower coherence. No clear interseismic signal can be seen in the mean velocity map, which show discrepancies with track D435 in their overlapping area.

Track D392: Track D392 show a long-wavelength signal consistent with left-lateral displacement, with a relatively low RMS misclosure. The profile along the track D392 (Fig. 4.10) presents a North-South contrast of 1.5 mm/yr along the Line of Sight. Assuming a pure left-lateral strike-slip fault, a model of arctangent shape (see section 2.27) can be computed, not centered on Doruneh but on the fault south of the Doruneh fault. However, there are two reasons to question the assumption that the observed signal correspond to a purely strike-slip interseismic deformation. First, there is no corresponding tectonic signal on neighbor tracks, D163 in the western side and D120 on eastern side of track D392. Second, the deformation is not centered on the fault but on the fault south of the Doruneh fault.

The fault located in southern Doruneh fault has been rather interpreted as a thrust fault by tectonician [Farbod et al., 2011], which suggests that a thrust component of the displacement should be taken into account in this segment of the Doruneh fault which is in agreement with the rigid block modeling (see section 3) showing that in the eastern part of Doruneh, shortening is the major slip component in contrast to the western part. However, the geometric relationship at depth of these close fault traces is not well known and it is possible that these two faults merge into a single fault plane at depth. Also the permanent GPS station THED north of the Doruneh fault (Fig 4.2) shows with 1.5 mm/yr of subsidence probably related to ground water extraction, which makes its tectonics interpretation difficult.

If we interpret the LOS measurement in terms of vertical displacement, the projection of LOS motion onto the vertical direction is compatible with uplift of the tectonic units south of the faults, and subsidence north of them. which is not consistent with the sense of thrusting indicated for the thrust faults in this NE part of the Lut block. The uncertainties about the tectonics displacement, make the interpretation of LOS velocity map difficult.

Track D120: Track D120 has the largest number of images and the best network of interferograms but it presents no specific signal with lower RMS misclosure values with respect to the other tracks. However, this track is not consistent with track D392 as its neighbor which has clear phase gradient along track This raise the question of the signal to noise ratio in our InSAR observation.

As general observations, it can be said that at first order, InSAR measurement are generally compatible with left-lateral displacement, but unwrapping problem may affect our result in some tracks, and that the differences between adjacent tracks in overlap-

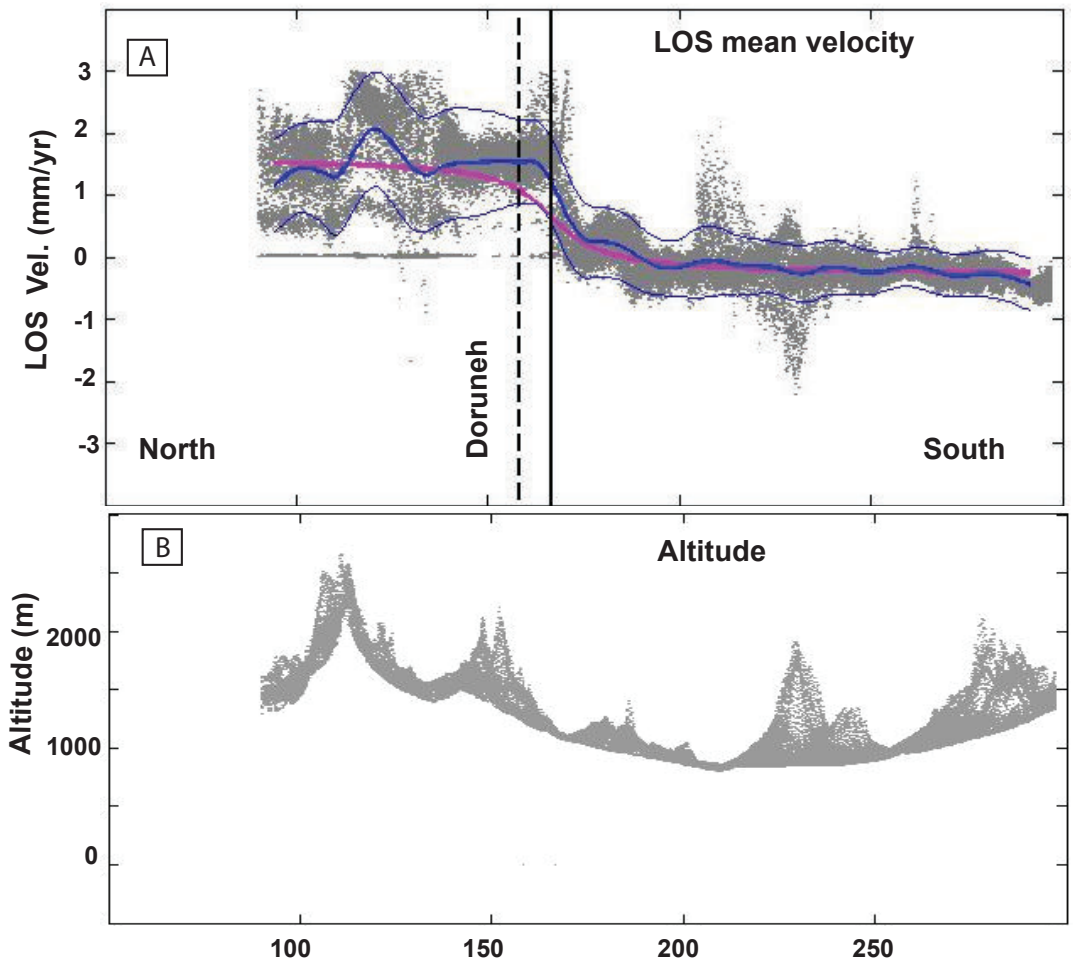

Figure 4.10 – A) Line-of-Sight velocity profile (gray dots) with 2-sigma (blue lines). The dashed black line presents the Doruneh fault and black line presents the fault which SAR signal is centered on it. B) Altitude profile corresponds to the Mean velocity porfile

ping area may be as large as the interseismic deformation which we are looking for and the inconsistency of the neighbor tracks make dominate the tectonic signal. This will be discussing in the following section.

4.6 Discussion

We used SAR ENVISAT data to measure the left-lateral interseismic slip rate on the Doruneh fault in all tracks from the west to the east, however, some geological complexity along the fault may complicate the interpretation of our results. This complexity comes from the possible thrust component in eastern part (track D120 and D392) of the Doruneh fault [Farbod et al., 2011]. This makes the LOS analysis more difficult as phase gradient may not be centered on the Doruneh fault (as in track D392 in Fig. 4.10). In addition track D392 as well as track D120 to the east shows no significant motion in particular on the EW trending, left-lateral Dasht-e-Bayaz fault (see location on figure 4.2), while this fault

has given place to two magnitude 7 earthquakes in 1968 and 1979 with clear left-lateral mechanisms. Another point to take into account is the fading out of active deformation in Central-Eastern Iran towards the Afghan border, as measured by GPS (Section 3, Walpersdorf et al. [2013]), which suggests that the amount of left-lateral movement decreases along the fault from west to east. The absence of deformation in the well-constrain track D120, and the compatibility of the other tracks with left-lateral interseismic signal are in agreement with such a decrease. This interpretation should be taken with care because of the signal variability between adjacent tracks.

Therefore, the mean velocity maps in LOS direction of 6 tracks providing a continuous spatial coverage of the Doruneh fault from longitude 56°E to 61°E do not show a clear and consistent tectonic signal having the shape of the expected interseismic deformation of a left-lateral strike-slip fault. Even if our SAR analysis is not able to give a reliable measurement of the slip rate of this fault (despite of its suitable orientation with respect to SAR LOS, the relatively arid climate and the lack of vegetation cover), we tried herebyc to estimate an upper-bound of the Doruneh slip-rate. Some upper-bound of the slip rate could be given by our observation.

Regarding the possible sources of errors, one can mention the desertic climate and sand dunes in the study region that caused a loss of coherence in parts of the SAR images and prevented us from unwrapping the images in these places. Therefore some discontinuities in the velocity maps can be created. This problem is highlighted by increased RMS misclosure and incites us to take with care the velocity gradient in track D435 in our analysis. The inconsistencies between adjacent tracks can have two main reasons: First, the correction of DEM, orbital, and stratified atmospheric errors are not certainly enough precise to detect the low interseismic deformation, and unwrapping errors are introducing a too high variability in the time series results. Second, on some tracks it may have some correlation between the interseismic tectonics signal and the topography, so that some of our corrections may be biased (by removing part of the tectonics signal or by adding artificial signal) differently from one track to another.

Overlapping band of two adjacent descending tracks should give very similar ground displacement measurement (the variation due to the slightly different look angle is small) so that comparing the overlapping bands gives an estimation of the uncertainty of the InSAR measurement:

- Comparison tracks 206- 435: differences of the order of 1 mm/yr in LOS
- Comparison tracks 435 -163: differences of the order of 1-1.5 mm/yr in LOS
- Comparison tracks 163- 392: differences of the order of 1 mm/yr in LOS
- Comparison tracks 392 -120: differences of the order of 1-1.5 mm/yr in LOS

From this comparison, we can make a rough estimation of about 1.5 mm/yr in LOS of uncertainty at the scale of the wavelength of the interseismic signal we are looking for, that is about 100km (bigger difference can be seen more locally, for instance in area

affected by strong subsidence).

It is noteworthy that when a significant regional contrast between areas north and south of the Doruneh Fault can be seen in the LOS velocity maps (like in tracks 156, 435 and 392), it is always consistent with a left-lateral displacement of Doruneh fault (even if the change of contrast is not exactly centered on the Doruneh fault that could be explained by the measurement uncertainty). This suggests that, even if the tectonics signal is below the noise of InSAR measurement, it is likely to be consistent with a left lateral displacement of the fault.

Taking into account a simple model of left-lateral displacement, and the track with the largest contrast in LOS velocity across the fault (Track 392, see Fig.4.10 where it reaches 1.5mm/year in LOS) can give the upper bound of the slip-rate. 1.5 mm/yr in LOS gives less than 4 mm/yr of horizontal velocity, assuming no vertical displacement and horizontal displacement parallel to the fault trace. Assuming that the slip on the fault is dominated by left-lateral displacement, we argue that the slip-rate of the Doruneh fault cannot exceed 4 mm/yr and is likely to be in the range of 1 to 3 mm/yr (corresponding to the range 0.5-1 mm/yr in LOS). This very rough estimation does not take into account the possible lateral variation of the slip rate along the fault, and possible thrust component on the fault, but it rather gives an upper-bound of the slip-rate. The estimation of the InSAR measurement uncertainty and how it propagates into the slip-rate estimation definitely deserve more investigation; however we think that at this stage we are able to perceive the first order of it.

4.7 Conclusion

The Doruneh fault with 700 km length and a clear surface expression is one the longest faults inside the political borders of Iran. However, its present-day kinematics is not clear in the geodetic deformation pattern. The geologic slip rate obtained based on the IRSL approach in a single site (mark site on velocity map and reference it here) yields 2.4 ± 0.4 mm/yr average slip rate over $\sim$ 10 ka. The GPS stations south and north of the Doruneh fault are sparse and not well distributed (concentrated in the east, far away from the fault in the west). The simple difference between average site velocities north and south of the fault is evaluated to 0.5 ± 1.1 mm/yr of left-lateral slip. The GPS slip rate (see section 3) is quantified to 2.1 ± 0.4 mm/yr of left-lateral slip rate using the rigid block modeling. However, the far away stations in the central and western part of the fault impose large and unique constraints on the rigid block model, while the extended regions bounding the fault to each side are probably not rigid. Therefore, the rigid block model possibly overestimates the Doruneh slip rate. Our InSAR study suggests that it should not exceed 4 mm/yr and it is likely to vary in the range of 1 to 3 mm/yr for this fault in contrast to the estimate of Pezzo et al. [2012] who obtain 5 ± 1 mm/yr left-lateral slip

rate for the central segment of Doruneh fault (see their smaller study location in Fig. 4.7). More investigation are definitely needed to be able to estimate more precisely slip rate of Doruneh fault.

Chapter 5

Present-day tectonic in North eastern Iran: Results from the Iranian GPS networks

Contents

5.1 Introduction

Northeastern Iran is one of the most densely populated parts of the country with almost 6.5 million inhabitants. The region has also an abundant historical record of destructive earthquakes. This chapter will present new, dense GPS data after the preliminary results of GPS networks in NE of Iran by Masson et al., [2007] and Tavakoli [2007] . In NE Iran, the pattern of faulting is complex and involves thrusts and left-lateral faults west of ∼58°E and right-lateral strike-slip faults east of ∼58°E. This complex faulting in NE Iran and specially the Kopeh Dagh has given place to different kinematic models which are proposed by [Hollingsworth et al., 2006] and [Shabanian et al., 2009a] to explain the regional deformation pattern (Fig. 5.1). However, in the absence of quantitative constraints it was difficult to demonstrate which model is able to describe the present-day kinematics in this zone. Hollingsworth et al. [2008] proposed that the shortening across the Kopeh Dagh is accommodated by oblique slip on range-bounding thrust faults east of 59° E, anticlockwise rotation of right-lateral strike-slip faults which cut obliquely across the range between 57°–59°E, and westward extrusion of the West Kopeh Dagh block between transpressional fault systems in the East Alborz and Kopeh Dagh-Balkan ranges (Fig. 5.1-a). According to Shabanian et al. [2009] Central Iran and western Kopeh Dagh are translated north-westward with respect to Eurasia by focalized intracontinental strike-slip faulting. Therefore the right lateral strike-slip faults (faults CF and NF in figure 5.1) can be considered as boundary between Iran and Eurasia. White arrows in figure 5.1-b present the present-day expected GPS velocity vector according to this model.

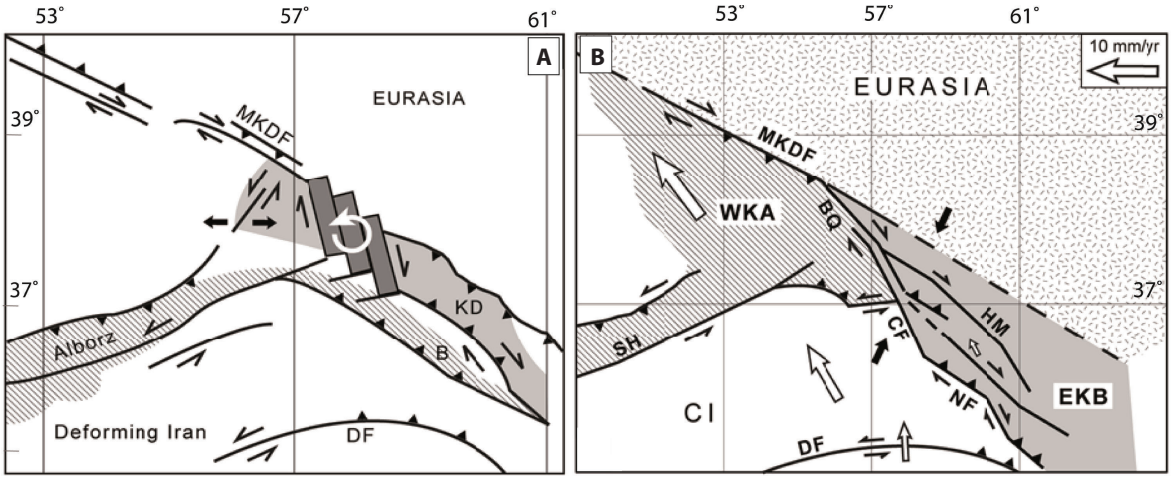

Figure 5.1 – Schematic kinematic model proposed by Hollingsworth et al., 2008 (A) and Shabanian et al., 2009(A). The abbreviations are: WKA, western Kopeh Dagh–Alborz tectonic domain, EKB: eastern Kopeh Dagh–Binalud tectonic domain, SH: Shahroud Fault system, HM: Hezar Masjed Fault system, CF: Chakaneh Fault system, MKDF: Main Kopeh Dagh Fault and NF: Neyshabur Fault system

This chapter describes the current deformation accommodation in the Kopeh Dagh region using a dense GPS velocity field based on campaign and permanent stations. Addi-

tionally, these new GPS data cover the South Caspian basin can help to better constrain the motion of this block. The South Caspian Block appears to be moving relative to its surroundings. This motion is accommodated by deformation across its boundaries, notably the Ashkabad and Astaneh-Shahroud fault systems. To calculate the slip rates at the boundaries of the South Caspian we constrain its motion relative to Eurasia and Iran. This motion has been described before both as a translation [Jackson et al., 2002]or a rigid-body rotation about an Euler pole sited east of the Caspian Sea [Djamour et al., 2010]. Finding the correct description has large implications for the slip rates on the bounding faults.

5.2 Global Positioning System constraints on the active tectonics of NE Iran and the South Caspian region

Z. Mousavi[1,2], A. Walpersdorf[1], R. T. Walker[3], F. Tavakoli[2], E. Pathier[1], H. Nankali[2],F. Nilfouroushan[4], Y. Djamour[2].

1. Institut des Sciences de la Terre, CNRS (UMR 5275), Université Joseph Fourier, Maison des Géosciences, 1381 rue de la piscine, 38400 Saint Martin d'Hères, France.
2. National Cartographic Center, Geodetic Department, Tehran, Iran.
3. Department of Earth Sciences, University of Oxford, South Parks Road, Oxford, OX1 3AN, UK.
4. Department of Earth Sciences, Uppsala University, Villavägen 16, 75236 Uppsala, Sweden.

Accepted for publication in Earth and Planetary Science Letters, July 2013

5.2.1 Summary

We present a velocity field compiled from a network of 27 permanent and 20 campaign GPS stations across NE Iran. This new GPS velocity field helps to investigate how Arabia-Eurasia collision deformation is accommodated at the northern boundary of the deforming zone. The present-day northward motion decreases eastward from 11 mm/yr at Tehran ($\sim$ 52°E) to 1.5 mm/yr at Mashhad ($\sim$60°E). N-S shortening across the Kopeh Dagh, Binalud and Koh-e-Sorkh ranges sums to 4.5 ± 0.5 mm/yr at longitude 59°E. The available GPS velocities allow a rigid-body rotation of the South Caspian about an Euler pole that is located further away than previously thought. We suggest that two new stations (MAVT and MAR2), which are sited far from the block boundaries, are most likely to indicate the full motion of the South Caspian basin. These stations suggest that NW motion is accommodated by right-lateral slip on the Ashkabad fault (at a rate of up to 7 mm/yr) and by up to 4-6 mm/yr of summed left-lateral slip across the Shahroud left-lateral strike-slip system. Our new GPS results are important for assessing seismic hazard in NE Iran, which contains numerous large population centers and possesses an abundant historical earthquake record. Our results suggest that the fault zones along the eastern Alborz and western Kopeh Dagh may accommodate slip at much faster rates than previously thought. Fully assessing the role of these faults, and the hazard that they represent, requires independent verification of their slip rates through additional GPS measurements and geological fieldwork.

5.2.2 Introduction

Active faulting in Iran results from the continental collision between Arabia and Eurasia. The distribution of earthquake epicenters (5.2) shows that most of the deformation is accommodated within the political borders of the country. GPS measurements also illustrate a similar pattern, with velocities of stations relative to Eurasia decreasing to zero at both the northern and eastern borders of Iran [Vernant et al., 2004a]. South of our study region (Fig. 5.2), the N-S right-lateral shearing between western Afghanistan (which is part of stable Eurasia) and central Iran is accommodated on N-S right-lateral faults within eastern Iran [Walker and Jackson, 2004, Meyer and Le Dortz, 2007]. Further north, however, the pattern of faulting is more complex and involves thrusts and left-lateral faults west of $\sim$58°E and right-lateral strike-slip faults east of $\sim$58°E. The pattern of faulting must also accommodate motion of the South Caspian Basin relative to its surroundings, though the form that this motion takes is debated [Jackson et al., 2002, Copley and Jackson, 2006, Djamour et al., 2010].

In recent years, constraints from GPS, earthquake investigations, and geological estimates of fault slip rate have allowed considerable advances in understanding the rates and kinematics of faulting across many parts of Iran [Tatar et al., 2002, Jackson et al., 2002,

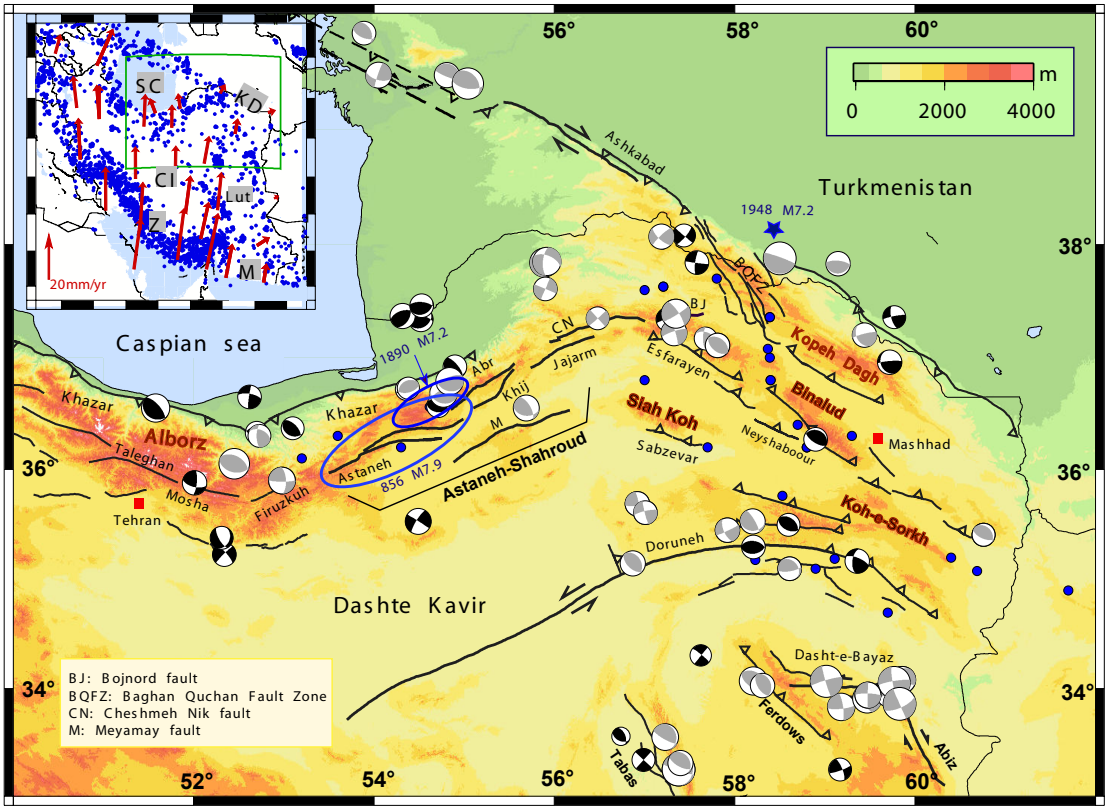

Figure 5.2 – Inset: Outline map of Iran with GPS velocities relative to Eurasia (in red; [Vernant et al., 2004b]. Epicenters of earthquakes Mw5 in the period 1976-2012 are shown as blue dots (from the Harvard catalogue http://www.globalcmt.org/CMTsearch.html). The green rectangle indicates the location of the map in the main figure. The abbreviations are CI: Central Iran, KD: Kopeh Dagh, Lut: Lut block, M: Makran subduction zone, SC: South Caspian basin, Z: Zagros. Main figure includes topographic map, known active faults and earthquake catalogue epicenters (Mw $\geq$ 5). The grey focal mechanisms are first-motion and waveform-modeled solutions from [McKenzie, 1972, Baker et al., 1993, Berberian and Yeats, 1999, Jackson et al., 2002, Walker and Jackson, 2004, Engdahl et al., 2006]. The black focal mechanisms are moment tensor solutions from the Harvard catalogue http://www.globalcmt.org/CMTsearch.html during the period 1976-2012. Historical earthquakes (blue dots) come from [Ambraseys and Melville, 1982].The blue ellipsoids and star are the location of 856 AD (M7.9), 1890 (M 7.2) and Ashkabad 1948 (M 7.2) [Ambraseys and Melville, 1982, Hollingsworth et al., 2010b].

Allen et al., 2003, Nilforoushan et al., 2003, Talebian and Jackson, 2004, Vernant et al., 2004b, Masson et al., 2005, Hessami et al., 2006, Walpersdorf et al., 2006, Tavakoli et al., 2008, Djamour et al., 2010, 2011]. Until now, however, there have been few constraints on the present-day distribution of deformation across the eastern and northeastern parts of the country. The rates of faulting are largely unknown, as is the relationship between the active faults and the overall tectonic motions. Furthermore, North Eastern Iran is one of the most densely populated parts of the country with almost 6.5 million inhabitants. The region has an abundant historical record of destructive earthquakes, including the Qumis 856 A.D. earthquake that killed 200,000 people [Ambraseys and Melville, 1982,

Hollingsworth et al., 2010b]. The widespread occurrence of significant earthquakes across NE Iran is less apparent, however, in instrumentally-recorded seismicity (e.g. Fig. 5.2); there is hence a large societal motivation in characterizing the slip directions and rates of movement across the active fault zones.

Here, we present a velocity field, composed of 47 GPS stations (20 campaign-mode and 27 permanent stations) and recorded over 11 years, which covers almost the entire NE of Iran. We use these velocities to refine estimates of the motion of the South Caspian Block relative to its surroundings, to estimate the present-day slip rate across the major fault systems of the region (making comparisons to geomorphological and geological estimates where available), and to examine the likely kinematics of faulting in NE Iran. We suggest that some of the fault zones in NE Iran may have much faster slip rates than is sometimes thought.

5.2.3 GPS data and processing

We incorporate both campaign and permanent GPS stations in our network. Campaign measurements were performed from 1999 to 2008 within a framework of French-Iranian cooperation with the support of the National Cartography Center in Tehran. Of the campaign stations, 10 (SHAM, JANA, GRME, GARD, DARG, BAKH, MAR2, KHAF, DOGH and BAJE) were installed and measured in 2004 and three other stations (BIAR, ESFN and ZVNG) were installed and measured in 2005. All these stations were re-measured in 2006 [Tavakoli, 2007]. Measurements were made with Ashtech Z12 or Trimble 4000SSI receivers with choke-ring antennas at least for 48 h. We also included five campaign stations (YAZT, SHIR, KORD, SEMN and KASH) in our study that were installed in 1999 by [Nilforoushan et al., 2003]. The campaign measurements are processed together with measurements from 27 stations of the Iranian Permanent GPS Network (IPGN). The permanent sites were installed in 2005-2006 and are all equipped with Ashtech CGRS receivers and choke ring antennas.

All campaign and IPGN sites were processed using the GAMIT/GLOBK software, version 10.4 [Herring et al., 2006] along with 28 GPS stations of the International GNSS Service (IGS) network in order to produce a stable reference frame. Daily positioning solutions were calculated along with the tropospheric zenith delays at each station every two hours from GPS phase observations, adjusting IGS final orbits and using coherent Earth orientation parameters (EOP). The variation of antenna phase centers is modeled using the absolute antenna phase center model IGS_05. The tropospheric mapping function VMF1 [Boehm et al., 2006] for tropospheric delay and FES2004 ocean tide model for ocean loading [Lyard et al., 2006] were used in the daily processing.

The daily solutions of permanent and campaign networks are combined with global daily solutions using the Kalman filter GLOBK to calculate a consistent set of coordinates

and velocities. Before estimating the velocity field, we clean all time series from outlier and offsets. Then a unique noise model for each permanent station is calculated to account for correlated errors in the time series analysis. The algorithm used to model the data noise spectrum assumes that each time series can be adequately modeled using a first-order Gauss Markov (FOGM) process noise [Gelb, 1974, Reilinger et al., 2006, Djamour et al., 2010].

The FOGM model is estimated from individual stations' time series by averaging the residuals over increasingly longer intervals that range from a minimum of 7 days to a maximum of 1/10th of the total time series span. Then this model is used to predict the site velocity uncertainty based on the time span of the time series [Reilinger et al., 2006, Djamour et al., 2010]. GLOBK could calculate the Random Walk (RW) noise model that would predict the same velocity uncertainty as the FOGM model at the time series time span interval. These RW process noise values are then used in the forward run of the GLOBK Kalman filter (using the same data as was used in the time series) to estimate site velocities and "realistic" uncertainties. Since this method of estimating site-dependent process noise is only applicable to continuous time series (as we need to be able to average over a range of time series sampling intervals), the RW process noise applied to campaign GPS sites in the North east Iran region was obtained by taking the median of the RW values for permanent sites in the region. This noise for Northeast Iran ranges from 0.32 to 1.3 $mm\sqrt{yr}$ with a median of 0.8 $mm\sqrt{yr}$ for horizontal and 1.1 to 4.3 $mm\sqrt{yr}$ with a median of 2.7 $mm\sqrt{yr}$ for vertical components. We used these median values for RW noise of campaign stations to obtain realistic velocity uncertainties. The Eurasia-fixed coordinate and velocity file of ITRF2008 [Altamimi et al., 2011] is used to establish the Eurasian reference frame and to calculate the velocity field of the Kopeh Dagh network with respect to stable Eurasia as presented in Table 5.2 and Figure 5.3.

5.2.4 Geodetic velocity field in NE Iran

The GPS stations in the southern part of our study area (at latitudes below ~34°, Fig. 5.3) show northward-directed velocities increasing linearly from zero at the eastern margin of Iran (e.g. stations SHKH, KHAF) to ~11 mm/yr (KHUR), consistent with distributed N-S right-lateral shear accommodated on N-S right-lateral faults across the eastern part of Iran south of latitude 34°N [Walker and Jackson, 2004, Vernant et al., 2004b, Meyer and Le Dortz, 2007]. The same general pattern is seen in northerly parts (about ~36°N) of the velocity field, with effectively zero velocity relative to Eurasia at Sarakhs (SARK) increasing to 11 mm/yr at Tehran (TEHR).

Stations in the NW of our network show a northwestward motion with respect to Eurasia. These northwestern stations are likely to represent motion of the South Caspian block [Djamour et al., 2010]. The South Caspian Basin is an aseismic block that is sur-

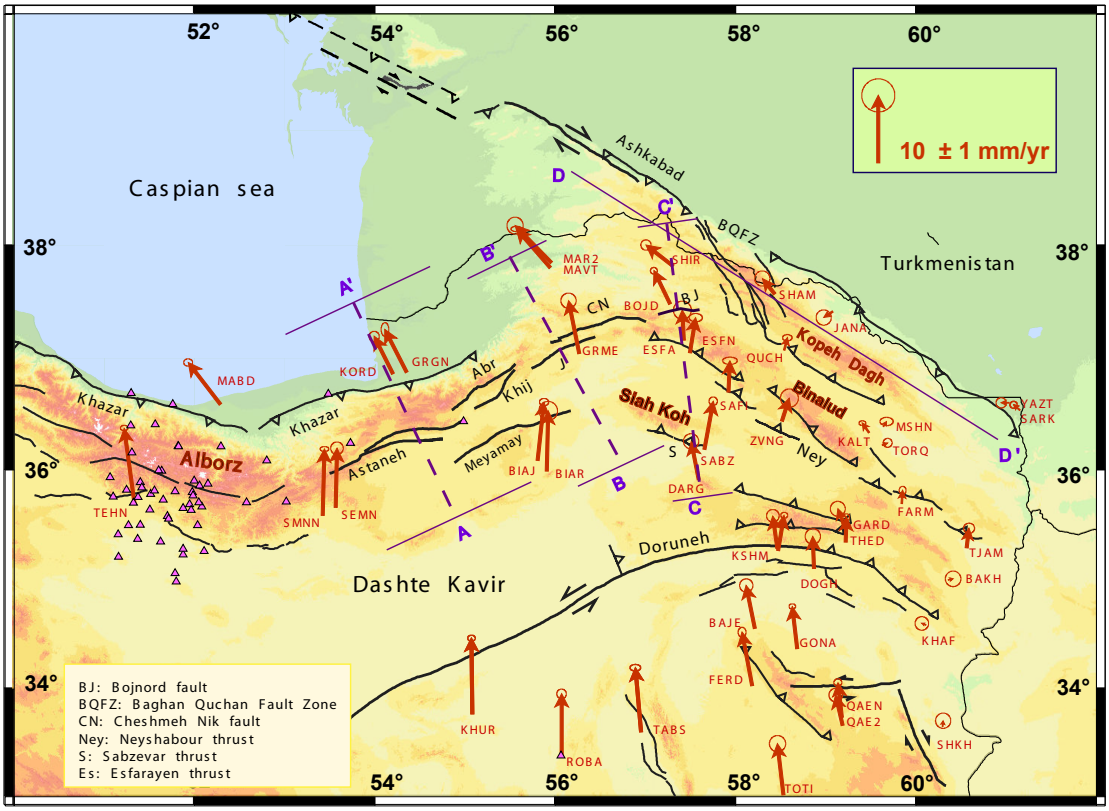

Figure 5.3 – Velocity field for the North East of Iran is shown with respect to Eurasia. The velocity field includes both campaign and permanent GPS stations. The scale vector corresponds to 10 mm/yr. The triangle symbols represent the GPS stations from Djamour et al., (2010), which are included in our block modeling analysis. The boxes AA', BB', CC' and lines DD' indicate the locations of cross sections presented in Fig. 5.8.

rounded by belts of intense earthquake activity [Jackson et al., 2002, Hollingsworth et al., 2008]. The basement of the South Caspian Basin may be thick oceanic crust [Mangino and Priestley, 1998] that is beginning to subduct beneath the continental crust of the northern Caspian Basin. The South Caspian Block appears to be moving relative to its surroundings, with this motion accommodated by deformation at its boundaries, along which the Ashkabad and Astaneh-Shahroud fault systems are situated (Fig. 1). However, to calculate the rates of slip at the boundaries of the South Caspian we must constrain its motion relative to Eurasia and Iran. This motion has been described both as a displacement with velocity and azimuth of the Caspian basing relative to its surroundings areas [Jackson et al., 2002] and a rigid-body rotation about an Euler pole sited east of the Caspian Sea [Djamour et al., 2010]. Finding the correct description has large implications for the slip rates calculated from the GPS measurements. This motion has been described both as a translation [Jackson et al., 2002] and a rigid-body rotation about an Euler pole sited east of the Caspian Sea [Djamour et al., 2010]. Finding the correct description has large implications for the slip rates calculated from the GPS measurements 5.7.

Site	Long	Lat	Ve	Vn	sig Ve	sig Vn	Corelation	Time span
BAJE	58.21463	34.55838	-1.12	6.4	0.4	0.4	0	2004, 2006
BAKH	60.36017	35.00179	0.7	0.19	0.47	0.47	-0.001	2004, 2006, 2007
BIAJ	55.80518	36.08609	1.11	8.66	0.28	0.22	-0.001	2006 - 2011
BIAR	55.90606	35.98844	0.24	8.94	0.56	0.57	-0.013	2005,2006, 2007
BOJD	57.27158	37.48033	-2.24	4.96	0.21	0.2	-0.002	2005 - 2011
DARG	57.58928	35.91483	-1.1	5.64	0.46	0.46	-0.005	2004, 2006, 2008
DOGH	58.86932	35.1084	-0.18	4.73	0.46	0.47	0.002	2004, 2006, 2007
ESFA	57.42698	37.1588	-0.19	4.46	0.54	0.55	-0.002	2005,2006, 2007
ESFN	57.49458	37.04951	1.06	5.24	0.4	0.25	-0.002	2006 - 2011
FARM	59.84298	35.69612	0.27	1.99	0.21	0.24	-0.002	2005 - 2011
FERD	58.18307	34.03065	-1.29	7.96	0.24	0.3	0	2006 - 2011
GARD	59.19725	35.49547	-0.85	2.53	0.45	0.45	-0.002	2004, 2006
GOLM	59.24776	36.55822	1.37	3.45	0.3	0.2	-0.002	2005 - 2011
GONA	58.68354	34.37307	-0.58	6.28	0.2	0.16	-0.003	2005 - 2011
GRGN	54.35327	36.87576	-3.06	6.36	0.23	0.41	0	2006 - 2011
GRME	56.26434	37.04163	-1.56	7.83	0.46	0.46	-0.001	2004, 2006
JANA	59.07557	37.41278	-1.31	-0.84	0.46	0.46	-0.001	2004, 2006
KADN	58.87825	35.59173	-2.41	2.16	0.46	0.26	0	2005 - 2011
KALT	59.64043	36.3913	0.6	0.76	0.4	0.25	-0.001	2005 - 2011
KASH	58.46361	35.29268	-0.91	4.79	0.38	0.38	0	1999, 2001, 2005
KHAF	60.1103	34.58881	-0.36	0.3	0.41	0.41	0.002	2004, 2006, 2007
KHUR	55.08126	33.76931	0.1	11.29	0.23	0.18	-0.002	2006 - 2011
KORD	54.19946	36.86046	-2.89	5.61	0.31	0.31	-0.002	1999, 2001, 2004, 2005, 2006
KSHM	58.473	35.27057	1.03	5.24	0.2	0.18	-0.002	2005 - 2011
MABD	52.28515	36.5884	-4.62	6.23	0.27	0.22	-0.001	2005 - 2011
MAR2	55.95556	37.8445	-5.39	5.5	0.49	0.51	0.001	2004, 2006, 2007
MAVT	55.94386	37.80098	-4.8	5.78	0.34	0.16	-0.001	2006 - 2011
MSHN	59.47982	36.33472	-0.94	1.45	0.21	0.14	0.001	2002-2011
NFRD	59.40127	36.45012	2.22	4.69	0.31	0.19	-0.002	2007 - 2011
NISH	58.82026	36.20704	-0.54	4.7	0.25	0.27	-0.001	2005 - 2011
QAE2	59.18771	33.66336	-0.93	4.53	0.41	0.41	0.001	2004, 2006
QAEN	59.17603	33.73995	-0.4	5.16	0.24	0.23	-0.002	2005 - 2011
QUCH	58.53728	37.07071	0.63	1.89	0.29	0.19	-0.002	2005 - 2011
ROBA	56.06975	33.36854	-0.12	9.36	0.29	0.29	-0.001	1999, 2001, 2004, 2005, 2006, 2007
SABZ	57.65283	36.18494	1.47	7.17	0.25	0.26	-0.002	2005 - 2011
SAFI	57.92129	36.69815	0.41	4.69	0.44	0.22	-0.001	2006-2011

Figure 5.4 – Site coordinates and horizontal velocities (mm/yr) with respect to Eurasia and observation span for North East Iran GPS stations. The stations with star are permanent stations of IPGN network. 10 stations (GRGN, KORD, MABD, ROBA, SEMN, SHIR, SMNN and TEHN) are published in Djamour et al. 2010 using the reduced data set.

[Jackson et al., 2002] use a plate-closure model to predict a rigid-body motion of the South Caspian Block relative to Eurasia at a rate of 7-10 mm/yr and azimuth 300°. [Copley and Jackson, 2006] revised these estimates to $\sim$11 $\pm$ 2 mm/yr at an azimuth of 330-340°. Copley and Jackson's (2006) estimate of the South Caspian motion yields

4.5-5.5 mm/yr of shortening and left-lateral strike-slip across the Alborz and 7-11 mm/yr of right-lateral strike-slip across the Ashkabad fault (assuming that all fault motion is localized onto this one structure). An alternative interpretation of the kinematics of the South Caspian was provided by [Djamour et al., 2010], who constrained its motion with GPS stations near the southern shore of the Caspian sea (TKBN, KORD, GRGN, MAHM, NKAD) and a sixth (SHIR) sited at the eastern end of the eastern Caspian lowlands. From these six stations they estimated the motion of the block as a clockwise rotation relative to Eurasia with an Euler pole located much closer to the basin at 59.1° E and 40.4° N (Fig. 5.5). The presence of this rigid-body rotation has a significant effect on the slip rates calculated for the fault zones that surround the block. For instance, using the block motions calculated by [Djamour et al., 2010], a right-lateral slip rate of only ∼3 mm/yr is calculated for the Ashkabad fault; a figure that is less than half that calculated by [Jackson et al., 2002] and [Copley and Jackson, 2006], and which has large implications for the assessment of hazard. To refine estimates of the motion of the South Caspian we have added data from 2 new permanent GPS stations (BOJD and MAVT), one new campaign station (MAR2), and have updated the velocity for station SHIR, which is now shown to be faster and directed more to the west than previously estimated. Adding these new and updated stations yields an Euler pole for rotation of the South Caspian that has moved 400 km to the NW from the pole calculated by [Djamour et al., 2010] to lie at 59.1° E and 40.4° N (Fig. 5.5). However, even with the revised Euler pole, there are still large residuals between the motions predicted from the block model and the observations from the MAVT and MAR2 stations (Fig. 5.5).

Much of the difficulty in estimating the motion of the South Caspian block is that most of its interior is covered by water, such that most measurements are made at its boundaries, in locations that may be contaminated by elastic strain accumulation. For instance, the SHIR and BOJD stations are sited within the central Kopeh Dagh, in a region of high topography, and in which large earthquakes have occurred in recent decades (Figs. 5.2 and 5.3). It is hence doubtful that they are representative of the full motion of the South Caspian. Similar arguments can be made for the stations along the southern boundary of the South Caspian, which are all situated close to the deforming Alborz range and therefore may be affected by elastic deformation at the block boundary. The two new stations MAVT and MAR2 are thus extremely important, given the uncertain degree to which any of the other GPS stations are representative of the motion of the interior of the South Caspian. Both are situated within a region of low-lying topography far from the major fault systems, and are therefore the most likely to be representative of the block motion. These stations, MAVT (permanent) and MAR2 (campaign) are located within 3 km of each other and are sited on pillar constructions. The time series of MAVT station does not show any outliers or jumps in five years of measurement. Their individual velocities (∼7 mm/yr at 317°N relative to Eurasia) are coherent and are comparable to

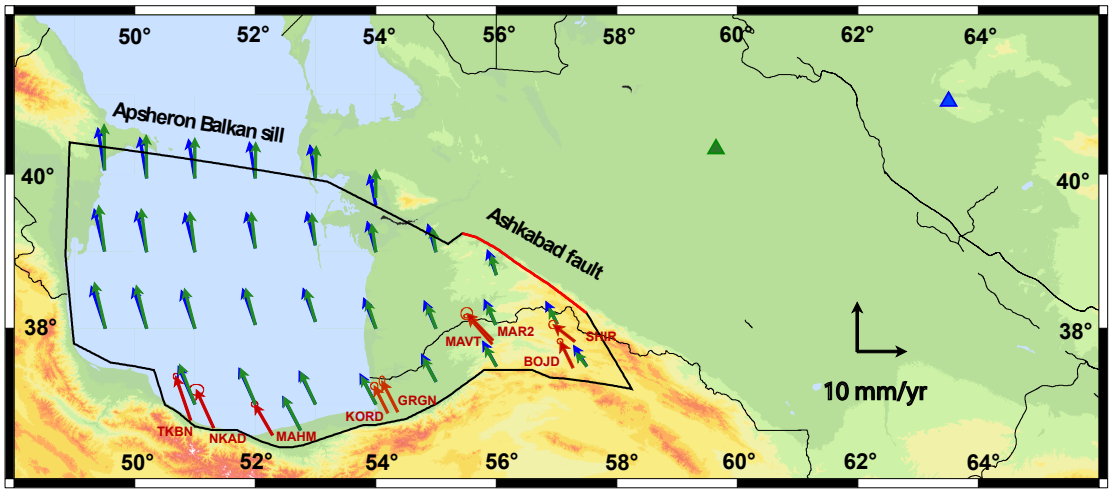

Figure 5.5 – Map showing the location of South Caspian Euler pole respect to Eurasia and the predicted block motion without taking into account the interseismic elastic strain along the block boundaries. The green vectors and Euler pole (represented by a triangle) show the predicted block motion of the SCB using 6 GPS stations (GRGN, KORD, MAHM, NAKD, SHIR and TKBN) by [Djamour et al., 2010]. The blue vectors and triangle indicate the predicted block motion of the SCB using 9 GPS stations (BOJD, GRGN, KORD, MAHM, MAR2, MAVT, NAKD, SHIR and TKBN). Note that there is still a large difference between the predicted and observed motion of stations MAVT and MAR2, which are the only stations to lie well within the interior of the block.

the 7-10 mm/yr and azimuth 300°N estimation of the South Caspian motion of [Jackson et al., 2002] but clearly lower than the $\sim 11 \pm 2$ mm/yr at an azimuth of 330-340° proposed by [Copley and Jackson, 2006].

Taking only the two coherent MAR2 and MAVT velocities to represent the motion of the South Caspian with respect to its surroundings yields upper limits on the slip rates across the Shahroud and Ashkabad faults. By using all available GPS stations to evaluate a rigid South Caspian block motion we obtain a clockwise rotation about an Euler pole at 63.58° E and 41.05° N, yielding lower fault slip rates at the block boundaries.. In the following discussion, we quantify the lower and the upper limits of relative motion across block boundaries by presenting rates computed both from a rigid block model constraint by all available GPS stations and from local profiles of along-fault and across-fault changes in velocity that do not take into account any block rotations.

Changes in the magnitude and orientation of velocities within the GPS network near active faults can be fitted by an arctangent function that is characteristic for elastic strain accumulation [Okada, 1985]. GPS station velocities on profiles across the Ashkabad and the Shahroud fault systems are plotted in Figs. 5.3 and 5.8. These profiles allow us to provide estimates of the cumulative slip rate across several of the main faults but, because the GPS measurements are still rather sparse, they do not allow us to assign slip rates to individual fault strands within these zones. Our GPS velocities are also used to constrain a simple, two-dimensional (2-D) elastic half-space model of rigid block kinematics (using the Defnode code: [Meade et al., 2002, McCaffrey, 2002, Meade and Hager, 2005, Reilinger et al., 2006, Djamour et al., 2010]. We combine our solution with the velocity field of [Djamour et al., 2010] for the Alborz (station locations shown as pink triangles, Fig. 5.3) to be able to constrain the South Caspian block and the Alborz block. SHIR has a different value in our work as it now has one more measurement epoch in comparison with [Masson et al., 2007] and [Djamour et al., 2010]. No significant earthquake has occurred during the time interval of the measurements in the Alborz [Djamour et al., 2010] and Kopeh Dagh that could affect the GPS velocity field.

For the rigid block model, we define five blocks: The South Caspian Basin (SCB), the Alborz (ALB), the South Doruneh Block (SDB), the Central Iran Block (CIB) and the Eurasian Block (EUB) (Fig. 5.6). Their boundaries are related to mapped faults, seismicity, and historic earthquakes. SCB is defined using 9 stations (BOJD, GRGN, KORD, MAHM, MAR2, MAVT, NKAD, SHIR and TKBN).The block boundaries coinciding with active faults are shown in dark gray lines while other block limitation that are necessary to close the block boundaries are presented in dotted lines in Fig. 5.6. We used the DEFNODE code by [McCaffrey, 2002] to solve for relative block motions by adjusting an Euler pole to the GPS motions within a same block in a least-square sense. We assume that all active faults along the block boundaries are locked to a depth of 15 km, so, realistically, some elastic deformation is taken into account along the block boundaries. The model allows no permanent deformation of the blocks or slip on unconnected faults; this implies that all the faults used must be on a block boundary [Djamour et al., 2010]. The WRMS values for estimation of Euler vectors relative to Eurasia for Alborz, South Caspian Basin, Central Iran and South Doruneh blocks are 0.91, 1.07, 1.03, 1.09 mm/yr, respectively, with no significant systematic residuals. The slip rates estimated from a block model using the DEFNODE code vary usually by approximately ± 1 mm/yr according to a statistical study [Karakhanyan et al., 2013]. Thus we consider 1 mm/yr as uncertainty of the fault slip rates computed by rigid block modeling.

In the following, we examine the constraints that our GPS measurements introduce for the rates of fault slip in individual parts of NE Iran. We present both the slip rates obtained from the kinematic block modeling, as described above, and from profiles of along-strike and across-strike velocity change across the main fault zones. The profiles

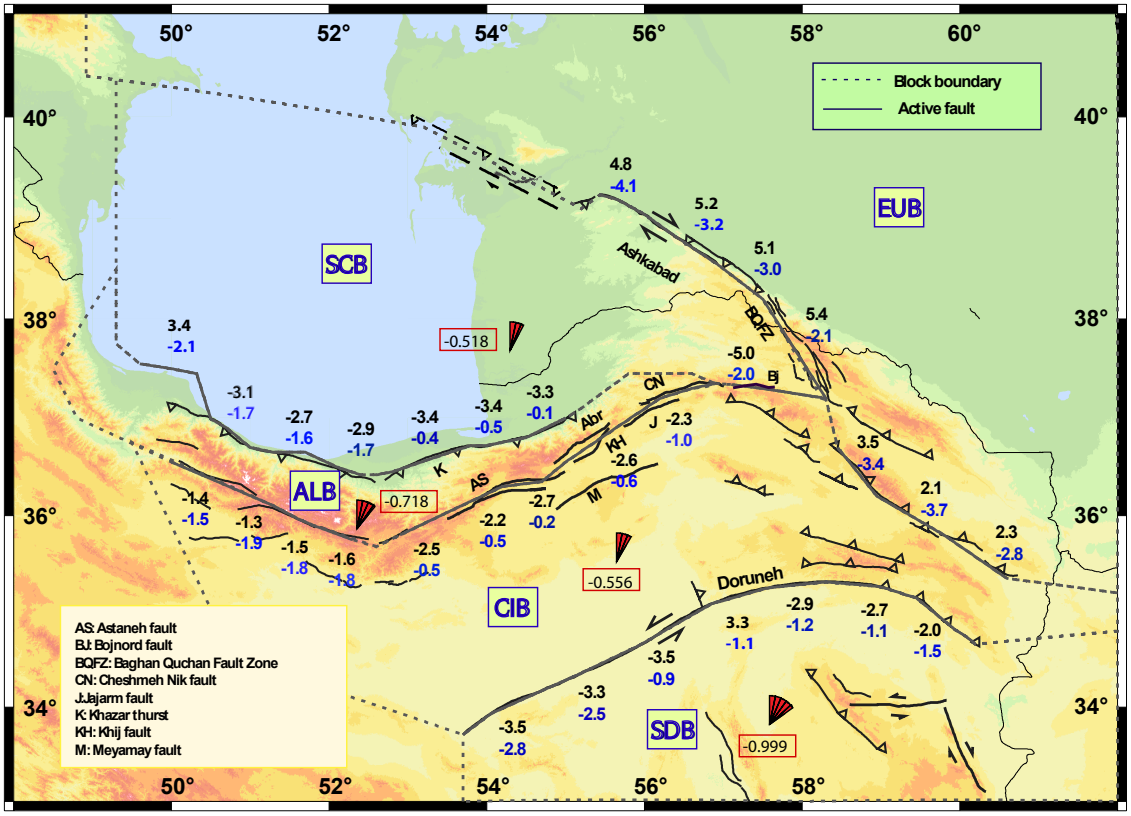

Figure 5.6 – Map showing slip rate variability (mm/yr) along the active faults from rigid block modeling. The upper values show the strike-slip component with (positive indicates right-lateral slip). The lower values indicate the fault-perpendicular slip rates (negative values indicate shortening). Dark gray lines represent active faults and dotted lines show block boundaries. The blocks are ALB: Alborz, CIB: Central Iran, EUB: Eurasian, SCB: South Caspian and SDB: South Doruneh blocks. Numbers inside the red rectangles are GPS block rotation rates in /Ma, in the center of each block, calculated from block modeling with locked faults. Counter clockwise rotation sense is positive.

assume that no significant rigid-body rotation occurs in the South Caspian. In Section 4, we compare the GPS-derived rates with existing late Quaternary slip rate measurements. All GPS and late Quaternary rates are listed in Table 5.7.

a) LUtEastern Alborz and the Astaneh-Shahroud strike-slip fault system

Earthquake slip vectors and large-scale geomorphology imply that deformation across the eastern Alborz is spatially separated (partitioned) into components of shortening on the Khazar thrust at the northern margin of the range and left-lateral strike-slip across the Shahroud fault along the southern slopes of the mountains [Jackson et al., 2002, Tatar et al., 2007, Hollingsworth et al., 2008, 2010a]. The Shahroud fault system is itself composed of a series of NE-SW trending segments [Hollingsworth et al., 2008, Javidfakhr et al., 2011a]. Along much of its length, the Shahroud fault system is composed of overlapping parallel strands that all display geomorphic indications of recent faulting (Fig. 5.2,

Fault name	Geodetic (mm/yr)	Block modelling (mm/yr)	Geologic (mm/yr)	Geologic time (kyr)
Shahroud Abr&Khij at 55°E Cheshmeh & Jajarm at 56°E	4.1- 6.5 LL	2.4± 1 LL, 0.8± 1 SH	3-4 (Abr) + 1-3 (Khij) LL (13)	115 ± 14 (13)
Astaneh	4.3±0.5 LL, 1.8± 0.8 SH	2.5± 1 LL, 2±1 LL (10)	1-7-2.5 * LL (12) , ~2 LL (14)	32–55 (14)
Eastern Khazar thrust		3.3±1 LL, 2-3 SH (10), 5±2 LL (10)	-	-
Bojnord	4.1 ± 1.5 LL	5.0± 1 LL,2.0±1 SH	-	-
Ashkabad	6.7± 0.5 RL, 1.5-3.5 SH,~3 RL (10), 5-12RL (16)	5.1±1 RL, 3.1± 0.2 SH, 3±1 RL (10)	4* RL (1), 3-8* RL (2), ~5.6* RL (9)	-
Baghan	4.7± 0.8 RL, 1.2±0.7 SH	5.4± 1 RL, 2.1± 1 SH	2.8 ± 1 RL (8), 1*(4)	280 ± 16 (8)
Quchan			4.3 ± 0.6 RL(8), 1.5*(4)	83 ± 4 (8)
Bajgirab			1.5 RL *(4)	-
Eastern Kopeh Dagh	2.4 ± 0.5 SH	2.7± 1 RL , 3.3± 1 SH	-	-
Binalud			2.4±0.5 (15) RL, 2.8±0.6 (15) SH	2.8±0.6 (15)
Kuh sorkh& Nishabur (59°E)	1.4±0.7 SH		0.4-1.7 SH (11)	24.1 ± 1.9 (11)
Siah Koh & Sabzevar	1.0±0.5 SH		<1 SH (3), 0.4-0.6 SH (11)	9-13 (3), 11 ± 2 (11)
Doruneh	~ 1 mm/yr LL	2-3.5 LL, 1.5-2.8 SH	2.4±0.3 (3)	10 (3)

Figure 5.7 – Table 2: Long term and current fault slip rates of the major active faults in North East Iran, 1. Trifonov 1978 ; 2. LyberisManby 1999 ; 3. Fattahi et al. 2006b ; 4. Hollingsworth et al. 2006 ; 5. Fattahi and Walker 2007 ; 6. Masson et al 2007 ; 7. Hollingsworth et al, 2008 ; 8. Shabanian et al. 2009a ; 9. Siame et al 2009 ; 10. Djamour et al 2010 ; 11. Hollingsworth et al, 2010a ; 12. Hollingsworth et al, 2010b ; 13. Javidfakhr et al. 2011 ; 14. Rizza et al. 2011; 15. Shabanian et al. 2012; 16. Walters et al. 2013. Numbers with star are the geologic slip rate without age constraint. The abbreviations are SH: shortening, LL: left lateral and RL: rigcht-lateral.

[Hollingsworth et al., 2008, 2010a, Javidfakhr et al., 2011a,b]. Several of these segments are likely to be associated with historical earthquakes. For instance, the Astaneh segment may have been responsible for the devastating 856 A.D. Qumis earthquake that killed 200,000 people and the 1890 Shahroud earthquake, with a magnitude of ∼7, is likely to have occurred on the Abr fault segment ([Hollingsworth et al., 2010a]; Fig. 5.2). To evaluate the strike-slip and shortening components across the eastern Alborz, and to examine whether fault slip rates may vary along the strike of the range, we projected fault-parallel and fault-normal components of GPS velocities onto profiles drawn perpendicular to the faults (AA', BB' and CC', Fig. 2). Profile AA' (Fig. 5.8) indicates 4.5± 0.5 mm/yr of left-lateral slip and 1.8±1.0 mm/yr of shortening across the Alborz at the longitude of the Shahroud fault zone. The block modeling approach provides lower estimates of 2.5± 1.0 mm/yr of left-lateral motion across Shahroud fault zone and 3.3 ± 1.0 mm/yr of left-lateral slip across Khazar thrust between longitude of 53°E to 56°E. There is no significant shortening across the zone (Fig. 5.6).

Further east, left-lateral strike-slip and shortening is accommodated across the Jajarm, Cheshmeh-Nik and Meyamay faults and Khazar thrust (Figs. 5.2 and 5.3). Fault-parallel velocities projected onto profile BB' (Fig. 5.8) show that the summed left-lateral strike-slip rate in this region is 6.5 ± 0.3 mm/yr. There is no significant shortening component across this part of the eastern Alborz (Figs. 5.3 and 5.8). Discriminating the individual slip rates of the Meyamay, Jajarm and Cheshmeh-Nik faults is difficult, due to their close

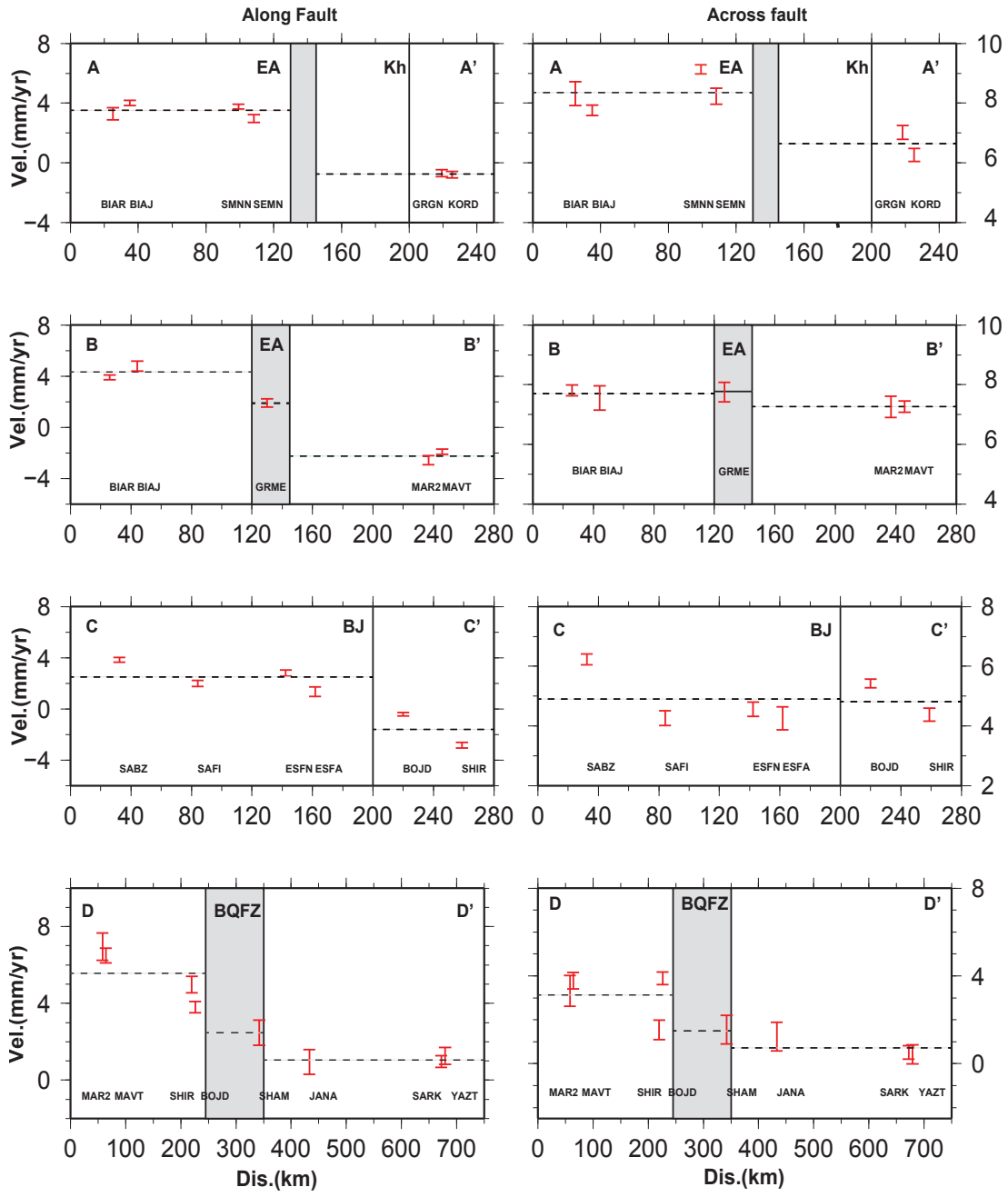

Figure 5.8 – Along (left) and across (right) velocity components (mm/yr) along profiles AA', BB', CC', and DD'. (See Figure 2 for location of profiles). Major active faults are marked as black lines and regions of known distributed faulting are highlighted in grey. Faults are labeled as in Figure 1. East Alborz is Astaneh-Shahroud fault which is the major fault in the eastern Alborz. BQFZ is Barkharden-Quchan Fault Zone.

spacing. Station GRME is located very close to the Jajarm fault, and therefore, depending on the locking depth of fault, it may be inside the deformation zone of this fault. If it is locked to a depth of less than 10 km, the GRME station can be located outside of the deformation zone. Then this station can be used to resolve the shear on individual faults. This would yield 4.1± 0.9 mm/yr of left-lateral movement for the Jajarm and Cheshmeh-Nik faults and 2.5±0.9 mm/y for the eastern part of Meyamay fault. However, the estimate of slip rate for the Jajarm and Cheshmeh-Nik faults may be underestimated, and that of the Meyamay fault overestimated, respectively. Our block model yields 2.5±1.0 mm/yr of left-lateral slip and 1.0±1.0 mm/yr of shortening for the Cheshmeh-Nik-Jajarm system and for the Abr-Khaj fault system in its prolongation to the west.

At the eastern end of the Shahroud fault system, profile CC' shows 3.9 ±1.4 mm/yr of left-lateral and 0.7±1.0 mm/yr of shortening in the vicinity of Bojnord (Figs. 5.3 and 5.8). NE-SW left-lateral faults are visible in the geomorphology and geology in the vicinity of Bojnord but no late Quaternary slip rate estimates exist on these structures [Hollingsworth et al., 2008, 2010b, Shabanian et al., 2009a,b].

b) Western Kopeh Dagh and the Ashkabad fault

The South Caspian basin, which is an apparently rigid block of possible oceanic origin, is moving relative to both Eurasia and to central Iran [Jackson et al., 2002, Masson et al., 2007, Tavakoli et al., 2008, Djamour et al., 2010]. Relative motion between the eastern part of the Caspian basin (in the eastern Caspian lowlands) and stable Eurasia to the north appears to be predominantly accommodated across the Ashkabad fault zone, which is the only major structure within this part of the collision zone, and which runs from the northern part of the eastern South Caspian basin to the central Kopeh Dagh (Fig. 5.2). The Ashkabad fault is located on the northern side of the eastern South Caspian basin and northwest of the Kopeh Dagh. The fault is a NW-SE right-lateral strike-slip fault with a thrust component and may have produced a large destructive earthquake (M=7.2) in 1948 at Ashkabad [Trifonov, 1978, Priestley et al., 1994, Allen et al., 2004, Hollingsworth et al., 2008].

The variation of GPS velocities along profile DD' (Figs. 5.3 and 5.8) from SARK station on the Turan shield to MAVT/MAR2 stations in the Kopeh Dagh west of the Quchan fault zone (Fig. 5.3) indicates ∼7 mm/yr of range-parallel extension along the trend of the Kopeh Dagh and Ashkabad fault. If the South Caspian motion relative to Eurasia can be represented by a rigid-body translation (as we describe near the beginning of Section 3), this extension will represent the westward extrusion of the South Caspian Basin with respect to Eurasia. As we have no GPS measurements from the other side of the border in Turkmenistan we assume that the northern side of the Ashkabad fault has zero velocity with respect to Eurasia (as implied by the near zero velocity of YAZT further east, and by the lack of seismicity within the Turan platform). The variation of

GPS velocities along profile DD' indicates 6.7 ± 0.5 mm/yr of right-lateral slip parallel to the Ashkabad fault and 3.4 ± 1.0 mm/yr of shortening perpendicular to it at longitude of ∼56° (MAR2 and MAVT stations). These values decrease eastwards along the range, with 4.3 ± 0.5 mm/yr of right-lateral movement at station SHIR (consistent with the 3 ± 1 mm/yr estimated for the Ashkabad fault by Masson et al. (2007) using the SHIR station alone). There is also 2.6± 1.0 mm/yr of shortening at longitude 57°E (SHIR station). The component of velocity parallel to the Ashkabad fault decreases rapidly towards its eastern end with only ∼2.4 mm/yr of right-lateral slip at the longitude of station SHAM. Our block model yields 5.1± 1.0 mm/yr of right-lateral slip and 3.1±1.0 mm/yr of shortening across the Ashkabad fault zone. These values are higher than those calculated in the block model of [Djamour et al., 2010]. The differences arise both from the inclusion of more stations to define the south Caspian block and more measurement epochs to refine some of the older stations. However, the block model estimates are again substantially lower than those estimated from the profiles, which neglect any influence of rigid-body rotation of the South Caspian relative to Eurasia.

Support for a relatively fast slip rate on the Ashkabad fault comes from an estimate of 5-12 mm/yr, with a best-fit at 9 mm/yr, obtained from the accumulation of interseismic strain imaged with InSAR [Walters et al., 2013]. The interseismic strain-rate measured across the Ashkabad fault thus agrees with our GPS-derived estimate of 6.7 ± 0.5 mm/yr for the right-lateral slip rate on the central Ashkabad fault and provides additional support that the motion of the South Caspian Basin may approximate as a rotation about a far-away Euler pole, corresponding to a motion at a rate and direction represented by stations MAR2 and MAVT.

c) Central Kopeh Dagh and the Barkharden-Quchan fault zone

The central Kopeh Dagh is cut by a series of four major NNW-SSE right-lateral strike-slip faults of the Barkharden-Quchan Fault Zone (BQFZ) that are named, from west to east, the Shirvan, Baghan, Quchan and Dorvadam faults [Hollingsworth et al., 2006, Shabanian et al., 2009a]. [Hollingsworth et al., 2006] proposed that the faults accommodate N-S convergence by a combination of right-lateral faulting and anticlockwise block rotation about a vertical axis, whereas [Shabanian et al., 2009b] suggest instead that Central Iran and the Kopeh Dagh are translated northwestward with respect to Eurasia by localized strike-slip faulting through the BQFZ.

Approximately 4.5 ±1.2 mm/yr of N-S shortening is accommodated across the central Kopeh Dagh (the northward velocity of stations ESFA/ESFN with respect to Eurasia) (Fig. 5.2). However, our GPS stations are too sparse to estimate the slip rate of the individual faults within the BQFZ, and we instead estimate the overall motions across the zone. Fault-parallel and fault-normal velocities calculated from the block modeling for the BQFZ indicate 5.2± 1.0 mm/yr of right-lateral displacement and 2.1± 1.0 mm/yr

of shortening summed across the zone (Figs. 5.6 and 5.8 [Masson et al., 2007] used the difference in velocity between stations SHIR and MSHN to estimate a slip rate for the BQFZ. They obtained 3± 1mm/yr of elongation along-strike of the Kopeh Dagh at the longitude of SHIR station (57° E).

d) The eastern Kopeh Dagh, Binalud and Koh-e-Sorkh ranges

Northward-directed GPS velocities relative to Eurasia show that contraction across NE Iran is accommodated in the eastern Kopeh Dagh and, further to the south, across the Binalud, Siah Koh and Koh-e-Sorkh ranges (Fig. 5.2; [Hollingsworth et al., 2006]. It is probable that additional shortening is accommodated on faults south of Koh-e-Sorkh and on additional structures within NE Iran (e.g [Hollingsworth et al., 2010a]). The amount of shortening varies with longitude, with the northward velocity with respect to Eurasia decreasing eastwards, reaching zero near the Afghan border. At longitude ∼59°E we estimate a total of 4.5± 0.5 mm/yr of N-S shortening between stations KSHM (or THED) and YAZT. Our estimate refines the previous rate of 5.0±0.9 mm/yr by [Masson et al., 2007]. The wide distribution of active faulting and seismicity within the region is visible in Fig. 5.2.

A number of permanent and campaign stations were installed in this eastern part of our area in order to provide details of strain accumulation in the vicinity of the large cities of Mashhad and Nishabur. However, the GPS data in this part of our network are affected by high rates of subsidence caused by water extraction. For instance, using GPS, InSAR and leveling data, [Motagh et al., 2007] measured 15 cm/yr of subsidence in the Mashhad Valley during the period 2003-2005. Our GPS vertical velocity estimations can give the gross value of subsidence for this area. We obtain 214, 89, 51, 9 and 3 mm/yr of subsidence for stations TOUS, NISH, NFRD, GOLM and KALT, respectively. Although some of these stations yield horizontal velocities that are consistent in magnitude and azimuth with surrounding stations, the horizontal movements can potentially be influenced by the subsidence of the area and therefore we do not use them in our analysis.

According to block modeling, there is 2.4-3.5 mm/yr of right-lateral slip and 2.7-3.3 mm/yr of shortening across the Binalud and Kopeh Dagh region (Fig. 5.6). The difference between the velocities of ZVNG and SARK/YAZT, located respectively to the south and north of the ranges, indicates 2.4 ± 0.5 of shortening across the Binalud and the eastern part of Kopeh Dagh at a longitude of ∼59°E. The distribution of the GPS velocities (Fig. 2) suggests that most of this deformation may accumulate in the Binalud rather than within the Kopeh Dagh region. The strike-slip and shortening deformation in this area may be partitioned on right-lateral and thrust faults. The strike-slip component might be accommodated on one single fault (the Nishabur fault, for instance), which is consistent with the model proposed by [Shabanian et al., 2009b], or on right-lateral faults within the Binalud mountains [Hollingsworth et al., 2010a]. [Hollingsworth et al., 2010a] determined

the late Quaternary rate of shortening across the Nishabur fault to be 0.4-1.7 mm/yr by OSL dating of vertically displaced alluvial terraces. Shabanian et al. (2012) provide a larger estimate of 2.4±0.5 and 2.8±0.6 mm/yr for right-lateral and reverse components of slip (corresponding to an oblique slip rate of 3.6±1.0 mm/yr) across the Nishabur fault using in situ-produced ^{1}0Be exposure dating. The rates calculated by [Shabanian et al., 2012] suggest that most of the shortening between ZVNG and SARK/YAZT is accommodated across the Nishabur fault, whereas the lower estimate by [Hollingsworth et al., 2010a] indicates that other structures in the region may still be important. Earthquakes within the region east of longitude ∼57°E mostly have reverse faulting mechanisms (Fig. 5.2). The earthquake slip-vector azimuths are directed N to NNE, orthogonal to the local strike of the range-bounding reverse faults, and suggesting that right-lateral strike-slip faulting occurs within these ranges as a consequence of oblique slip [Hollingsworth et al., 2008].

The 1.0 ± 0.6 mm/yr difference in velocity between stations GONA and KSHM is likely accommodating on reverse faults between Kashmar and Gonabad in accommodating shortening. Further west, the difference between DARG and SAFI stations indicates possible activity of 1.0 ± 0.5 mm/yr of shortening across the Siah Koh mountain belt and the Sabzevar reverse fault (Fig. 5.3). The SABZ station is located exactly on the Sabzevar thrust, so it is not possible to separate the contributions to the deformation from the Sabzevar fault and other potential faults within the Siah Koh mountain range. [Fattahi et al., 2006a] estimate a Holocene shortening rate of 0.4-0.6 mm/yr across the Sabzevar fault. However, a rate of ∼1 mm/yr is possible if the reverse fault flattens into a decollement at depth [Hollingsworth et al., 2010a].

South of latitude 36° N the major structures are the E-W Doruneh and Dasht-e-Bayaz left-lateral faults. [Fattahi et al., 2006b] estimate ∼ 2.5 mm/yr for the Holocene left-lateral slip rate across the Doruneh fault. Our block model yields ∼2mm/yr of left-lateral slip along the eastern part of the Doruneh fault, rising to 3.5 mm/yr in the west.

5.2.5 Discussion

Our geodetic measurements add new constraints on the rates of faulting and the present-day kinematics of major fault zones in NE Iran. In North East Iran, a striking feature of the velocity field is that the vectors across the entire eastern and southern parts of the network are directed northwards relative to Eurasia (Fig. 5.3). The northward-directed velocities decrease linearly towards the eastern border of Iran, they also decrease smoothly towards the northern border. This distribution of velocities suggests a broad zone of N-S right-lateral shearing through eastern Iran that must be accompanied by clockwise rotation about a vertical axis, which is seen in the kinematic block model (Fig. Fig-block). An important consequence of the observed GPS velocities is that the shear is not localized in a narrow zone at the eastern border of Iran as envisaged by [Shabanian et al., 2009b].

Further west, there is an abrupt change in the orientation in the velocity vectors across the Shahroud fault zone in the eastern Alborz, such that all vectors north and west of the eastern Alborz point northwest relative to Eurasia. These velocities have been used to describe the motion of the South Caspian basin as a clockwise rigid-body rotation about an Euler pole sited near the eastern Kopeh Dagh [Djamour et al., 2010]. However, most of the existing GPS measurements used to constrain the motion of the South Caspian are sited close to its margins, as the interior of the basin is mostly covered by water. Two stations (MAVT and MAR2) that we have presented for the first time in this paper have velocities that are not consistent with the rigid-body rotation about a near-by rotation pole as defined by the remainder of the Caspian stations. The velocities of MAVT and MAR2 are, however, consistent with the motions predicted from a translation of the South Caspian relative to its surroundings [Jackson et al., 2002, Copley and Jackson, 2006]. Although we cannot rule out significant rotation of the South Caspian about a near-by pole, our new GPS data, along with an independent constraint on fast interseismic strain accumulation across the Ashkabad fault [Walters et al., 2013], indicate that its motion is likely to be a clockwise rotation relative to Eurasia about a pole that is much further away than that calculated by [Djamour et al., 2010].

A consequence of the resulting northwest motion of the South Caspian region relative to Eurasia is that it must introduce extension between the eastern Caspian lowlands and the eastern Kopeh Dagh (which is moving northwards relative to Eurasia). The difference in the velocities of stations JANA and SHIR projected onto a profile parallel to the trend of the Kopeh Dagh showing ∼7 mm/yr of extension is accommodated in a narrow zone of the central Kopeh Dagh (Figs. 5.3, 5.8).This range-parallel extension, which has a trend of ∼ N35°W, is coincident with the right-lateral strike-slip faults of the BQFZ. [Hollingsworth et al., 2006] provide a scenario of 'bookshelf faulting' that can account for the observed deformation across the BQFZ. An important consequence of the bookshelf model of faulting is that the slip rates across individual faults within the BQFZ cannot simply be summed to find the overall rates of deformation across the zone (5.1-a). Instead, the slip rates on the faults are related to the along-strike extension and across-strike shortening and vary depending on the width of the fault-bounded blocks and the rates of vertical axis rotation. We estimate 3.3-5.4 mm/yr of cumulative right-lateral slip across the BQFZ in the central Kopeh Dagh. The summed right-lateral bedrock displacement across the zone is ∼45 km [Hollingsworth et al., 2006, Shabanian et al., 2009a]. At the present-day rate, the 45 km of displacement would accumulate in 8.3-15 Ma. [Shabanian et al., 2009a] estimate long-term slip rates of 2.8 ± 1.0 mm/yr and 4.3 ± 0.6 mm/yr for the Baghan and Quchan faults, respectively, which, given that they displace bedrock right-laterally by 10 km and 15 km, may have started as little as 4 Ma ago (5.1-b). The cumulative GPS slip rate across the BQFZ faults is consistent with the lower boundary of the sum of the long-term slip rates on the Baghan and Quchan faults. These two faults

appear to accommodate the major part of right-lateral displacement in the BQFZ, but this comparison does not take into account any anticlockwise vertical axis rotation that might occur in allowing the faults to accommodate extension between the eastern Kopeh Dagh and the South Caspian (e.g. [Hollingsworth et al., 2006, 2008, 2010a]).

Comparison of our geodetic slip rates with geological rates allows us to test for agreement between slip rates derived over different timescales. Comparison with long-term geological estimates of displacement across the faults also permits us to provide constraints on the possible timing of initiation of faulting. In Table 2 we summarize the geodetic short-term (decadal) slip rate estimates derived from our GPS velocities and include the long-term (late Quaternary) estimates where available. Comparison of these two sets show that the two estimates generally agrees, indicating that the GPS velocities can be reasonably extrapolated to be representative of fault slip rates over the last ∼10 ka. If this is the case, for faults with only GPS-based slip estimates, our geodetic results allow us to infer long-term slip rates for the left-lateral faults of eastern Alborz east of 55° E.

In the eastern Alborz, the strike-slip component and shortening are accommodated on the Astaneh segment of the Shahroud fault system and the Khazar thrust (Figs. 5.3, 5.6 and 5.8). At a longitude of 55°E, the GPS velocity field (both in the AA' and BB' profiles and in the block modeling) shows 4.4-6.5 mm/yr of left-lateral displacement and 0.5-2 mm/yr of shortening across the eastern part of the Shahroud fault and Khazar thrust. This amount agrees with existing late Quaternary slip rate estimates of 3–4 mm/yr and 1-3 mm/yr of left-lateral slip across the Abr and Khij Faults ([Javidfakhr et al., 2011a], which are the two main active strands at the longitude of Profile AA', and which do not show any obvious component of dip-slip in the geomorphology. Comparison between geologic and geodetic slip rates hence suggests that most of the strike-slip component occurs south of Alborz range, while the shortening component is accommodated north of the range [Djamour et al., 2010].

[Djamour et al., 2010] used GPS measurements to evaluate 2 ± 1 mm/yr of left-lateral displacement rate for the Astaneh fault, at the far western end of our study region. [Hollingsworth et al., 2010b] suggested 1.7-2.5 mm/yr of slip rate for the Astaneh fault - the SW section of the left-lateral Shahroud fault system - by assuming the 50-60 m fan offset in this region has been accommodated in the last 22-30 kyr. [Rizza et al., 2011] measured a maximum left-lateral slip rate of 2.0 ± 0.3 mm/yr by IRSL dating of geomorphic features displaced 112 ± 15 m across the Astaneh fault at a longitude of 54°E. The 30–40 km total offset across the Astaneh section of Shahroud fault system proposed by [Hollingsworth et al., 2008] would accumulate in 13-23 Ma at the late Quaternary rates of [Rizza et al., 2011], or in 7.6-16 Ma if it accommodates all the left-lateral shearing observed by GPS [Djamour et al., 2010]. [Ritz, 2009], however, suggests the total displacement across the Astaneh fault is much less than 30-40 km, such that the fault may have initiated later.

The Kopeh Dagh, the mountain range at the northern limit of the Arabian-Eurasian collision zone, accommodates the northernmost part of the NS convergence. Considering the GPS velocity field, the Kopeh Dagh can be divided in 3 parts; west, central and east. The western Kopeh Dagh is accommodating, together with the Shahroud fault system, the westward extrusion of the South Caspian basin. Here, the right-lateral Ashkabad fault shows close to ∼5 mm/yr of along-strike motion (if the South Caspian motion involves a clockwise rotation about a nearby pole, as seen in the block modeling results) and up to 6.7 ± 0.5 mm/yr at the longitude of Maraveh-Tapeh as estimated from the profile D-D' (Fig. 5) , with this figure reducing to 4.3 ± 0.5 mm/yr at the longitude of Shirvan. The westward motion therefore decreases towards the east. The geodetic rates are consistent with the 3-8 mm/yr geological estimation of [Lyberis and Manby, 1999]. They are also consistent with InSAR-constrained interseismic strain accumulation across the Ashkabad fault at a rate of 5-12 mm/yr [Walters et al., 2013]. Our estimate is larger than the ∼4 mm/yr estimated from the displacement of a Qanat (an underground water canal) suggesting that it is younger than the ∼2.5 ka age assumed by [Trifonov, 1978]. A total geological right-lateral offset of 35 km was recognized close to SHIR station [Lyberis and Manby, 1999, Hollingsworth et al., 2008], though we note that the robustness of the geological displacements has been the matter of some discussion [Ritz, 2009, Siame et al., 2009, Hollingsworth et al., 2009]. If we assume that the presently measured geodetic slip rate of ∼5 mm/yr on the Ashkabad fault at SHIR station has been constant throughout its history, the initiation of strike-slip faulting would have been at ∼7 Ma. If, however, the 35 km of displacement accumulated at the full rate of 6.7 ± 0.5 mm/yr measured further west on the Ashkabad fault, the faulting may be as young as ∼5 Ma. The eastern part of the Kopeh Dagh, according to the GPS velocity field (Fig. 5.3), absorbs NS shortening between SARK and MSHN. If we consider that most of the 3.2 ± 1.5 mm/yr of shortening between ZVNG and Eurasia is accommodating in the Binalud, assuming a constant shortening rate since initiation of faulting, it takes 20-24 Ma to accommodate the ∼60 km shortening across Binalud which is proposed by [Hollingsworth et al., 2006]. If we assume that the ∼30 km of total NS shortening across the eastern Alborz can apply for Binalud, it takes 12 Ma to accommodate this shortening across Binalud.

5.2.6 Conclusion

A regional deformation field has been estimated from GPS measurements that covers NE Iran and shows that distributed right-lateral shearing is accommodated across a wide part of eastern Iran. In the NE, this right-lateral shearing is converted into shortening across the Koh-e-Sorkh, Binalud and Kopeh Dagh ranges. At the longitude of Kashmar, the N-S shortening is at a rate of ∼4.5 ± 0.5 mm/yr, which decreases toward the east and dies out at the Afghanistan border. Our new GPS data suggest that the South Caspian Basin

is moving at up to ∼7 mm/yr relative to Eurasia at an azimuth of 317°N, constraining a rigid block rotation around an Euler pole that is further away than previously thought. This maximum relative motion between the South Caspian Basin and its surroundings would result in ∼7 mm/yr of right-lateral strike-slip motion along the Ashkabad Fault and 4 to 6.5 mm/yr of left-lateral strike-slip motion within the eastern Alborz Mountains (profile BB') depending on the locking depth of the fault system. These estimates are much faster than previously assumed, though there is additional support for a fast slip rate on the Ashkabad fault from measurements of elastic strain accumulation [Walters et al., 2013], and highlight a potentially acute hazard associated with these fault zones, particularly given the overall lack of recent or historic earthquakes on them. Testing our assertions requires further GPS stations in the eastern Caspian lowlands to determine the South Caspian motion, and direct measurements of the slip rate of the main faults of the eastern Alborz.

Chapter 6

Space-borne Radar Interferometry measurements of interseismic deformation across the eastern Shahroud fault, eastern Alborz range, Iran

Contents

6.1 Introduction

The Alborz range of northern Iran, along with the Zagros in the south, accommodates the major part of the northward motion of Arabia relative to Eurasia, which is at a rate of 22 mm/yr at longitude 57°E [McClusky et al., 2003, Nilforoushan et al., 2003, Vernant et al., 2004a, Reilinger et al., 2006]. The Alborz is located between the plateau of central Iran and the south Caspian basin, and is V-shaped in map view, with a NW-SE trend in the west, and a NE-SW trend in the east. More details about its seismicity and geomorphology can be found in the previous studies [Berberian and Yeats, 2001, Allen et al., 2003, Ritz et al., 2006, Hollingsworth et al., 2010b, Djamour et al., 2010, Javidfakhr et al., 2011a].

It is likely that in addition to taking up N–S regional shortening, the range also accommodates the relative motion between the Iranian plateau and the South Caspian basin, which is an aseismic block that appears to be moving independently of its surroundings [Jackson et al., 2002, Djamour et al., 2010]. The lateral South Caspian motion relative to Iran is accommodated on the left-lateral Astaneh-Shahroud fault system [Wellman, 1966, Tatar et al., 2007, Hollingsworth et al., 2008], whereas shortening across the Alborz is likely to be taken up on the range-parallel Khazar thrust (Fig. 6.1). An eastwards reduction in the height of the Alborz suggests an eastwards reduction in the component of shortening across the range (Fig. 6.1).

Although the kinematics of the eastern Alborz is broadly understood from studies of geomorphology, seismicity, and GPS geodesy [Jackson et al., 2002, Allen et al., 2003, Vernant et al., 2004b, Ritz et al., 2006, Tatar et al., 2007, Djamour et al., 2010, Mousavi et al., 2013], there are still several first-order unknowns. In particular, the slip rate of the major faults in the eastern Alborz are not known, but have the potential to help constrain the relative motion between Iran and the South Caspian [Jackson et al., 2002, Djamour et al., 2010, Mousavi et al., 2013], as well as providing data relevant for seismic hazard estimations.

The Astaneh-Shahroud left-lateral fault system, in the eastern Alborz between longitudes 53°E and 58°E, is 200 km long and consists of a number of discontinuous northeast-trending left-lateral fault segments (the Abr, Khij, Jajarm, Cheshmeh-Nik faults) [Wellman, 1966, Hollingsworth et al., 2008, Javidfakhr et al., 2011a, Rizza et al., 2011]. There have been no large instrumental earthquakes on the Shahroud fault system in the last 50 years, but destructive earthquakes are known from the historical record, including an event directly north of Shahroud in 1890 [Ambraseys and Melville, 1982]. Strike-slip faults within more westerly parts of the Alborz range have also shown the potential for large, destructive, earthquakes. The Astaneh fault (Fig. 6.1) is likely to have been responsible for the 856 A.D. Qumis earthquake, which killed over 200,000 people [Ambraseys and Melville, 1982, Hollingsworth et al., 2010b] and the Rudbar fault, in western Alborz ruptured in an Mw7.1 earthquake in 1991 that resulted in 13 000–40 000 deaths and made a further

500,000 homeless [Berberian et al., 1992, Tatar and Hatzfeld, 2009, Berberian and Walker, 2010].

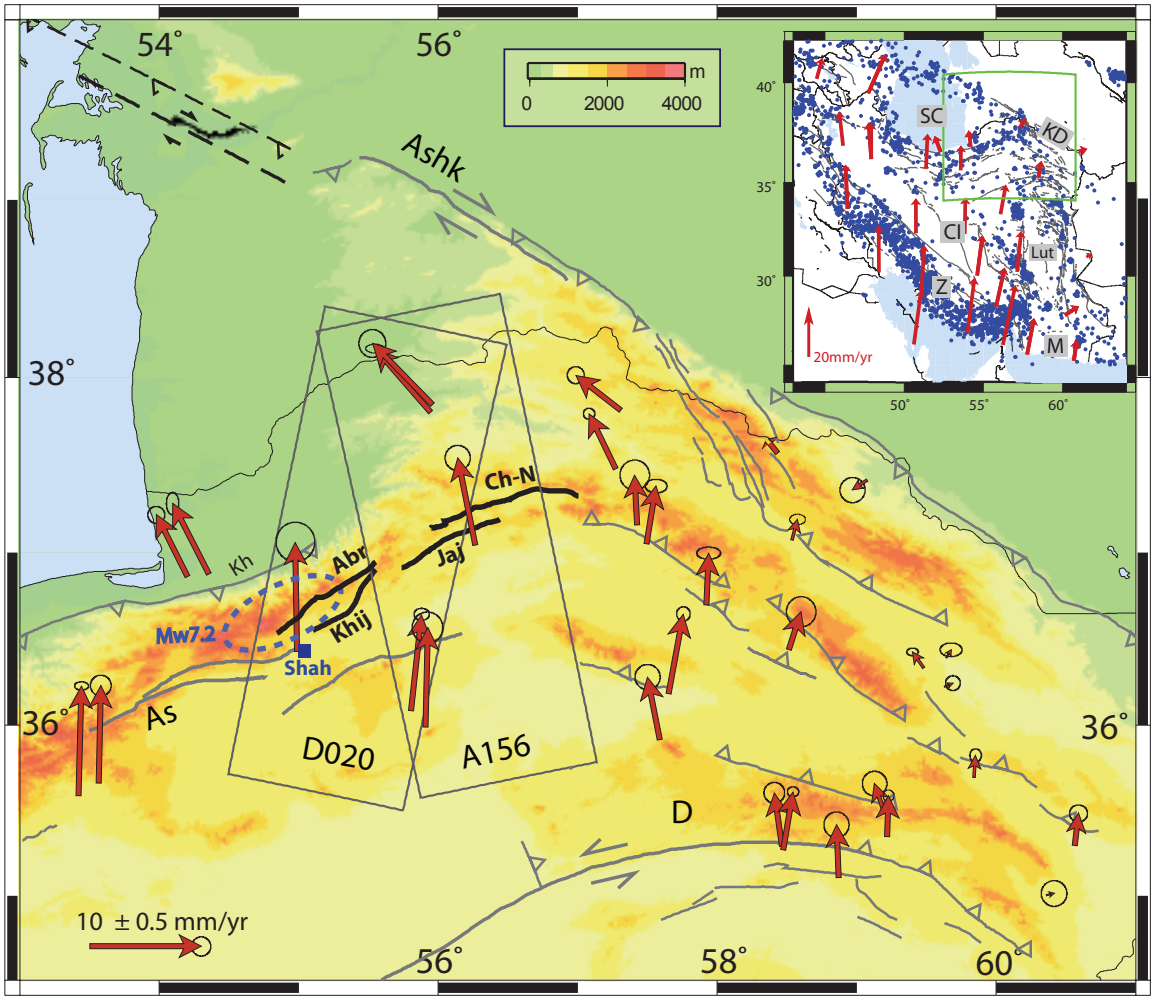

Figure 6.1 – Inset: Outline map of Iran with GPS vectors shown relative to Eurasia (in red; [Vernant et al., 2004b] showing that approximately N–S shortening between Arabia and Eurasia is accommodated throughout Iran. Blue dots are earthquakes epicenters (Mw $\geq$ 5) in Iran extracted from the Harvard catalogue (http://www.globalcmt.org/CMTsearch.html) during the period 1976-2012. The green rectangle indicates the location of the map in the main figure. The abbreviations are CI: Central Iran, KD: Kopeh Dagh, Lut: Lut block, M: Makran subduction zone, SC: South Caspian basin, Z: Zagros. Main figure: tectonic map of the Eastern Alborz showing the location of the Shahroud Fault system (bold fault trace). Fault traces are superimposed on the Shuttle Radar Topography Mission (SRTM) Digital Elevation Model (DEM). Fault name abbreviations: Abr: Abr Fault, Khij: Khij fault, Jaj: Jajarm fault, Ch-N: Cheshmeh-Nik fault, AS: Astaneh fault and D: Doruneh. Dashed blue ellipse indicates the approximate place of the 1890 (Mw7.2) Earthquake close to the Damghan and Shahroud regions [Ambraseys and Melville, 1982], Gray rectangles show the coverage of analyzed ENVISAT SAR data, with their track numbers (A for ascending, D for descending). The red vectors and ellipses present the GPS velocity field with respect to Eurasia from [Djamour et al., 2010, Mousavi et al., 2013]. Note the change in direction of GPS vector through the Shahroud Fault System. The thin black line is the political border between Iran and Turkmenistan.

No historical earthquakes are recorded on the easternmost 150 km of the Shahroud fault system, which consists of the parallel Jajarm and Cheshmeh-Nik faults. The geological slip rates of these fault segments are unknown, and yet these faults pose a substantial hazard to local populations: the Jajarm fault is 20 km north of Jajarm city, and strikes NE for more than 130 km [Hollingsworth et al., 2008, 2010b, Javidfakhr et al., 2011a], and the 120 km-long Cheshmeh-Nik fault terminates in the east at the city of Bojnord. Using GPS measurements, Mousavi et al. [2013] estimated between 2.5±1 mm/yr and 4-6.5 mm/yr of summed left-lateral displacement across Jajarm and Cheshmeh-Nik faults. The lower value (2.5±1 mm/yr) result from a block modeling approach, in which the South Caspian rotates about an Euler pole located immediately NE of Iran, whereas the higher value (4-6.5 mm/yr) results from simply taking profiles of fault-parallel velocities, in which the South Caspian rotates about an Euler pole located further away from previous thought. Jackson et al. [2002] and Copley and Jackson [2006] estimate 4.5-5.5 mm/yr of shortening and left-lateral strike-slip across the Alborz based on a plate-closure model to predict a rigid-body motion of the South Caspian Block relative to Eurasia. Determining the slip rate across the Shahroud fault system will thus help to constrain the movement of the South Caspian basin, as well as providing data useful for hazard estimation.

In this study we provide the first direct measurement of interseismic deformation across the eastern Shahroud fault, where both the slip rate and earthquake history are unknown. We process 2 tracks of ENVISAT-ASAR images (see Fig.6.1 for location) with a temporal span of 8 yrs, from 2003 to 2010. Firstly, we present the image data set, then the multitemporal differential SAR interferometry (InSAR) processing strategy to increase signal to noise ratio, then the SBAS technique of time series analysis, and finally the 2-D interseismic modeling based on the line of sight (LOS) velocity map.

6.2 InSAR data and processing

Synthetic Aperture Radar (SAR) images from the ASAR instrument (wavelength of 5.6 cm) on board the ENVISAT satellite have been used in this study to investigate interseismic deformation across the Shahroud Fault system. In the "image mode" of the ASAR instrument (swath of 100km), the studied area is covered by one descending and one ascending track (D020 and A159, see location in figure 6.1), over a 60000 km2 area. The data set was acquired during 2003-2010 with 22 and 23 images for tracks D020 and A159, respectively (Fig. 6.2). The raw radar images (Processing Level 0) were processed with ROI_PAC (Repeat Orbit Interferometry PACkage) [Rosen et al., 2004]. The topographic phase contribution was estimated from the 90m SRTM DEM (Shuttle Radar Topography Mission Digital Elevation Model) [Farr and Kobrick, 2000], which has been oversampled to 45m, and referenced to the WGS84 ellipsoid. Precise DORIS orbital data for ENVISAT satellite provided by ESA has been used for interferometric processing.

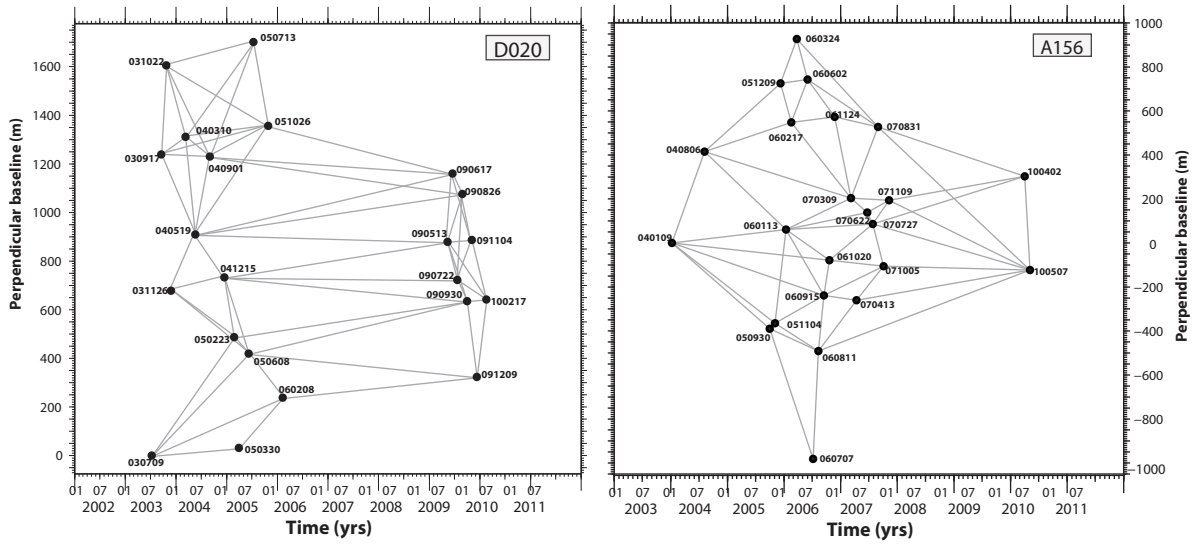

Figure 6.2 – Diagrams of all processed interferograms selected using a maximum perpendicular baseline criterion (500m). Perpendicular baselines with respect to the July 2003 orbit for descending track D020 (left plot), and January 2004 orbit for ascending track A156 (right plot), are plotted as function of acquisition dates. Track D020 uses 22 images that are combined into 63 interferograms and track A156 uses 23 images that are combined into 51 interferograms.

We processed the Single Look Complex (SLC) images with a common Doppler banding with a minimum of 90% overlap. After choosing a master image maximizing a criteria called total coherence [Zebker and Villasenor, 1992, Hooper et al., 2007], all SLC images are coregistered to the master image geometry taking into account image deformation simulated from orbital and DEM data [Jolivet et al., 2012]. We processed interferograms with perpendicular baselines smaller than 500m and temporal baseline larger than 2 months and less than 4 years. These values were found to be a good compromise in terms of signal-to-noise ratio and coherence.

Interferograms were down-sampled using 4 looks in range and 20 looks in azimuth (ground pixels are 90m ×90 m).The resulting differential interferogram phase Φ^{ij} between dates i and j is related to phase change contributions from the deformation signal, tropospheric delay, orbital and DEM residual and noise (equation1).

$$\Phi_{ij} = \phi_{ij}^{DEM\_res} + \phi_{ij}^{orb\_res} + \phi_{ij}^{atmo} + \phi_{ij}^{disp} + \phi_{ij}^{noise} \tag{6.1}$$

Where $\phi_{ij}^{orb\_res}$ is the phase component related to the residual orbital delay, ϕ_{ij}^{atmo} is the difference of atmospheric delay (Atmospheric Phase Screen, APS) between the 2 dates, $\phi_{ij}^{DEM\_res}$ is related to residual DEM errors, ϕ_{ij}^{disp} is ground displacement and $\phi_{ij}^{noise}$is the noise from co-registration and unwrapping. In order to estimate interseismic deformation from interferograms, it is necessary to overcome the trade-offs between the tectonic signal and both orbital errors and atmospheric phase delays [Zebker et al., 1997, Massonnet and Feigl, 1998]. It is useful to correct orbital and DEM errors as well as tropospheric delay

before unwrapping in order to improve the spatial phase coherency in the unwrapping step.

The tropospheric delays can be split up into turbulent and stratified components. The effect of turbulent patterns on InSAR acquisitions can be considered as random in space and time and is mostly topography independent. Therefore it can be reduced by stacking or time series analysis [Peltzer et al., 2001, Wright et al., 2001, Schmidt et al., 2005, Ferretti et al., 2001, Berardino et al., 2002, Schmidt and Bürgmann, 2003, Cavalié et al., 2007, 2008, Shirzaei and Bürgmann, 2012]. The vertically stratified component, correlated with topography, is not random in space [Doin et al., 2009]. Until now, several approaches have been used to mitigate the tropospheric phase delay, either empirically [Remy et al., 2003, Biggs et al., 2007, Cavalié et al., 2008, Lin et al., 2010] or based on corrections from a range of external data, such as MODIS (MODerate resolution Imaging Spectrometer, [Li et al., 2005]), MERIS (MEdium Resolution Imaging Spectrometer onboard ENVISAT [Li et al., 2006c,b]), large GPS network data [Webley et al., 2002, Li et al., 2006a], global atmospheric models [Doin et al., 2009, Jolivet et al., 2011] or wavelet transforms [Shirzaei and Bürgmann, 2012]. Here we use the global atmospheric model ERA-Interim provided by the European Center for MediumRange Weather Forecast (ECMWF) to estimate the tropospheric delay map [Jolivet et al., 2011]. ERAI is a global atmospheric model on a 75 km grid, generated four times per day on 37 pressure levels. We did a spatial bilinear interpolation for the delay function of ERA data and then a spline interpolation for altitude to predict the delay map for each single image. Differential delay maps corresponding to each interferogram can be estimated by comparing these delay maps.

The residual orbital components due to unmodelled orbital errors can still be significant, particularly when studying low rates of deformation. Such errors are reduced by searching for a best fitting ramp in range, varying linearly in azimuth, followed by a best fitting ramp in azimuth, using the wrapped interferometric phase.

The interferometric phase component due to DEM errors varies with the perpendicular baseline between the two acquisitions and is estimated from unwrapped interferograms following the methodology from Ducret et al. [2013]. Refinements of the DEM error map are retrieved by least mean square of local DEM errors. This map is produced based on high coherence reference points. After, the DEM error map is harmonized by a median filter. This map can be used to reduce the DEM error in all interferogram phases [Ducret et al., 2013]. At this step, to increase the coherence, the unwrapped interferograms are down-sampled using 16 looks in range and 5*16 looks in azimuth. Then, interferograms are filtered using Goldstein's filter [Goldstein and Werner, 1998] and unwrapped using a branch-cut algorithm [Goldstein et al., 1988].

A careful visual inspection of the corrected interferograms was performed to investigate short wavelength signals (1-10 km scale) that could be related to superficial creep along faults. Local deformations related to subsidence phenomena were found in some val-

leys but there is no evidence over the 2003 to 2010 period for any sharp creep deformation signal located along the faults. To investigate the long wavelength tectonic signal due to interseismic strain accumulation, a time series analysis of the selected images has been performed on a pixel basis in order to enhance signal to noise ratio.

6.3 Smoothed constrained time series analysis

Once all interferograms corrected from residual errors unwrapped and referenced, we perform a time series analysis for each track. The time series is applied based on the phase evolution through time in the small baseline interferograms network. The interferograms are chosen with perpendicular orbital separation less than 500 m and temporal baseline less than 4 years (figure 6.2). To obtain the phase delay time series by least square inversion, we invert the following linear system for each pixel in the interferograms [Berardino et al., 2002, Lanari et al., 2004]:

$$\Phi_{ij} = \sum_{k=i}^{j-1} \delta\phi_k \qquad while \qquad \phi_1 = 0 \tag{6.2}$$

Where Φ_{ij} is the propagation delay for interferogram i and j and $\delta\phi_k$ is the incremental delay between images k and $(k+1)$ for each pixel. To be able to solve this inversion using the least square method, in spite of incoherency in some areas, and disconnections between some groups of pixels from the remainder of the points through time, we add a constraint component [López-Quiroz et al., 2009, Doin et al., 2011, Jolivet et al., 2011].

$$\sum_{k=1}^{n-1} \delta\phi_k - \alpha B_n^{\perp} - \phi_n^{smooth} = 0 \tag{6.3}$$

Where α is proportional to the DEM error and $B_n^{\perp}$ is the perpendicular baseline of acquisition n, with respect to the first acquisition. This component is affected by turbulent tropospheric pattern of each image. We weight this component based on the amplitude of atmospheric patterns $(1/ASP_n)$. We add one more constraint which is a temporal smoothing, obtained by minimizing the curvature of the inverted temporal phase evolution [Schmidt and Bürgmann, 2003, Cavalié et al., 2007, Doin et al., 2011].

$$\frac{\partial \phi_n^{smooth}}{\partial t^2} = 0 \tag{6.4}$$

We choose the weighting of this component in the inversion system equal to Δt_l, the mean time interval across the five-point differential operator, to be able to smooth less in the densely spaced acquisitions and smooth more in scattered space acquisitions [Cavalié et al., 2007, Doin et al., 2011].

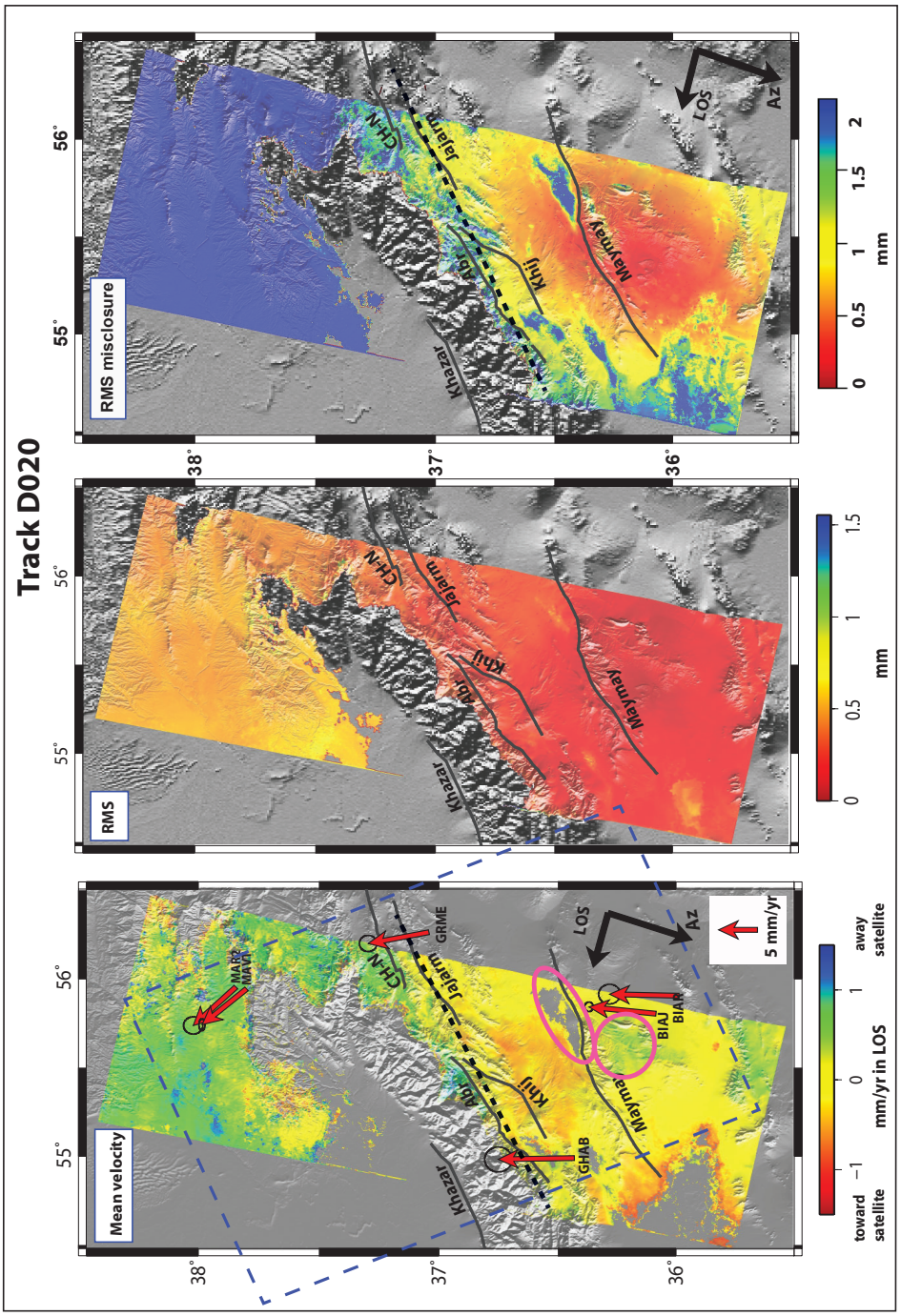

Figure 6.3 – Ground surface mean Line-Of-Sight velocity map from InSAR time series analysis for track D020. RMS map presents the time series variability and the RMS misclosure presents the network consistency. Black arrows show the satellite displacement (Az) and Line of Sight direction (LOS). Background is a shaded-relief DEM (SRTM) and red arrows present the GPS velocity field of this area with respect to Eurasia. Black lines are fault traces along the Shahroud fault system. Blue boxes, oriented perpendicular to the Shahroud Fault system, show location of profiles in figure 6.6. CH-N is Cheshmeh-Nik fault. The high amount of ground water extraction has resulted in a fast displacement rate in an arid area like Iran. The subsidence areas are masked for inversion (pink circles). The dashed line indicates the fault location which is used for the 2D-modelling.

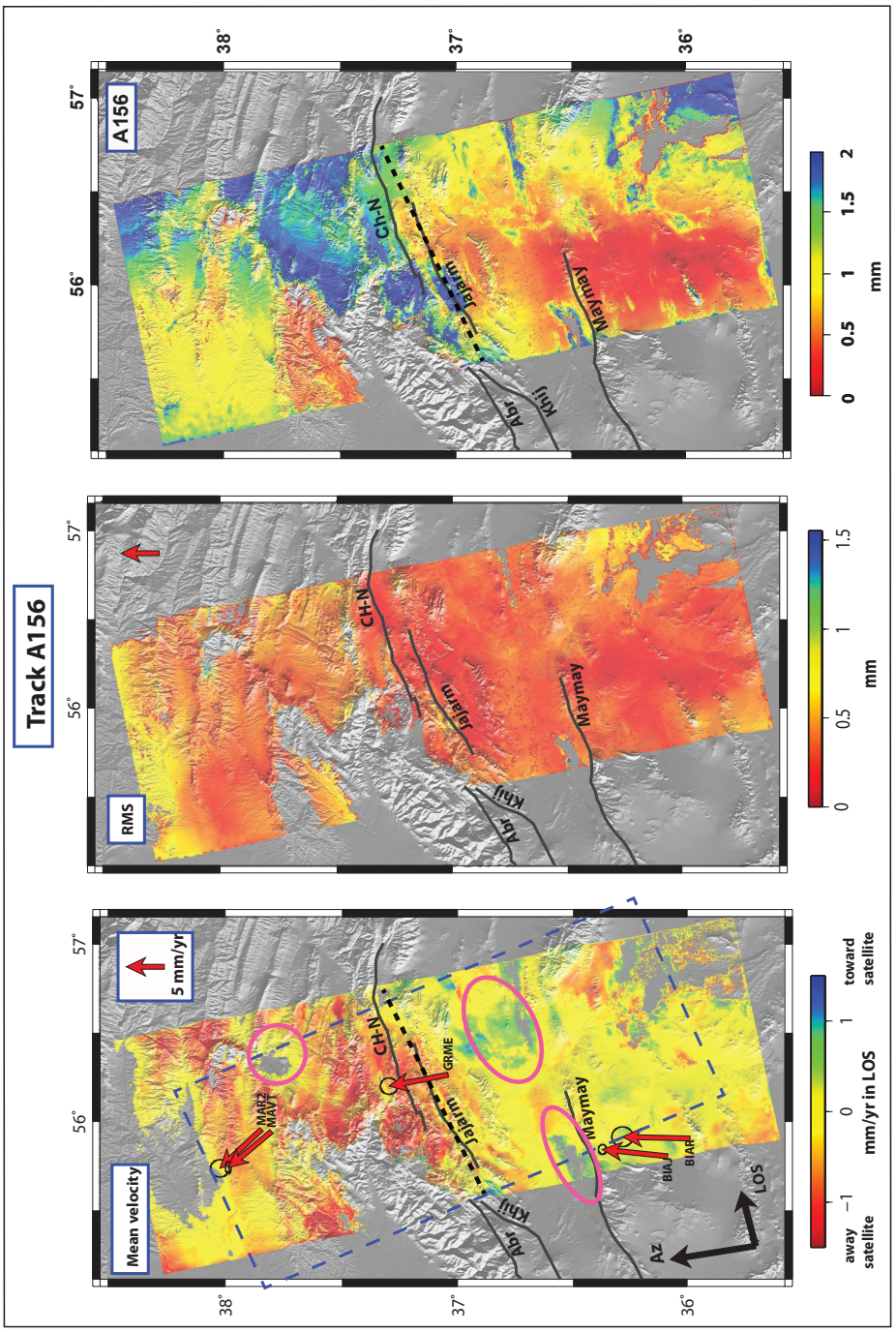

Figure 6.4 – Ground surface mean Line-Of-Sight velocity map from InSAR time series analysis for track A156. RMS map presents the time series variability and the RMS misclosure presents the network consistency. Black arrows show the satellite displacement (Az) and Line of Sight direction (LOS). Background is a shaded-relief DEM (SRTM) and red arrows present the GPS velocity field of this area with respect to Eurasia. Black lines are fault traces along the Shahroud fault system. Blue boxes, oriented perpendicular to the Shahroud Fault system, show location of profiles in figure 6.6. CH-N is Cheshmeh-Nik fault. The high amount of ground water extraction has resulted in a fast displacement rate in an arid area like Iran. The subsidence areas are masked for inversion (pink circles). The dashed line indicates the fault location which is used for the 2D-modelling.

Now we can invert this system using the least square inversion [López-Quiroz et al., 2009, Jolivet et al., 2011] to investigate the long wavelength tectonic signal due to interseismic strain accumulation. Figures 6.3 and 6.4 show the mean velocity map derived from time series for two descending and ascending tracks after georeferencing to the DEM geometry. The first noticeable point is the LOS velocity change across the Shahroud fault system on the two tracks. This gradient has opposite signs on descending and ascending tracks, consistent with left-lateral motion, and reaches up to 2 mm/yr in LOS direction. Also Fig. 6.5 shows that there is no clear correlation between the topography and the mean-velocity map.

Figure 6.6 presents the perpendicular profiles to the Shahroud fault system for both tracks which is overall consistent with a classic arctangent shape predicted by an elastic model across a strike-slip fault [Savage and Burford, 1973]. These interseismic strain accumulation profiles across the Shahroud fault system are in good agreement with the local velocity measurements at existing GPS stations (red dots in figure 6.6) [Mousavi et al., 2013, Djamour et al., 2010].

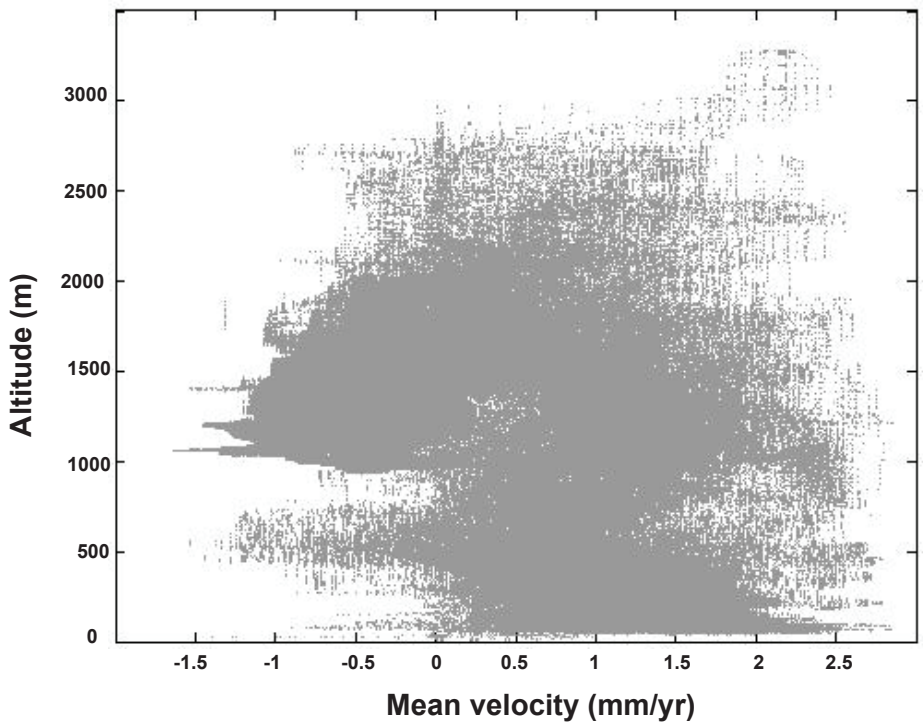

Figure 6.5 – Velocity versus altitude for the area covered by track D020, from which it is clear that there is no correlation between altitude and deformation.

6.4 Interseismic deformation modeling

To help the interpretation of the LOS mean velocity map, we used a simple elastic model with single fault geometry. A North-South velocity change is clearly visible across

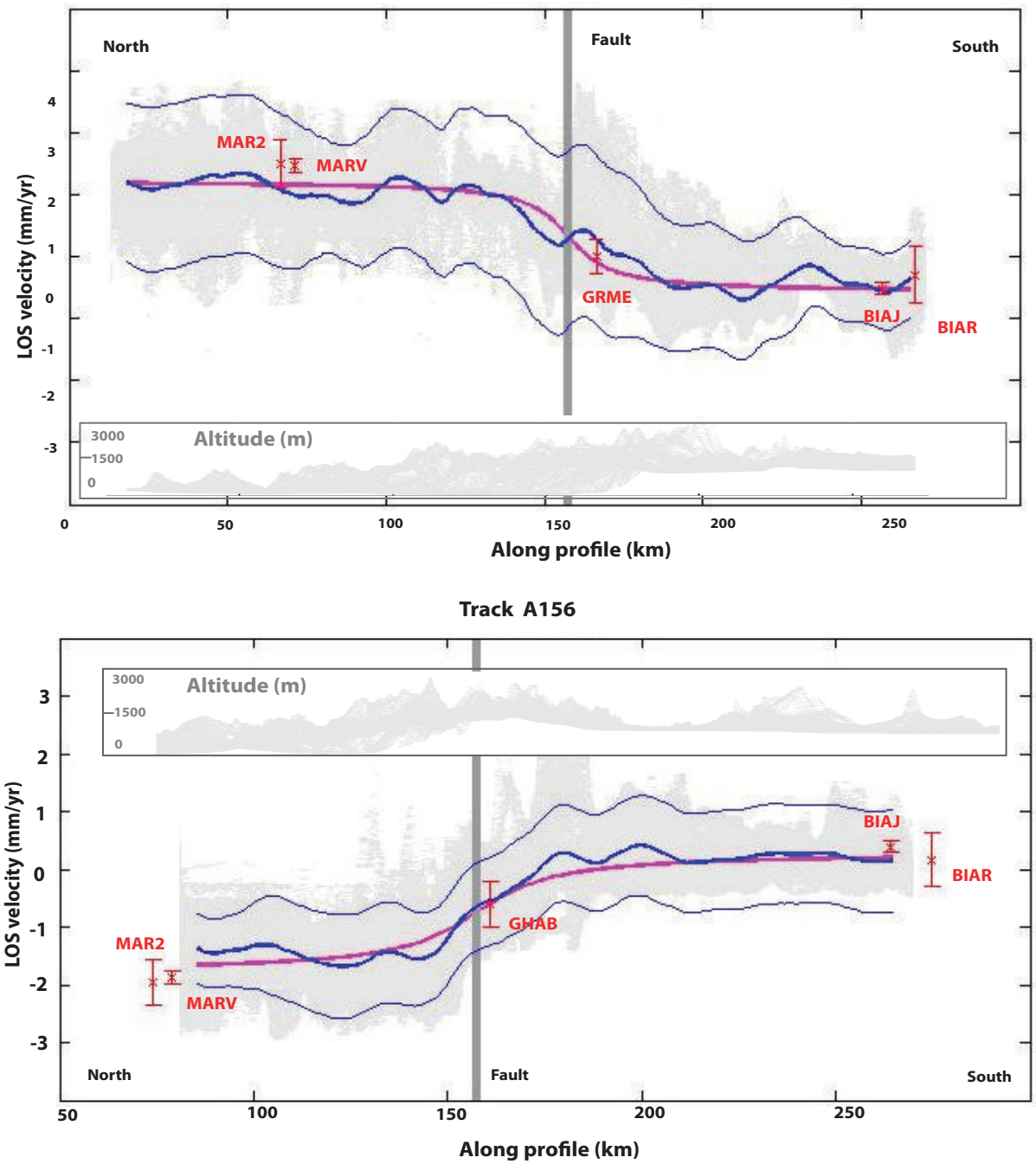

Figure 6.6 – Mean Line-Of-Sight velocity profiles (gray dots) with 2-sigma deviation (blue lines). All the points within the blue rectangle shown in figure 6.3 are projected onto the profile as gray dots. The gray boxes show the elevation profile for the same area. The dark gray line shows the location of the Shahroud Fault system. The pink line is the best-fitting model with slip rate 4.75 ±0.8 mm/yr and 10±4 km locking depth. The red stars with error bars are the LOS velocity derived from five continuous GPS stations (see location in figures 6.3 and 6.4). Note that the sign of the signal is inversed between ascending and descending track, which is consistent with surface displacement due to the left lateral fault seen from the two different satellite points of view (see the two LOS vectors in figures 6.3 and 6.4).

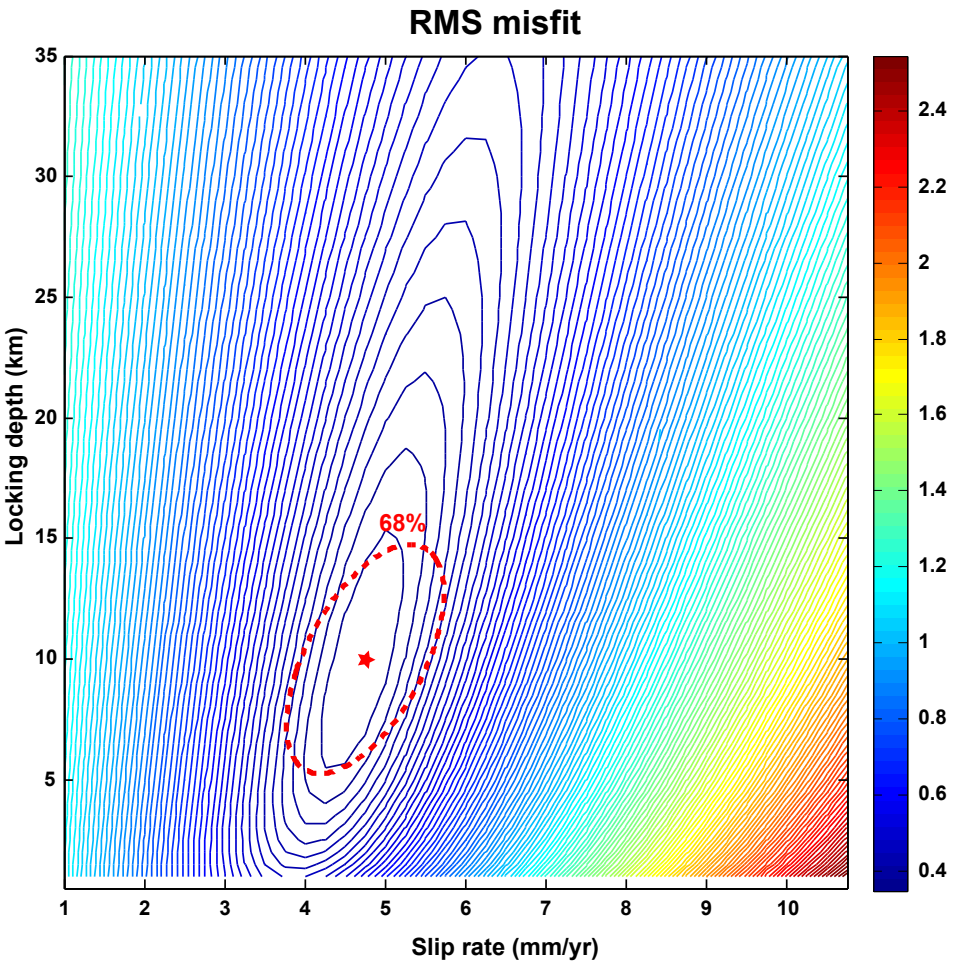

Figure 6.7 – Solution–space plot for our model showing results of the Monte Carlo error analysis for joint ascending track A156 and descending track D020. Contours show the RMS misfit in mm/yr for the unperturbed dataset. The red star show the best fitting solution (Locking depth: 10±4 km and Slip rate: 4.75 ±0.8 mm/yr), the 68% confidence ellipse is estimated from the Monte Carlo error analysis using perturbated dataset.

the Shahroud fault system. Figures 6.3 and 6.4 show that the mean velocity varies close to the Jajarm fault in track A156, but for track D020 it is hard to distinguish the responsible fault for velocity changing. That is why we decide to model the fault system by a single vertical dislocation with the surface trace located on the dashed line on figures 6.3 and 6.4. We also assume a pure strike-slip fault with no vertical deformation. This hypothesis seems justified by the lack of relief around the fault trace. We determine the slip rate and locking depth of the fault based on the Savage and Burford [1973] analytical solution which provides the surface displacement parallel to the fault at a given perpendicular distance x from the fault, knowing the slip rate s and the locking depth d: $y = (s/\pi) \times arctan(x/d)$. The parameter estimation is based on the minimization of the sum of the RMS misfit between the observed and modeled velocity profiles (figure 6.6) estimated for each track.

We used a systematic parameter search over the ranges 1-10 mm/yr for slip rate and 1-35 km for locking depth, at 0.5 mm/yr and 0.5 km intervals, respectively. We perform

this search for the assumed fault trace, centered on the Jajarm fault in track A156 and on Abr fault in track D020 (dashed line in figures 6.3 and 6.4). Our bestfit model for the joint inversion is the sum of the two RMS misfits for ascending and descending tracks. This minimum RMS misfit is corresponding to a slip rate of 4.75 mm/yr and a locking depth of 10 km (see red star on Figure 6.7).

After the corrections we applied on each interferogram (see section 6.2), the main source of remaining errors are turbulent atmospheric changes. Therefore, we try to estimate the impact of such perturbations in our fault parameter estimation. To do that, one hundred of perturbed mean-velocity maps are generated and used in the same inversion scheme than for the non-perturbed dataset. The mean-velocity map is the result of the SBAS time series analysis starting from the network of corrected interferograms. In order to introduce a realistic noise in the mean-velocity map, we choose to attribute to each date of the network an Atmospheric Phase Screen (APS) and then to combine the APS of the dates to produced synthetic interferograms. The time series analysis is then applied on the network of synthetic interferograms the same way than on the original data, and the result is added to the original mean-velocity map.

To generate the simulated atmospheric phase screen for each date, we used interferograms with 35 days or 70 days, in which we assume that phase variations are only due to atmospheric delay changes, and because the number of such short-time interferograms is less than the number of acquisition dates in the network, we also generate synthetic atmospheric phase screens using an approach similar to Parsons et al. [2005] (see Fig. 6.8 and also [Biggs et al., 2007]). In that approach, the statistical characteristics of the contribution of the turbulent atmosphere to a short-time interferogram is described using a 1-D covariance function [Hanssen, 2001] which is used along with a full variance–covariance matrix to simulate the correlated noise. To create 100 different perturbed velocity maps, simulated atmospheric phase screens are randomly attributed to each date of the network. The parameter uncertainties were determined based on 100 runs of estimating RMS misfit using the Monte Carlo method. Standard deviation of the 100 runs to modeled slip and locking depth is used as uncertainty estimation (see ellipsoid in Fig 6.7) leading to the following values: 4.75±0.8 of slip rate and 10±4 km of locking depth.

6.5 Discussion

Our mean velocity map confirms the general left-lateral kinematics of the Shahroud fault system and simple 2-D modeling gives some constraints about the slip rate and locking depth. Our model implies a left-lateral displacement across Shahroud fault system of 4.75±0.8 mm/yr and 10 ± 4 km of locking depth. This ∼5mm of displacement is accommodated on the Abr (∼ longitude 55°) and Jajarm (∼ longitude 56°) strands of Shahroud fault system. The new result of the InSAR study of the Shahroud fault system

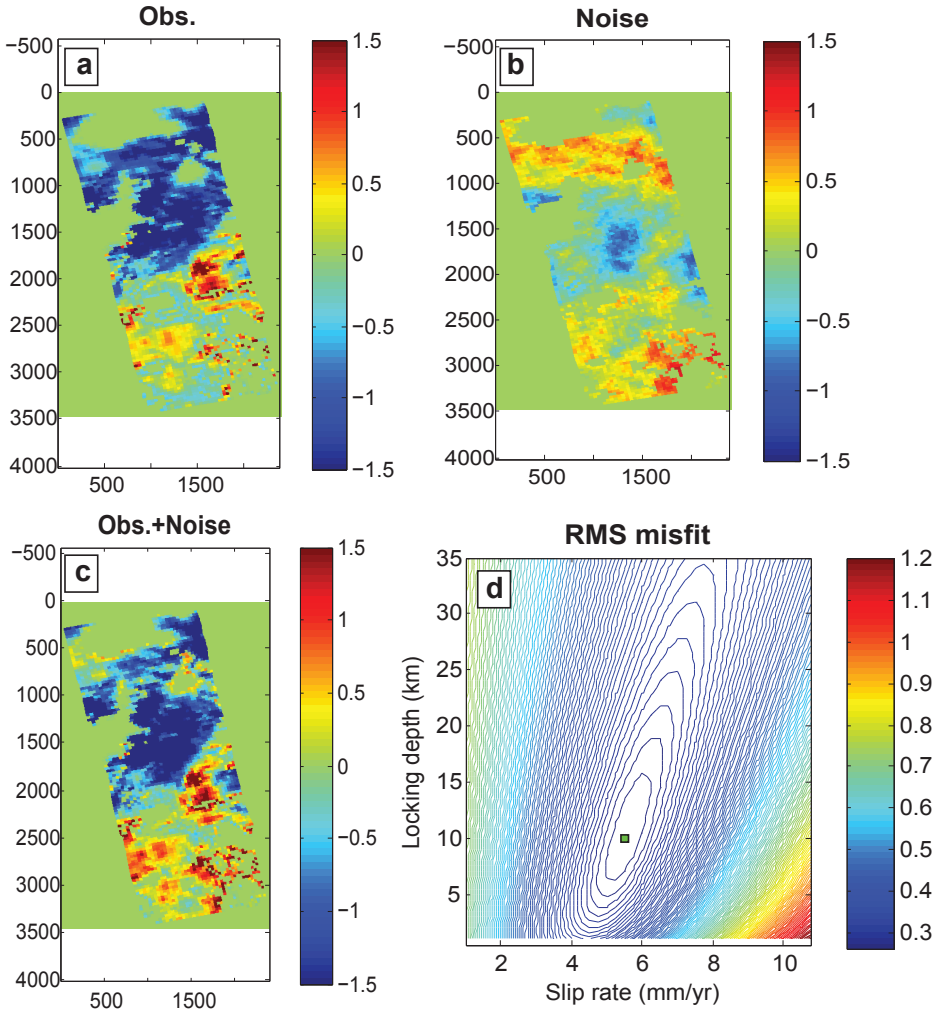

Figure 6.8 – One example of a perturbed dataset: a) the original interferogram, b) the perturbation image c) perturbed data d) the RMS misfit for perturbed data.

with respect to other quantitative data available on the present day deformation field (by GPS, [Mousavi et al., 2013, Djamour et al., 2010]) is that the fault system is effectively locked with no shallow creep. One of the assumptions in our inversion is that there is no vertical deformation, so that we can convert displacement in LOS direction into horizontal displacement parallel to the fault. As the independent GPS data are in a good agreement with the InSAR profile (Fig 6.6, GPS error bar), and both ascending and descending data are consistent with the model, it is likely that there is no significant vertical tectonic signal and certainly no major interseismic shortening in this part of the fault system. The reduction of shortening in the east of Alborz with respect to the western part and the lack of the relief around the faults is also consistent with the assumption of a purely vertical strike-slip fault.

The choice of a single fault model was motivated by the fact that there is no clear individual fault signature in the geomorphology through the Shahroud fault system. The position of the fault has been tested by modeling the location of the fault trace for track

D020 using a 12 km locking depth as suggested by Engdahl et al. [2006] (Fig. 6.9). This locking depth is the average depth of the regional seismicity [Engdahl et al., 2006]. We found the best fit model is corresponding to the dashed line close to Abr and Jajarm faults in Track D020 and it also confirms that the Jajarm fault accommodates the strain in track A156 (6.1). It may be possible that the different strands visible at the surface (Jajarm and CH-N) are merged in one single fault below 10 km depth. This could explain why our model is not sensitive to the geometric complexity of the shallower part of the faults, located in the locked zone of the model.

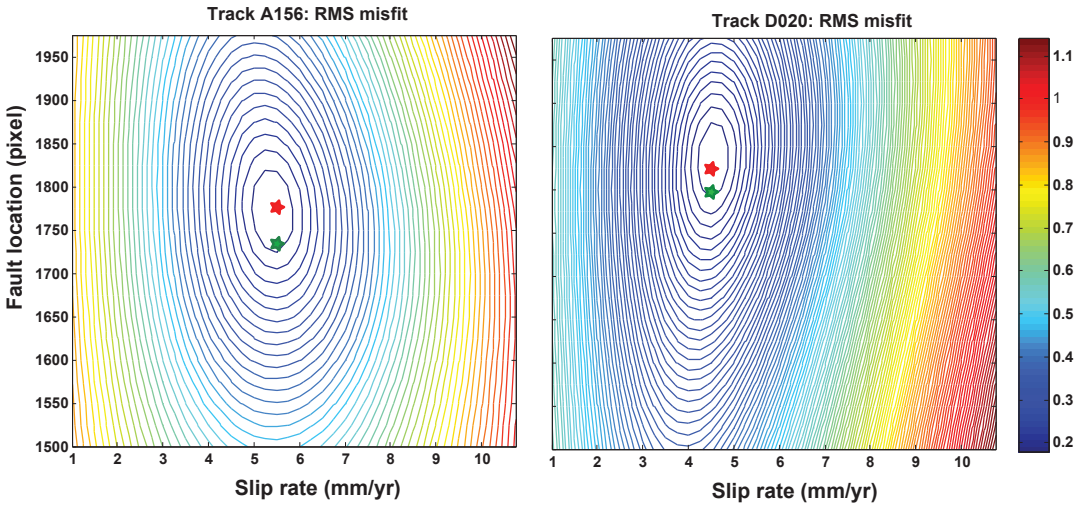

Figure 6.9 – Solution space plot for modeling the location of fault and slip rate for the two tracks A156 (left) and D020 (right). The red stars are the best-solution of modeling the location and slip rate of fault based on fix locking depth at 12km and the green stars are the location of fault that we choose for the 2d modeling of slip rate and locking depth.

6.6 Conclusion

Previous geodetic results based on a regional GPS network [Djamour et al., 2010, Mousavi et al., 2013]) evaluated slip on the Astaneh segment in the western part of the Shahroud fault system to 2±1 mm/yr from the rigid block motion of the South Caspian Basin with respect to Iran, that shows however persistent residuals with respect to critical GPS observations. The GPS analysis yields a slip rate of 4-6 mm/yr when projecting GPS station velocities on a profile across the fault and neglecting rigid block rotation. The InSAR result is in good agreement with the GPS profiles rather than with the rigid block modeling. This indicates that most of the left-lateral displacement is accommodated in southern Alborz, along the Shahroud fault system. Also, the InSAR result is in favor of a South Caspian Basin rigid rotation about a faraway pole related to a fast interseismic strain accumulation on the Shahroud fault system, compatible with a fast slip rate of the

Ashkabad fault at the NE limit of the South Caspian Basin ([Mousavi et al., 2013, Walters et al., 2013], Fig. 6.1).

This new information provides precious insights into the seismogenic potential of the fault system. If we use the Hanks and Bakun [2008] Magnitude-Area relationship for area $\geq 537km^2$, for length $\sim$100 km and width = 10km for the Jajarm fault, one strand of the Shahroud fault system, and assuming that the whole segment can break in one earthquake and do not take into account the recurrence time of earthquake, it may have the possibility of an earthquake of magnitude Mw = 7.08 on each of them. The existence of a large historical earthquake (Mw 7.2) on the Abr segment of the Shahroud fault system in 1890, and the large number of inhabitants ($\sim$1.5 million) in this region, shows the requirement for geomorphological and palaeoseismological investigations to fill the gap of required information on the behavior of individual fault strands. Such studies will give a more complete assessment of slip rates and recurrence intervals in order to estimate the seismic hazard along these important active faults.

Chapter 7

Conclusion

Contents

7.1 Conclusion

A general deformation pattern of Iran can be depicted as follows:

The active tectonics of Iran is dominated by the northward motion of the Arabia plate relative to Eurasia. The earthquake distribution indicates that the convergence is accommodated by a mixture of thrust and strike-slip faulting inside Iran. Therefore, this convergence is absorbed by shortening, thickening of the crust, and strike-slip motions on major faults. The characteristic feature of the convergence along Iran's southern border is the longitudinal variation in style, from continental collision in the west to oceanic subduction in the east (east of 58°E). In the west, shortening is mainly accommodated in the Zagros and Alborz-Caucasus mountain belt, while east of 58°E most of the convergence is accommodated by the Makran subduction zone [Vernant et al., 2004b], with the remaining shortening taken up by the Kopeh Dagh and other mountain ranges in NE Iran.

The eastern and northeastern Iranian deformation pattern is imposed by the NS shear resulting from the E-W variation in accommodation of the convergence. A major part of this shear is absorbed on the Lut block boundaries, while the residual NS shortening north of the Lut block provides the boundary conditions for the Kopeh Dagh and Eastern Alborz present-day deformation. These latter deformation patterns finally constrain the present kinematics of the South Caspian Basin in the west.

7.1.1 Geodetic velocity field

Here, in this thesis, we analyzed GPS and SAR data to investigate the interseismic deformation in Central-Eastern Iran. We have processed GPS networks (permanent and campaign) spanning the Lut, Kopeh Dagh and Eastern Alborz. We analyzed 11 years of GPS data from 130 (permanent and campaign) stations covering Eastern Iran from south to north. Six out of the analyzed stations had to be removed from the tectonic interpretation as they were suffering from significant subsidence due to ground water extraction. The average formal uncertainties quantified by the GAMIT/GLOBK software are 1.45, 1.7 and 5.25 mm/yr on North, East and Up component, respectively. This dense and precise data set allowed us to present the up-to-date current kinematics. The new geodetic velocity field can complete and detail the previous studies about the current deformation inside the political borders of Iran [Nilforoushan et al., 2003, Vernant et al., 2004a,b, Masson et al., 2005, 2007, Talebian and Jackson, 2002, Walpersdorf et al., 2006, Tavakoli et al., 2008] (see figure 7.1).

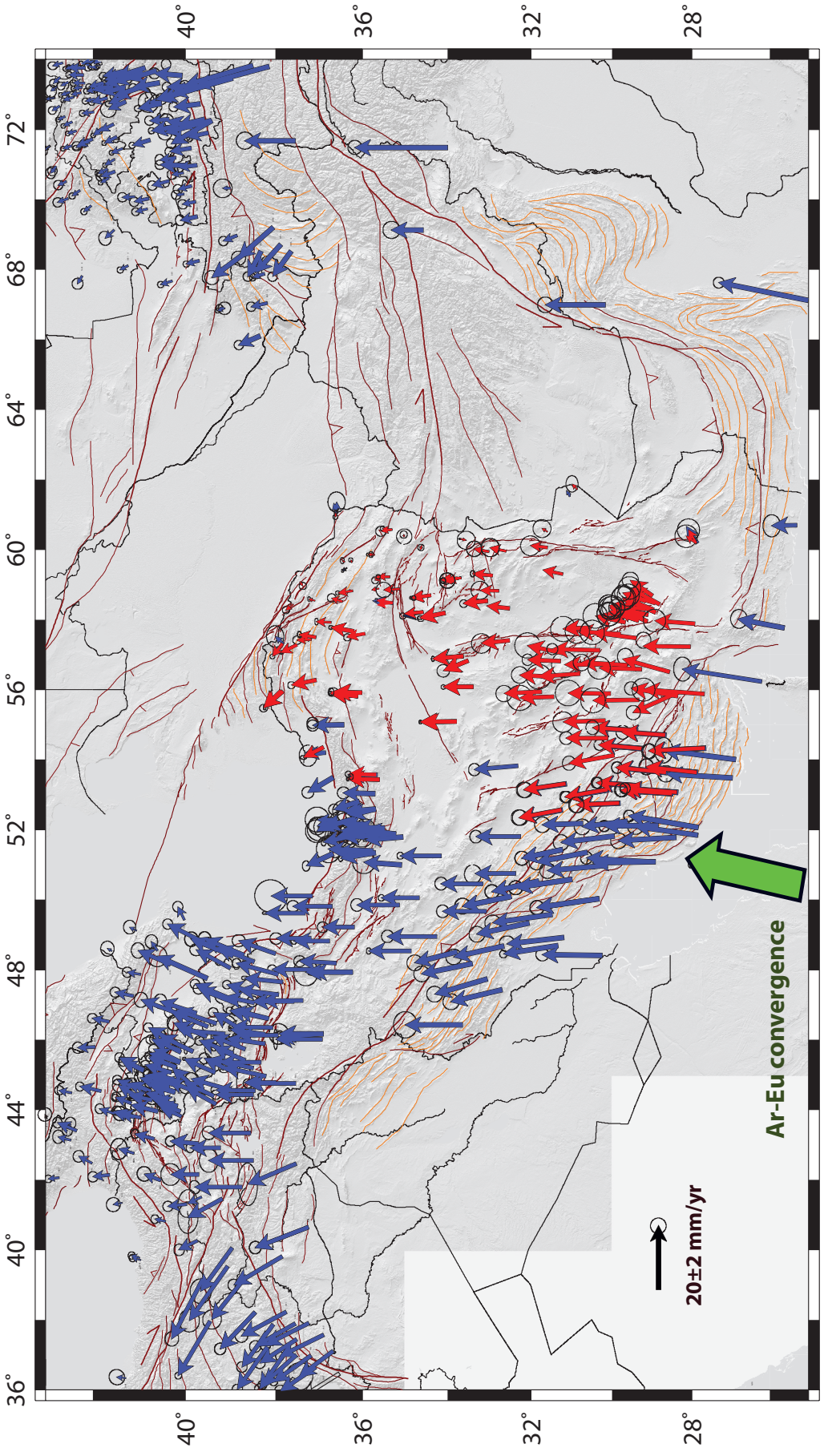

Figure 7.1 – Geodetic velocity of Alpine-Himalayan belt. The red vectors are from previous studies [Vernant et al., 2004a,b, Masson et al., 2005, 2007, Walpersdorf et al., 2006, Tavakoli et al., 2008, Djamour et al., 2010, 2011] and the dark blue are from this thesis. The green rectangle is the Doruneh campaign network and light blue are the IPGN station which are not published yet in particular at Makran subduction zone.

Beside the GPS data, we processed also SAR data to measure interseismic strain accumulation across two major faults, the Doruneh and the Shahroud fault, in Eastern Iran. The InSAR processing strategy was based on SBAS short baseline analysis. We used the ROI_pac software and NSBAS package to produce the interferograms. The tropospheric delay, orbital residual and DEM residual corrections have been done before unwrapping. Tropospheric delays were corrected using the ERA_Interim meteorological model. The SAR data for the Doruneh fault are 6 overlapping tracks covering the Doruneh from west to east. The Shahroud fault interseismic deformation has been measured by 2 tracks (1 ascending and 1 descending track) and cover the Abr, Khij and Jajarm fault, strands of the Shahroud fault system. The result of the SAR processing contributes to the geodetic velocity field for eastern Iran.

7.1.2 Geodetic fault slip rates

The geodetic data have been used to estimate the slip rates on most faults located inside the Lut region, Kopeh Dagh and Eastern Alborz. The short-term (geodetic) slip rates are coherent with available long-term (geologic) rates for most of the major faults in eastern Iran (figure 7.2).

Central-Eastern Iran :

Central-Eastern Iran is characterized by five NS right-lateral faults and further north, EW trending left-lateral faults. The NS right-lateral faults are the East Lut, West Lut, Kuhbanan, Anar and Deshir faults. They are currently active and slipping laterally at 5.6 $\pm$ 0.6, 4.4 $\pm$ 0.4, 3.6 $\pm$ 1.3, 2.0 $\pm$ 0.7, 1.4 $\pm$ 0.9 mm/yr, respectively. These five faults are delimiting six blocks which are moving towards the NNE with respect to Eurasia at rates between 12.7, 12.9, 12.6, 9.0, 5.7, 1.2 mm/yr from west to east (figure **??**. Each block rotates counterclockwise in the horizontal plane at rates ranging from 0.1 to 0.8°/Ma. A vertical axis block rotation model was suggested by Allen et al. [2011] describing the Central Iranian kinematics 10 Ma ago. Following this, Mattei et al. [2012] confirm counterclockwise rotation for three of the blocks. Our GPS results are suggesting that northward convergence can be accommodated in Central-Eastern Iran in two ways. First, the five large NS trending faults separate semi-rigid blocks which are moving northward at fast rates (6-13 mm/yr) with respect to Eurasia. Second, these faults accommodate NS shear between Central Iran and Afghanistan by counterclockwise rotation in the horizontal plane. This highlights the possibility that the vertical axis block rotation is still occurring in central Iran. Also, the short-term fault slip rates are approximately close to the long-term and Holocene slip rates in this area. It allowed us to propose that the counterclockwise rotations might have been operating at a similar rate since at least 10 Ma. Another mechanism for accommodating oblique convergence in central Iran is strain partitioning, as suggested by Allen et al. [2011]

. Unfortunately, our GPS network is not dense enough to be able to provide evidence for such a mechanism, and using SAR data to constrain two different mechanisms in one image is still a challenge, as we cannot distinguish both vertical and horizontal deformation when using only one SAR geometry.

Doruneh fault:

At the northern limit of the Lut block and other block slivers to the west, the EW trending Doruneh fault is one of the longest and most prominent faults in Iran (700 km length). The kinematic role of this dominant fault is not well known but it is thought to accommodate part of the tectonics of N-S right-lateral shear observed across Central Iran and the Lut block [Vernant et al., 2004b, Walker and Jackson, 2004]. The geodetic velocity field show $\sim$ 7 mm/yr NS shear [Vernant et al., 2004b] south of the Doruneh fault between the Lut block and Eurasian. A previous SBAS InSAR analysis covering a temporal span of 8 yr was suggesting 5 $\pm$1 mm/yr of left-lateral interseismic deformation along the Central part of the Doruneh fault [Pezzo et al., 2012]. In contrary, our GPS data suggest that the fault has a current left-lateral slip rate in the range 0.5-2.1 mm/yr (associated to a 2.1 $\pm$0.4 mm/yr compression) which is close to 2.4 $\pm$0.3 mm/yr of long-term slip rate [Fattahi et al., 2006b]. Our improved SBAS DInSAR analysis with better spatial coverage and with most up-to-date methods to reduce errors, in particular tropospheric delay and residuals of DEM and orbital errors indicates less than 5mm/yr of slip rate accommodated on this fault. This result has still to be refined in order to ensure the consistency of geodetic measurement, and to be able to discuss the variation between present-day and longer-term slip rate. We would like to investigate more the Doruneh fault by a new GPS campaign network around the fault (green rectangle in Fig. 7.1). All presently available GPS stations are either too far from this fault (in particular in its western side) or too close to the fault (like in its eastern part) to be able to distinguish the deformation across the fault, in particular in its eastern part, and to localize the deformation on the fault, in its western part.

North East of Iran :

North of the Doruneh fault, the GPS data show distributed right-lateral shearing that is accommodated across NE of Iran from 5mm/yr to 0 mm/yr at the Afghan border (figure 7.2). This shear is converted into shortening across the dominant mountain ranges, e.g. Kopeh Dagh, Binalud and Koh-e-Sorkh and dies out at the northern border of Iran. Comparisons of GPS fault slip estimations with geological slip rates can be done on several strike-slip faults in Central Kopeh Dagh. We estimate 3.3-5.4 mm/yr of cumulative right-lateral slip across the Baghan-Quchan fault zone (BQFZ) where Shabanian et al. [2009b] estimated long-term slip rates of 2.8$\pm$1 mm/yr and 4.3$\pm$ 0.6 mm/yr for the Baghan and Quchan faults, respectively. This means that the short-term slip rate is consistent with the lower boundary of the sum of the long-term slip rates on the BQFZ without taking into account any anticlockwise vertical axis rotation that might occur [Hollingsworth et al., 2006, 2008]. Also, in the western part of BQFZ, the Bojnord fault which is visible in the

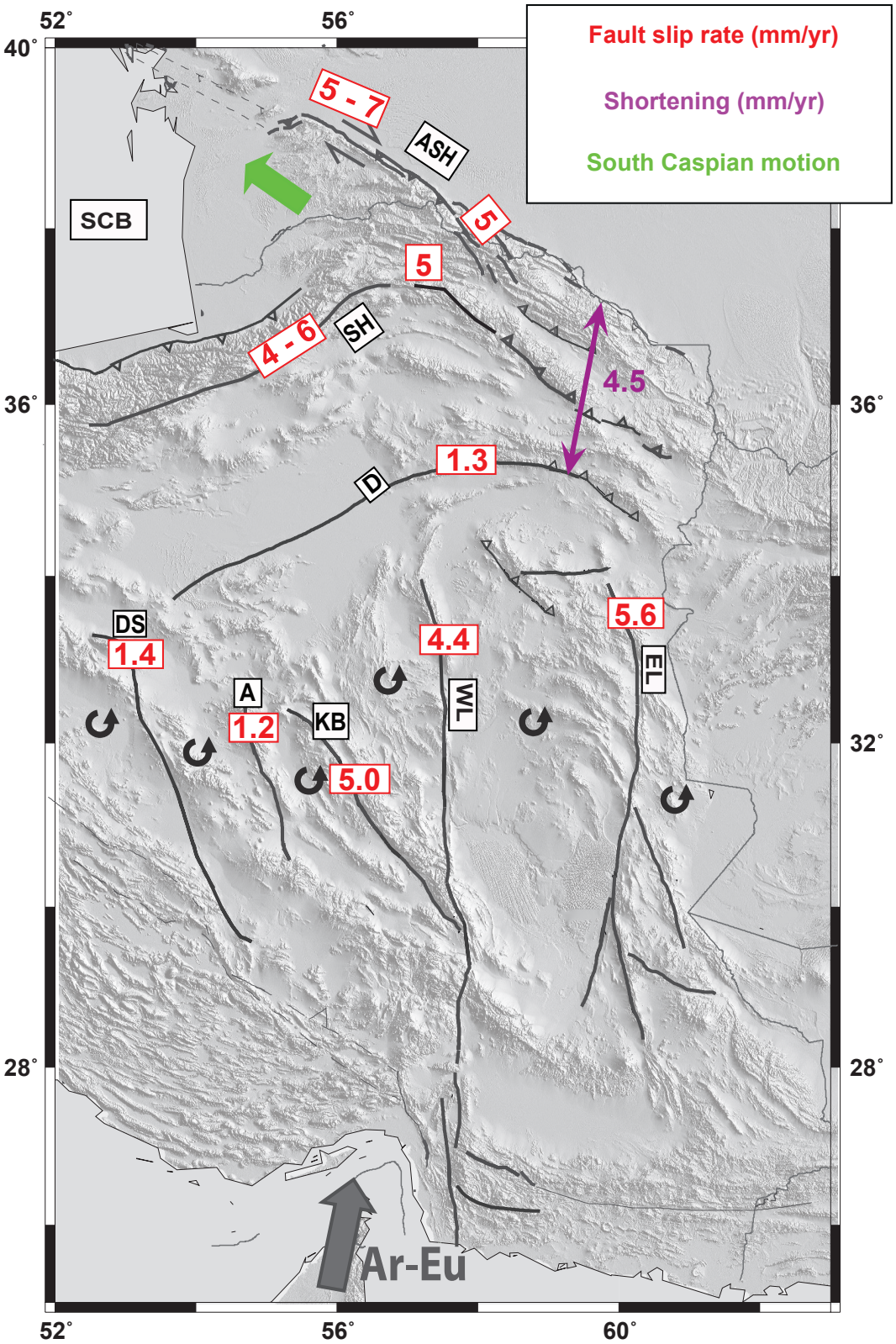

Figure 7.2 – Summary sketch of the tectonic pattern in the Eastern Iran. Overall Arabia-Eurasia motions is shown by the large gray arrow.

geomorphology and geology has 5.0± 1 mm/yr of left-lateral movement while there is no late Quaternary slip rate is available.

Further west, the GPS data also suggest that the South Caspian Basin is moving at ∼ 7 mm/yr with respect to Eurasia at an azimuth of 317°N. According to our GPS result, this motion can be described by a rigid block rotation around an Euler pole that is further away from NE Iran than previously thought. This north-westward motion results in 4-6mm/yr of left-lateral movement across Eastern Alborz. If partioning is occurring across the Alborz range [Jackson et al., 2002, Tatar et al., 2007, Hollingsworth et al., 2008, 2010a], this means that all the left-lateral movement is accommodated on the Shahroud Fault System (SFS) along the southern range of Alborz rather than on the Khazar thrust running along the northern range of Alborz. However, according to the rigid block modeling using DEFNODE, a left-lateral slip rate of about 2.4±1.0 mm/yr is attributed to the Khazar thrust [Mousavi et al., 2013]. This motivated us to do a SAR investigation to be able to distinguish the slip rate on the SFS from the Khazar thrust as the SFS might be responsible for the most destructive earthquake inside the Iranian plateau, the 856 A.D. Qumis earthquake that killed 200,000 people [Ambraseys and Melville, 1982, Hollingsworth et al., 2010b].

Shahroud Fault System:

I processed two SAR tracks (one ascending and one descending) across the SFS to measure interseismic strain accumulation. Removing atmospheric signals was the most challenging part of the SAR analysis for this area, as the SAR images cover mountainous, vegetation covered and arid areas together in one frame. We corrected the interferograms for atmospheric variability using the ECMWF ERA-Interim numerical weather model [Jolivet et al., 2011]. We constructed the constraint smoothed time series of the two tracks and estimated the mean velocity map that confirms the general left-lateral kinematics of the fault. The 2-D modeling using an elastic half-space [Savage and Burford, 1973], constrains the slip rate and locking depth to 4.75±0.65 mm/yr and 10±4 km, respectively. The ∼ 5mm/yr of left-lateral slip are localized on the Abr fault and further east on the Jajarm fault, two strands of the Shahroud fault system. The current slip rate at the Abr fault agrees with existing late Quaternary slip rate estimates of 3–4 mm/yr of left-lateral slip across the Abr Fault using the in situ-produced ^{10} Be cosmogenic dating method [Javidfakhr et al., 2011a]. However, there is no long term slip rate estimation for the Jajarm fault. Also the InSAR result is in good agreement with slip rate estimates from a simple GPS profile (4-6 mm/yr) rather than with the rigid block modeling (2±1mm/yr). This indicates that partitioning might occur in this part of Eastern Alborz and that most of the left-lateral displacement is accommodated on its southern limit, along the Shahroud Fault System. Moreover, the InSAR result is in good agreement with a faraway rotation

pole of the South Caspian Basin. This kinematic pattern is compatible with a fast slip rate of the Ashkabad fault at the NE limit of the South Caspian Basin [Walters, 2012]

7.1.3 Perspectives

The GPS velocity field in Eastern Iran is able to constrain the kinematics of the major blocks and faults in this region. Two exceptions are the Makran subduction zone with a sparse permanent GPS network that is not yet fully exploited and the Doruneh fault investigation with a new campaign network. Therefore, the first perspective will be to process the permanent network close to the Makran subduction zone to obtain constraints on the initial convergence south of the Lut block, and the new Doruneh campaign network to fill the observation gap in the desertic zone around the fault trace.

Campaign and permanent GPS networks, established since 1997 in Iran, provide crustal deformation data that are reasonably dense in most regions around faults. These data constrain average crustal velocity estimations inside the political borders of Iran. However, until now, no attention is paid to detecting and estimating transient deformation signals in the permanent network. Continuous GPS stations can provide a precise measurement of the average interseismic velocity field by fitting a constant velocity to the positioning time series. The measured interseismic deformation by GPS mostly is very close to steady-state in time [Savage and Lisowski, 1995]. But dense and continuous GPS stations can provide more information than simply average velocity. These data can help us to investigate the slip rate pattern in space and time. In Iran, until now, slip rate estimations for known faults were based on campaign networks, but now the IPGN network opens the possibility to constrain time varying slip rates. These transient deformations concern post-seismic slip (after slip, visco-elastic, poreelastic), slow slip events and loading phenomena (atmospheric, oceanic and hydrological).

Our future work might have implications on the understanding of current strain accumulation on active faults in Central-Eastern Iran. The planned geodetic measurement can be added to estimate the strain rate maps which can be used for seismic hazard evaluation. The hazard maps were usually based only on seismic data, but nowadays some insurance companies starts to include geodetic measurements in their processing of hazard maps. One project that is using the GPS, VLBI and DORIS measurements to map strain rate is the Global Strain Rate Map (GSRMP) [Kreemer and Haines, 2003]. The mission of the GSRM project is to determine a globally self-consistent strain rate and velocity field model, consistent with geodetic and geologic field observations. A complete global strain rate map will provide a large amount of information that is important for our understanding of continental dynamics and for the quantification of seismic hazards. Constructing a regular detailed strain rate map is even important for Iran if we keep in mind that the earthquakes in Iran often happen not on major fault strands, but on

secondary faults. If we can provide a very precise and high resolution strain rate map, we obtain independent and complementary information with respect to existing fault maps. This may bring new information for seismic hazard estimation in Iran.

To achieve this kind of hazard map for the Iranian plateau in the future, our work can complete preceding GPS studies that have been set up inside the political border of Iran [Vernant et al., 2004a,b, Djamour et al., 2010, 2011, Tavakoli et al., 2008, Walpersdorf et al., 2006, Masson et al., 2005, 2007]. While the GPS data have been used successfully to understand the current strain accumulation on active faults inside Iran since 1997, using InSAR remains a challenge because many of the faults are moving with less than a few mm per year inside Iran. Despite using the latest method in correcting the atmospheric and DEM residual errors, we were not successful to measure the low rate of interseismic deformation of the Doruneh fault, which was below the noise level. However, the same method was successful to estimate an interseismic deformation for faster faults like Shahroud (∼5 mm/yr of slip rate). The tropospheric delay still remains the most challenging error in the InSAR technique for slow-slip faults.

The new project of ESA of, two new C-band SAR satellites, might help us to do more investigation of slow-slip faults in the coming years. The two satellites, Sentinel-1A and Sentinel-1B are planned to launch in late 2013 and 2014, respectively. The twin satellites will have a 12-days orbit cycle with a combined revisit time of 6 days. Sentinel-1 is also planned to have a 100 m orbital tube, and this tighter orbital constraint should lead to better coherence in regions of significant topographic relief. As mentioned before, the atmospheric delays are the major source of limitations in the DInSAR technique. A new service known as OSCAR (Online Services for the Correction of Atmosphere for Radar) is close to being released. This service will combine operational ECMWF model outputs at 25 km resolution with MODIS estimates of water vapor to generate delay maps for InSAR [von Allmen et al., 2011, Walters, 2012].

Therefore, we expect that the new global SAR dataset with better coverage, high resolution and precision creates a great opportunity to the geophysicists to answer tectonic questions. This new dataset can help us to investigate remote areas without dense GPS networks coverage. If this new satellite system is helped with new methods of correcting errors and delay, it will be able to detect slow deformation beyond the present-day limitation (∼5mm/yr). Unknown or less important faults were responsible for the last two destructive earthquakes, the Mw 7.3 Rudbar and Mw 6.6 Bam earthquakes. These kinds of faults which are not well known before they produce a significant earthquake are not well observed by the GPS network. Therefore, the upcoming SAR images may highlight previously unknown areas of deformation and it can provide new information for seismic hazard maps.

Bibliography

G. D. Acton, S. Stein, and J. F. Engeln. Block rotation and continental extension in afar: A comparison to oceanic microplate systems. *Tectonics*, 10(3):501–526, 1991.

M. Allen, M. Ghassemi, M. Shahrabi, and M. Qorashi. Accommodation of late cenozoic oblique shortening in the alborz range, northern iran. *Journal of structural geology*, 25 (5):659–672, 2003.

M. Allen, J. Jackson, and R. Walker. Late cenozoic reorganization of the arabia-eurasia collision and the comparison of short-term and long-term deformation rates. *Tectonics*, 23(2):TC2008, 2004.

M. Allen, C. Saville, E. Blanc, M. Talebian, E. Nissen, et al. Orogenic plateau growth: Expansion of the turkish-iranian plateau across the zagros fold-and-thrust belt. *Tectonics*, 32:171–190, 2013.

M. B. Allen, E. J.-P. Blanc, R. Walker, J. Jackson, M. Talebian, and M. R. Ghassemi. Contrasting styles of convergence in the arabia-eurasia collision: Why escape tectonics does not occur in iran. *Geological Society of America Special Papers*, 409:579–589, 2006.

M. B. Allen, M. Kheirkhah, M. H. Emami, and S. J. Jones. Right-lateral shear across iran and kinematic change in the arabia–eurasia collision zone. *Geophysical Journal International*, 184(2):555–574, 2011.

Z. Altamimi, P. Sillard, and C. Boucher. Itrf2000: A new release of the international terrestrial reference frame for earth science applications. *Journal of Geophysical Research: Solid Earth (1978–2012)*, 107(B10):ETG–2, 2002.

Z. Altamimi, X. Collilieux, J. Legrand, B. Garayt, and C. Boucher. Itrf2005: A new release of the international terrestrial reference frame based on time series of station positions and earth orientation parameters. *Journal of Geophysical Research: Solid Earth (1978–2012)*, 112(B9), 2007.

Z. Altamimi, X. Collilieux, and L. Métivier. Itrf2008: an improved solution of the international terrestrial reference frame. *Journal of Geodesy*, 85(8):457–473, 2011.

N. Ambraseys and C. Melville. *A History of Persian Earthquakes*. Cambridge University Press, Cambridge, 1982.

N. Ambraseys and J. Tchalenko. The dasht-e bayāz (iran) earthquake of august 31, 1968: A field report. *Bulletin of the Seismological Society of America*, 59(5):1751–1792, 1969.

J. Askne and H. Nordius. Estimation of tropospheric delay for microwaves from surface weather data. *Radio Science*, 22(3):379–386, 1987.

D. Bachmanov, V. Trifonov, K. T. Hessami, A. Kozhurin, T. Ivanova, E. Rogozhin, M. Hademi, and F. Jamali. Active faults in the zagros and central iran. *Tectonophysics*, 380(3):221–241, 2004.

C. Baker, J. Jackson, and K. Priestley. Earthquakes on the kazerun line in the zagros mountains of iran: strike-slip faulting within a fold-and-thrust belt. *Geophysical Journal International*, 115(1):41–61, 1993.

R. Bamler. Principles of synthetic aperture radar. *Surveys in Geophysics*, 21(2-3):147–157, 2000.

R. Bamler and P. Hartl. Synthetic aperture radar interferometry. *Inverse problems*, 14(4): R1, 1998.

R. Bayer, J. Chery, M. Tatar, P. Vernant, M. Abbassi, F. Masson, F. Nilforoushan, E. Doerflinger, V. Regard, and O. Bellier. Active deformation in zagros–makran transition zone inferred from gps measurements. *Geophysical Journal International*, 165(1):373–381, 2006.

B. Bean and E. Dutton. Radio meteorology. national bureau of standards monogr, 1968.

O. Bellier, S. Över, A. Poisson, and J. Andrieux. Recent temporal change in the stress state and modern stress field along the north anatolian fault zone (turkey). *Geophysical Journal International*, 131(1):61–86, 1997.

R. A. Bennett. Instantaneous deformation from continuous gps: Contributions from quasi-periodic loads. *Geophysical Journal International*, 174(3):1052–1064, 2008.

P. Berardino, G. Fornaro, R. Lanari, and E. Sansosti. A new algorithm for surface deformation monitoring based on small baseline differential sar interferograms. *Geoscience and Remote Sensing, IEEE Transactions on*, 40(11):2375–2383, 2002.

M. Berberian. *Contribution to the Seismotectonics of Iran (part II-III): In Commemoration of the 50th Anniversary of the Pahlavi Dynasty*. Number 39. Ministry of Industry and Mines, Geological Survey of Iran, Tectonic and Seismotectonic Section, 1976.

M. Berberian. Active faulting and tectonics of iran. *Geodynamics Series*, 3:33–69, 1981.

M. Berberian and M. Qorashi. Coseismic fault-related folding during the south golbaf earthquake of november 20, 1989, in southeast iran. *Geology*, 22(6):531–534, 1994.

M. Berberian and R. Walker. The rudbār mw 7.3 earthquake of 1990 june 20; seismotectonics, coseismic and geomorphic displacements, and historic earthquakes of the western 'high-alborz', iran. *Geophysical Journal International*, 182(3):1577–1602, 2010.

M. Berberian and R. S. Yeats. Patterns of historical earthquake rupture in the iranian plateau. *Bulletin of the Seismological Society of America*, 89(1):120–139, 1999.

M. Berberian and R. S. Yeats. Contribution of archaeological data to studies of earthquake history in the iranian plateau. *Journal of Structural Geology*, 23(2):563–584, 2001.

M. Berberian, I. Asudeh, and S. Arshadi. Surface rupture and mechanism of the bob-tangol (southeastern iran) earthquake of 19 december 1977. *Earth and Planetary Science Letters*, 42(3):456–462, 1979.

M. Berberian, M. Qorashi, J. Jackson, K. Priestley, and T. Wallace. The rudbar-tarom earthquake of 20 june 1990 in nw persia: preliminary field and seismological observations, and its tectonic significance. *Bulletin of the Seismological Society of America*, 82(4): 1726–1755, 1992.

M. Berberian, J. Jackson, M. Qorashi, M. Khatib, K. Priestley, M. Talebian, and M. Ghafuri-Ashtiani. The 1997 may 10 zirkuh (qa'enat) earthquake (mw 7.2): faulting along the sistan suture zone of eastern iran. *Geophysical Journal International*, 136(3): 671–694, 1999.

M. Berberian, J. Jackson, M. Qorashi, M. Talebian, M. Khatib, and K. Priestley. The 1994 sefidabeh earthquakes in eastern iran: blind thrusting and bedding-plane slip on a growing anticline, and active tectonics of the sistan suture zone. *Geophysical Journal International*, 142(2):283–299, 2000.

M. Berberian, J. Jackson, E. Fielding, B. Parsons, K. Priestley, M. Qorashi, M. Talebian, R. Walker, T. Wright, and C. Baker. The 1998 march 14 fandoqa earthquake (mw 6.6) in kerman province, southeast iran: Re-rupture of the 1981 sirch earthquake fault, triggering of slip on adjacent thrusts and the active tectonics of the gowk fault zone. *Geophysical Journal International*, 146(2):371–398, 2001.

A. L. Berman. The prediction of zenith range refraction from surface measurements of meteorological parameters. *Unknown*, 1, 1976.

H. Berrada Baby, P. Gole, and J. Lavergnat. A model for the tropospheric excess path length of radio waves from surface meteorological measurements. *Radio science*, 23(6): 1023–1038, 1988.

G. Beutler, E. Brockmann, S. Fankhauser, W. Gurtner, J. Johnson, L. Mervart, M. Rothacher, S. Schaer, T. Springer, and R. Weber. Bernese gps software version 4.0. *Astron. Inst., Univ. of Bern, Bern, Switzerland*, 1996.

M. Bevis, S. Businger, T. A. Herring, C. Rocken, R. A. Anthes, and R. H. Ware. Gps meteorology: Remote sensing of atmospheric water vapor using the global positioning system. *Journal of Geophysical Research: Atmospheres (1984–2012)*, 97(D14):15787–15801, 1992.

M. Bevis, S. Businger, S. Chiswell, T. A. Herring, R. A. Anthes, C. Rocken, and R. H. Ware. Gps meteorology: Mapping zenith wet delays onto precipitable water. *Journal of applied meteorology*, 33(3):379–386, 1994.

G. Biessy. *Quantification et caractérisation des mouvements verticaux aux courtes échelles de temps dans les zones dites stables.* PhD thesis, Uuniversité de Rennes 1, 2009.

J. Biggs, T. Wright, Z. Lu, and B. Parsons. Multi-interferogram method for measuring interseismic deformation: Denali fault, alaska. *Geophysical Journal International*, 170 (3):1165–1179, 2007.

G. Blewitt. Carrier phase ambiguity resolution for the global positioning system applied to geodetic baselines up to 2000 km. *Journal of Geophysical Research: Solid Earth (1978–2012)*, 94(B8):10187–10203, 1989.

G. Blewitt. An automatic editing algorithm for gps data. *Geophysical Research Letters*, 17(3):199–202, 1990.

G. Blewitt. Gps data processing methodology: From theory to applications. In *GPS for Geodesy*, pages 231–270. Springer, 1998.

G. Blewitt. Self-consistency in reference frames, geocenter definition, and surface loading of the solid earth. *Journal of geophysical research*, 108(B2):2103, 2003.

G. Blewitt, D. Lavallée, P. Clarke, and K. Nurutdinov. A new global mode of earth deformation: Seasonal cycle detected. *Science*, 294(5550):2342–2345, 2001.

Y. Bock, S. A. Gourevitch, C. C. Counselman III, R. W. King, and R. I. Abbot. Interferometric analysis of gps phase observations. *Manuscripta geodaetica*, 11:282–288, 1986.

J. Boehm and H. Schuh. Vienna mapping functions in vlbi analyses. *Geophysical Research Letters*, 31(1), 2004.

J. Boehm, B. Werl, and H. Schuh. Troposphere mapping functions for gps and very long baseline interferometry from european centre for medium-range weather forecasts operational analysis data. *Journal of Geophysical Research*, 111(B2):B02406, 2006.

J. Böhm, A. Niell, P. Tregoning, and H. Schuh. Global mapping function (gmf): A new empirical mapping function based on numerical weather model data. *Geophysical Research Letters*, 33(7):L07304, 2006.

C. Boucher. Terrestrial coordinate systems and frames. *Encyclopedia of Astronomy and Astrophysics*, 1:1906, 2000.

G. Boudouris. On the index of refraction of air, the absorption and dispersion of centimeter waves by gases(refractive index of atmospheric gases, dry air and damp air and absorption and dispersion of chloroform and ammonia vapors, using a microwave spectrometer). *JOURNAL OF RESEARCH*, 67:631–684, 1963.

R. Bürgmann and G. Dresen. Rheology of the lower crust and upper mantle: Evidence from rock mechanics, geodesy, and field observations. *Annu. Rev. Earth Planet. Sci.*, 36:531–567, 2008.

R. Bürgmann, E. Fielding, and J. Sukhatme. Slip along the hayward fault, california, estimated from space-based synthetic aperture radar interferometry. *Geology*, 26(6): 559–562, 1998.

R. Bürgmann, P. A. Rosen, and E. J. Fielding. Synthetic aperture radar interferometry to measure earth's surface topography and its deformation. *Annual Review of Earth and Planetary Sciences*, 28(1):169–209, 2000.

R. Bürgmann, M. E. Ayhan, E. J. Fielding, T. J. Wright, S. McClusky, B. Aktug, C. Demir, O. Lenk, and A. Türkezer. Deformation during the 12 november 1999 düzce, turkey, earthquake, from gps and insar data. *Bulletin of the Seismological Society of America*, 92(1):161–171, 2002.

S. Businger, S. R. Chiswell, M. Bevis, J. Duan, R. A. Anthes, C. Rocken, R. H. Ware, M. Exner, T. VanHove, and F. S. Solheim. The promise of gps in atmospheric monitoring. *Bulletin of the American Meteorological Society*, 77(1):5–18, 1996.

O. Cavalié, M.-P. Doin, C. Lasserre, and P. Briole. Ground motion measurement in the lake mead area, nevada, by differential synthetic aperture radar interferometry time series analysis: Probing the lithosphere rheological structure. *Journal of geophysical research*, 112(B3):B03403, 2007.

O. Cavalié, C. Lasserre, M.-P. Doin, G. Peltzer, J. Sun, X. Xu, and Z.-K. Shen. Measurement of interseismic strain across the haiyuan fault (gansu, china), by insar. *Earth and Planetary Science Letters*, 275(3):246–257, 2008.

O. Cavalié, E. Pathier, M. Radiguet, M. Vergnolle, N. Cotte, A. Walpersdorf, V. Kostoglodov, and F. Cotton. Slow slip event in the mexican subduction zone: Evidence of shallower slip in the guerrero seismic gap for the 2006 event revealed by the joint inversion of insar and gps data. *Earth and Planetary Science Letters*, 367:52–60, 2013.

C. W. Chen and H. A. Zebker. Network approaches to two-dimensional phase unwrapping: intractability and two new algorithms. *JOSA A*, 17(3):401–414, 2000.

F. Cifelli, M. Mattei, H. Rashid, and J. Ghalamghash. Right-lateral transpressional tectonics along the boundary between lut and tabas blocks (central iran). *Geophysical Journal International*, 193(3):1153–1165, 2013.

H. S. Cobb. *GPS pseudolites: Theory, design, and applications.* PhD thesis, Stanford University, 1997.

A. Copley and J. Jackson. Active tectonics of the turkish-iranian plateau. *Tectonics*, 25 (6):TC6006, 2006.

J. C. Curlander and R. N. McDonough. Synthetic aperture radar- systems and signal processing(book). *New York: John Wiley & Sons, Inc, 1991.*, 1991.

J. Davis, P. Elósegui, J. Mitrovica, and M. Tamisiea. Climate-driven deformation of the solid earth from grace and gps. *Geophysical research letters*, 31(24), 2004.

D. Dee, S. Uppala, A. Simmons, P. Berrisford, P. Poli, S. Kobayashi, U. Andrae, M. Balmaseda, G. Balsamo, P. Bauer, et al. The era-interim reanalysis: Configuration and performance of the data assimilation system. *Quarterly Journal of the Royal Meteorological Society*, 137(656):553–597, 2011.

C. Delacourt, P. Briole, and J. Achache. Tropospheric corrections of sar interferograms with strong topography. application to etna. *Geophysical Research Letters*, 25(15):2849–2852, 1998.

Y. Djamour, P. Vernant, R. Bayer, H. R. Nankali, J.-F. Ritz, J. Hinderer, Y. Hatam, B. Luck, N. Le Moigne, M. Sedighi, et al. Gps and gravity constraints on continental deformation in the alborz mountain range, iran. *Geophysical Journal International*, 183 (3):1287–1301, 2010.

Y. Djamour, P. Vernant, H. R. Nankali, and F. Tavakoli. Nw iran-eastern turkey present-day kinematics: Results from the iranian permanent gps network. *Earth and Planetary Science Letters*, 307(1):27–34, 2011.

M.-P. Doin, C. Lasserre, G. Peltzer, O. Cavalié, and C. Doubre. Corrections of stratified tropospheric delays in sar interferometry: Validation with global atmospheric models. *Journal of Applied Geophysics*, 69(1):35–50, 2009.

M.-P. Doin, S. Guillaso, R. Jolivet, C. Lasserre, F. Lodge, G. Ducret, and R. Grandin. Presentation of the small-baseline nsbas processing chain on a case example: The etna deformation monitoring from 2003 to 2010 using envisat data. In *Proceedings of the European Space Agency Symposium "Fringe", Frascati, Italy, 19–23 September 2011*, pages 303–304, 2011.

D. Dong, P. Fang, Y. Bock, M. Cheng, and S. Miyazaki. Anatomy of apparent seasonal variations from gps-derived site position time series. *Journal of Geophysical Research*, 107(B4):2075, 2002.

D. Dong, T. Yunck, and M. Heflin. Origin of the international terrestrial reference frame. *Journal of Geophysical Research: Solid Earth (1978–2012)*, 108(B4), 2003.

D. Dong, P. Fang, Y. Bock, F. Webb, L. Prawirodirdjo, S. Kedar, and P. Jamason. Spatiotemporal filtering using principal component analysis and karhunen-loeve expansion approaches for regional gps network analysis. *Journal of Geophysical Research: Solid Earth (1978–2012)*, 111(B3), 2006.

D.-N. Dong and Y. Bock. Global positioning system network analysis with phase ambiguity resolution applied to crustal deformation studies in california. *Journal of Geophysical Research*, 94(B4):3949–3966, 1989.

J. M. Dow, R. Neilan, and C. Rizos. The international gnss service in a changing landscape of global navigation satellite systems. *Journal of Geodesy*, 83(3-4):191–198, 2009.

G. Ducret, M. P. Doin, R. Grandin, C. Lasserre, and S. Guillaso. Dem corrections before unwrapping in a small baseline strategy for insar time series analysis. In *Geoscience and Remote Sensing Symposium (IGARSS), 2011 IEEE International*, pages 1353–1356. IEEE, 2011.

G. Ducret, M. P. Doin, R. Grandin, C. Lasserre, and S. Guillaso. Dem corrections before unwrapping in a small baseline strategy for insar time series analysis. In *IEEE GEOSCIENCE AND REMOTE SENSING LETTERS*. IEEE, 2013.

J. Elliott, J. Biggs, B. Parsons, and T. Wright. Insar slip rate determination on the altyn tagh fault, northern tibet, in the presence of topographically correlated atmospheric delays. *Geophysical Research Letters*, 35(12), 2008.

T. R. Emardson and H. J. Derks. On the relation between the wet delay and the integrated precipitable water vapour in the european atmosphere. *Meteorological Applications*, 7 (1):61–68, 2000.

E. Engdahl and A. Villaseñor. 41 global seismicity: 1900–1999. *International Geophysics*, 81:665–XVI, 2002.

E. R. Engdahl, J. A. Jackson, S. C. Myers, E. A. Bergman, and K. Priestley. Relocation and assessment of seismicity in the iran region. *Geophysical Journal International*, 167 (2):761–778, 2006.

P. England and J. Jackson. Uncharted seismic risk. *Nature Geoscience*, 4(6):348–349, 2011.

A. Fadil, L. Sichoix, J.-P. Barriot, P. Ortéga, and P. Willis. Evidence for a slow subsidence of the tahiti island from gps, doris, and combined satellite altimetry and tide gauge sea level records. *Comptes Rendus Geoscience*, 343(5):331–341, 2011.

Y. Farbod, O. Bellier, E. Shabanian, and M. R. Abbassi. Geomorphic and structural variations along the doruneh fault system (central iran). *Tectonics*, 30(6), 2011.

T. G. Farr and M. Kobrick. Shuttle radar topography mission produces a wealth of data. *Eos, Transactions American Geophysical Union*, 81(48):583–585, 2000.

T. G. Farr, P. A. Rosen, E. Caro, R. Crippen, R. Duren, S. Hensley, M. Kobrick, M. Paller, E. Rodriguez, L. Roth, et al. The shuttle radar topography mission. *Reviews of geophysics*, 45(2), 2007.

W. Farrell. Deformation of the earth by surface loads. *Reviews of Geophysics*, 10(3): 761–797, 1972.

M. Fattahi and R. T. Walker. Luminescence dating of the last earthquake of the sabzevar thrust fault, ne iran. *Quaternary Geochronology*, 2(1):284–289, 2007.

M. Fattahi, R. Walker, J. Hollingsworth, A. Bahroudi, H. Nazari, M. Talebian, S. Armitage, and S. Stokes. Holocene slip-rate on the sabzevar thrust fault, ne iran, determined using optically stimulated luminescence (osl). *Earth and Planetary Science Letters*, 245(3): 673–684, 2006a.

M. Fattahi, R. Walker, M. Khatib, A. Dolati, and A. Bahroudi. Slip-rate estimate and past earthquakes on the doruneh fault, eastern iran. *Geophysical Journal International*, 168(2):691–709, 2006b.

M. Fattahi, H. Nazari, M. Bateman, B. Meyer, M. Sébrier, M. Talebian, K. Le Dortz, M. Foroutan, F. Ahmadi Givi, and M. Ghorashi. Refining the osl age of the last earthquake on the dheshir fault, central iran. *Quaternary Geochronology*, 5(2):286–292, 2010.

M. Fattahi, R. Walker, M. Talebian, R. Sloan, and A. Rasheedi. The structure and late quaternary slip rate of the rafsanjan strike-slip fault, se iran. *Geosphere*, 7(5):1159–1174, 2011.

A. Ferretti, C. Prati, and F. Rocca. Nonlinear subsidence rate estimation using permanent scatterers in differential sar interferometry. *Geoscience and Remote Sensing, IEEE transactions on*, 38(5):2202–2212, 2000.

A. Ferretti, C. Prati, and F. Rocca. Permanent scatterers in sar interferometry. *Geoscience and Remote Sensing, IEEE Transactions on*, 39(1):8–20, 2001.

M. B. S. S. A. B. O. M. N. M. S. Foroutan, M. and M. Eskandari. Primary report of konarak earthquake 2010 dec 20 (rigan, kerman). Technical report, Geological Survey of Iran, 2010.

T. Fournier, M. E. Pritchard, and N. Finnegan. Accounting for atmospheric delays in insar data in a search for long-wavelength deformation in south america. *Geoscience and Remote Sensing, IEEE Transactions on*, 49(10):3856–3867, 2011.

A. Franco. *Cinématique Actuelle du Nord de l'Amérique Centrale: Zone de Jonction Triple Amérique du Nord Amérique-Cocos-Caraïbe. Apport des données sismologiques et géodésiques aux modèles régionaux.* PhD thesis, Université Paris Sud-Paris XI, 2008.

A. Franco, C. Lasserre, H. Lyon-Caen, V. Kostoglodov, E. Molina, M. Guzman-Speziale, D. Monterosso, V. Robles, C. Figueroa, W. Amaya, et al. Fault kinematics in northern central america and coupling along the subduction interface of the cocos plate, from gps data in chiapas (mexico), guatemala and el salvador. *Geophysical Journal International*, 189(3):1223–1236, 2012.

R. Freund. Rotation of strike slip faults in sistan, southeast iran. *The Journal of Geology*, pages 188–200, 1970.

R. Freund. Kinematics of transform and transcurrent faults. *Tectonophysics*, 21(1):93–134, 1974.

A. Gelb. *Applied optimal estimation.* The MIT press, 1974.

R. M. Goldstein and C. L. Werner. Radar interferogram filtering for geophysical applications. *Geophysical Research Letters*, 25(21):4035–4038, 1998.

R. M. Goldstein, H. A. Zebker, and C. L. Werner. Satellite radar interferometry: Two-dimensional phase unwrapping. *Radio Science*, 23(4):713–720, 1988.

A. L. Gray, K. E. Mattar, and G. Sofko. Influence of ionospheric electron density fluctuations on satellite radar interferometry. *Geophysical Research Letters*, 27(10):1451–1454, 2000.

S. Guillaso. *Complémentarité polarimétrie/interférométrie pour la détection et la caractérisation de cibles.* PhD thesis, Institut d'Electronique et des Télécommunications de Rennes, 2003.

J. Haase, E. Calais, J. Talaya, A. Rius, F. Vespe, R. Santangelo, X.-Y. Huang, J. Davila, M. Ge, L. Cucurull, et al. The contributions of the magic project to the cost 716 objectives of assessing the operational potential of ground-based gps meteorology on an international scale. *Physics and Chemistry of the Earth, Part A: Solid Earth and Geodesy*, 26(6):433–437, 2001.

R. F. Hanssen. *Radar interferometry: data interpretation and error analysis*, volume 2. Kluwer Academic Pub, 2001.

D. Hatzfeld and P. Molnar. Comparisons of the kinematics and deep structures of the zagros and himalaya and of the iranian and tibetan plateaus and geodynamic implications. *Reviews of Geophysics*, 48(2), 2010.

T. Herring, R. King, and S. McClusky. Global kalman filter vlbi and gps analysis program, globk reference manual, release 10.3. *Massachussetts: MIT, Cambridge*, 2006.

T. Herring, R. King, and S. McClusky. Introduction to gamit/globk. *Mass. Inst. of Technol., Cambridge, Mass*, 2008.

T. Herring, R. King, and S. McClusky. Introduction to gamit/globk 10.4. *Mass. Inst. of Technol., Cambridge, Mass*, 2010.

T. A. Herring. *Treatise on geophysics.* Elsevier, New York, 2007.

T. A. Herring, J. L. Davis, and I. I. Shapiro. Geodesy by radio interferometry: The application of kalman filtering to the analysis of very long baseline interferometry data. *Journal of Geophysical Research: Solid Earth (1978–2012)*, 95(B8):12561–12581, 1990.

K. Hessami, F. Nilforoushan, and C. J. Talbot. Active deformation within the zagros mountains deduced from gps measurements. *Journal of the Geological Society*, 163(1): 143–148, 2006.

R. Hill, R. Lawrence, and J. Priestley. Theoretical and calculational aspects of the radio refractive index of water vapor. *Radio Science*, 17(5):1251–1257, 1982.

R. J. Hill. Dispersion by atmospheric water vapor at frequencies less than 1 thz. *Antennas and Propagation, IEEE Transactions on*, 36(3):423–430, 1988.

B. Hofmann-Wellenhof, H. Lichtenegger, and J. Collins. Global positioning system. theory and practice. *Global Positioning System. Theory and practice., by Hofmann-Wellenhof, B.; Lichtenegger, H.; Collins, J.. Springer, Wien (Austria), 1993, 347 p., ISBN 3-211-82477-4, Price DM 79.00. ISBN 0-387-82477-4 (USA).*, 1, 1993.

B. Hofmann-Wellenhof, H. Lichtenegger, and E. Wasle. *Gnss: Global Navigation Satellite Systems: Gps, Glonass, Galileo, and More*. Springer, 2008.

J. Hollingsworth, J. Jackson, R. Walker, M. Reza Gheitanchi, and M. Javad Bolourchi. Strike-slip faulting, rotation, and along-strike elongation in the kopeh dagh mountains, ne iran. *Geophysical Journal International*, 166(3):1161–1177, 2006.

J. Hollingsworth, J. Jackson, R. Walker, and H. Nazari. Extrusion tectonics and subduction in the eastern south caspian region since 10 ma. *Geology*, 36(10):763–766, 2008.

J. Hollingsworth, J. Jackson, R. Walker, and H. Nazari. Extrusion tectonics and subduction in the eastern south caspian region since 10 ma: Reply. *Geology*, 37(12):e199–e200, 2009.

J. Hollingsworth, M. Fattahi, R. Walker, M. Talebian, A. Bahroudi, M. J. Bolourchi, J. Jackson, and A. Copley. Oroclinal bending, distributed thrust and strike-slip faulting, and the accommodation of arabia–eurasia convergence in ne iran since the oligocene. *Geophysical Journal International*, 181(3):1214–1246, 2010a.

J. Hollingsworth, H. Nazari, J.-F. Ritz, R. Salamati, M. Talebian, A. Bahroudi, R. T. Walker, M. Rizza, and J. Jackson. Active tectonics of the east alborz mountains, ne iran: Rupture of the left-lateral astaneh fault system during the great 856 ad qumis earthquake. *Journal of Geophysical Research*, 115(B12):B12313, 2010b.

A. Hooper. A multi-temporal insar method incorporating both persistent scatterer and small baseline approaches. *Geophysical Research Letters*, 35(16), 2008.

A. Hooper, H. Zebker, P. Segall, and B. Kampes. A new method for measuring deformation on volcanoes and other natural terrains using insar persistent scatterers. *Geophysical research letters*, 31(23), 2004.

A. Hooper, P. Segall, and H. Zebker. Persistent scatterer interferometric synthetic aperture radar for crustal deformation analysis, with application to volcán alcedo, galápagos. *Journal of Geophysical Research: Solid Earth (1978–2012)*, 112(B7), 2007.

H. Hopfield. Two-quartic tropospheric refractivity profile for correcting satellite data. *Journal of Geophysical research*, 74(18):4487–4499, 1969.

I. Ifadis. The atmospheric delay of radio waves: modeling the elevation dependence on a global scale. Technical report, School of Electrical and Computer Engineering, Chalmers University of Technology, Goteborg, Sweden, 1986.

J. Jackson. Fatal attraction: living with earthquakes, the growth of villages into megacities, and earthquake vulnerability in the modern world. *Philosophical Transactions of the Royal Society A: Mathematical, Physical and Engineering Sciences*, 364(1845):1911–1925, 2006.

J. Jackson and D. McKenzie. Active tectonics of the alpine–himalayan belt between western turkey and pakistan. *Geophysical Journal of the Royal Astronomical Society*, 77(1):185–264, 1984.

J. Jackson and D. McKenzie. The relationship between plate motions and seismic moment tensors, and the rates of active deformation in the mediterranean and middle east. *Geophysical Journal*, 93(1):45–73, 1988.

J. Jackson, J. Haines, and W. Holt. The accommodation of arabia-eurasia plate convergence in iran. *Journal of Geophysical Research: Solid Earth (1978–2012)*, 100(B8): 15205–15219, 1995.

J. Jackson, K. Priestley, M. Allen, and M. Berberian. Active tectonics of the south caspian basin. *Geophysical Journal International*, 148(2):214–245, 2002.

B. Javidfakhr, O. Bellier, E. Shabanian, L. Siame, L. Léanni, D. Bourlès, and S. Ahmadian. Fault kinematics and active tectonics at the southeastern boundary of the eastern alborz (abr and khij fault zones): Geodynamic implications for nne iran. *Journal of Geodynamics*, 52(3):290–303, 2011a.

B. Javidfakhr, O. Bellier, E. Shabanian, S. Ahmadian, and A. Saidi. Plio–quaternary tectonic regime changes in the transition zone between alborz and kopeh dagh mountain ranges (ne iran). *Tectonophysics*, 506(1):86–108, 2011b.

K. H. Ji and T. A. Herring. Transient signal detection using gps measurements: Transient inflation at akutan volcano, alaska, during early 2008. *Geophysical Research Letters*, 38 (6), 2011.

H. O. Johnson and D. C. Agnew. Monument motion and measurements of crustal velocities. *Geophysical research letters*, 22(21):2905–2908, 1995.

K. Johnson and P. Segall. Viscoelastic earthquake cycle models with deep stress-driven creep along the san andreas fault system. *Journal of Geophysical Research: Solid Earth (1978–2012)*, 109(B10), 2004.

R. Jolivet. *Déformation intersismique le long de la faille de Haiyuan, Chine*. PhD thesis, Joseph Fourier University, 2011.

R. Jolivet, R. Grandin, C. Lasserre, M.-P. Doin, and G. Peltzer. Systematic insar tropospheric phase delay corrections from global meteorological reanalysis data. *Geophysical Research Letters*, 38(17), 2011.

R. Jolivet, C. Lasserre, M.-P. Doin, S. Guillaso, G. Peltzer, R. Dailu, J. Sun, Z.-K. Shen, and X. Xu. Shallow creep on the haiyuan fault (gansu, china) revealed by sar interferometry. *Journal of Geophysical Research: Solid Earth (1978–2012)*, 117(B6), 2012.

S. Jonsson, P. Segall, R. Pedersen, and G. Björnsson. Post-earthquake ground movements correlated to pore-pressure transients. *Nature*, 424(6945):179–183, 2003.

Y. Kaneko, Y. Fialko, D. Sandwell, X. Tong, and M. Furuya. Interseismic deformation and creep along the central section of the north anatolian fault (turkey): Insar observations and implications for rate-and-state friction properties. *Journal of Geophysical Research: Solid Earth*, 2013.

A. Karakhanyan, P. Vernant, E. Doerflinger, A. Avagyan, H. Philip, R. Aslanyan, C. Champollion, S. Arakelyan, P. Collard, H. Baghdasaryan, et al. Gps constraints on continental deformation in the armenian region and lesser caucasus. *Tectonophysics*, 2013.

S. Kedar, G. A. Hajj, B. D. Wilson, and M. B. Heflin. The effect of the second order gps ionospheric correction on receiver positions. *Geophysical Research Letters*, 30(16), 2003.

R. King and Y. Bock. Documentation for the gamit gps software analysis, release 10.05. *Mass. Inst. of Technol. Cambridge*, 2001.

M. C. Kleinrock and R. Hey. Migrating transform zone and lithospheric transfer at the galapagos 95.5 w propagator. *Journal of Geophysical Research: Solid Earth (1978–2012)*, 94(B10):13859–13878, 1989.

W. E. H. Kreemer, C. and A. J. Haines. An integrated global model of present-day plate motions and plate boundary deformation. *Geophysical Journal International*, 154:8–34, 2003.

R. Lanari, P. Berardino, S. Borgström, C. Del Gaudio, P. De Martino, G. Fornaro, S. Guarino, G. Ricciardi, E. Sansosti, and P. Lundgren. The use of ifsar and classical geodetic techniques for caldera unrest episodes: application to the campi flegrei uplift event of 2000. *Journal of Volcanology and Geothermal Research*, 133(1):247–260, 2004.

J. Langbein. Noise in gps displacement measurements from southern california and southern nevada. *Journal of Geophysical Research: Solid Earth (1978–2012)*, 113(B5), 2008.

K. M. Larson and D. C. Agnew. Application of the global positioning system to crustal deformation measurement: 1. precision and accuracy. *Journal of Geophysical Research: Solid Earth (1978–2012)*, 96(B10):16547–16565, 1991.

K. Le Dortz, B. Meyer, M. Sébrier, H. Nazari, R. Braucher, M. Fattahi, L. Benedetti, M. Foroutan, L. Siame, D. Bourlès, et al. Holocene right-slip rate determined by cosmogenic and osl dating on the anar fault, central iran. *Geophysical Journal International*, 179(2):700–710, 2009.

K. Le Dortz, B. Meyer, M. Sébrier, R. Braucher, H. Nazari, L. Benedetti, M. Fattahi, D. Bourlès, M. Foroutan, L. Siame, et al. Dating inset terraces and offset fans along the dehshir fault (iran) combining cosmogenic and osl methods. *Geophysical Journal International*, 185(3):1147–1174, 2011.

F. Li and R. Goldstein. Studies of multi-baseline spaceborne interferometric synthetic aperture radars. In *IGARSS'87-International Geoscience and Remote Sensing Symposium*, volume 1, pages 1545–1550, 1987.

Z. Li, J.-P. Muller, P. Cross, and E. J. Fielding. Interferometric synthetic aperture radar (insar) atmospheric correction: Gps, moderate resolution imaging spectroradiometer (modis), and insar integration. *Journal of Geophysical Research: Solid Earth (1978–2012)*, 110(B3), 2005.

Z. Li, E. J. Fielding, P. Cross, and J.-P. Muller. Interferometric synthetic aperture radar atmospheric correction: Gps topography-dependent turbulence model. *Journal of Geophysical Research: Solid Earth (1978–2012)*, 111(B2), 2006a.

Z. Li, E. J. Fielding, P. Cross, and J.-P. Muller. Interferometric synthetic aperture radar atmospheric correction: medium resolution imaging spectrometer and advanced synthetic aperture radar integration. *Geophysical Research Letters*, 33(6):L06816, 2006b.

Z. Li, J.-P. Muller, P. Cross, P. Albert, J. Fischer, and R. Bennartz. Assessment of the potential of meris near-infrared water vapour products to correct asar interferometric measurements. *International Journal of Remote Sensing*, 27(2):349–365, 2006c.

S. M. Lichten and J. S. Border. Strategies for high-precision global positioning system orbit determination. *Journal of Geophysical Research: Solid Earth (1978–2012)*, 92 (B12):12751–12762, 1987.

Y.-n. N. Lin, M. Simons, E. A. Hetland, P. Muse, and C. DiCaprio. A multiscale approach to estimating topographically correlated propagation delays in radar interferograms. *Geochemistry Geophysics Geosystems*, 11(9):Q09002, 2010.

Y.-A. Liou and C.-Y. Huang. Gps observations of pw during the passage of a typhoon. *Earth Planets and Space*, 52(10):709–712, 2000.

Y.-A. Liou, Y.-T. Teng, T. Van Hove, and J. C. Liljegren. Comparison of precipitable water observations in the near tropics by gps, microwave radiometer, and radiosondes. *Journal of applied meteorology*, 40(1):5–15, 2001.

P. López-Quiroz, M.-P. Doin, F. Tupin, P. Briole, and J.-M. Nicolas. Time series analysis of mexico city subsidence constrained by radar interferometry. *Journal of Applied Geophysics*, 69(1):1–15, 2009.

F. Lyard, F. Lefevre, T. Letellier, and O. Francis. Modelling the global ocean tides: modern insights from fes2004. *Ocean Dynamics*, 56(5-6):394–415, 2006.

N. Lyberis and G. Manby. Oblique to orthogonal convergence across the turan block in the post-miocene. *AAPG bulletin*, 83(7):1135–1160, 1999.

K. Macdonald, J.-C. Sempere, and P. Fox. East pacific rise from siqueiros to orozco fracture zones: Along-strike continuity of axial neovolcanic zone and structure and evolution of overlapping spreading centers. *Journal of Geophysical Research: Solid Earth (1978–2012)*, 89(B7):6049–6069, 1984.

D. MacMillan and J. M. Gipson. Atmospheric pressure loading parameters from very long baseline interferometry observations. *Journal of Geophysical Research: Solid Earth (1978–2012)*, 99(B9):18081–18087, 1994.

C. F. Mader GL. The block iia satellite – calibrating antenna phase centers. *GPS World*, 13(4):40–46, 2002.

A. Maggi, J. Jackson, K. Priestley, and C. Baker. A re-assessment of focal depth distributions in southern iran, the tien shan and northern india: do earthquakes really occur in the continental mantle? *Geophysical Journal International*, 143(3):629–661, 2000.

G. Mandl. Tectonic deformation by rotating parallel faults: the "bookshelf" mechanism. *Tectonophysics*, 141(4):277–316, 1987.

S. Mangino and K. Priestley. The crustal structure of the southern caspian region. *Geophysical Journal International*, 133(3):630–648, 1998.

I. Manighetti, P. Tapponnier, V. Courtillot, Y. Gallet, E. Jacques, and P.-Y. Gillot. Strain transfer between disconnected, propagating rifts in afar. *Journal of Geophysical Research: Solid Earth (1978–2012)*, 106(B7):13613–13665, 2001.

I. Manighetti, M. Campillo, S. Bouley, and F. Cotton. Earthquake scaling, fault segmentation, and structural maturity. *Earth and Planetary Science Letters*, 253(3):429–438, 2007.

I. Manighetti, D. Zigone, M. Campillo, and F. Cotton. Self-similarity of the largest-scale segmentation of the faults: Implications for earthquake behavior. *Earth and Planetary Science Letters*, 288(3):370–381, 2009.

C. C. C. P. Manighetti I., L. De Barros and F. Cappa. Deterministic, self-similar slip and stress heterogeneity on seismogenic faults. In *AGU Fall Meeting Abstracts*, 2013.

A. Mao, C. G. Harrison, and T. H. Dixon. Noise in gps coordinate time series. *Journal of Geophysical Research: Solid Earth (1978–2012)*, 104(B2):2797–2816, 1999.

F. Martínez, R. N. Hey, and P. D. Johnson. The east ridge system 28.5–32 s east pacific rise: Implications for overlapping spreading center development. *Earth and planetary science letters*, 151(1):13–31, 1997.

F. Masson, J. Chéry, D. Hatzfeld, J. Martinod, P. Vernant, F. Tavakoli, and M. Ghafory-Ashtiani. Seismic versus aseismic deformation in iran inferred from earthquakes and geodetic data. *Geophysical Journal International*, 160(1):217–226, 2005.

F. Masson, Y. Djamour, S. Van Gorp, J. Chéry, M. Tatar, F. Tavakoli, H. Nankali, and P. Vernant. Extension in nw iran driven by the motion of the south caspian basin. *Earth and Planetary Science Letters*, 252(1):180–188, 2006.

F. Masson, M. Anvari, Y. Djamour, A. Walpersdorf, F. Tavakoli, M. Daignieres, H. Nankali, and S. Van Gorp. Large-scale velocity field and strain tensor in iran inferred from gps measurements: New insight for the present-day deformation pattern within ne iran. *Geophysical Journal International*, 170(1):436–440, 2007.

D. Massonnet and K. L. Feigl. Radar interferometry and its application to changes in the earth's surface. *Reviews of geophysics*, 36(4):441–500, 1998.

D. Massonnet, M. Rossi, C. Carmona, F. Adragna, G. Peltzer, K. Feigl, and T. Rabaute. The displacement field of the landers earthquake mapped by radar interferometry. *Nature*, 364(6433):138–142, 1993.

M. Mattei, F. Cifelli, G. Muttoni, A. Zanchi, F. Berra, F. Mossavvari, and S. A. Eshraghi. Neogene block rotation in central iran: Evidence from paleomagnetic data. *Geological Society of America Bulletin*, 124(5-6):943–956, 2012.

R. McCaffrey. Crustal block rotations and plate coupling. *Plate Boundary Zones, Geodyn. Ser*, 30:101–122, 2002.

R. McCaffrey. Block kinematics of the pacific–north america plate boundary in the southwestern united states from inversion of gps, seismological, and geologic data. *Journal of Geophysical Research*, 110(B7):B07401, 2005.

R. McCaffrey, M. D. Long, C. Goldfinger, P. C. Zwick, J. L. Nabelek, C. K. Johnson, and C. Smith. Rotation and plate locking at the southern cascadia subduction zone. *Geophysical Research Letters*, 27(19):3117–3120, 2000.

J. P. McCalpin and A. R. Nelson. Introduction to paleoseismology. *International Geophysics*, 62:1–32, 1996.

S. McClusky, S. Balassanian, A. Barka, C. Demir, S. Ergintav, I. Georgiev, O. Gurkan, M. Hamburger, K. Hurst, H. Kahle, et al. Global positioning system constraints on plate kinematics and dynamics in the eastern mediterranean and caucasus. *Journal of Geophysical Research: Solid Earth (1978–2012)*, 105(B3):5695–5719, 2000.

S. McClusky, R. Reilinger, S. Mahmoud, D. Ben Sari, and A. Tealeb. Gps constraints on africa (nubia) and arabia plate motions. *Geophysical Journal International*, 155(1): 126–138, 2003.

D. McKenzie. Active tectonics of the mediterranean region. *Geophysical Journal of the Royal Astronomical Society*, 30(2):109–185, 1972.

D. McKenzie and J. Jackson. A block model of distributed deformation by faulting. *Journal of the Geological Society*, 143(2):349–353, 1986.

N. McQuarrie, J. Stock, C. Verdel, and B. Wernicke. Cenozoic evolution of neotethys and implications for the causes of plate motions. *Geophysical Research Letters*, 30(20):2036, 2003.

B. J. Meade and B. H. Hager. Block models of crustal motion in southern california constrained by gps measurements. *Journal of Geophysical Research: Solid Earth (1978–2012)*, 110(B3), 2005.

B. J. Meade, B. H. Hager, S. C. McClusky, R. E. Reilinger, S. Ergintav, O. Lenk, A. Barka, and H. Özener. Estimates of seismic potential in the marmara sea region from block models of secular deformation constrained by global positioning system measurements. *Bulletin of the Seismological Society of America*, 92(1):208–215, 2002.

W. G. Melbourne. The case for ranging in gps-based geodetic systems. In *Proc. 1st Int. Symp. on Precise Positioning with GPS, Rockville, Maryland (1985)*, pages 373–386, 1985.

S. Metzger, S. Jónsson, and H. Geirsson. Locking depth and slip-rate of the húsavík flatey fault, north iceland, derived from continuous gps data 2006–2010. *Geophysical Journal International*, 187(2):564–576, 2011.

B. Meyer and K. Le Dortz. Strike-slip kinematics in central and eastern iran: Estimating fault slip-rates averaged over the holocene. *Tectonics*, 26(5), 2007.

B. Meyer, F. Mouthereau, O. Lacombe, and P. Agard. Evidence of quaternary activity along the deshir fault: implication for the tertiary tectonics of central iran. *Geophysical Journal International*, 164(1):192–201, 2006.

S. Mohadjer, R. Bendick, A. Ischuk, S. Kuzikov, A. Kostuk, U. Saydullaev, S. Lodi, D. Kakar, A. Wasy, M. Khan, et al. Partitioning of india-eurasia convergence in the pamir-hindu kush from gps measurements. *Geophysical Research Letters*, 37(4), 2010.

W. D. Mooney, G. Laske, and T. G. Masters. Crust 5.1: A global crustal model at 5× 5. *Journal of Geophysical Research: Solid Earth (1978–2012)*, 103(B1):727–747, 1998.

A. Moore et al. Igs site guidelines. *Jet Propulsion Laboratory*, 2004.

J. P. Morgan and M. C. Kleinrock. Transform zone migration: Implications of bookshelf faulting at oceanic and icelandic propagating ridges. *Tectonics*, 10(5):920–935, 1991.

M. Motagh, Y. Djamour, T. R. Walter, H.-U. Wetzel, J. Zschau, and S. Arabi. Land subsidence in mashhad valley, northeast iran: results from insar, levelling and gps. *Geophysical Journal International*, 168(2):518–526, 2007.

Z. Mousavi, A. Walpersdorf, R. Walker, T. F., P. E., N. H., N. F., and D. Y. Global positioning system constraints on the active tectonics of ne iran and the south caspian region. *Earth and Planetary Science Letters*, in press, 2013.

S. Nahmani, O. Bock, M.-N. Bouin, A. Santamaría-Gómez, J.-P. Boy, X. Collilieux, L. Métivier, I. Panet, P. Genthon, C. Linage, et al. Hydrological deformation induced by the west african monsoon: Comparison of gps, grace and loading models. *Journal of Geophysical Research: Solid Earth (1978–2012)*, 117(B5), 2012.

H. Nazari, M. Fattahi, B. Meyer, M. Sébrier, M. Talebian, M. Foroutan, K. Le Dortz, M. Bateman, and M. Ghorashi. First evidence for large earthquakes on the deshir fault, central iran plateau. *Terra Nova*, 21(6):417–426, 2009.

A. Niell. Global mapping functions for the atmosphere delay at radio wavelengths. *Journal of Geophysical Research: Solid Earth (1978–2012)*, 101(B1):3227–3246, 1996.

A. Niell. Improved atmospheric mapping functions for vlbi and gps. *Earth Planets and Space*, 52(10):699–702, 2000.

F. Nilforoushan, F. Masson, P. Vernant, C. Vigny, J. Martinod, M. Abbassi, H. Nankali, D. Hatzfeld, R. Bayer, F. Tavakoli, et al. Gps network monitors the arabia-eurasia collision deformation in iran. *Journal of Geodesy*, 77(7-8):411–422, 2003.

J.-M. Nocquet. Apport de la geodesie spatial a la connaissance de la geodynamique en europe et en mediterranee. Technical report, University of Nic Sophia Antipolis, 2011.

A. A. Nowroozi and A. Mohajer-Ashjai. Fault movements and tectonics of eastern iran: boundaries of the lut plate. *Geophysical Journal of the Royal Astronomical Society*, 83 (1):215–237, 1985.

R. Nozaem, M. Mohajjel, F. Rossetti, M. Della Seta, G. Vignaroli, A. Yassaghi, F. Salvini, and M. Eliassi. Post-neogene right-lateral strike–slip tectonics at the north-western edge of the lut block (kuh-e–sarhangi fault), central iran. *Tectonophysics*, 2013.

A. Nur and G. Mavko. Postseismic viscoelastic rebound. *Science*, 183(4121):204–206, 1974.

A. Nur, H. Ron, and O. Scotti. Fault mechanics and the kinematics of block rotations. *Geology*, 14(9):746–749, 1986.

Y. Okada. Surface deformation due to shear and tensile faults in a half-space. *Bulletin of the seismological society of America*, 75(4):1135–1154, 1985.

F. Onn and H. Zebker. Correction for interferometric synthetic aperture radar atmospheric phase artifacts using time series of zenith wet delay observations from a gps network. *Journal of Geophysical Research: Solid Earth (1978–2012)*, 111(B9), 2006.

K. J. Ouellette, C. de Linage, and J. S. Famiglietti. Estimating snow water equivalent from gps vertical site-position observations in the western united states. *Water Resources Research*, 2013.

K. C. Outerbridge. *Investigations into the Estimation of Tropospheric Delay and Wet Refractivity Using GPS Measurements*. PhD thesis, University of Miami, 2011.

B. Parsons, T. Wright, P. Rowe, J. Andrews, J. Jackson, R. Walker, M. Khatib, M. Talebian, E. Bergman, and E. Engdahl. The 1994 sefidabeh (eastern iran) earthquakes revisited: new evidence from satellite radar interferometry and carbonate dating about the growth of an active fold above a blind thrust fault. *Geophysical Journal International*, 164(1):202–217, 2006.

E. Pathier. *Apports de l'interférométrie RADAR différentielle à l'étude de la tectonique active de Taiwan*. PhD thesis, 2003.

G. Peltzer, P. Rosen, F. Rogez, and K. Hudnut. Poroelastic rebound along the landers 1992 earthquake surface rupture. *Journal of Geophysical Research*, 103(B12):30131–30, 1998.

G. Peltzer, F. Crampé, S. Hensley, and P. Rosen. Transient strain accumulation and fault interaction in the eastern california shear zone. *Geology*, 29(11):975–978, 2001.

N. Penna and M. Stewart. Aliased tidal signatures in continuous gps height time series. *Geophysical Research Letters*, 30(23), 2003.

N. T. Penna, M. A. King, and M. P. Stewart. Gps height time series: Short-period origins of spurious long-period signals. *Journal of Geophysical Research: Solid Earth (1978–2012)*, 112(B2), 2007.

L. Petrov and J.-P. Boy. Study of the atmospheric pressure loading signal in very long baseline interferometry observations. *Journal of Geophysical Research: Solid Earth (1978–2012)*, 109(B3), 2004.

G. Pezzo, C. Tolomei, S. Atzori, S. Salvi, E. Shabanian, O. Bellier, and Y. Farbod. New kinematic constraints of the western doruneh fault, northeastern iran, from interseismic deformation analysis. *Geophysical Journal International*, 190(1):622–628, 2012.

F. F. Pollitz. Gravitational viscoelastic postseismic relaxation on a layered spherical earth. *Journal of Geophysical Research: Solid Earth (1978–2012)*, 102(B8):17921–17941, 1997.

K. Priestley, C. Baker, and J. Jackson. Implications of earthquake focal mechanism data for the active tectonics of the south caspian basin and surrounding regions. *Geophysical Journal International*, 118(1):111–141, 1994.

B. Puysségur, R. Michel, and J.-P. Avouac. Tropospheric phase delay in interferometric synthetic aperture radar estimated from meteorological model and multispectral imagery. *Journal of Geophysical Research: Solid Earth (1978–2012)*, 112(B5), 2007.

R. Reilinger, S. McClusky, P. Vernant, S. Lawrence, S. Ergintav, R. Cakmak, H. Ozener, F. Kadirov, I. Guliev, R. Stepanyan, et al. Gps constraints on continental deformation in the africa-arabia-eurasia continental collision zone and implications for the dynamics of plate interactions. *Journal of Geophysical Research: Solid Earth (1978–2012)*, 111 (B5), 2006.

D. Remy, S. Bonvalot, P. Briole, and M. Murakami. Accurate measurements of tropospheric effects in volcanic areas from sar interferometry data: Application to sakurajima volcano (japan). *Earth and Planetary Science Letters*, 213(3):299–310, 2003.

J.-F. Ritz. Extrusion tectonics and subduction in the eastern south caspian region since 10 ma: Comment. *Geology*, 37(12):e191–e191, 2009.

J.-F. Ritz, H. Nazari, A. Ghassemi, R. Salamati, A. Shafei, S. Solaymani, and P. Vernant. Active transtension inside central alborz: A new insight into northern iran–southern caspian geodynamics. *Geology*, 34(6):477–480, 2006.

M. Rizza, S. Mahan, J.-F. Ritz, H. Nazari, J. Hollingsworth, and R. Salamati. Using luminescence dating of coarse matrix material to estimate the slip rate of the astaneh fault, iran. *Quaternary Geochronology*, 6(3):390–406, 2011.

H. Ron, R. Freund, Z. Garfunkel, and A. Nur. Block rotation by strike-slip faulting: Structural and paleomagnetic evidence. *Journal of Geophysical Research*, 89(B7):6256–6270, 1984.

H. Ron, A. Aydin, and A. Nur. Strike-slip faulting and block rotation in the lake mead fault system. *Geology*, 14(12):1020–1023, 1986.

P. A. Rosen, S. Hensley, I. R. Joughin, F. K. Li, S. N. Madsen, E. Rodriguez, and R. M. Goldstein. Synthetic aperture radar interferometry. *Proceedings of the IEEE*, 88(3): 333–382, 2000.

P. A. Rosen, S. Hensley, G. Peltzer, and M. Simons. Updated repeat orbit interferometry package released. *Eos, Transactions American Geophysical Union*, 85(5):47–47, 2004.

M. Rothacher. Comparison of absolute and relative antenna phase center variations. *GPS solutions*, 4(4):55–60, 2001.

J. Saastamoinen. Atmospheric correction for the troposphere and stratosphere in radio ranging satellites. *Geophysical Monograph Series*, 15:247–251, 1972.

E. Saria, E. Calais, Z. Altamimi, P. Willis, and H. Farah. A new velocity field for africa from combined gps and doris space geodetic solutions: Contribution to the definition of the african reference frame (afref). *Journal of Geophysical Research: Solid Earth*, 2013.

J. Savage. A dislocation model of strain accumulation and release at a subduction zone. *Journal of Geophysical Research: Solid Earth (1978–2012)*, 88(B6):4984–4996, 1983.

J. Savage and R. Burford. Geodetic determination of relative plate motion in central california. *Journal of Geophysical Research*, 78(5):832–845, 1973.

J. Savage and M. Lisowski. Changes in long-term extension rates associated with the morgan hill and loma prieta earthquakes in california. *Geophysical research letters*, 22 (7):759–762, 1995.

J. Savage and W. Prescott. Asthenosphere readjustment and the earthquake cycle. *Journal of Geophysical Research: Solid Earth (1978–2012)*, 83(B7):3369–3376, 1978.

H.-G. Scherneck. A parametrized solid earth tide model and ocean tide loading effects for global geodetic baseline measurements. *Geophysical Journal International*, 106(3): 677–694, 1991.

R. Schmid, G. Mader, and T. Herring. From relative to absolute antenna phase center corrections. In *Celebrating a Decade of the International GPS Service, Workshop and Symposium 2004*, pages 209–221, 2005a.

R. Schmid, M. Rothacher, D. Thaller, and P. Steigenberger. Absolute phase center corrections of satellite and receiver antennas. *GPS solutions*, 9(4):283–293, 2005b.

R. Schmid, P. Steigenberger, G. Gendt, M. Ge, and M. Rothacher. Generation of a consistent absolute phase-center correction model for gps receiver and satellite antennas. *Journal of Geodesy*, 81(12):781–798, 2007.

D. Schmidt, R. Bürgmann, R. Nadeau, and M. d'Alessio. Distribution of aseismic slip rate on the hayward fault inferred from seismic and geodetic data. *Journal of Geophysical Research: Solid Earth (1978–2012)*, 110(B8), 2005.

D. A. Schmidt and R. Bürgmann. Time-dependent land uplift and subsidence in the santa clara valley, california, from a large interferometric synthetic aperture radar data set. *Journal of Geophysical Research: Solid Earth (1978–2012)*, 108(B9), 2003.

C. H. Scholz. Scaling laws for large earthquakes: consequences for physical models. *Bulletin of the Seismological Society of America*, 72(1):1–14, 1982.

E. W. Schwiderski. On charting global ocean tides. *Reviews of Geophysics*, 18(1):243–268, 1980.

P. Segall and J. L. Davis. Gps applications for geodynamics and earthquake studies. *Earth Planet. Science.*, 25(1):301–336, 1997.

G. F. Sella, T. H. Dixon, and A. Mao. Revel: A model for recent plate velocities from space geodesy. *Journal of Geophysical Research: Solid Earth (1978–2012)*, 107(B4):ETG–11, 2002.

A. Şengör. A new model for the late palaeozoic—mesozoic tectonic evolution of iran and implications for oman. *Geological Society, London, Special Publications*, 49(1):797–831, 1990.

A. Şengör and W. Kidd. Post-collisional tectonics of the turkish-iranian plateau and a comparison with tibet. *Tectonophysics*, 55(3):361–376, 1979.

E. Shabanian, O. Bellier, L. Siame, N. Arnaud, M. R. Abbassi, and J.-J. Cochemé. New tectonic configuration in ne iran: Active strike-slip faulting between the kopeh dagh and binalud mountains. *Tectonics*, 28(5), 2009a.

E. Shabanian, L. Siame, O. Bellier, L. Benedetti, and M. R. Abbassi. Quaternary slip rates along the northeastern boundary of the arabia–eurasia collision zone (kopeh dagh mountains, northeast iran). *Geophysical Journal International*, 178(2):1055–1077, 2009b.

E. Shabanian, O. Bellier, L. Siame, M. R. Abbassi, D. Bourlès, R. Braucher, and Y. Farbod. The binalud mountains: A key piece for the geodynamic puzzle of ne iran. *Tectonics*, 31(6), 2012.

M. Shirzaei and R. Bürgmann. Topography correlated atmospheric delay correction in radar interferometry using wavelet transforms. *Geophysical Research Letters*, 39(1), 2012.

S. M. Shrestha. *Investigations into the Estimation of Tropospheric Delay and Wet Refractivity Using GPS Measurements*. PhD thesis, University of Calgary, 2003.

S. Shu-Li, W.-Y. Zhu, J.-C. Ding, X.-H. LIAO, Z.-Y. CHENG, and Q.-X. Ye. Near real-time sensing of pwv from sgcan and the application test in numerical weather forecast. *Chin J Geophys*, 40:719–727, 2004.

S. Shuli, W. Zhu, J. Ding, and J. Peng. 3d water-vapor tomography with shanghai gps network to improve forecasted moisture field. *Chinese Science Bulletin*, 51(5):607–614, 2006.

L. L. Siame, E. Shabanian, and O. Bellier. Extrusion tectonics and subduction in the eastern south caspian region since 10 ma: Comment. *Geology*, 37(12):e197–e198, 2009.

E. K. Smith and S. Weintraub. The constants in the equation for atmospheric refractive index at radio frequencies. *Proceedings of the IRE*, 41(8):1035–1037, 1953.

S. W. Smith and M. Wyss. Displacement on the san andreas fault subsequent to the 1966 parkfield earthquake. *Bulletin of the Seismological Society of America*, 58(6):1955–1973, 1968.

F. S. Solheim, J. Vivekanandan, R. H. Ware, and C. Rocken. Propagation delays induced in gps signals by dry air, water vapor, hydrometeors, and other particulates. *Journal of geophysical research*, 104(D8):9663–9670, 1999.

P. Steigenberger, M. Rothacher, R. Dietrich, M. Fritsche, A. Rülke, and S. Vey. Reprocessing of a global gps network. *Journal of Geophysical Research: Solid Earth (1978–2012)*, 111(B5), 2006.

M. Talebian and J. Jackson. Offset on the main recent fault of nw iran and implications for the late cenozoic tectonics of the arabia–eurasia collision zone. *Geophysical Journal International*, 150(2):422–439, 2002.

M. Talebian and J. Jackson. A reappraisal of earthquake focal mechanisms and active shortening in the zagros mountains of iran. *Geophysical Journal International*, 156(3): 506–526, 2004.

M. Talebian, E. J. Fielding, G. J. Funning, M. Ghorashi, J. Jackson, H. Nazari, B. Parsons, K. Priestley, P. A. Rosen, R. Walker, et al. The 2003 bam (iran) earthquake: Rupture of a blind strike-slip fault. *Geophysical Research Letters*, 31(11), 2004.

M. Talebian, J. Biggs, M. Bolourchi, A. Copley, A. Ghassemi, M. Ghorashi, J. Hollingsworth, J. Jackson, E. Nissen, B. Oveisi, et al. The dahuiyeh (zarand) earthquake of 2005 february 22 in central iran: reactivation of an intramountain reverse fault. *Geophysical Journal International*, 164(1):137–148, 2006.

P. Tapponnier and P. Molnar. Slip-line field theory and large-scale continental tectonics. *Nature*, 264(25):319–324, 1976.

P. Tapponnier, R. Armijo, I. Manighetti, and V. Courtillot. Bookshelf faulting and horizontal block rotations between overlapping rifts in southern afar. *Geophysical Research Letters*, 17(1):1–4, 1990.

M. Tatar and D. Hatzfeld. Microseismic evidence of slip partitioning for the rudbar-tarom earthquake (ms 7.7) of 1990 june 20 in nw iran. *Geophysical Journal International*, 176 (2):529–541, 2009.

M. Tatar, D. Hatzfeld, J. Martinod, A. Walpersdorf, M. Ghafori-Ashtiany, and J. Chéry. The present-day deformation of the central zagros from gps measurements. *Geophysical Research Letters*, 29(19):33–1, 2002.

M. Tatar, J. Jackson, D. Hatzfeld, and E. Bergman. The 2004 may 28 baladeh earthquake (mw 6.2) in the alborz, iran: overthrusting the south caspian basin margin, partitioning of oblique convergence and the seismic hazard of tehran. *Geophysical Journal International*, 170(1):249–261, 2007.

O. Tatar, F. Poyraz, H. Gürsoy, Z. Cakir, S. Ergintav, Z. Akpınar, F. Koçbulut, F. Sezen, T. Türk, K. Ö. Hastaoğlu, et al. Crustal deformation and kinematics of the eastern part of the north anatolian fault zone (turkey) from gps measurements. *Tectonophysics*, 518: 55–62, 2012.

F. Tavakoli. *Present-day deformation and kinematics of the active faults observed by GPS in the Zagros and east of Iran*. PhD thesis, Thesis, 2007.

F. Tavakoli, A. Walpersdorf, C. Authemayou, H. Nankali, D. Hatzfeld, M. Tatar, Y. Djamour, F. Nilforoushan, and N. Cotte. Distribution of the right-lateral strike–slip motion from the main recent fault to the kazerun fault system (zagros, iran): Evidence from present-day gps velocities. *Earth and Planetary Science Letters*, 275(3):342–347, 2008.

M. Taylor and G. Peltzer. Current slip rates on conjugate strike-slip faults in central tibet using synthetic aperture radar interferometry. *Journal of Geophysical Research: Solid Earth (1978–2012)*, 111(B12), 2006.

J. Tchalenko and M. Berberian. Dasht-e baaz fault, iran: Earthquake and earlier related structures in bed rock. *Geological Society of America Bulletin*, 86(5):703–709, 1975.

G. D. Thayer. An improved equation for the radio refractive index of air. *Radio Science*, 9(10):803–807, 1974.

P. Tregoning and T. Herring. Impact of a priori zenith hydrostatic delay errors on gps estimates of station heights and zenith total delays. *Geophysical Research Letters*, 33 (23), 2006.

P. Tregoning and T. Van Dam. Atmospheric pressure loading corrections applied to gps data at the observation level. *Geophysical Research Letters*, 32(22), 2005.

V. G. Trifonov. Late quaternary tectonic movements of western and central asia. *Geological society of America bulletin*, 89(7):1059–1072, 1978.

S. Usai. A least squares database approach for sar interferometric data. *Geoscience and Remote Sensing, IEEE Transactions on*, 41(4):753–760, 2003.

S. Usai and R. Klees. Sar interferometry on a very long time scale: a study of the interferometric characteristics of man-made features. *Geoscience and Remote Sensing, IEEE Transactions on*, 37(4):2118–2123, 1999.

T. Van Dam and T. Herring. Detection of atmospheric pressure loading using very long baseline interferometry measurements. *Journal of geophysical research*, 99(B3):4505–4517, 1994.

T. Van Dam and J. Wahr. Displacements of the earth's surface due to atmospheric loading: Effects on gravity and baseline measurements. *Journal of Geophysical Research: Solid Earth (1978–2012)*, 92(B2):1281–1286, 1987.

T. Van Dam, J. Wahr, P. Milly, A. Shmakin, G. Blewitt, D. Lavallée, and K. Larson. Crustal displacements due to continental water loading. *Geophysical Research Letters*, 28(4):651–654, 2001.

H. Vedel. Magic project radiosonde data specification document. *MAGIC Project Rep. D*, 5210:4, 2000.

M. Vergnolle, M.-N. Bouin, L. Morel, F. Masson, S. Durand, J. Nicolas, and S. Melachroinos. Gps estimates of ocean tide loading in nw-france: Determination of ocean tide loading constituents and comparison with a recent ocean tide model. *Geophysical Journal International*, 173(2):444–458, 2008.

M. Vergnolle, A. Walpersdorf, V. Kostoglodov, P. Tregoning, J. Santiago, N. Cotte, and S. Franco. Slow slip events in mexico revised from the processing of 11 year gps observations. *Journal of Geophysical Research: Solid Earth (1978–2012)*, 115(B8), 2010.

P. Vernant. *Cinématique actuelle et dynamique de l'Iran: GPS et modélisation numérique.* PhD thesis, Universite Montpellier II, 2003.

P. Vernant, F. Nilforoushan, J. Chery, R. Bayer, Y. Djamour, F. Masson, H. Nankali, J.-F. Ritz, M. Sedighi, and F. Tavakoli. Deciphering oblique shortening of central alborz in iran using geodetic data. *Earth and Planetary Science Letters*, 223(1):177–185, 2004a.

P. Vernant, F. Nilforoushan, D. Hatzfeld, M. Abbassi, C. Vigny, F. Masson, H. Nankali, J. Martinod, A. Ashtiani, R. Bayer, et al. Present-day crustal deformation and plate kinematics in the middle east constrained by gps measurements in iran and northern oman. *Geophysical Journal International*, 157(1):381–398, 2004b.

S. Vey, E. Calais, M. Llubes, N. Florsch, G. Woppelmann, J. Hinderer, M. Amalvict, M. Lalancette, B. Simon, F. Duquenne, et al. Gps measurements of ocean loading and its impact on zenith tropospheric delay estimates: a case study in brittany, france. *Journal of Geodesy*, 76(8):419–427, 2002.

P. von Allmen, E. Fielding, Z. Xing, L. Pan, and E. Fishbein. Web service infrastructure for correcting insar imaging. In *AGU Fall Meeting Abstracts*, volume 1, page 1440, 2011.

G. Wadge, P. Webley, I. James, R. Bingley, A. Dodson, S. Waugh, T. Veneboer, G. Puglisi, M. Mattia, D. Baker, et al. Atmospheric models, gps and insar measurements of the tropospheric water vapour field over mount etna. *Geophysical Research Letters*, 29(19): 11–1, 2002.

F. Walker and M. B. Allen. Offset rivers, drainage spacing and the record of strike-slip faulting: The kuh banan fault, iran. *Tectonophysics*, 530:251–263, 2012.

R. Walker and J. Jackson. Offset and evolution of the gowk fault, se iran: a major intra-continental strike-slip system. *Journal of Structural Geology*, 24(11):1677–1698, 2002.

R. Walker and J. Jackson. Active tectonics and late cenozoic strain distribution in central and eastern iran. *Tectonics*, 23(5), 2004.

R. Walker and M. Khatib. Active faulting in the birjand region of ne iran. *Tectonics*, 25 (4), 2006.

R. Walker, J. Jackson, and C. Baker. Surface expression of thrust faulting in eastern iran: source parameters and surface deformation of the 1978 tabas and 1968 ferdows earthquake sequences. *Geophysical Journal International*, 152(3):749–765, 2003.

R. Walker, J. Jackson, and C. Baker. Active faulting and seismicity of the dasht-e-bayaz region, eastern iran. *Geophysical Journal International*, 157(1):265–282, 2004.

R. Walker, P. Gans, M. Allen, J. Jackson, M. Khatib, N. Marsh, and M. Zarrinkoub. Late cenozoic volcanism and rates of active faulting in eastern iran. *Geophysical Journal International*, 177(2):783–805, 2009.

R. Walker, M. Talebian, R. Sloan, A. Rasheedi, M. Fattahi, and C. Bryant. Holocene slip-rate on the gowk strike-slip fault and implications for the distribution of tectonic strain in eastern iran. *Geophysical Journal International*, 181(1):221–228, 2010.

R. Walker, E. Bergman, W. Szeliga, and E. Fielding. Insights into the 1968–1997 dasht-e-bayaz and zirkuh earthquake sequences, eastern iran, from calibrated relocations, insar and high-resolution satellite imagery. *Geophysical Journal International*, 187(3):1577–1603, 2011.

R. Walker, E. Bergman, J. Elliott, E. Fielding, A.-R. Ghods, M. Ghoraishi, J. Jackson, H. Nazari, M. Nemati, B. Oveisi, et al. The 2010–2011 south rigan (baluchestan) earthquake sequence and its implications for distributed deformation and earthquake hazard in southeast iran. *Geophysical Journal International*, 193(1):349–374, 2013.

R. T. Walker and M. Fattahi. A framework of holocene and late pleistocene environmental change in eastern iran inferred from the dating of periods of alluvial fan abandonment, river terracing, and lake deposition. *Quaternary Science Reviews*, 30(9):1256–1271, 2011.

A. Walpersdorf. *L'observation de la tectonique active en Asie du Sud-Est par géodésie spatiale : un projet GPS*. PhD thesis, ENS, Paris, 1997.

A. Walpersdorf, D. Hatzfeld, H. Nankali, F. Tavakoli, F. Nilforoushan, M. Tatar, P. Vernant, J. Chéry, and F. Masson. Difference in the gps deformation pattern of north and central zagros (iran). *Geophysical Journal International*, 167(3):1077–1088, 2006.

A. Walpersdorf, M.-N. Bouin, O. Bock, and E. Doerflinger. Assessment of gps data for meteorological applications over africa: Study of error sources and analysis of positioning accuracy. *Journal of atmospheric and solar-terrestrial physics*, 69(12):1312–1330, 2007.

A. Walpersdorf, N. Cotte, V. Kostoglodov, M. Vergnolle, M. Radiguet, J. A. Santiago, and M. Campillo. Two successive slow slip events evidenced in 2009–2010 by a dense gps network in guerrero, mexico. *Geophysical Research Letters*, 38(15), 2011.

R. Walters. *Geodetic observation and modelling of continental deformation in Iran and Turkey*. PhD thesis, Department of Earth Sciences, University of Oxford, 2012.

R. Walters, J. Elliott, B. Parsons, and Z. Li. Rapid strain accumulation on the ashkabad fault (turkmenistan) from atmosphere-corrected insar. *Journal of Geophysical Research: Solid Earth*, 2013.

H. Wang and T. Wright. Satellite geodetic imaging reveals internal deformation of western tibet. *Geophysical Research Letters*, 39(7), 2012.

S. Wdowinski, Y. Bock, J. Zhang, P. Fang, and J. Genrich. Southern california permanent gps geodetic array: Spatial filtering of daily positions for estimating coseismic and post-seismic displacements induced by the 1992 landers earthquake. *Journal of Geophysical Research: Solid Earth (1978–2012)*, 102(B8):18057–18070, 1997.

P. Webley, R. Bingley, A. Dodson, G. Wadge, S. Waugh, and I. James. Atmospheric water vapour correction to insar surface motion measurements on mountains: results from a dense gps network on mount etna. *Physics and Chemistry of the Earth, Parts A/B/C*, 27(4):363–370, 2002.

H. Wellman. Active wrench faults of iran, afghanistan and pakistan. *Geologische Rundschau*, 55(3):716–735, 1966.

D. L. Wells and K. J. Coppersmith. New empirical relationships among magnitude, rupture length, rupture width, rupture area, and surface displacement. *Bulletin of the Seismological Society of America*, 84(4):974–1002, 1994.

L. R. Wetzel, D. A. Wiens, and M. C. Kleinrock. Evidence from earthquakes for bookshelf faulting at large non-transform ridge offsets. 1993.

S. Williams. The effect of coloured noise on the uncertainties of rates estimated from geodetic time series. *Journal of Geodesy*, 76(9-10):483–494, 2003.

S. Williams, Y. Bock, and P. Fang. Integrated satellite interferometry: Tropospheric noise, gps estimates and implications for interferometric synthetic aperture radar products. *Journal of Geophysical Research: Solid Earth (1978–2012)*, 103(B11):27051–27067, 1998.

S. D. Williams, Y. Bock, P. Fang, P. Jamason, R. M. Nikolaidis, L. Prawirodirdjo, M. Miller, and D. J. Johnson. Error analysis of continuous gps position time series. *Journal of Geophysical Research: Solid Earth (1978–2012)*, 109(B3), 2004.

T. Wright, B. Parsons, J. Jackson, M. Haynes, E. Fielding, P. England, and P. Clarke. Source parameters of the 1 october 1995 dinar (turkey) earthquake from sar interferometry and seismic bodywave modelling. *Earth and Planetary Science Letters*, 172(1): 23–37, 1999.

T. Wright, B. Parsons, and E. Fielding. Measurement of interseismic strain accumulation across the north anatolian fault by satellite radar interferometry. *Geophysical Research Letters*, 28(10):2117–2120, 2001.

T. J. Wright, B. E. Parsons, and Z. Lu. Toward mapping surface deformation in three dimensions using insar. *Geophysical Research Letters*, 31(1), 2004.

X. Wu, M. B. Heflin, E. R. Ivins, D. F. Argus, and F. H. Webb. Large-scale global surface mass variations inferred from gps measurements of load-induced deformation. *Geophysical research letters*, 30(14):1742, 2003.

G. Xu. *GPS: theory, algorithms and applications*. Springer, 2003.

W. Xu, Z. Li, X. Ding, and J. Zhu. Interpolating atmospheric water vapor delay by incorporating terrain elevation information. *Journal of Geodesy*, 85(9):555–564, 2011.

R. Zandbergen, M. Otten, P. Righetti, D. Kuijper, and J. Dow. Routine operational and high-precision orbit determination of envisat. *Advances in Space Research*, 31(8): 1953–1958, 2003.

H. A. Zebker. Studying the earth with interferometric radar. *Computing in Science & Engineering*, 2(3):52–60, 2000.

H. A. Zebker and J. Villasenor. Decorrelation in interferometric radar echoes. *Geoscience and Remote Sensing, IEEE Transactions on*, 30(5):950–959, 1992.

H. A. Zebker, P. A. Rosen, and S. Hensley. Atmospheric effects in interferometric synthetic aperture radar surface deformation and topographic maps. *Journal of Geophysical Research*, 102(B4):7547–7563, 1997.

J. Zhang, Y. Bock, H. Johnson, P. Fang, S. Williams, J. Genrich, S. Wdowinski, and J. Behr. Southern california permanent gps geodetic array: Error analysis of daily position estimates and site velocities. *Journal of Geophysical Research*, 102(B8):18035–18, 1997.

A. V. Zubovich, X.-q. Wang, Y. G. Scherba, G. G. Schelochkov, R. Reilinger, C. Reigber, O. I. Mosienko, P. Molnar, W. Michajljow, V. I. Makarov, et al. Gps velocity field for the tien shan and surrounding regions. *Tectonics*, 29(6), 2010.

Chapter 8

Supporting Information

8.1 Gamit settings files

8.1.1 Supporting Information 2-A:Sestbl file

The session table (sestbl.) for IPGN network processing:

```
Processing Agency = MIT

Satellite Constraint = Y       ; Y/N  (next two lines are free-format but 'all' must be present)
                        all     a     e     i     n     w     M    rad1  rad2  rad3  rad4  rad5  rad6  rad7  rad8  rad9;
                       0.01  0.01  0.01  0.01  0.01  0.01  0.01  0.01  0.01  0.01  0.01  0.01  0.01  0.01  0.01  0.01

Choice of Experiment = RELAX.                    ; BASELINE/RELAX./ORBIT
Type of Analysis = 1-ITER                        ; 1-ITER/0-ITER (no postfit autcln)/PREFIT
This now redundant AUTCLN Postfit = R            ; Run autcln for postfit run; R causes repeat run.
Choice of Observable = LC_AUTCLN                 ; L1_SINGLE/L1&L2/L1_ONLY/L2_ONLY/LC_ONLY/
                                                 ; L1,L2_INDEPEND./LC_HELP/LC_AUTCLN
Station Error = ELEVATION 10 5                   ; 1-way L1, a**2 + (b**2) (L**2) in mm, ppm, default = 10. 0.
Use N-file = Y                                   ; Y/N (default no): automatic procedure to reweight by station
AUTCLN Command File = autcln.cmd                 ; Filename; default none (use default options)
Decimation Factor =1                             ; FOR SOLVE, default = 1
Quick-pre decimation factor = 1                  ; 1st iter or autcln pre, default same as Decimation Factor
Quick-pre observable = LC_ONLY                   ; for 1st soln, default same as Choice of observable

Ionospheric Constraints =  0.0 mm + 8.00 ppm
Ambiguity resolution WL = 0.15 0.15 1000. 99. 500.          ; used for LC_HELP only
Ambiguity resolution NL = 0.15 0.15 1000. 99. 15000.        ; Allow long baselines with LC_AUTCLN

Zenith Delay Estimation = Y          ; Yes/No  (default No)
Interval zen = 2                     ; 2 hrs = 13 knots/day  (default is 1 ZD  per day)
Zenith Constraints = 0.50            ; zenith-delay a priori constraint in meters (default 0.5)
Zenith Variation = 0.02 100.         ; zenith-delay variation, tau in meters/sqrt(hr), hrs (default .02 100.)
Elevation Cutoff = 0                 ; default 0 to use value in autcln.cmd
Atmospheric gradients = Y            ; Yes/Np  (default No)
Number gradients = 1                 ; number of gradient parameters per day (NS or ES); default 1
Gradient Constraints = 0.01          ; gradient at 10 deg elevation in meters; default 0.03 m

Update T/L files = L_ONLY            ; T_AND_L (default), T_ONLY, L_ONLY, NONE
Update tolerance = .3                ; minimum adjustment for updating L-file coordinates, default .3 m

Met obs source = ufile GPT 50        ; hierarchical list:  RNX ufile GPT/STP [humid value]; default GTP 50
Output met = N                       ; write the a priori met values to a z-file (Y/N)
Use met.list = N
Use met.grid = N
DMap = VMF1                                  ; GMF(default)/NMFH/VMF1
WMap = VMF1                                  ; GMF(default)/NMFW/VMF1
Use map.list = N


Use map.grid = Y
Yaw Model = Y                                ; Y/N  default = Y
Radiation Model for ARC = BERNE
Inertial frame = J2000
Tides applied = 31           ;  Binary coded: 1 earth  2 freq-dep  4 pole  8 ocean  16 remove mean for pole
                                 ; tide 32 atmosphere;  default = 31
Use otl.list = N
Use otl.grid = Y
Use atl.list = N
Use atl.grid = Y
Etide model = IERS03                 ; IERS96/IERS03
Apply atm loading = Y                ; Y/N for atmospheric loading
Use atml.list = N
Use atml.grid = Y
Antenna Model = ELEV                 ; NONE/ELEV/AZEL default = ELEV
SV antenna model = ELEV              ; NONE/ELEV      default = NONE
SV antenna off = N                   ; Y/N to estimate satellite antenna offsets (default N)

Delete AUTCLN input C-files = Y              ; Y/N; default Y to force rerun of MODEL
Scratch directory = /tmp
```

8.1.2 Supporting Information 2-B: Sittbl file

The site table (sittbl.) for IPGN network processing:

```
SITE                 FIX    --COORD.CONSTR.--
   << default for regional stations >>
ALL                  NNN    10.   10.    10.
   << IGS core stations >>
ASC1     asc1_gps        NNN    0.004 0.008  0.013
ARTU     artu_gps        NNN    0.005 0.005  0.010
BAHR     bahr_gps        NNN    0.005 0.005  0.010
BJFS     bjfs_gps        NNN    0.007 0.007  0.018
BRAZ     braz_gps        NNN    0.009 0.013  0.023
CAS1     cas1_gps        NNN    0.005 0.005  0.010
CHAT     chat_gps        NNN    0.005 0.005  0.010
COCO     coco_gps        NNN    0.005 0.006  0.011
CRO1     cro1_gps        NNN    0.004 0.006  0.012
DGAR     dgar_gps        NNN    0.025 0.025  0.050
FLIN     flin_gps        NNN    0.005 0.005  0.010
GRAS     gras_gps        NNN    0.005 0.005  0.010
GLPS     glps_gps        NNN    0.006 0.011  0.015
GUAM     guam_gps        NNN    0.025 0.025  0.050
HOFN     hofn_gps        NNN    0.025 0.025  0.050
IISC     iisc_gps        NNN    0.025 0.025  0.050
IRKT     irkt_gps        NNN    0.005 0.005  0.010
JOZE     joze_gps        NNN    0.005 0.005  0.010
KARR     karr_gps        NNN    0.005 0.005  0.010
KELY     kely_gps        NNN    0.005 0.005  0.010
KERG     kerg_gps        NNN    0.005 0.005  0.010
KOKB     kokb_gps        NNN    0.050 0.050  0.050
LHAZ     lhaz_gps        NNN    0.050 0.050  0.100
MANA     mana_gps        NNN    0.007 0.006  0.011
MAC1     mac1_gps        NNN    0.005 0.005  0.010
MALI     mali_gps        NNN    0.004 0.009  0.013
MAS1     mas1_gps        NNN    0.005 0.005  0.010
MAW1     maw1_gps        NNN    0.005 0.005  0.010
MDO1     mdo1_gps        NNN    0.005 0.005  0.010
NAMA     nama_gps        NNN    0.025 0.025  0.050
NICO     nico_gps        NNN    0.005 0.005  0.010
NKLG     nklg_gps        NNN    0.003 0.006  0.011
NYA1     nya1_gps        NNN    0.004 0.006  0.018
PERT     pert_gps        NNN    0.003 0.004  0.011
PETP     petp_gps        NNN    0.005 0.005  0.010
PIMO     pimo_gps        NNN    0.011 0.014  0.031
POL2     pol2_gps        NNN    0.005 0.005  0.010
QUIN     quin_gps        NNN    0.005 0.005  0.010
RAMO     ramo_gps        NNN    0.005 0.008  0.014
RIOG     riog_gps        NNN    0.005 0.005  0.010
SANT     sant_gps        NNN    0.005 0.008  0.013
STJO     stjo_gps        NNN    0.005 0.005  0.010
SUTH     suth_gps        NNN    0.008 0.012  0.019
TEHN     tehn_gps        NNN    0.003 0.006  0.011
THTI     thti_gps        NNN    0.004 0.008  0.013
TIXI     tixi_gps        NNN    0.004 0.004  0.011
TOW2     tow2_gps        NNN    0.005 0.005  0.010
TRAB     trab_gps        NNN    0.005 0.005  0.010
TRO1     tro1_gps        NNN    0.005 0.005  0.010
TSKB     tskb_gps        NNN    0.005 0.005  0.010
VILL     vill_gps        NNN    0.005 0.005  0.010
UNSA     unsa_gps        NNN    0.005 0.006  0.014
USNO     usno_gps        NNN    0.004 0.006  0.015
WHIT     whit_gps        NNN    0.007 0.008  0.018
WTZR     wtzr_gps        NNN    0.005 0.005  0.010
```

8.1.3 Supporting Information 2-C: Glorg file for repeatabilities

```
      *
* Glorg command file for daily repeatabilities and combination
* A priori station coordinates
* apr_file ../tables/iran.apr
apr_file ../tables/coord_08.apr
eq_file ../tables/IGS08_iran.eq
* Use IGS core
* NCC stab_site
*
use_site clear
use_site ineg_gps asc1_gps artu_gps bahr_gps bjfs_gps braz_gps cas1_gps chat_gps
use_site coco_gps cro1_gps dgar_gps flin_gps gras_gps graz_gps glsv_gps glps_gps
use_site guam_gps hofn_gps hrao_gps iisc_gps irkt_gps joze_gps karr_gps kely_gps
use_site kerg_gps kit3_gps kokb_gps lhas_gps lhaz_gps mana_gps mac1_gps mali_gps
use_site mas1_gps maw1_gps mdo1_gps mkea_gps nama_gps nico_gps nklg_gps nssp_gps
use_site nya1_gps penc_gps pert_gps petp_gps pimo_gps pol2_gps pots_gps quin_gps
use_site ramo_gps riog_gps sant_gps sele_gps sofi_gps stjo_gps suth_gps thti_gps
use_site tixi_gps tow2_gps trab_gps tro1_gps tskb_gps vill_gps unsa_gps usno_gps
use_site whit_gps wtzr_gps wuhn_gps zeck_gps zimm_gps
*
* Estimate orientation and translation
pos_org xtran ytran ztran xrot yrot zrot
* Iterations and editing
stab_ite 4 0.8 4.
* loosen height tolerance
cnd_hgtv 1000 1000 2.0 10.0
```

8.1.4 Supporting Information 2-C: Glorg file for repeatabilities

```
      *
* Globk command file for daily repeatabilities and combination
*
* Required files (usually temporary)
eq_file ../tables/IGS08_iran.eq
make_svs ../tables/sat.apr
com_file globk_rep.com
srt_file globk_rep.srt
sol_file globk_rep.sol
* Optional additional command file
* eq_file rename.eq
*
* A priori station coordinates and Earth orientation table
* apr_file ../tables/iran.apr
* apr_file ../tables/iran.apr
apr_file ../tables/coord_08.apr
in_pmu ../tables/pmu.usno
*
* Input data filter - chi2 and a.p. tolerances high to pass most data
max_chi 100 10000.
*
* Commands to estimate parameters
apr_neu all 5 5 5 0 0 0
apr_svs all 100 100 100 10 10 10 1R
apr_wob 100. 100. 10. 10.0 0.0 0.0 0.0 0.0
apr_ut1 100. 10. 0.0 0.0 0.0 0.0
*
* downweighting of epochs with offset antennas
sig_neu far2 0.05 0.05 0.05 2004 11 01 00 00 2004 11 15 00 00
sig_neu svr2 0.05 0.05 0.05 2004 11 01 00 00 2004 11 15 00 00
sig_neu arda 0.05 0.05 0.05 2004 11 01 00 00 2004 11 15 00 00
sig_neu bakh 0.05 0.05 0.05 2006 06 01 00 00 2006 07 30 00 00
sig_neu khaf 0.05 0.05 0.05 2006 06 01 00 00 2006 07 30 00 00
sig_neu dogh 0.05 0.05 0.05 2006 06 01 00 00 2006 07 30 00 00
sig_neu kerm 0.50 0.50 0.50 1999 09 26 00 00 1999 09 27 00 00
sig_neu khas 0.50 0.50 0.50 1999 09 26 00 00 1999 09 27 00 00
sig_neu musc 0.50 0.50 0.50 1999 09 26 00 00 1999 09 27 00 00
```

```
sig_neu nehb 1.00 1.00 1.00 2007 01 20 00 00 2007 04 22 00 00
sig_neu shkh 1.00 1.00 1.00 2008 01 01 00 00 2008 12 31 00 00
*
*
* Print options - minimal for globk since using glorg output
prt_opt GDLF cdms eras
* glorg command file, print options, and output file
*
org_cmd glorg_rep.cmd
org_opt BLEN CMDS PSUM
org_out globk_rep.org
*
```

8.1.5 Supporting Information 3-A:

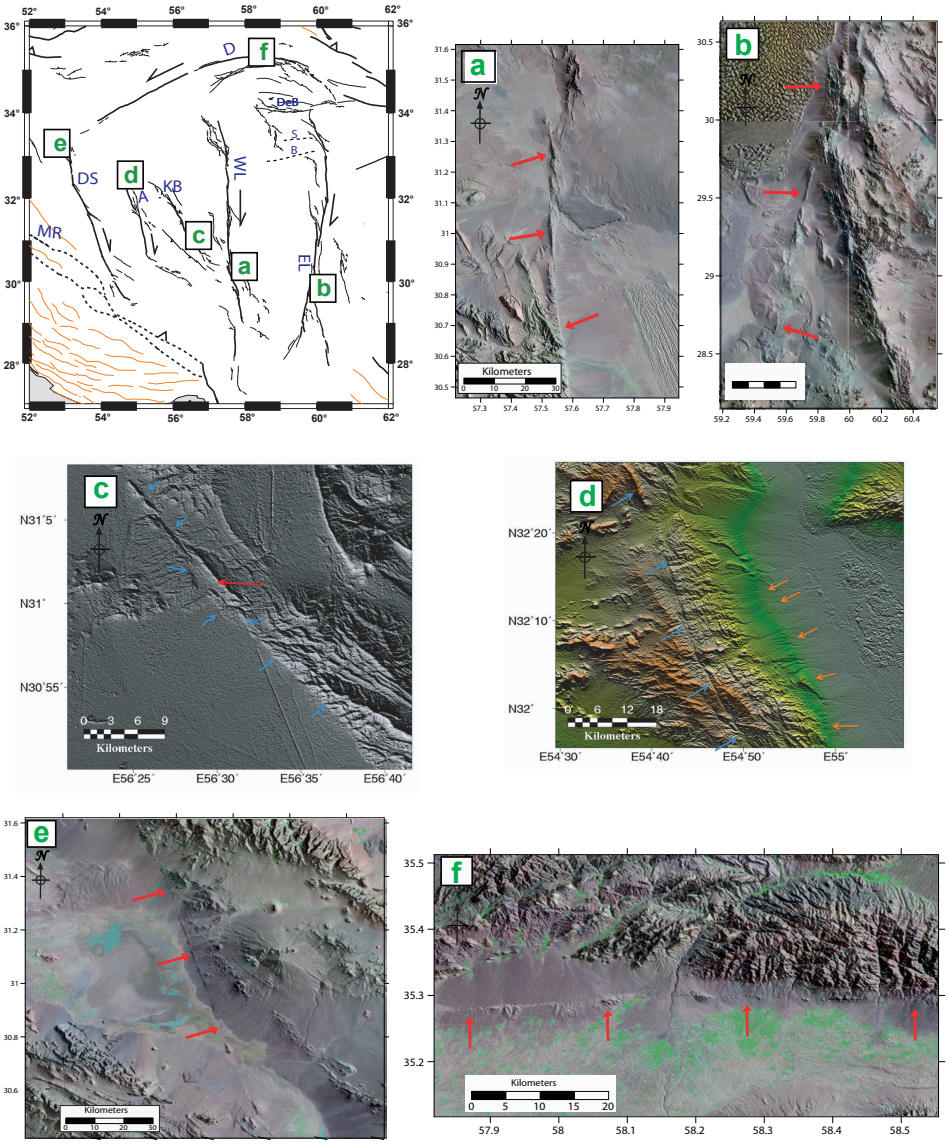

Supporting Information A: Close-up views of traces of major active faults in Central-Eastern Iran. Locations on inset. (a) View of the WL fault, that shows a fresh, linear and narrow trace (red arrows) cutting across the present sedimentary plain and active drainage network, and forming locally a small, steep and hence well-preserved scarplet. (b) View of the EL fault at its southern termination, that shows a fresh, linear and narrow trace (red arrows) cutting across the present sedimentary plain and active drainage network. (c) View of the Kuhbanan fault, that shows a fresh, linear and narrow trace (blue arrows) cutting across the present sedimentary plain and small active channels. The fault trace is punctuated by a pull-apart basin in the center of the view (red arrow) that is in keeping with its right-lateral sense of slip. (d) View of the Anar fault, that shows a fresh, linear and narrow trace (blue arrows) cutting across an ancient topographic relief.

The fault is associated with an active reverse fault in the east (orange arrows) that offsets and folds the recent and present alluvial sediments. (e) View of the Dehshir fault, that shows a fresh, linear and narrow trace (red arrows) cutting across the present sedimentary plain. (f) View of the Doruneh fault that shows a fresh, linear and narrow trace (red arrows) cutting across the present sedimentary plain and left-laterally offsetting various morphological and topographic features. More images can be found in references cited in the text.

8.1.6 Supporting Information 3-B:

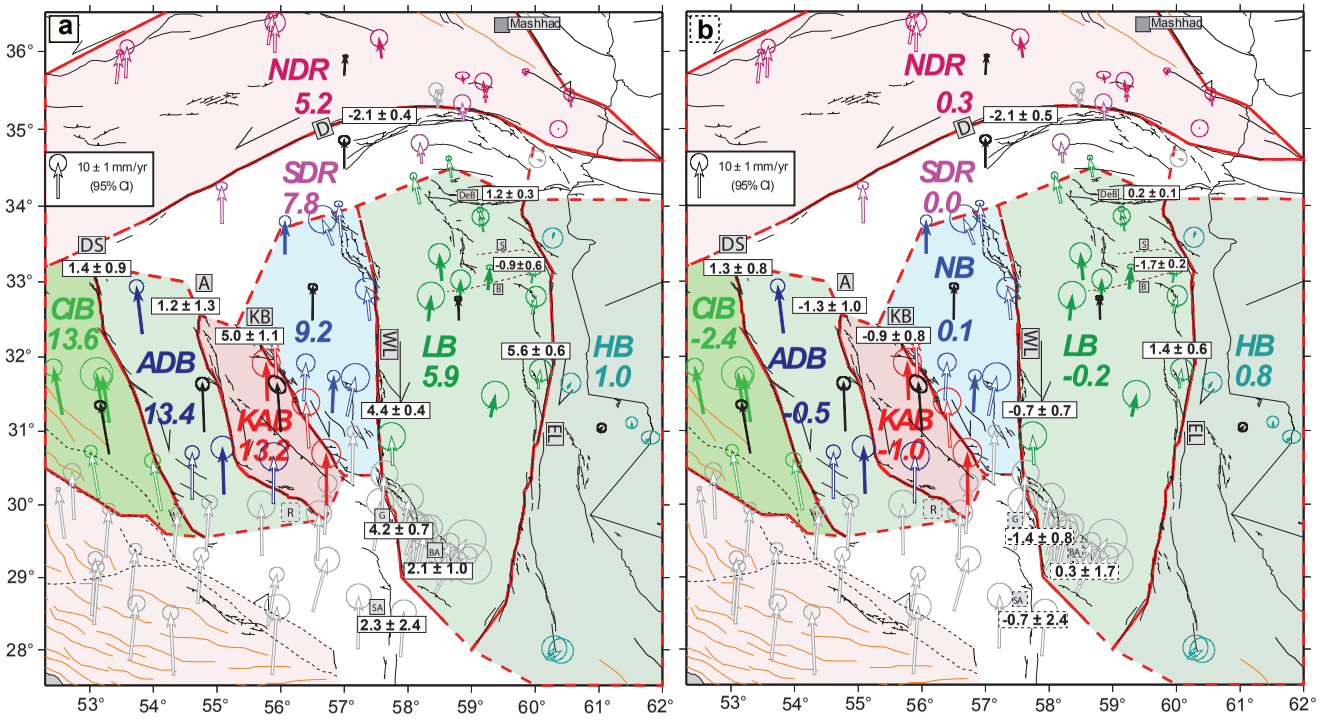

Supporting Information B: GPS velocity field with respect to Eurasia. Plot corresponding to Fig. 3.6 with block velocities expressed in N (a) and E (b) direction instead of NNE and WNW. The vector error ellipses represent a confidence interval of 95%. Filled vectors indicate class 1 stations, open vectors class 2 stations (see Table 3.1). Red lines depict the rigid block contours used in the block model with continuous lines where block contours coincide with known active faults and dashed lines for schematic limits needed to close the block contours. For each block the central velocity obtained from the model with locked faults is represented by a black vector (Table 3.3). Bold colored numbers indicate the block velocity component in N direction (a) and in E direction (b). With the N block velocities (a), fault parallel slip is indicated for NS faults (positive values are right lateral), fault perpendicular slip for EW faults (positive values are extension) (Table 3.4). With the E block velocities (b), fault perpendicular slip is indicated for NS faults, fault parallel slip for EW

faults. Fault velocities are block model predictions considering locked faults. Fault names as in Fig. 3.4 and 3.5. Major block names as in Fig. 3.6.

8.1.7 Supporting Information 3-C:

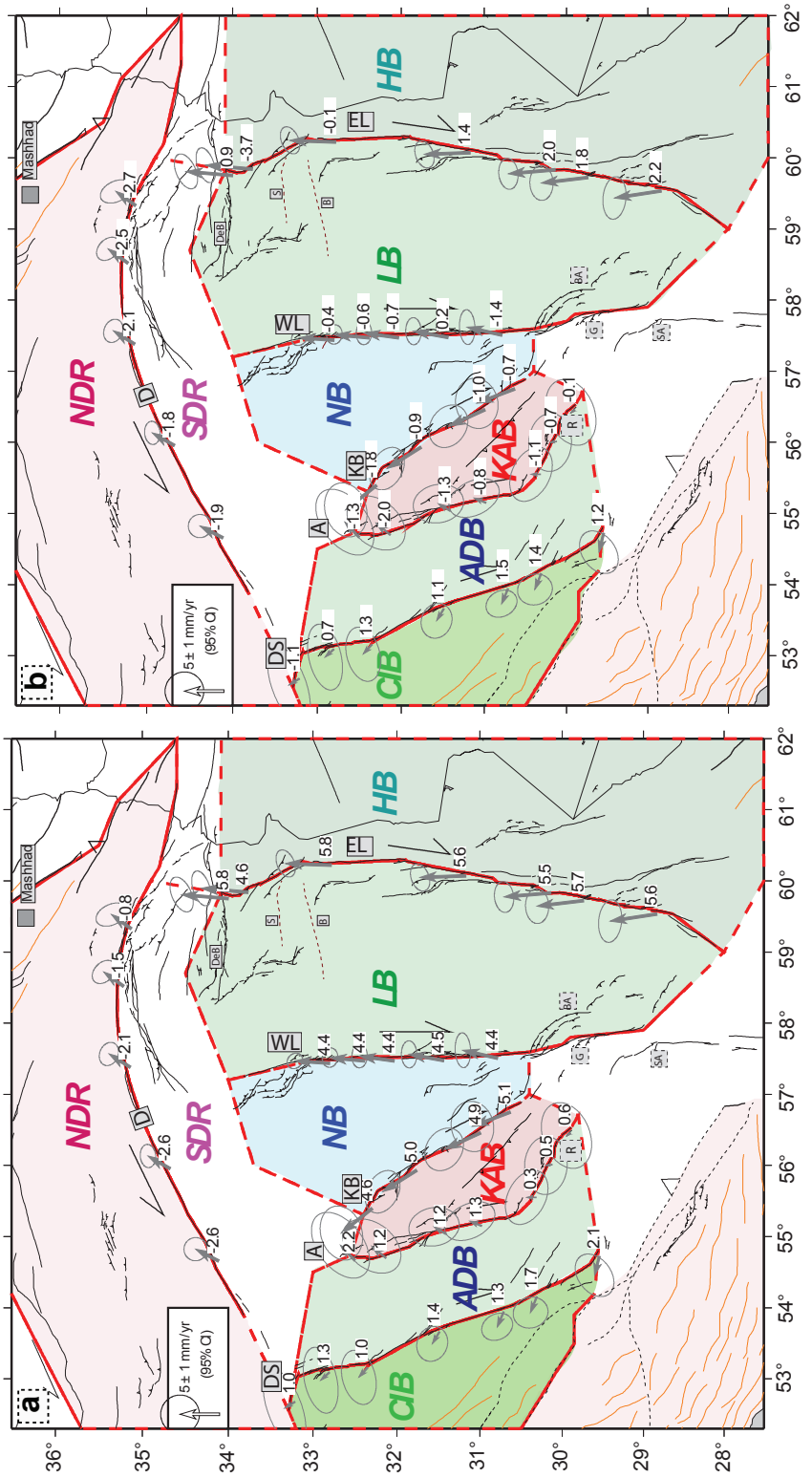

Supporting Information C. Slip rate variability along the faults from block model with locked faults. In plot (a), numbers indicate fault parallel slip (positive values are right lateral), in plot (b) fault perpendicular slip (positive values are extension). Fault names as in Fig. 3.4 and **??**. Major block names as in Fig. 3.6.

8.1.8 Supporting Information 3-D:

Calculation of the eastward and westward velocities of the rotating fault tips.

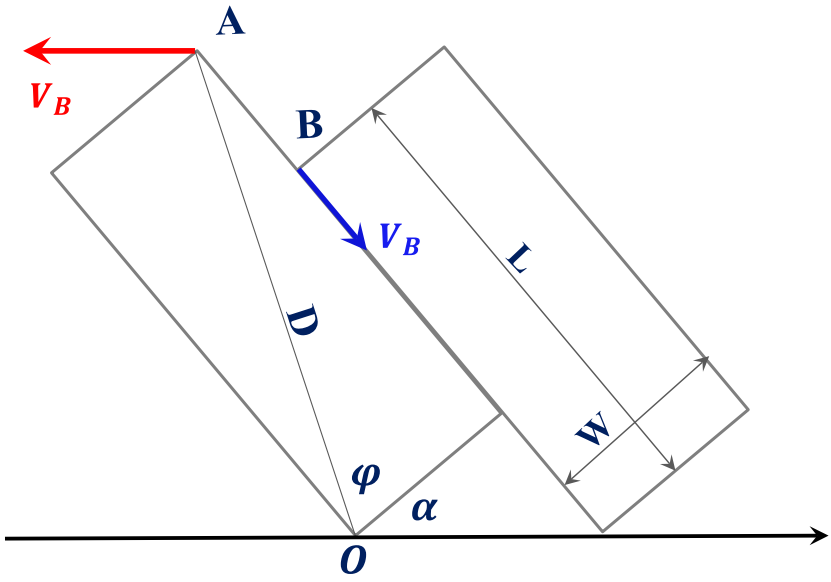

Blocks are rigid. The position of point A with respect to the position of fixed point O is given by $x_A = Dcos(a + f)$.
The velocity of point A, V_A, is $V_A = -Dsin(\alpha + \phi)d\alpha/dt$
With D the diagonal of the block and $f = atan(L/W)$. The point B is at the distance AB from A, equal to W tan α. The velocity of B with respect to A thus is: $V_B = (W/cos^2\alpha)(d\alpha/dt)$

This implies that:

$V_B = -(cos\alpha.V_A)/(cos^2\alpha sin(\alpha + \phi))$ and thus $V_A = -(V_B.cos^2\alpha sin(\alpha + \phi))/cos\phi$

The parameters for the Central-Eastern Iranian faults are:

	Deshir	Anar	KB	WL	EL
$\alpha(°)^*$	25	25	30	5	5
$\phi(°)$	67	68	63	74	69
$V_B(mm/yr)^*$	1.4	2	3.7	4.4	5.6
$V_A/2(mm/yr)$	1.5	2	3	7.5	7.5

V_A is the velocity of point A with respect to fixed point O; or $VA/2$ is the velocity of point A (towards the left) and is also the velocity of point O (towards the right) with respect to block center.

$*$: α is deduced from approximate orientation of faults (Fig. 3.2); V_B is current lateral slip rate measured in GPS data (Table 3.6).